Readout of polymer gel dosimeters using a prototype fan-beam optical computed tomography scanner

by

Warren Gerard Campbell

B.Sc., Thompson Rivers University, 2007

M.Sc., University of Victoria, 2010

A Dissertation Submitted in Partial Fulfillment of the

Requirements for the Degree of

DOCTOR OF PHILOSOPHY

in the Department of Physics and Astronomy

Readout of polymer gel dosimeters using a prototype fan-beam optical computed tomography scanner

by

Warren Gerard Campbell

B.Sc., Thompson Rivers University, 2007

M.Sc., University of Victoria, 2010

Supervisory Committee

Dr. Andrew Jirasek, Co-Supervisor

(Department of Physics and Astronomy)

Dr. Derek Wells, Co-Supervisor

(Department of Physics and Astronomy)

Dr. Michelle Hilts, Member

(Department of Physics and Astronomy)

Dr. Dennis Hore, Outside Member

(Department of Chemistry)

Supervisory Committee

Dr. Andrew Jirasek, Co-Supervisor
(Department of Physics and Astronomy)

Dr. Derek Wells, Co-Supervisor
(Department of Physics and Astronomy)

Dr. Michelle Hilts, Member
(Department of Physics and Astronomy)

Dr. Dennis Hore, Outside Member
(Department of Chemistry)

ABSTRACT

New radiation therapy (RT) techniques for treating cancer are continually under development. Our ability to demonstrate the safe and accurate implementation of new RT treatment techniques is dependent on the information provided by current dosimetric tools. Advanced dosimetric tools will become increasingly necessary as treatments become more complex. This work examines the readout of an advanced dosimeter — the polyacrylamide, gelatin, and tetrakis (hydroxymethyl) phosphonium chloride (PAGAT) dosimeter — using a prototype fan-beam optical computed tomography (CT) scanner.

A number of developments sought to improve the performance of the optical CT device. A new fan-creation method (laser diode module) and new matching tank were introduced. Artefact removal techniques were developed to remove flask seam artefacts and ring artefacts

via sinogram space. A flask registration technique was established to achieve reproducible placement of flasks in the optical CT scanner. A timing-correction technique was implemented to allow for the scanning of continuously rotating samples.

A number of experiments examined factors related to the PAGAT dosimeter. Comparisons of post-irradiation scans to pre-irradiation scans improved dosimeter readout quality. Changes to the PAGAT dosimeter cooling/scanning routine provided further improvements to dosimeter readout. Evaluations of calibration curves showed that a linear calibration curve was less capable of describing PAGAT dose response than a quadratic calibration curve. Intra-gel calibration using another dose distribution was shown to be no less accurate than self calibration, but inter-gel calibrations saw a statistically significant increase in absolute readout errors.

A set of investigations examined how optical CT scanning protocols affected readout quality for PAGAT dosimeters. Doubling the dose delivered to the dosimeter doubled the signal-to-noise ratio. Acquiring and averaging additional light profiles at each projection angle provided only slight reductions in readout noise. Sampling a higher number of projection angles provided substantial reductions in readout noise. Those reductions in readout noise were not lost when sinograms with many projections were encapsulated into sinograms of fewer projection angles. Detector element binning (sinogram space) and pixel binning (image space) also provided substantial reductions in readout noise. None of these elements of the scanning protocol had statistically significant effects on readout errors.

Finally, distinct imaging artefacts seen throughout this work were shown to be caused by radiation-induced refractive index changes in PAGAT dosimeters. Radiation-induced refraction (RIR) artefacts result when dose gradients caused the refraction of fan-beam raylines towards high dose regions. A filtering technique was developed to remove RIR artefacts in sinogram space, but this technique caused substantial blurring to the measured dose distribution.

Table of Contents

List of Tables

List of Figures

List of Abbreviations

2D: two-dimensional

3D: three-dimensional

4D: four-dimensional (i.e., 3D + time)

AAA: analytic anisotropic algorithm (dose calculation algorithm)

AM: adaptive mean (filter)

ArcCHECK™: name of commercially available diode array QA device

ASM: age-standardized mortality (rate)

a.u.: arbitrary units

B_0: external magnetic field (nuclear magnetic resonance)

BANG®: "bisacrylamide, acrylamide, nitrogen, and gelatin" (type of dosimeter)

BCCA: British Columbia Cancer Agency

C: coulombs (unit of charge) *or* Celsius (scale of temperature)

CCD: charge-coupled device

cGy: centigray

cm: centimetre

CT: computed tomography

DC: direct current

Delta^4: name of commercially available diode array QA device

dexel: detector element

DLOS: "Duke large optical CT scanner"

DMOS: "Duke midsized optical CT scanner"

DNA: deoxyribonucleic acid

EPID: electronic portal imaging device

ESTRO: "European Society for Radiotherapy & Oncology"

GE: General Electric

GRIN: gradient refractive index (optics)

Gy: Gray

HeNe: helium-neon (laser)

I: "measurement" light intensity

I_o: "reference" light intensity

IGRT: image guided radiation therapy

ISG: iterative Savitzky-Golay (filter)

ISL: inverse-square law

kV: kilovolt

L: litre

LDM: laser diode module

LED: light-emitting diode

MATLAB: "matrix laboratory" (mathematical software)

MB: megabyte

MeV: mega electronvolt

MH: multi-hole (collimator for the prototype fan-beam optical CT scanner)

MHz: megahertz

mL: millilitre

MLC: multi-leaf collimator

mm: millimetre

MOSFET: metal oxide-silicon field effect transistor

MR: magnetic resonance (imaging)

ms: milliseconds

MU: monitor unit, a measurement of linear accelerator output

mW: milliWatts

n: refractive index

NIPAM: N-isopropylacrylamide (type of polymer gel dosimeter)

nm: nanometer

nMAG: normoxic methacrylic acid and gelatin (type of polymer gel dosimeter)

nPAG: normoxic polyacrylamide and gelatin (type of polymer gel dosimeter)

NMR: nuclear magnetic resonance (imaging)

OCTOPUS™: name of commercially available pencil-beam optical CT scanner

OD: optical density

OSL: optically stimulated luminescent (dosimeter)

PAGAT: "polyacrylamide, gelatin, and THPC" (type of polymer gel dosimeter)

PC: personal computer

PGD: polymer gel dosimeter

PRESAGE™: name of commercially available dye-based plastic dosimeter

QA: quality assurance

R_1: spin-lattice relaxation rate

R_2: spin-spin relaxation rate

RD: radio-density

RF: radio frequency

RI: refractive index

RIR: radiation-induced refraction (artefacts)

ROI: region of interest

s: seconds

SS: single-slot (collimator for the prototype fan-beam optical CT scanner)

T: transmission (proportion of transmitted light) *or* tesla (magnetic flux density)

T_1: spin-lattice relaxation time

T_2: spin-spin relaxation time

THPC: tetrakis (hydroxymethyl) phosphonium chloride

TLD: thermoluminescent dosimeter

TPS: treatment planning software

USB: Universal Serial Bus

UVic: University of Victoria

VIC: Vancouver Island Centre

Vista^{TM}: name of commercially available cone-beam optical CT scanner

VMAT: volumetric modulated arc therapy

Z: atomic number

θ: theta, angle

λ: lambda, wavelength (light) *or* gyromagnetic ratio (nuclear magnetic resonance)

μ: mu, mean (average) *or* linear attenuation coefficient

μs: microseconds

σ: sigma, standard deviation

ω_0: precessional frequency

ACKNOWLEDGEMENTS

First and foremost, I want to thank my supervisors, Dr. Andrew Jirasek and Dr. Derek Wells. They both gave me the freedom to tinker with ideas, but still reined me in when necessary. They both offered invaluable advice that helped me tackle all of the challenges I've encountered. I would also like to thank my committee members, Dr. Michelle Hilts and Dr. Dennis Hore. Their unique viewpoints and helpful input helped strengthen this work.

I must also acknowledge the other people that have been involved with this project over the years. This project began, before I ever arrived at UVic, with David Rudko; his master's thesis brought this scanner into existence. Nicolas Braam (UVic Electronics) worked on multiple versions of data acquisition hardware and firmware for the scanner; that work produced a motherboard and set of daughterboards that are so low noise, only one light profile measurement per projection angle is necessary. Dave Yardley and Steve Gray (BCCA-VIC machine shop) provided critical support by performing custom repairs for a one-of-a-kind prototype; Steve also helped with the design and construction of matching tank 2.0. Sean Adams (UVic glassblower) was able to provide a key component for said matching tank: a custom cut glass cylinder. Finally, I would like to thank Holly Johnston and Evan Maynard for their help with dosimeter irradiations; I could talk about gels with you guys for hours.

I would like to thank all of the students, scientists, and staff in the UVic Physics & Astronomy Department and the BCCA-VIC Physics Department. Even during the hard times[1], you have filled the last seven years with a healthy supply of happy memories.

Finally, I would like to thank my loved ones for their unfaltering support. Mom, Dad, Tyler, and many other friends and family members. Most of you will never read this document, but I love you all the same. Here's to finally becoming a doctor[2].

[1] Quantum Mechanics.

[2] *"Well, no, not that kind of a doctor... a 'Science Doctor.'"*

DEDICATION

"'Is this good enough?' Good enough for what?

Is this good enough to throw out the window?

Is this good enough to crumple up, or set on fire?

What do you mean by 'good enough?'

[sigh]

Warren, you shouldn't be aiming for 'good enough.'

You should be aiming for 'great!'

Go back to your desk and keep working."

To my third grade teacher — **Mrs. York** — for forcefully instilling in me a desire to aim for 'great!'

Chapter 1

Introduction

This doctoral thesis examines the readout of polymer gel dosimeters using a prototype fan-beam optical computed tomography scanner. The ultimate intent of such a system — dosimeters and scanner — is to measure the radiation dose distribution delivered to the volume of the dosimeter. Such measurements would help clinicians validate advanced radiation therapy techniques for treating cancer.

1.1 Motivation, Part I: Cancer & Radiation Therapy

Cancer is the new, unceasing replication of dysfunctional cells. When left unaddressed, this unceasing replication can lead to a long list of serious health complications. It is Canada's number one killer, responsible for 30% of all deaths [1]. According to the most recent numbers available from Statistics Canada (CANSIM table 102-0561), Canada's top 5 causes of death are shown in Figure 1.1. The latest statistics from the Canadian Cancer Society estimate that 76,600 Canadians will die of the disease in 2014 [2]. In general, it would appear that the early detection techniques and methods used to prevent and/or treat cancer are improving

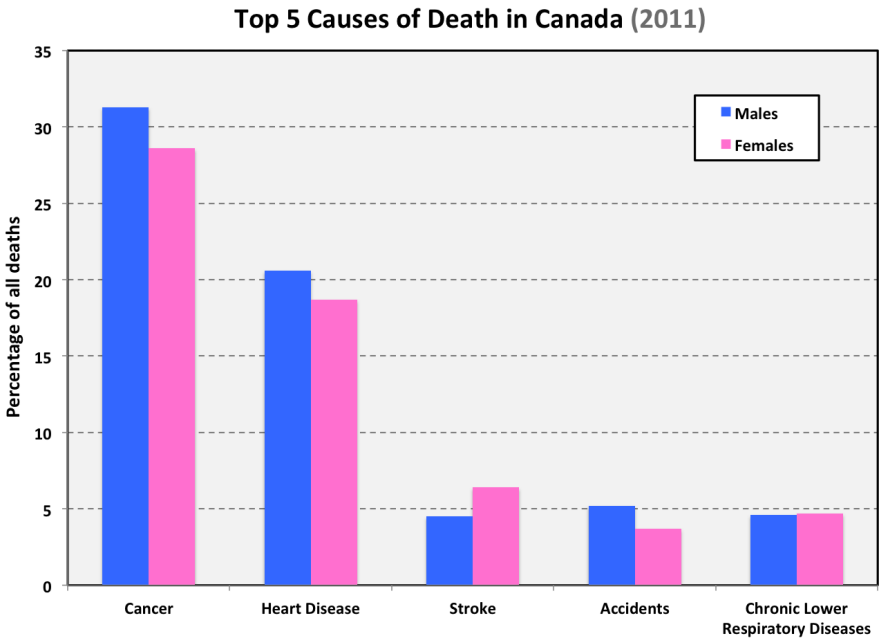

Figure 1.1: The top 5 causes of death in 2011 for males and for females in Canada. Source: Statistics Canada, CANSIM table 102-0561.

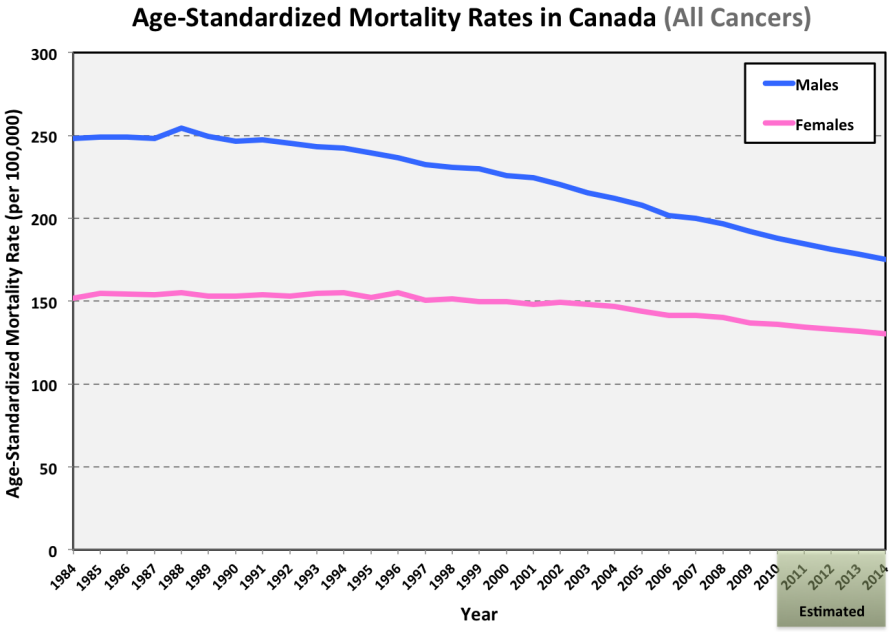

Figure 1.2: Age-standardized mortality rates for all cancers in Canada since 1984. Source: "Canadian Cancer Society 2014 Statistics"

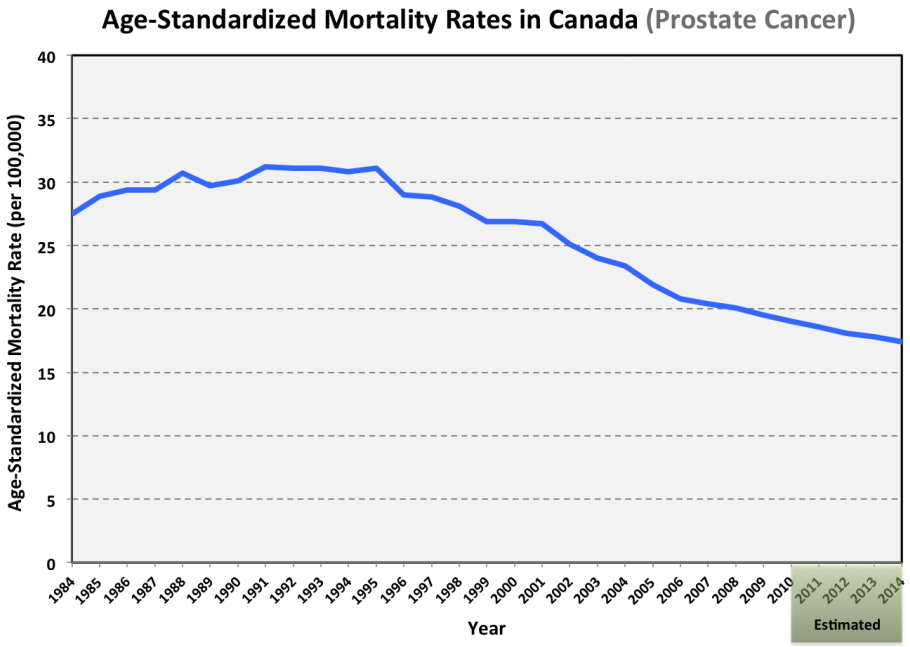

Figure 1.3: Age-standardized mortality rates for prostate cancer in Canada since 1984. Source: "Canadian Cancer Society 2014 Statistics"

over time (see Figure 1.2). Taking into consideration all types of cancer, the overall age-standardized mortality (ASM) rate for cancer has been steadily decreasing over the last 20 years.[1] Since 1994, cancer ASM rates have decreased by 28% for men and 16% for women. However, when examining specific tumour sites, different trends reveal themselves.

The most common cancer among men is prostate cancer. Between 1984 and the mid-1990s, mortality rates for prostate cancer were gradually increasing (see Figure 1.3). Since then, prostate cancer mortality rates have been declining, with the decline becoming significant between 2001 and 2009 ($\sim$3.9% per year) [2]. The Canadian Cancer Society attributes this recent decline to the introduction of hormonal therapies and advances in radiation therapy. As such, many researchers are motivated by the hope that continuing to improve radiation therapy techniques will result in continued improvements in patient outcomes.

[1] Age-standardized mortality rates are mortality rates that have been adjusted to represent a consistent age distribution. Here, rates have been adjusted to match the population of Canada in 1991.

1.2 Radiation Therapy

The fundamental task in successfully treating a patient with cancer is to prevent the incessant growth of cancer cells from disrupting the wellbeing of the patient. Early treatments took an obvious approach: cut out the tumour. Today, that approach still remains: removing the tumour would be ideal. So, surgery is commonly considered a first choice treatment. Nevertheless, surgery is not always an option. In some cases, surgery is not an option due to the patient's physical fortitude. Can they survive the physical demands that accompany an operation? In some cases, it is simply a matter of anatomy. Can the tumour be cut out of the patient without undue harm to surrounding organs? In some cases, it is a matter of patient choice. Side effects that affect the patient's quality of life need to be evaluated when surgery is being considered. Comparing radical prostatectomy and radiation therapy for the treatment of prostate cancer, patients undergoing surgery have experienced higher rates of incontinence and impotence [3]. If the tumour cannot be successfully removed from the patient without undesirable consequences, an alternative approach is to kill tumour cells. This can be achieved using radiation, chemotherapy, or a combination of radiation and chemotherapy[2].

Relatively speaking, the treatments offered by modern radiation therapy are fairly new. However, cancer is a very old disease. The earliest known case of cancer is believed to be outlined in a doctor's notes from ancient Egypt. In approximately the year 2625 BC, a physician wrote about a case of *'bulging masses on the breast,'* and indicated that he knew of no treatment for such a case [4]. Around 4500 years later, Wilhelm Röntgen stumbled upon the existence of x-rays in 1895 [5]. Following the discovery of these *new kind of rays*, physicians were quick to experiment with their use for the treatment of cancer [6].

[2]Chemotherapy is a class of systemic treatments that use chemical substances to kill tumour cells. These treatments preferentially attack rapidly dividing cells in the body, which includes cancer cells along with a number of normal cell types (e.g., hair follicles, bone marrow, and cells in the digestive tract).

Today, ionizing radiation is commonly used for the treatment of cancer. According to the British Columbia Cancer Agency, approximately 55% of cancer patients receive some form of radiation therapy as part of their treatment [7]. Over the past century, improvements in medical imaging, advancements in our understanding of radiobiology, and development of new technologies for radiation delivery have allowed health professionals to induce tumour death while reducing harm to the normal, healthy tissues that surround the tumour. To gain a better understanding of how radiation can be used to cause tumour death, one should first consider how radiation interacts with matter.

1.2.1 Interactions of Ionizing Radiation with Matter

Radiation is often delivered using beams of photons in the mega electron volt (MeV) energy range. Photons interact with matter discretely as they traverse a medium, and they transfer energy to that medium in three main types of events: the photoelectric effect, the Compton effect, and pair production [8, 9]. Diagrams for these three events are shown in Figure 1.4. In the photoelectric effect, a photon is fully absorbed by an atomic electron, ejecting it from the atom. The ejected electron takes with it the entire energy of the incident photon minus the electron's atomic binding energy. Of the three interaction types indicated, the

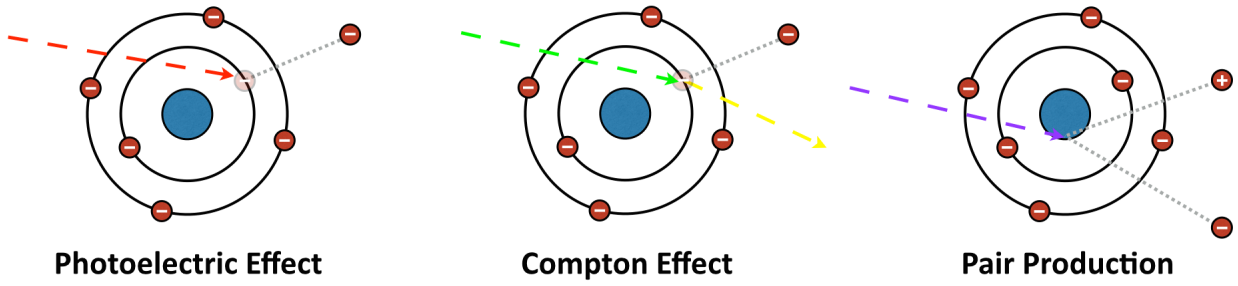

Figure 1.4: Illustrations of the three main types of interactions that occur when high-energy photons interact with matter: the photoelectric effect, the Compton effect, and pair production.

photoelectric effect is the dominant interaction type in water for photons with energies less than 26 kilovolts (kV). In the Compton effect, only a portion of an incoming photon's energy is imparted on the electron. As a result, the electron and the photon both scatter, leaving the photon with a reduced energy. The Compton effect is the dominant interaction type in water for photons with energies in the range of 0.03 MV to 24 MV. For pair production, a high-energy photon interacts with the nucleus of an atom and the entire energy of the photon is converted into a matter/anti-matter pair of particles: an electron and a positron. Excess photon energy that is not expended in the creation of these particles is imparted on the two particles as kinetic energy. Pair production only occurs for photon energies above a threshold[3] of 1.022 MV, but it begins to become the dominant interaction type in water for photons with energies greater than 24 MV.

When used to treat a patient, the energy deposited by ionizing radiation (in this case, the dose) causes ionizations within cells that can result in cell death. It has been shown that a cell's most sensitive target is its nucleus, specifically the deoxyribonucleic acid (DNA) macromolecule [10]. Radiation dose is prescribed in units of Gray (Gy), with 1 Gy = 1 Joule/kilogram. To gain a sense of how dose affects a single cell, 1 Gy of radiation will cause approximately 100,000 ionizations, 20–40 double-strand DNA breaks, and will kill a mammalian cell ∼30% of the time [11]. Ionizing radiation does not discriminate between tumour cell or healthy cell. So, clinicians need to act judiciously when using ionizing radiation for therapeutic purposes.

1.2.2 External Beam Radiation Therapy

External beam radiation therapy is a common form of radiation delivery, and it has continued to evolve over the past century [8, 9]. Improvements to patient outcomes are the result of

[3]The energy threshold for pair production is equal to the total of rest mass energies for the two particles, 0.511 MV each.

two treatment priorities: (i) ensure the adequate coverage of the tumour volume, and (ii) limit the radiation exposure to surrounding healthy tissues. The first step that was taken to reduce dose to normal tissues was to use multiple, simple treatment fields from multiple treatment angles. This way, each beam could contribute a portion of the tumour's prescribed dose, while the burden of entry and exit dose was shared amongst a larger volume of normal tissues. A higher volume of normal tissue was irradiated, but these tissues were exposed to lower, more tolerable levels of radiation.

Due to advancements in imaging technologies, oncologists became more capable of measuring the shape of the tumour, which allowed for better definitions of the target intended to be hit by radiation. This allowed therapists to limit the shapes of these multiple fields to the shape of the target rather than using rectangular-shaped beams. Physical compensators — blocks of dense materials[4] with thicknesses that varied in 2D — were developed to modulate the intensity map of each beam [12]. However, this method of modulation affected the energy spectrum of the beam. Beam intensity modulation was enhanced further following the development of multi-leaf collimators (MLCs), which allowed the intensity maps of individual beams to be modulated within the outline of the target without affecting the spectrum of the beam [13]. With this new tool, treatment planners became capable of choosing a set of treatment fields and a desired dose distribution around a target volume, and then calculating the dynamic MLC motion that would best achieve that desired dose distribution (i.e., inverse-planning) [14].

Recent advancements in radiation delivery expanded from using a set of individual treatment fields to using a continuous rotation of treatment fields. Volumetric modulated arc therapy (VMAT) can spread entry and exit dose more evenly among normal tissues even further by calculating the MLC motion necessary to modulate the treatment field while the beam is rotated about the patient [15]. This technique can allow for sharper dose gradi-

[4]Typically, lead or tungsten.

ents to be achieved around the tumour volume, providing the opportunity to treat tumours that are in close proximity to vital organs. Additionally, VMAT can be performed with less beam-on time and shorter treatment times [15].

Due to the steep dose gradients that are typically present in VMAT treatments, treatment accuracy becomes more important. Steep dose gradients near organs at risk are more sensitive to positioning errors. Image guided radiation therapy (IGRT) is aimed at addressing this need for accuracy by taking advantage of imaging equipment on the radiation treatment unit to ensure accurate patient positioning [16]. Image guidance becomes especially important for tumour sites that are mobile from day-to-day (e.g., prostate movement due to the filling and voiding of the bladder and rectum). Other tumour sites are mobile during treatment. New research aims at improving radiation therapy in cases involving tumour motion during treatment, such as the motion of lung cancers due to breathing [17]. These treatments plan to target the patient in 4D (3D + time) to account for changes in the target volume over time.

Developments that have occurred in radiation therapy over the past century demonstrate a considerable increase in treatment complexity. Developments in radiation dosimetry need to keep pace with developments in radiation delivery. Although researchers are already trying to make 4D radiation therapies a reality, most clinics still rely on point dosimeters and 2D dosimeters for treatment verification. The primary intention of this thesis is to advance our knowledge of 3D dosimeters, to work on their implementation, and to ultimately expand the dosimetry toolset that is available to clinicians.

1.3 Radiation Dosimetry

The accuracy and reliability of any radiation therapy technique needs to be established before it can be used to treat patients. In order to evaluate the accuracy of a given technique,

measurements are taken while the technique is rehearsed using a phantom[5]. To evaluate the reliability of the technique, measurements are taken while practice runs are repeated. Additionally, alterations can be made to these practice runs in order to determine how sensitive the technique will be to modifications, such as errors in patient positioning or changes in the patient's anatomy that occur over time. In any case, the radiation dosimetry tools used for these measurements must be capable of providing all of the information necessary to verify the new treatment technique. The following subsections describe a variety of different dosimetry tools that are intended for use in the clinic.

1.3.1 Point Dosimeters

Point dosimeters provide a single measurement of dose at a given position in space. Five main types of point dosimeters are used in the modern cancer clinic: (i) ionization chambers, (ii) thermoluminescent dosimeters, (iii) optically stimulated luminescent dosimeters, (iv) semiconductor dosimeters, and (v) diamond detectors [18].

Ionization chambers consist of an isolated mass of gas between two electrodes. When the ionization chamber is exposed to ionizing radiation, charges are freed within the gas. By applying a known voltage across the electrodes, the charges freed from the gas can be collected and measured. By knowing the amount of work required to free these charges from the specific type of gas, one can calculate the amount of absolute dose, in Gray, that has been delivered to the gas. Then, one can calculate the absolute dose that would have been delivered to water (or a patient[6]) at the position of the ion chamber. Absolute dose measurements are useful for commissioning the beam outputs of new treatment machines and for monitoring their output over their lifetime.

[5]A 'phantom' refers to a physical object that is used to simulate a patient. This can be as simple as a cylinder of water, or as realistic as an actual human skeleton embedded into a anthropomorphic dummy made out of radiologically water-equivalent plastics (i.e., the RANDO® phantom).

[6]Human tissues are radiologically water-equivalent. So, with the exception of prosthetics and implants, patient data is often considered to be analogous to 'various densities of water.'

Thermoluminescent dosimeters (TLDs) are crystals[7] that contain "traps" in higher energy bands where electrons excited by ionizing radiation can be detained for long periods of time. The accumulation of these trapped electrons becomes the physical quantity that represents a TLD's measurement. In order to readout this quantity, the TLD is heated so that these trapped electrons are released from their higher energy band and allowed to fall back to their ground states. During this transition to their ground state, visible photons are emitted. The intensity of this visible light is measured, providing information about the amount of radiation the crystal has been exposed to. In order to convert these light quantities to dose, the dose–response needs to be calibrated by correlating the amount of light released to the amount of dose absorbed by the dosimeter. TLDs are often used for point-measurements during treatment and for the routine monitoring of personnel radiation exposure.

Optically stimulated luminescent (OSL) dosimeters are similar to TLDs in that the amount of dosage they absorbs can be ascertained by the amount of light given off by an OSL [19]. OSL materials[8] trap electrons in a higher energy band [20]. However, rather than using heat to initiate the release of trapped electrons, visible light is used. To stimulate this release, the OSL is bombarded by photons in the infrared range (∼540 nm), and emitted photons (i.e., the photons representative of the dose absorbed by the OSL) occur in the visible range (∼420 nm) [20]. Compared to TLDs, OSLs have the advantage of not needing to be heated, so they can be configured into materials that are less heat-resistant.

Semiconductors can also be used for point measurements. Ionizing radiation generates charges in doped semiconducting materials[9]. Measurement of these charges gives a proportional representation of the energy deposited in the semiconductor. At therapeutic x-ray energies, diodes can serve as a substitute for an ionization chamber [18]. Metal oxide-silicon field effect transistors (MOSFETs) can be used for *in vivo* dosimetry [21]. The higher den-

[7]Typically, calcium fluoride or lithium fluoride.
[8]Typically, a sulfide doped with cerium, samarium, or europium.
[9]Typically, silicon or germanium.

sities and higher Z-values of semiconductors make them more sensitive to radiation than ion chambers. Also, their small size can be beneficial in cases where resolution is important, such as small-field dosimetry.

Diamond detectors are also used for point dosimetry. Diamond detectors collect charge similar to semiconductor materials, but with a Z-value closer to that of tissue (e.g., $Z_{silicon}$=14, Z_{carbon}=6, $Z_{tissue}\approx$7.42) [22]. Very small diamond crystals[10] can be made synthetically, which also makes them suitable for measurements where good resolution is important [23]. Furthermore, due to their near-tissue Z-value, diamond detectors are relatively energy independent [24].

Point dosimeters are useful — and in some instances, mandatory — for many clinical tasks (e.g., linac commissioning, output monitoring, absolute measurements for treatment validation). However, to evaluate the spatial distributions of dose delivered by modern radiation therapy techniques, one cannot rely solely on point dosimeters.

1.3.2 Planar Dosimeters

Planar dosimeters measure dose distributions in two dimensions (i.e., 2D dosimeters). There are two main types of 2D dosimeters in use in the clinic today: (i) films, and (ii) flat panel detector arrays [18].

For film measurements, photographic film was originally used to measure 2D intensity maps of a treatment beam. Photographic films feature a 2D distribution of silver bromide granules, which undergo changes when exposed to ionizing radiation that allow them to be developed chemically. Development of photographic film removes the bromine from the granule, leaving behind granules of silver. This results in increased optical density for higher doses. Newer, dye-based films (e.g., GafChromic films; International Specialty Products; Wayne, NJ, USA) have been developed that are near tissue-equivalent and do not need to

[10]For example, the microDiamond detector (PTW; Freiburg, Germany) has a 0.004 mm^3 active volume.

be chemically developed [25, 26]. For both types of film, their dose–response needs to be calibrated. Using a calibration curve, one is able to convert measured film opacity into measured dose.

Flat panel detector arrays consist of a planar 2D arrangement of electronic point dosimeters (e.g., a 512×384 rectangular arrangement of detectors with 0.784 mm spacing between detectors) [27]. Each detector in the array represents a single pixel for the image recorded by the device. Typically, these point dosimeters are amorphous silicon photodiodes [28, 29]. Measuring ionizing radiation indirectly, a flat panel detector uses an x-ray intensifier material[11] to convert x-rays into visible photons, which are then detected by photodiodes [30]. Flat panel detectors cannot be used within a phantom due to their bulky electronics. Instead, one or two flat panel detectors are often equipped on the treatment unit. One of these devices is positioned opposite of the head of the treatment unit in order to record the therapeutic beam of the machine. In such an arrangement, this device is referred to as the electronic portal imaging device (EPID). Megavoltage images acquired by the EPID can be used for patient positioning verification purposes [31]. For treatment units with two flat panel detectors, the second is a lower energy (kV) imaging device intended specifically for patient positioning verification. Usually, this device and its kV x-ray source are set up orthogonal to the EPID and the treatment unit head.

Films and EPIDs are both very useful for acquiring 2D dose measurements with good spatial resolution. The flexibility of films allow them to be used in a variety of different phantom setups. However, the dose–response of film has an angular dependence that needs to be considered for accurate results [32]. For treatment plans that consist of multiple beams at static gantry angle[12] positions, portal images[13] provide sufficient data for treatment verification purposes [30]. However, for treatment plans that have the gantry angle changing

[11] Typically, gadolinium oxysulfide or caesium iodide.
[12] 'Gantry angle' refers to the angular position of the gantry of a treatment unit (e.g., a linear accelerator).
[13] A 'portal image' refers to the 2D image that is obtained on an electronic portal imaging device.

while the beam is on (i.e., arc therapy treatments), films cannot be used for portal imaging. This is because films accumulate the dose they are exposed to, so a film-based portal image cannot provide information on beam output with respect to gantry angle. EPIDs are capable of taking multiple measurements during treatment, making them much more suitable for arc therapy treatments [29]. Nonetheless, 2D verifications of beam output only assess whether or not a treatment machine is performing as expected. These measurements alone do not provide 3D dose information.

1.3.3 Indirect 3D Dosimetry

Theoretically, one could create a 3D arrangement of point dosimeters in an attempt to acquire dose measurements for a 3D volume. In reality, this would not be practical. First, due to their higher densities and higher Z-values, radiation would not traverse a volume of point dosimeters in the same manner as it would traverse through tissues. The presence of these dosimeters would perturb the measured dose distribution.

Alternatively, point dosimeters can be used more sparingly in a 3D arrangement to obtain 3D dose information with less perturbation [33]. Two examples of 3D diode arrays embedded into plastic cylindrical phantoms are commercially available. First, the Delta^4 diode array phantom (ScandiDos AB; Uppsala, Sweden) uses two perpendicular planar arrays of diodes in an "X" shape [34]. Second, the ArcCHECK^{TM} quality assurance (QA) device (Sun Nuclear; Melbourne, FL, USA) uses a helical array of diodes in an "O" shape [35]. These devices use point measurements from their array to reconstruct the 3D dose distribution realized within their cylindrical volume. Additionally, due to the fact that diode measurements can be monitored over time, these devices are capable of calculating 4D dose distributions as well [36]. However, diodes in these devices are sparsely distributed. So, rather than directly measuring dose in a 3D volume, 3D diode arrays measure dose at a sampling of points in

that volume and reconstruct an assumed dose for the remainder.

EPID measurements can also be used to calculate 3D dose distributions. Using 2D measurements of a photon beam's output in free air, one can calculate the hypothetical 3D dose distribution that would have been realized in a virtual cylindrical volume [27]. Hence, EPID measurements can also allow for the reconstruction of a 3D dose distribution from 2D measurements.

Techniques that indirectly evaluate 3D dose distributions undoubtedly provide useful information for the clinician. For instance, such measurements can demonstrate whether or not a treatment machine is capable of delivering the treatment as expected. However, the indirect 3D dosimetry methods mentioned above only evaluate machine performance. Any inferences made about the dose realized within the patient demand that assumptions be made about the patient's positioning. Portal images can be collected during actual treatment, allowing indirect 3D dosimetry to be performed with the patient in place using transit dosimetry methods [31, 37]. However, transit dosimetry with the patient in place can only be performed for treatment techniques that have already been approved for the treatment of actual patients.

It is in this gap — between *making assumptions about a new treatment* and *verifying a treatment that has already been vetted* — where 3D dosimeters show their highest value. Before a complex new treatment is approved for patient treatment, 3D dosimeters can be used as synthetic patients[14] to demonstrate whether or not the new technique is being performed accurately and reliably.

[14]Obviously, 3D dosimeters do not exhibit the true complexity of a real patient (e.g., variations in density, tissue deformations mid-treatment, changes in anatomy over the course of multiple treatments, etc.). Functioning as a synthetic patient, a volume of homogenous gel is fairly basic. However, one could argue that if you cannot perform a complex treatment on a volume of homogenous gel, you should not expect the treatment of actual patients to be any simpler.

1.3.4 3D Dosimeters

A 3D dosimeter consists of a volume of near tissue-equivalent substance that responds to radiation in such a way that the intensity and spatial distribution of its radiation-induced response can be measured. By measuring these changes in 3D and calibrating the dose–response relationship of the substance, one can obtain a measurement of the 3D dose distribution realized within the dosimeter. For instance, a polymer gel dosimeter turns opaque when irradiated and its opacity can be measured using an optical computed tomography (optical CT) scanner. Simply put, one can consider a 3D dosimeter to be a 'practice patient.' These practice patients can allow clinicians to experiment more freely with new radiation therapy techniques before such techniques could ever ethically be used to treat actual patients. The topic of 3D dosimeters and polymer gel dosimetry will be described in greater detail in Chapter 2. The 3D dosimeter readout method used in this work — optical CT — will be discussed in Chapter 3.

1.4 Motivation, Part II: Verification of Advanced Radiotherapy Techniques

Whenever a new radiation therapy technique is introduced, its accuracy and reliability needs to be established. In practice, this entails a lot of planning to establish the goals of the new technique and the means by which those goals will be achieved. Then, the new technique is rehearsed and measurements need to be taken during practice runs to demonstrate whether or not the technique achieves what it set out to do. For example, if a researcher were to devise a new technique for treating lung cancer, then measurements using 2D dosimeters or point dosimeters would likely not suffice. The lungs are four-dimensional. They expand and contract as the patient inhales and exhales. This makes them challenging to treat.

Nevertheless, the lungs are worthy of added consideration. At this time, lung cancer is arguably the most important type of cancer that Canadians should be tackling.

Lung cancer is the number one killing cancer in Canada. Although prostate cancer and breast cancer are well known as the most common cancers, respectively, for men and women, lung cancer has a higher mortality rate per case. Figure 1.5 shows incidence and death rates for the three most common cancers, which are also the top three killing cancers for males and females [2]. For both men and women, lung cancer accounts for 27% of all cancer deaths in Canada today.

Additionally, lung cancer age-standardized mortality rates among women have been increasing in recent decades (see Figure 1.6). Since 1984, the lung cancer ASM rate for women has grown by more than 60%. An opposite trend was observed among men. Although current lung cancer mortality rates are still higher for men than they are for women, the lung cancer ASM rate for men has decreased by more than 40% since 1984. The convergence of male and female lung cancer rates has been attributed to a matching convergence of the smoking habits of men and women [38, 39]. The overall decline of lung cancer deaths has been attributed to smoking cessation trends [39, 40]. Fortunately, since 2006, lung cancer ASM rates for women have no longer been increasing [2]. Nevertheless, lung cancer kills more Canadians today than any other type of cancer, regardless of gender.

Recently, it was proposed that the radiation therapy community's emphasis on safety has been a hindrance on the introduction of new radiation therapy technologies and treatment strategies [41]. In April of 2014, a debate session on this topic was held at the 33^{rd} annual scientific meeting for the European Society for Radiotherapy & Oncology (ESTRO[15]). There, Dr. Håkan Nyström — chief physicist at the Skandion Clinic in Sweden — argued *for* the

[15]ESTRO: European SocieTy for Radiotherapy & Oncology

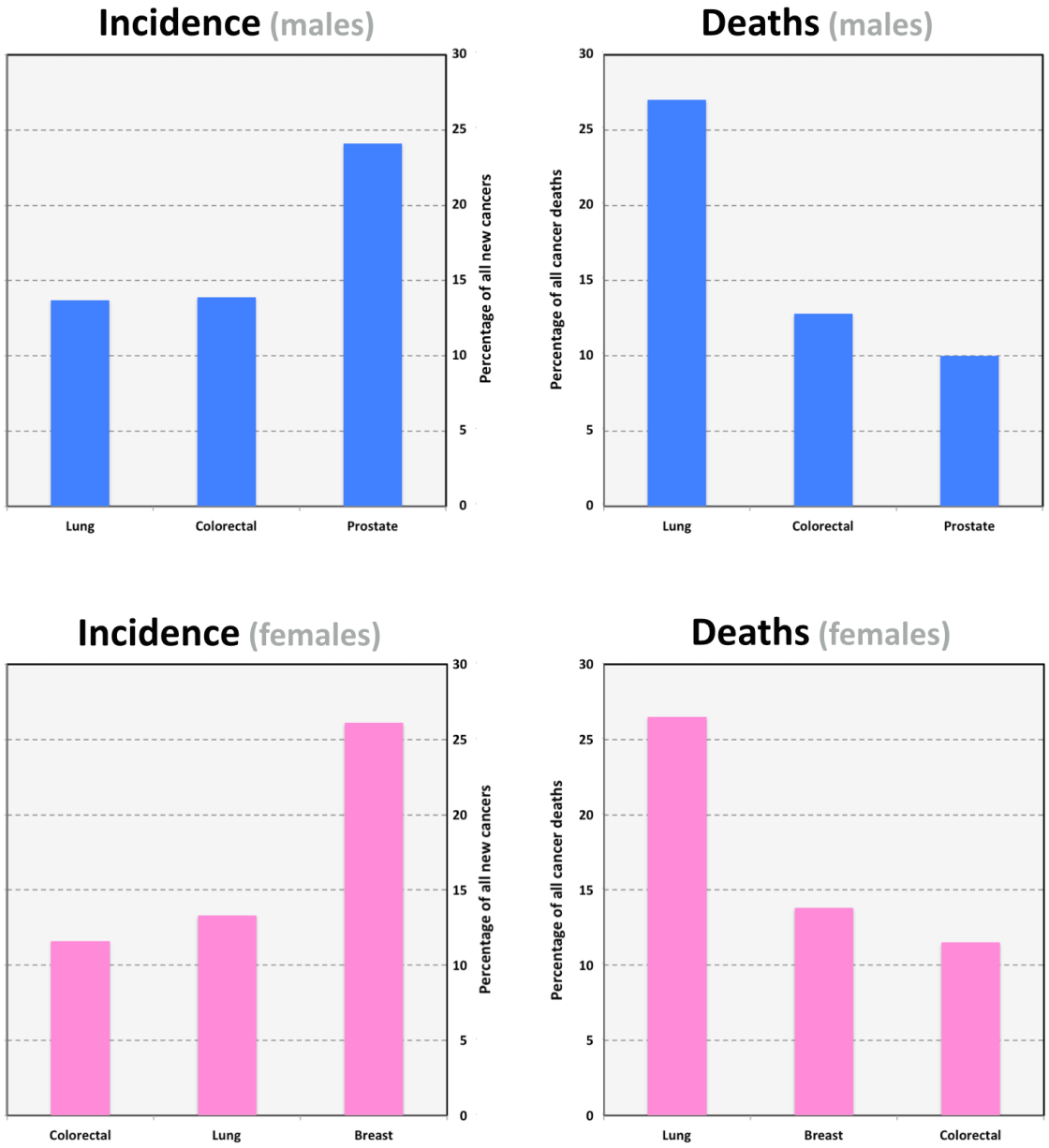

Figure 1.5: Estimated 2014 incidence and death rates for the three most common cancers in Canada for males and females. Source: "Canadian Cancer Society 2014 Statistics"

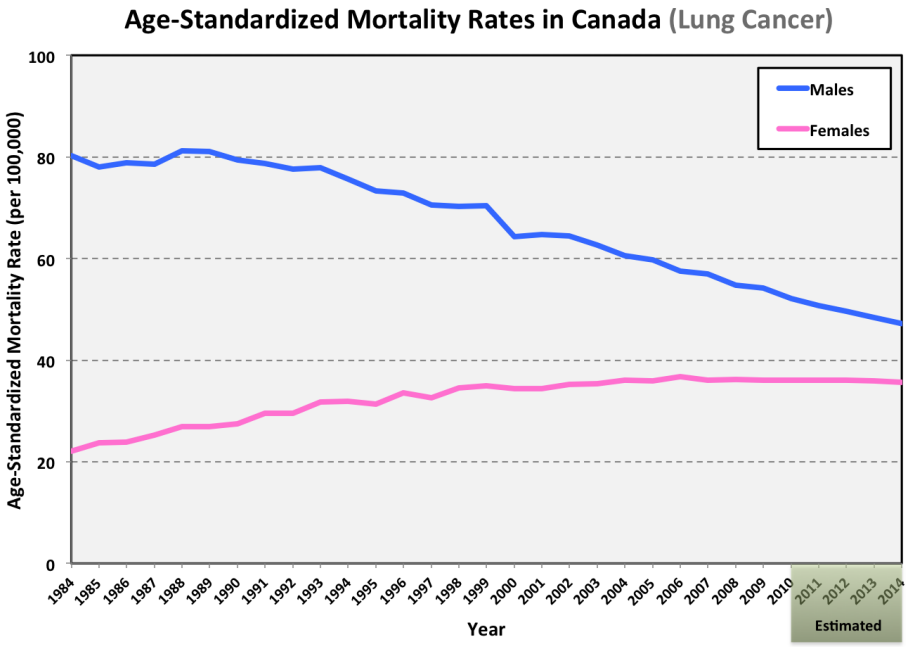

Figure 1.6: Age-standardized mortality rates for lung cancer in Canada since 1984. Source: "Canadian Cancer Society 2014 Statistics"

motion that radiation protection and safety is a hindrance[16]. He emphasized that radiation therapy is technology-driven and that continuous developments over the years have led to better outcomes for millions of cancer patients. However, he argued that the adoption of IMRT was slower than ideal, with some cancer centres still not implementing the technique today. He suggested that many patients who could have benefited from IMRT received an inferior treatment because the widespread introduction of IMRT took too long. To support his position, he cited a 2011 Harvard study that examined error rates for conventional radiation therapy treatments and for IMRT treatments at the Dana Farber Cancer Institute in Boston, MA. That study showed that error rates were low overall (0.06%) and were lower for IMRT (0.03% for IMRT versus 0.07% for conventional) [42]. Furthermore, of the 241,546 treatment fractions examined in the study, none of the errors detected were clinically

[16]Specific wording of the motion being debated according to the ESTRO33 abstract book: "This house believes that the strong focus on radiation protection and safety is delaying / hampering introduction of new technologies / treatment strategies."

significant. Nyström added that media coverage overemphasizes radiotherapy accidents and increases public anxiety. He concluded his argument by comparing a fear of radiation to a fear of flying, "The reason for being afraid to fly is not rational, it's emotional." [41]

Dr. Robin Garcia — head physicist at the Institut Sainte Catherine in France — argued *against* the motion. He focused on personnel training as one of the most important steps in implementing a new radiotherapy technique. Increasing complexity requires users to be experts in the new technique before it can be used on patients. He contended that situations can arise where a new technology is provided to clinicians without proper training, which can lead to serious accidents. As an example, he pointed to the case of systematic mistreatments of hundreds of patients in Epinal, France between 2001 and 2006 [43]. There, two key missteps — the incorrect calibration of new radiotherapy machines and dose calculation errors — led to 448 prostate cancer patients receiving overdoses, leading to 12 deaths and several patients suffering from urinary problems, digestive problems, and sexual dysfunction [44]. For their part in these mistreatments, two physicians and a physicist were given prison sentences. Garcia concluded with an affirmation, "Every time that we introduce a new technology, we should start with a safety phase." [41] Unswayed by the discussion, those in attendance appeared to agree with Garcia. Before the debate began and after the debate concluded, a show-of-hands indicated that the majority of the audience believed that safety concerns do not hamper the introduction of new technologies.

New radiation therapy techniques will continue to be developed to improve patient outcomes. Ideally, clinicians who are interested in implementing a bold new radiation therapy technique would have moving, deformable, 3D, tissue-equivalent, anthropomorphic dosimeters at their disposable. Realistically, clinicians at least need dosimeters that are comprehensive enough to properly validate the technique being implemented. In this regard, advancements in radiation therapy need to be made alongside corresponding advancements in radiation dosimetry. Modern day radiation therapy is on the cusp of "not being able to

validate" new and improved radiation therapy techniques using the dosimetry tools typically available in the clinic today. This is a problem that the current work intends to confront.

1.5 Thesis Scope

This work examines the development of a prototype optical CT scanner and polymer gel dosimetry system that was developed at the University of Victoria (UVic) and the British Columbia Cancer Agency (BCCA). The optical CT scanner scanner was designed, constructed and preliminary testing was performed by former UVic graduate student David Rudko. Subsequently, the author of this doctoral thesis took over the optical CT project for a master's thesis. In that work, modifications were made to the scanner and various aspects of the scanning procedure were investigated using scattering solutions as test objects for imaging purposes. Results from that work informed a number of changes to the system's scanning protocol. At the end of that work, a polymer gel dosimeter was irradiated and scanned in order to assess the capacity of the device at that time. The current work commences from where the previous work left off.

The next three chapters build the foundation necessary for the subsequent three results chapters. Chapter 2 provides background information related to 3D dosimeters with an emphasis on polymer gel dosimeters. Chapter 3 provides an overview of optical CT. The last section of that chapter describes challenges that the system was still facing at the conclusion of the previous work. Chapter 4 provides specific details about the scanner, polymer gel dosimeters and various methods used throughout the current investigations. Chapter 5 presents a number of developments that affect the practical use of the prototype, including new artefact removal techniques, scanner modifications, flask registration, gel dosimetry, and continuous motion scanning. Chapter 6 investigates the importance of six key scan parameters with respect to their effects on readout quality. Chapter 7 presents a new class of imaging

artefacts — radiation-induced refraction artefacts — that affect the optical CT readout of polymer gel dosimeters. Finally, Chapter 8 summarizes the results of these investigations and offers directions for future work.

Chapter 2

Polymer Gel Dosimetry

As was described in Chapter 1, energy that is deposited in the body of a patient by ionizing radiation can cause ionizations that can cause cell death. Killing or halting the growth of tumour cells is the goal of radiation therapy. The goal of radiation dosimetry is to measure the energy deposited by ionizing radiation. As such, most radiation dosimetry methods measure this energy indirectly by measuring the electrical charges of ions[1]. For example, measurements with a ion chamber evaluate dose by collecting the ions released by radiation. The quantity being measured is the charge (in coulombs, C) collected by the ion chamber. These measurements of charge are then converted to dose by applying the proper conversion factors in accordance to well-established reference dosimetry protocols [45].

Ions induced by radiation are also the quantity being measured by a 3D dosimeter. However, the measurement of ions with a 3D dosimeter is even less direct. In a 3D dosimeter, ions induced by radiation cause chemical reactions to occur within the dosimeter. These chemical reactions can lead to a variety of changes in the properties of the dosimeter. The primary challenge in 3D dosimetry is in accurately measuring the three dimensional distribution of these property changes. By measuring these changes and using calibration techniques to

[1]One exception being calorimetry, which uses changes in temperature to measure absorbed energy.

establish the dosimeter's dose-response, property changes can be converted to dose.

This chapter provides an overview of 3D dosimeters, with added emphasis on polymer gel dosimeters (PGDs). To start, Section 2.1 provides a summary of various historical developments in 3D dosimetry. Section 2.2 outlines the basic techniques involved in gel dosimetry, from manufacture to readout. Section 2.3 examines the basic principles of the three most common techniques currently used for the readout of 3D dosimeters: magnetic resonance imaging (MRI), x-ray computed tomography (x-ray CT), optical computed tomography (optical CT). Finally, Section 2.4 looks at some recent examples of 3D dosimeters being used in ways that are difficult or impossible with other dosimetry methods.

2.1 An Abbreviated History of 3D Dosimeters

Prior to the 1980s, long before the development of today's complex radiation therapy techniques, researchers were investigating a variety of radiation-induced effects that are closely tied to modern day 3D dosimeters. In 1927, Fricke & Morse showed that ionizing radiation can convert ferrous ions into ferric ions (i.e., Fe^{2+} into Fe^{3+}) [46, 47]. In 1950, Day & Stein experimented with gels containing dyes that changed colour upon irradiation [48]. In 1954, Alexander *et al* showed that polymers can cross-link when irradiated [49]. In 1957, Andrews *et al* developed a gel that changed its pH and electrical conductivity values upon irradiation, which could be made visible using an indicator dye [50]. In 1958, Hoecker & Watkins developed a liquid capsule dosimeter that polymerized when irradiated [51]. In 1961, Boni used radiation-induced viscosity changes to measure dose in a polyacrylamide dosimeter [52]. And, in 1977, McLaughlin *et al* developed radiochromic plastics (in this instance, as film), which changed colour upon irradiation [25]. Although one can recognize the importance of all of these findings, the radiation-induced chemical changes described by those works were not yet easily measured in 3D.

It could be argued that modern day 3D dosimetry did not begin until 1984 when Gore *et al* described a method to measure radiation dose distributions using MRI [53]. In that work, they demonstrated that MRI[2] could measure the amount of ferric ions that are produced when a solution of ferrous ammonium sulphate was irradiated. They proposed that ferrous ions could be spatially fixed in a gelatin matrix to create a 3D dosimeter — a Fricke-gel dosimeter. After irradiation, the 3D distribution of ferric ions in the dosimeter could be measured using MRI. In 1987, such dosimeters were created and imaged by Appleby *et al* [54]. Unfortunately, it was later shown in 1992 that the ferric ions in these dosimeters diffuse throughout the gel [55]. As a result, imaging of Fricke-gel dosimeters would need to take place within 2 hours before the integrity of their spatial integrity was lost.

In the early 1990s, researchers shifted their interest toward polymer gel dosimeters. In 1993, Maryañski *et al* developed gel dosimeters containing a monomer and a cross-linker: respectively, acrylamide and N,N'-methylene-bis-acrylamide[3] [56]. Upon irradiation, monomers form polymer chains, and cross-linkers cause those polymer chains to knot together, forming webs or beads [57]. Distributions of these polymers could be measured using MRI. Also, polymer molecules did not suffer from the diffusion issues that were experienced using Fricke-gel dosimeters. This gel recipe was later released commercially by MGS Research Inc., marketed as the BANG® (Bisacrylamide, Acrylamide, Nitrogen, and Gelatin) gel dosimeter [58–60].

In addition to radiation-induced changes that could be measured using MRI, polymer gel dosimeters also turned noticeably opaque upon irradiation. Taking advantage of this property change, two matching papers were published in 1996 that described the development of an optical CT scanner (Gore *et al*) and examined the optical properties of the BANG® polymer gel (Maryañski *et al*) [61, 62]. Optical CT readout of 3D dosimeters is analogous to

[2]Also known as nuclear magnetic resonance (NMR) imaging.
[3]Also known as bisacrylamide.

the x-ray CT readout of patients, except where x-ray CT uses an x-ray beam to measure a patient's density, optical CT uses a beam of visible light to measure a dosimeter's opacity. A variety of different optical CT scanner geometries have been developed over the years. The basic principles of x-ray CT and optical CT will be discussed in Sections 2.3.2 and 2.3.3, and Chapter 3 will discuss optical CT in more detail.

In 1998, Kelly *et al* developed a Fricke-based radiochromic gel dosimeter that used gelatin instead of agarose[4], allowing it to be scanned using optical CT [63]. By adding a colour indicator (xylenol orange) to the Fricke-gel recipe, the ferric change induced by radiation was visualized, exhibited as changes in opacity. However, xylenol orange Fricke-gel dosimeters still suffered from the diffusion seen in Fricke-gel dosimeters. Subsequently, a number of dye-based 3D dosimeters would be developed whose dose-dependent changes could only be readout using optical CT. In 2004, Adamovics and Maryañski introduced a hard plastic dosimeter containing radiochromic leuco-dyes that turned green upon irradiation [64]. These would be released commercially as the PRESAGE^{TM} dosimeter [65]. In 2009, a pair of investigations by Jordan & Avvakumov and Babic *et al* would introduce gel dosimeters containing radiochromic leuco-dye micelles, which turned violet upon irradiation [66, 67]. In 2013, Nasr *et al* evaluated the use of diacetylenes as reporter molecules in a gel dosimeter, which both polymerized and turned blue upon irradiation [68].

In 2000, Hilts *et al* showed that radiation-induced polymerization in polymer gel dosimeters also caused slight increases in the density of the gel, which allowed dose distribution measurements to be made using x-ray CT [69]. Although x-ray CT readout had low sensitivity, Audet *et al* quickly showed that the technique could be suitable for the measurement of 3D stereotactic radiotherapy [70]. Later, data filtering techniques were developed to improve the quality of dose distributions measured by x-ray CT [71, 72]. Additionally, in 2010 and 2011, Jirasek *et al* and Chain *et al* showed that modifications to the polymer gel recipe were

[4]Agarose-based gels feature a baseline opacity that makes their use with optical CT challenging.

able to improve the dosimeter's x-ray CT sensitivity [73, 74].

The "Nitrogen" in the BANG® acronym referred to the need to purge a polymer gel of oxygen during preparation by bubbling nitrogen gas through its solution and keeping it in an oxygen-free environment, typically a nitrogen-filled glove box [58, 69, 75, 76]. Oxygen inhibits the polymerization process in polymer gels, so contamination by oxygen would render polymer gel dosimeters inert [56]. In 2001, Fong *et al* introduced a new gel dosimeter recipe with added ingredients — in this case, copper(II) and ascorbic acid — that bound free oxygen, thereby allowing polymerization to still occur [77]. This allowed for the fabrication of polymer gel dosimeters in normal atmospheric conditions (i.e., normoxic conditions), making their preparation much simpler. In 2002, De Deene *et al* showed that an alternative oxygen scavenger — tetrakis (hydroxymethyl) phosphonium chloride (THPC) — was able to bind to oxygen at a higher rate than copper(II) [78].

In 2002, Mather *et al* investigated the feasibility of using ultrasound for the readout of polymer gel dosimeters [79]. They showed that acoustic speed of propagation, attenuation, and transmitted intensity all varied as a function of dose in polymer gels. In 2003, Mather & Baldock developed a prototype ultrasound computed tomography device that examined transmitted intensity and time of flight to [80]. More recently, in 2014, Khoei *et al* developed their own prototype ultrasound computed tomography scanner that evaluated bulk attenuation and broadband ultrasound attenuation [81]. Although these studies showed that readout of polymer gel dosimeters using ultrasound might be feasible, the three main imaging modalities used to evaluate 3D dosimeters continue to be MRI, x-ray CT, and optical CT.

2.2 3D Dosimetry Methodology

As can be appreciated from the summarized history above, there are many different types of 3D dosimeters that are currently under development. In addition to the broad variety of dosimeter types, the dosages recorded by these dosimeters can be evaluated in a number of different ways. Furthermore, because many groups that are investigating 3D dosimeters do so using non-commercialized and non-standardized methods that they have developed for themselves, each group may address specific challenges in their dosimetry protocol in their own way. However, a fairly consistent basic protocol is common amongst most dosimeter types and imaging modalities. So, in order to provide a framework on how gel dosimetry is typically performed in practice, this section describes the routine that is followed by most 3D dosimetrists.

Before using 3D dosimeters, any given facility needs to determine two things: (i) the type of 3D dosimeter that will be used, and (ii) the imaging modality that will be used to evaluate that dosimeter. These two decisions are fairly interconnected. Deciding on a certain type of dosimeter can often limit the options available for dosimeter readout. Additionally, once a readout method is decided on, aspects of the dosimeter (e.g., its chemical composition) can often be adjusted to complement the strengths and weaknesses of the readout method. There is no one solution that is right for every situation, so these decisions need to be addressed on a facility-by-facility and a case-by-case basis.

Five main steps take place in the 3D dosimetry workflow, which is illustrated in Figure 2.1. First, the dosimeter is manufactured. Gel dosimeters are often prepared in a chemistry lab at the facility. However, some dosimeters (e.g., some commercially available Fricke-gel dosimeters, the BANG® dosimeter, and the PRESAGE™ dosimeter) can be manufactured offsite and shipped to the user. Second, simulation scans of the dosimeter are acquired

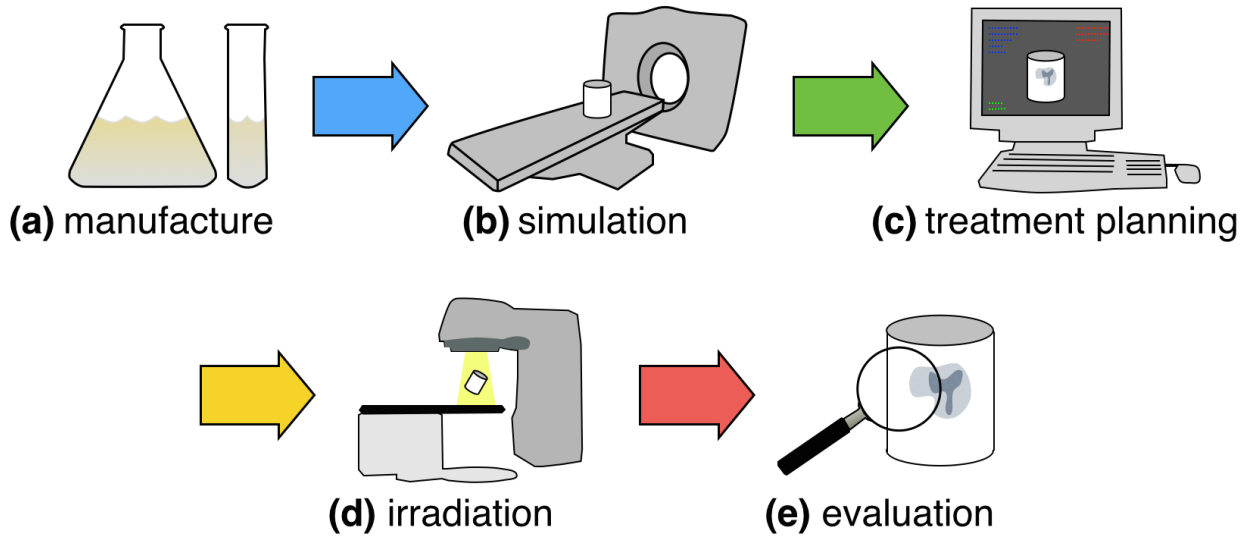

Figure 2.1: Illustration of the basic workflow for 3D dosimetry: (a) manufacture, (b) simulation, (c) treatment planning, (d) irradiation, (e) evaluation.

using an x-ray CT scanner[5]. These simulation scans collect information about the density distributions of the dosimeter. Once this density information is collected, a treatment plan can be put together. During the treatment planning stage, the manner in which the radiation therapy unit will irradiate the dosimeter is established. For each treatment plan, treatment planning software (TPS) will calculate the dose distribution that is expected to be realized within the dosimeter. Next, the dosimeter is irradiated in a manner that matches the details outlined in the treatment plan. Finally, the dose distribution that was actually realized within the dosimeter is evaluated. In some cases, the dosimeter may be evaluated both before and after irradiation. This allows pre-irradiation and post-irradiation evaluations to be contrasted with the intention of only observing changes that have occurred in the dosimeter due to radiation.

For experiments that are meant to investigate the reliability of a given dosimeter and its imaging modality, simpler treatment techniques are used. Then, the measured dose distribution (as obtained by the dosimeter and its imaging modality) will be compared against the

[5]Similar simulation scans of patients are acquired when they are being prepared for radiation therapy.

expected dose distribution (as calculated by the TPS). It is assumed that TPS-calculated dose distributions will be representative of actual dose distributions when using simpler treatment techniques. Experiments that are intent on investigating complex radiation therapy techniques should only take place after the facility has established the reliability of a dosimeter/imaging modality pair. Investigators need to be familiar with the accuracy and precision of the dosimeter's measurements, which will allow them to discern whether a given discrepancy should be attributed to the dosimeter or should be attributed to the radiotherapy technique.

2.3 Readout of 3D Dosimeters

The majority of 3D dosimeter investigations utilize one of three main readout methods: MRI, x-ray CT, and optical CT. In this section, the basic principles for these readout methods will be described and their use in imaging polymer gel dosimeters will be discussed. Although section 2.3.3 provides a brief introduction to optical CT, a more detailed exploration of optical CT is provided in Chapter 3.

2.3.1 Magnetic Resonance Imaging

The following is a simplified explanation of the basic principles underlying MRI. A good resource for the finer details of MRI is the textbook *"MRI in Practice"* by Westbrook *et al* [82].

Hydrogen is abundant in the human body. Typically, in the form of its isotope protium, hydrogen has a single proton in its nucleus. This form of hydrogen — a single electron orbiting a single proton — is the most important element for MRI because of its abundance and because it provides a relatively strong MR signal compared to other MR-active nuclei. The proton in hydrogen's nucleus is continually spinning, which creates a magnetic moment

along the axis of its spin. In a normal environment, the orientations of spinning nuclei are random (see Figure 2.2a).

When an external magnetic field, B_0, is applied to a group of hydrogen nuclei, they will align their average magnetic moments to be parallel or anti-parallel to this external magnetic field (see Figure 2.2b). Most nuclei will have low energy, so they will align parallel to B_0. Fewer nuclei will have high energy, allowing them to align anti-parallel to B_0. In addition to nuclei aligning their average magnetic moment with B_0, a wobbling of their magnetic moment exists. Referred to as precession, the magnetic moment of each nuclei rotates in a circular path around the longitudinal axis of B_0 (see Figure 2.2c). The frequency of this precession, ω_0, is described by the Larmor equation:

$$\omega_0 = B_0 \times \lambda \tag{2.1}$$

where λ is a physical property referred to as the gyromagnetic ratio, which indicates the precessional frequency that a given magnetic field will cause in a nucleus. The gyromagnetic ratio is different for each MR-active nucleus[6].

At this point, nuclear magnetic moments are precessing about the longitudinal axis of B_0 and, at any given point in time, the phase of these precessions are randomly distributed (see Figure 2.2d). However, using a radio frequency (RF) pulse with the same frequency as the precessional frequency (i.e., ω_0), energy is transferred to nuclei and nuclear precessions can be synchronized. This state of synchronized precession is referred to as resonance. When nuclei precess in unison, they can induce a fluctuating voltage in a nearby electrical coil (see Figure 2.2e). This voltage will fluctuate at the same frequency as the resonance frequency ω_0. By using multiple RF pulses to manipulate nuclear spins and then analyzing the voltages that are detected by the nearby electrical coil, one can determine two key quantities: (i) T_1, the

[6]For example, the gyromagnetic ratios for hydrogen, carbon-13, and oxygen-17 are 42.57 MHz/T, 10.71 MHz/T, and 5.77 MHz/T, respectively.

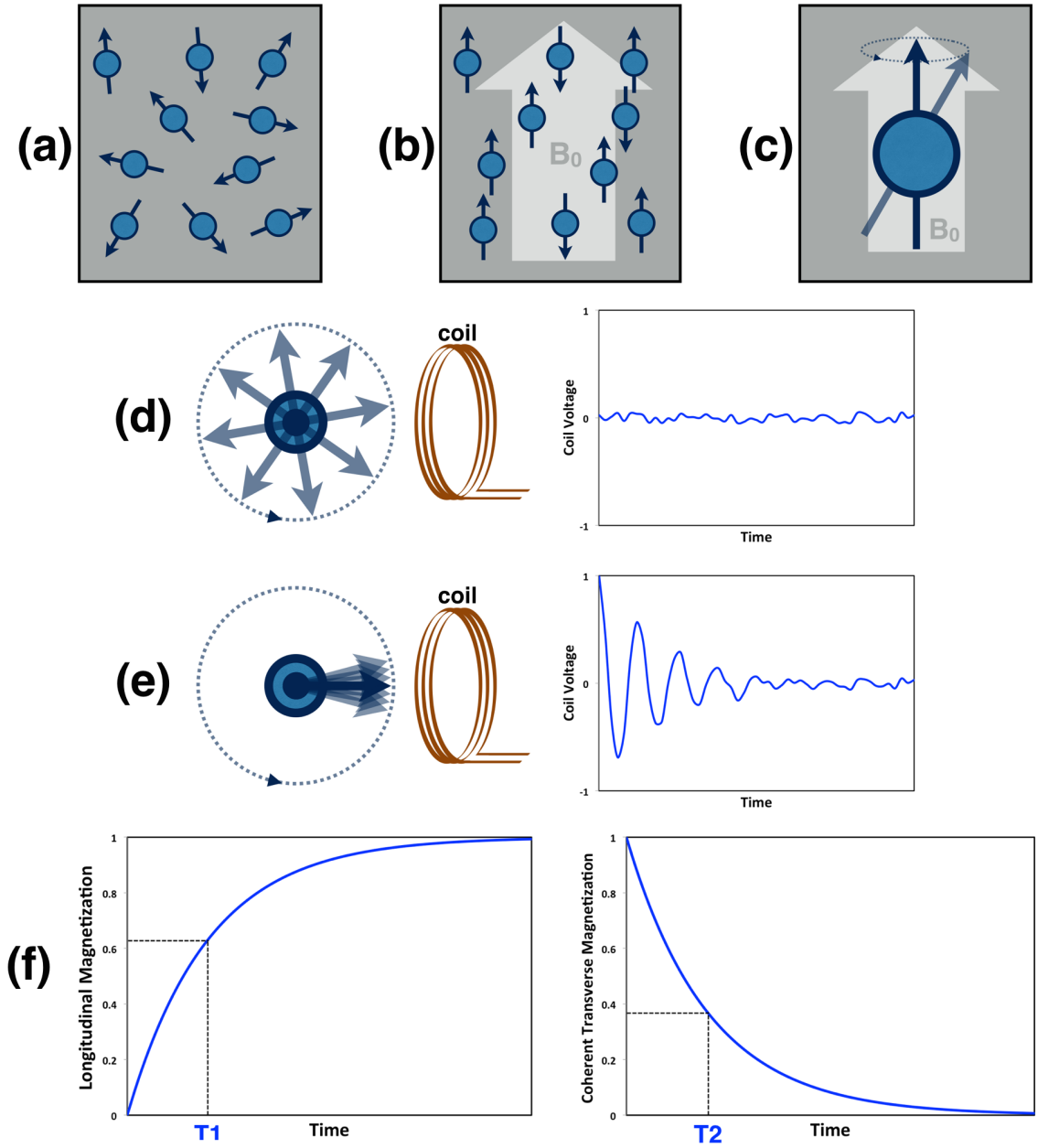

Figure 2.2: The basic principles of MRI: (a) hydrogen nuclei with randomly oriented magnetic moments, (b) when placed in an external magnetic field (B_0), hydrogen nuclei align their magnetic moment with the external field, (c) a secondary precession of each nucleus' magnetic moment rotates around its average magnetic moment, (d) at any given moment, the orientation of individual nuclei are randomly distributed, (e) a radio frequency pulse is used to synchronize their precessions, which can be detected as a voltage signal in a nearby electrical coil, (f) using multiple RF pulses, voltage signals can be analyzed to determine how quickly nuclei return their magnetic moments to their original orientation with B_0 (i.e., T_1), and how quickly they lose coherence with one another (i.e., T_2).

time it takes for nuclei to return their magnetic moments to their original orientation with B_0, and (ii) T_2, the time it takes for nuclei to lose coherence with one another. Specifically, T_1 and T_2 refer to the time it takes each signal to decay an amount of (1/e) towards their original distribution (i.e., to 63% of their original orientation with B_0 for T_1, and to 37% synchronicity for T_2).

The resonant frequency ω_0 is linearly dependant on the magnitude of B_0. So, in order to take measurements of the 3D distribution of MR-active nuclei, an MRI scanner places the patient in a magnetic field gradient. The value of B_0 is varied in 3D. As a result, an RF pulse of a certain frequency will only cause resonance in a specific volume of the scanner. The strength of the voltage signal detected by the nearby electrical coil will be representative of the number of MR-active nuclei present in that specific volume. Through these means, the MRI scanner is able to probe the density of MR-active nuclei throughout the entire volume of the scanner.

Since the first MRI scans of Fricke-gel dosimeters in 1984 and of polymer gel dosimeters in 1993, 3D dosimeter evaluation using MRI has benefited from a lot of investigative attention [53, 56]. However, a recent set of investigations by Vandecasteele & De Deene provides a good look at MRI's current capabilities for evaluating polymer gel dosimeters using refined methods [83–85]. The following synopsis of the current status of polymer gel dosimeter readout by MRI is largely informed by those investigations.

Relaxation times T_1 and T_2 are often converted into their corresponding relaxation rates R_1 and R_2:

$$R_1 = \frac{1}{T_1} \tag{2.2}$$

$$R_2 = \frac{1}{T_2} \tag{2.3}$$

and the most relevant MRI variable used for the evaluation of polymer gel dosimeters is the relaxation rate R_2, also known as spin-spin relaxation. Spin-spin relaxation is an indicator of

energy-exchanging interactions between MR-active nuclei, with more interactions resulting in higher relaxation rates and quicker loss of resonance. In polymer gel dosimeters, as polymerization increases, R_2 also increases. This agrees with what one might expect from an increasingly polymerized dosimeter. As monomers are polymerized, they chain together and cross-link with themselves [57]. As polymers are formed, hydrogen nuclei are bound closer and closer to one another, allowing for easier exchange of energy between nuclei.

Investigations into the MRI evaluation of polymer gel dosimeters have shown that added care must be taken to ensure that the entire volume of the dosimeter has uniform temperature during readout. Increasing the temperature of polymer gel during readout has been shown to reduce the slope of its dose-R_2 response curve. For example, a difference of 1°C was shown to cause errors of up to 15.6% [85]. As a result, a dosimeter that is uniformly warm will provide a smaller MR signal than a dosimeter that is uniformly cold, and a dosimeter with varying temperature will cause readout errors due to its varying dose-R_2 curves. The size of the container used to house a polymer gel dosimeter has also been shown to affect the dose-R_2 curve for the same recipe of gel [84]. In 2002, Salomons *et al* suggested that the gel's temperature during irradiation might affect the reaction dynamics of polymerization, thereby causing local differences in dose response [86]. However, it was shown that dosimeter temperature during irradiation did not influence polymerization reactions, and that dosimeter temperature during evaluation is more important [84, 85].

2.3.2 X-Ray Computed Tomography

The following is a simplified explanation of the basic principles underlying x-ray CT. A good resource for the finer details of x-ray CT is the textbook *"Computed Tomography: Principles, Design, Artifacts, and Recent Advances"* by Hsieh [87].

X-ray CT uses x-rays in the diagnostic energy range of 20 kV to 140 kV. Photons in this

energy range predominantly interact with matter via the photoelectric effect and the Compton effect. The likelihood of photons interacting with a given material via the photoelectric effect is proportional to the material's atomic number cubed (i.e., Z^3). The likelihood of photons interacting via the Compton effect is proportional to the material's electron density. Nevertheless, the likelihood of photons interacting by either effect is typically combined into a single factor — the linear attenuation coefficient.

Using measurements of x-ray intensities, one can calculate the radio-density — an integration of linear attenuation coefficients along a given path — of a given length of material. When a beam of x-rays passes through a homogenous material, the material's radio-density (RD) equals the product of its linear attenuation coefficient (μ) and the path length (x) through the material (see Figure 2.3a). Radio-density can be calculated according to the Beer–Lambert Law:

$$I = I_o 10^{-\mu x} \tag{2.4}$$

$$I = I_o 10^{-RD} \tag{2.5}$$

$$RD = log_{10} \frac{I_o}{I} \tag{2.6}$$

where I_o is the intensity of the x-ray beam before it encounters the material[7], and I is the intensity of the outgoing beam after it traverses the material. So, by comparing the intensity of the beam before and after it passes through the material, one can calculate its RD.

When an x-ray beam traverses a heterogeneous material, the comparison of I to I_o will still only provide a measurement of its overall RD, which is a sum of the material's various attenuation coefficients (see Figure 2.3b). In order to image a 2D slice of an object, one first must obtain multiple linear measurements of RD by translating an x-ray beam and a

[7]Actually, I_o is the intensity of the outgoing beam in the case where the material is absent. Even in a vacuum, the inverse-square law (ISL) will reduce the beam's intensity. But, for ease of discussion, we will assume that the beam source is located at $-\infty$. In that scenario, the beam is non-divergent and its intensity will not reduce according to ISL.

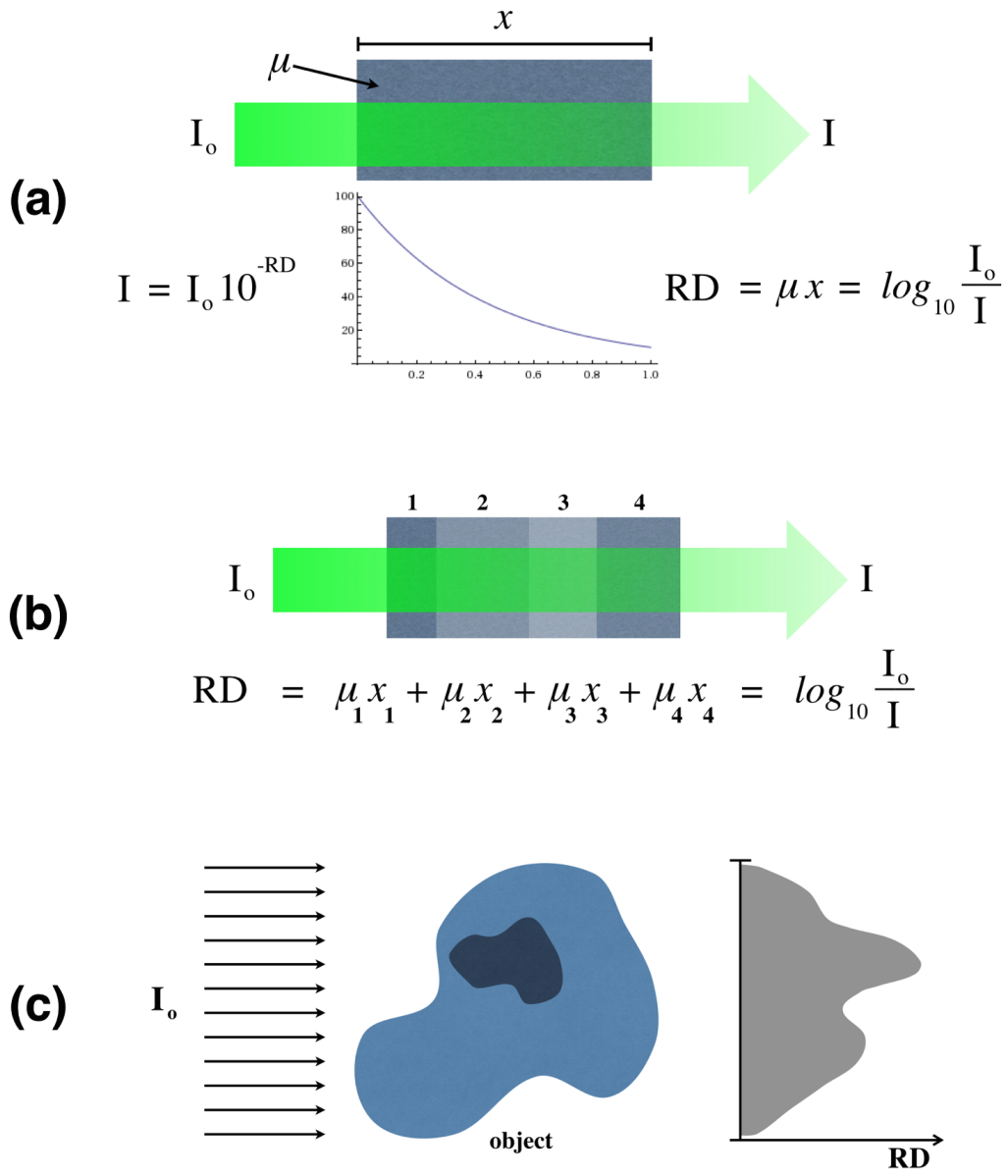

Figure 2.3: The basic principles of x-ray CT. In (a), the intensity of an x-ray beam (I) is attenuated from its initial intensity (I_o) as it traverses a homogenous material with a single attenuation coefficient (μ). The radio-density (RD) of the entire path is the product μx, which can be calculated by comparing I to Io. In (b), the beam passes through four materials of differing lengths and attenuation coefficients, and the comparison of I to I_o still only indicates the RD of the entire path. In (c), multiple x-ray beams pass through an object, providing a 1D projection of that object's radio-densities. By obtaining many such projections from many angles around the object, one can construct a 2D distribution of the object's attenuation coefficients. A 3D distribution can be obtained by scanning multiple slices of the object.

detector across the object, thereby collecting a 1D projection of the object's RD values (see Figure 2.3c). Then, by collecting these 1D projections at many angles around the object, one can reconstruct a 2D map of the object's attenuation coefficients [88]. A 3D distribution of the object's attenuation coefficients is collected by taking such measurements for multiple slices of the object.

Hilts *et al* first investigated the feasibility of using x-ray CT for evaluating polymer gel dosimeters in 2000 [69]. That work demonstrated that the density of polymer gels increases with dose. However, this increase in density is small. As a result, sensitivity is the biggest challenge in using x-ray CT for evaluating PGDs. To compensate for this, dosimeters are scanned multiple times, and then scans are averaged in order to improve the signal-to-noise ratio (SNR). Also, Jirasek *et al* have shown that specially designed filtering techniques are capable of reducing the structured noise that is inherent to the gelatin matrix, thereby improving SNR even further [72]. In 2010 and 2011, Jirasek *et al* and Chain *et al* respectively showed that increasing the proportion of reactive chemicals in their polymer gel dosimeter recipe — using the monomer N-isopropylacrylamide (NIPAM) — can improve the sensitivity of the dosimeter [73, 74]. However, Johnston *et al* showed that the NIPAM gel dosimeter exhibited an undesirable dose-rate dependence [89]. Examining two normoxic PGD recipes, De Deene *et al* also found that an nMAG — normoxic Methacrylic Acid and Gelatin — recipe exhibited dose-rate dependence, while an nPAG — normoxic PolyAcrylamide and Gelatin — recipe showed no dose-rate dependence [90].

2.3.3 Optical Computed Tomography

The description of the basic principles of x-ray CT in Section 2.3.2 is very representative of the basic principles of optical CT. CT uses changes in a beam's intensity to evaluate how attenuating a sample is. Although, where x-ray CT uses x-ray beams to evaluate radio-

density, optical CT uses beams of visible light to evaluate optical density (OD). With these substitutions — visible light for x-rays and OD for RD — the explanation in Section 2.3.2 is entirely analogous. However, there are two more subtle differences that arise from use of visible light in optical CT: (i) refraction, and (ii) the attenuation of visible light. These factors alter the approach needed when using optical CT for evaluating 3D dosimeters.

Unlike x-rays, visible light will refract (i.e., change its trajectory) when it transitions between two different materials at a non-perpendicular angle if those materials do not share the same refractive index (RI)[8]. As a result, the design of an optical CT scanner needs to account for the refraction that occurs when light encounters the dosimeter. Figure 2.4 shows a polymer gel dosimeter and a diagram that illustrates this issue. When laser light is used to scan a dosimeter in a medium of air, rays of the laser will tend to refract towards the bulk of the dosimeter and will not follow parallel paths through the gel. This issue is typically resolved by submerging the dosimeter in a matching fluid that has an RI equal to the RI of the gel. In this case, there will still be slight inward refraction at the wall of the flask because the RI of the flask is typically not equal to the RI of the gel. But, when the RI of the medium equals the RI of the gel, rays will follow parallel paths through the gel, and radial distortion caused by the mismatching RI value of the flask is acceptably small (i.e., sub-millimetre) [91].

Visible light is attenuated via two different interaction types: (i) absorption, or (ii) scatter. These are illustrated in Figure 2.5. When visible light is attenuated via absorption, attenuated photons are absorbed locally within the medium. When visible light is attenuated via scatter, attenuated photons are redirected with a new trajectory at a random angle. The scattered photon continues traversing the medium, only in a new direction. The likelihood of visible light being scattered in a given material varies depending on the size of scattering molecules relative to the incident wavelength, whereas the likelihood of visible

[8]Actually, x-ray refraction does occur. But, its effects are too small to be of any concern in x-ray CT.

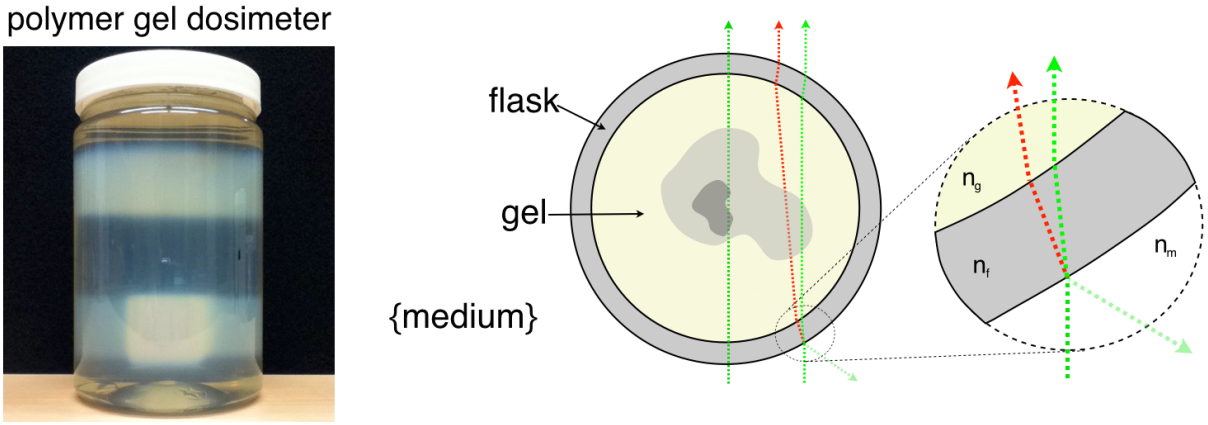

Figure 2.4: Diagram of the refraction of visible light that occurs with a gel dosimeter housed in a plastic flask. When the refractive index of the scanning medium matches the gel dosimeter (i.e., $n_m = n_g$), light rays follow a parallel trajectory through the gel (green rays). When there is a mismatch (i.e., $n_m \neq n_g$), light ray trajectory through the gel becomes non-parallel (red rays). Here, it is assumed that $n_f > n_m$, which is typically the case for plastic or glass containers.

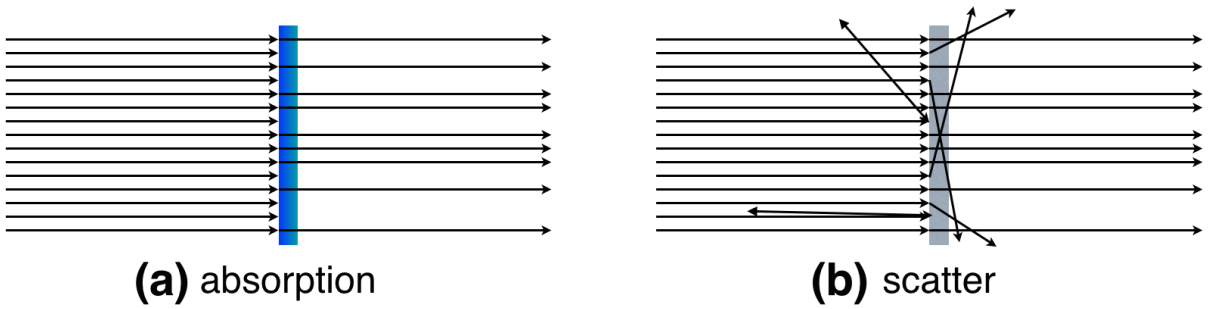

Figure 2.5: Photons of visible light are shown being attenuated by their two primary interaction types: (a) absorption, and (b) scattering.

light being absorbed by the material varies due to molecular energy levels either matching or not matching the energy of incident photons [92]. Polymer gel dosimeters are primarily scattering dosimeters, and dosimeters based on dyes are primarily absorptive dosimeters.

When the goal is to measure only the attenuation of a beam, absorption is a more desirable interaction type than scatter. This is because scattered photons can potentially return into the beam's path via multiple scattering events. As a result, the transmitted beam can become contaminated by scattered photons, leading to an over-representation of the beam's intensity. For this reason, many investigators that use optical CT for dosimeter readout have abandoned polymer gel dosimeters and shifted their focus towards absorptive, dye-based 3D dosimeters [63, 66–68, 93, 94].

Despite their primary optical attenuation mechanism being scatter, polymer gel dosimeters have a number of desirable dosimetric qualities. Polymer gels maintain their spatial integrity, not suffering from the diffusion seen in many dye-based gel dosimeters [57, 63, 66, 67, 95]. Conventional recipes of polyacrylamide gel dosimeters have been shown not to suffer from significant energy dependence or dose-rate dependence that can affect some dye-based gels [59, 90, 94, 95]. Polyacrylamide gels are more radiologically water-equivalent than the hard-plastic PRESAGE^{TM} dosimeter [96]. Furthermore, PGDs can be prepared on-site, whereas the PRESAGE^{TM} dosimeter needs to be shipped from its manufacturer. For these reasons, overcoming the challenge of scatter in optical CT is indeed a worthwhile goal. The prototype optical CT scanner used in this work was designed to achieve this goal. That scanner and the challenges it addresses are discussed in much more detail in Chapter 3.

2.3.4 Availability of Readout Methods

At facilities that use radiation to treat cancer, x-ray CT is the most widely available of the three imaging modalities discussed. This is because patients receiving radiation therapy need to be scanned using x-ray CT for treatment planning purposes. However, compared to x-ray CT and MRI scanners, optical CT scanners are relatively inexpensive. Additionally, an optical CT scanner would be a dedicated device, meant only for imaging dosimeters. As a result, dosimetrist with an optical CT scanner available would not need to compete for time on an x-ray CT or MRI, which are often busy performing diagnostic scans of patients.

2.4 Applications Using 3D Dosimeters

Polymer gel dosimeters — and 3D dosimeters in general — have not reached widespread clinical use. Nevertheless, a 2010 review article by Baldock *et al* outlines a considerable number of investigations on polymer gel dosimeters, dosimetry techniques, and dosimeter readout protocols [57]. That review article also outlines a number of other investigations that have demonstrated the usefulness of 3D dosimeters for acquiring comprehensive 3D dose measurements pertaining to current radiation therapy techniques. In 1998, Oldham *et al* used a BANG gel dosimeter to investigate a nine-field IMRT delivery [97]. In 1999, Farajollahi *et al* used a BANG gel dosimeter to investigate low dose rate brachytherapy [98]. In 2000, Cosgrove *et al* used polyacrylamide gel dosimeters to evaluate conformal radiotherapy treatments [99]. In 2001, Grebe *et al* used polymer gel phantoms to investigate dynamic arc radiosurgery and radiotherapy [100]. In 2002, Jirasek & Duzenli considered the feasibility of using a polyacrylamide gel for proton beam therapy [101]. In 2010, Ceberg *et al* used a normoxic polyacrylamide gel to verify a volumetric arc therapy technique [102]. Although polymer gel dosimeters can be a useful tool for validating current radiotherapy techniques, one can appreciate the great potential they have for allowing the exploration of

more advanced radiotherapy techniques.

The potential for 3D dosimeters is particularly recognizable when one considers the treatment of lung cancer. The lungs are dynamic, 4D organs. As such, current radiotherapy techniques typically acquire 4D patient data that demonstrates how tumours in the lung move while the patient breathes. Then, that 4D data set is fused into a single 3D data set by looking only at maximum intensity projections — the maximum density measured at each point during the entire breathing cycle [103]. In 2006, Bradley *et al* concluded that this type of technique can accurately account for the full range of tumour motion in patients with consistent breathing patterns [104]. However, in 2012 St. James *et al* demonstrated that this technique can be less reliable for patients whose breathing patterns vary significantly from day to day [105]. Regardless of whether or not the patient's breathing motion data is representative of actual tumour motion, the intent of the maximum intensity projection technique is to expand the target volume in order to fully encompass all locations where the tumour could be at any point during the breathing cycle. This technique ensures that the tumour receives its prescribed dose, and it accepts the unfortunate fact that healthy tissues will be irradiated as they move in and out of the target volume. However, if the position of the tumour could be tracked in real-time, lung treatments could be modified in order to reduce the dose delivered to these nearby healthy tissues.

In recent years, a number of investigations have used 3D dosimeters to explore issues related to lung cancer treatments. Some of these investigations examined respiratory-like motion. In 2008, Ceberg *et al* used polymer gel dosimeters to show that, as one might expect, respiratory-like motion causes a blurring of the dose distribution [106]. Subsequently in 2010, Brady *et al* used the PRESAGE^{TM} dosimeter to show that, if breathing motion is accounted for using treatment gating — where radiation is only delivered at a given point in the breathing cycle — then this blurring can be greatly reduced [107]. Other investigations examine tissue deformation. In February of 2012, Niu *et al* were the first to demonstrate

the use of a deformable polymer-based gel dosimeter with and without controlled compressions [108]. In April of 2012, Yeo *et al* used a normoxic polyacrylamide gel to demonstrate that considerable dose discrepancies can arise due to target deformation [109]. In 2013, using a deformable version of the PRESAGE dosimeter, Juang *et al* demonstrated that a commercially available deformable image registration tool was incapable of correcting for a very simple compression [110]. Other groups are investigating low-density polymer gels in order to develop more realistic, lung-like dosimeters. De Deene *et al* and Haraldsson *et al* have respectively demonstrated the feasibility of producing low-density 3D dosimeters using either foamed gels or adding styrofoam beads [111, 112]. These three different attributes — motion, deformation, low-density — might one day be combined to create the ideal test phantom for lung cancer treatments.

2.5 Chapter Summary

As can be appreciated from the above review, many researchers are pursuing the means of measuring radiation dose distributions delivered to 3D dosimeters. These are valuable pursuits. Our ability to provide better radiation therapy techniques to patients relies upon our ability to demonstrate that such techniques are safe, accurate, and reliable. No new technique may be more complex than our ability to accurately demonstrate its results. The complexity of Tomorrow's radiation therapy techniques is limited by the capabilities of Today's radiation dosimetry tools.

For this work, polymer gel dosimeters were pursued, and the optical CT scanner used for dosimeter readout was specifically designed to address the challenge of scattered light. Chapter 3 will discuss the basic principles of optical CT, describe issues related to dosimeter readout, recognize optical CT scanner designs from the literature, and introduce the prototype fan-beam optical CT scanner.

Chapter 3

Optical Computed Tomography

This chapter provides a frame of reference for where our prototype optical CT scanner stands with respect to the design approaches of other optical CT scanners. Section 3.1 begins with a description of optical computed tomography's basic principles. Section 3.2 introduces a number of challenges that are relevant to optical CT. Section 3.3 presents a number of different scanner designs that have been presented in the literature, some of which were released as commercial products. Finally, section 3.4 introduces the prototype fan-beam optical CT scanner that was used for this work, including a discussion on the status of the scanner as it existed at the beginning of this work and the challenges it was still facing at that time.

3.1 Basic Principles of Optical CT

When a beam of visible light traverses an opaque material, the intensity of the beam will decrease as some of its photons interact with the material. Depending on the nature of its opacity, some photons might be absorbed locally, while others might be scattered away and continue traversing the material at a random scattering angle [92]. Regardless, one can

calculate the optical density of a sample by measuring how much the sample attenuates the beam of light. Typically, this is done by comparing a "measurement" light intensity to a "reference" light intensity:

$$OD = -log_{10}\frac{I}{I_o} \tag{3.1}$$

$$T = \frac{I}{I_o} \tag{3.2}$$

where, in the case of 3D dosimeters, I_o is the reference intensity of light traversing the dosimeter prior to irradiation, I is the measurement intensity of light traversing the dosimeter after irradiation, and T is transmission (i.e., the fraction of light that survives the trip through the dosimeter). By comparing pre-irradiation and post-irradiation scans of the dosimeter (reference and measurement scans, respectively), the resulting OD should be representative of the opacity change caused by radiation. However, a single transmission measurement only provides information regarding the dosimeter's OD along a single ray at a single projection angle through the dosimeter. To obtain a 2D image of the dosimeter's radiation-induced opacity in a given slice, computed tomography is used.

Optical computed tomography allows one to reconstruct a 2D map of an object's internal opacity values using only external measurements of transmission values. This principle was first proven mathematically by Johann Radon in 1917 [88]. Essentially, if one can obtain many 1D integrations of the object's properties at many different angles, one can reconstruct the object. In Figure 3.1, a test object is examined using either a fan-beam or a parallel-beam geometry. For each ray, a beam enters the object, and a detector is positioned on the other side of the object in order to measure the beam's intensity after it exits the object. Here, two projection angles are shown as an example.

For a parallel-beam geometry, one will notice that projections with projection angles 180° apart from one another will simply be mirrored representations of the other. These corresponding projections in a parallel-beam sinogram are redundant. Theoretically, if one

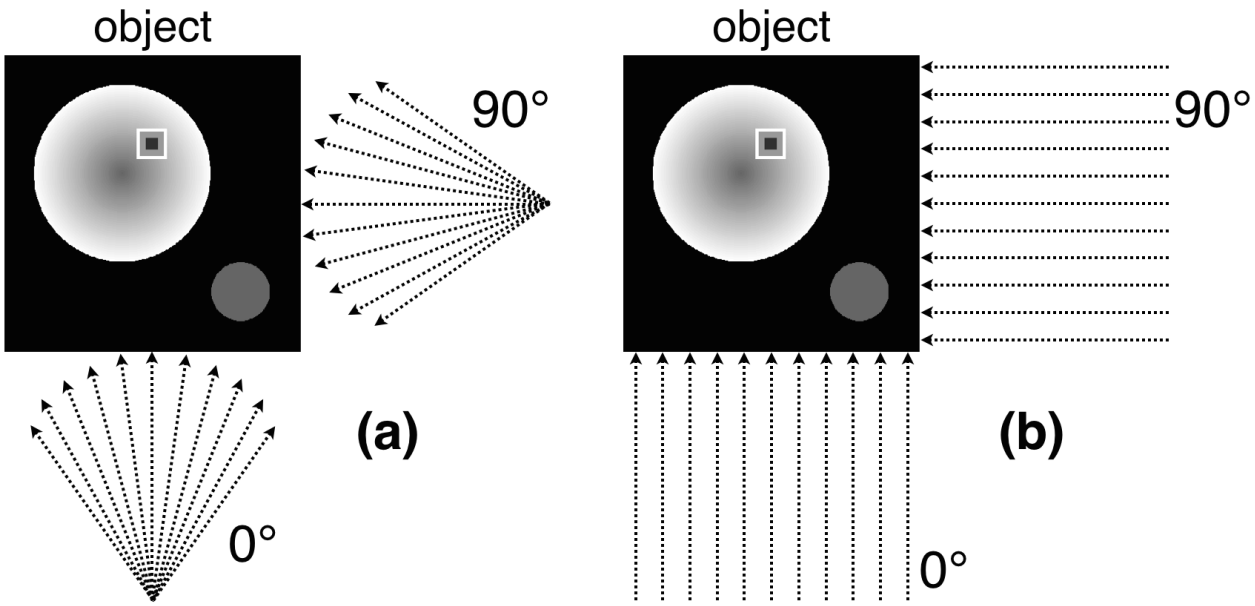

Figure 3.1: A simulated test object is imaged along raylines that sample it using (a) a fan-beam geometry, or (b) a parallel-beam geometry. For computed tomography, samples are acquired from many different projection angles (e.g., projections at angles 0° and 90° are shown here). Not shown are the detectors for the scan, which are positioned on the opposite side of the object in order to detect rayline intensities after traversing the object. Note that parallel-beam projections that are 180° apart will be mirrored representations of one another, containing redundant information. Theoretically, only 180° of parallel-beam projection data is necessary to reconstruct the object.

is using a parallel-beam geometry, one only needs to scan an object with a half-rotation from 0° to 180° in order to reconstruct it. Practically, scanning an object using a full rotation allows one to obtain a pair of measurements for each rayline in the scan, with each ray traversing the same volume but in opposite directions.

If one were to integrate the opacity attenuation values along each rayline in a projection, one would obtain OD projections similar to those seen in Figure 3.2. Shown here are OD projections of the same test object shown in Figure 3.1 from 4 different projection angles using either a fan-beam geometry or a parallel-beam geometry. However, OD values are not directly measured during a CT scan. Instead, a CT scan measures transmission values, as shown in Figure 3.3. Each transmission projection represents how much light is attenuated by the test object. Again, note that parallel-beam projections at 0° and 90° are respectively mirrored representations of their corresponding projections at 180° and 270°.

In order to reconstruct a reasonably accurate facsimile of the object, projections are obtained from many different projection angles. When these projections are organized according to their projection angle, they form what is referred to as a sinogram[1] (see Figure 3.4). Here, sinograms of optical density values and transmission values are shown in fan-beam and parallel-beam geometries. In this format, the mirrored symmetry of parallel-beam sinograms is again recognizable.

Fortunately, the redundancy of parallel-beam sinograms can be obtained from a fan-beam geometry sinogram[2]. As is illustrated in Figure 3.5, each ray in a fan-beam projection corresponds to an equivalent ray from a parallel-beam projection with different projection angles. When comparing fan-beam and parallel-beam sinograms, one will notice that fan-

[1] In reference to their discoverer, obtaining sinogram data for a known object is referred to as taking its Radon transform.

[2] Approximately. Each ray in a fan-beam is the shape of a narrow wedge. As such, each 'redundant' pair of rays in a 360° fan-beam sinogram, which traverse the same path but in opposite directions, will traverse slightly different volumes. Both of these rays will traverse some common volume, but each will traverse some volume that the other does not.

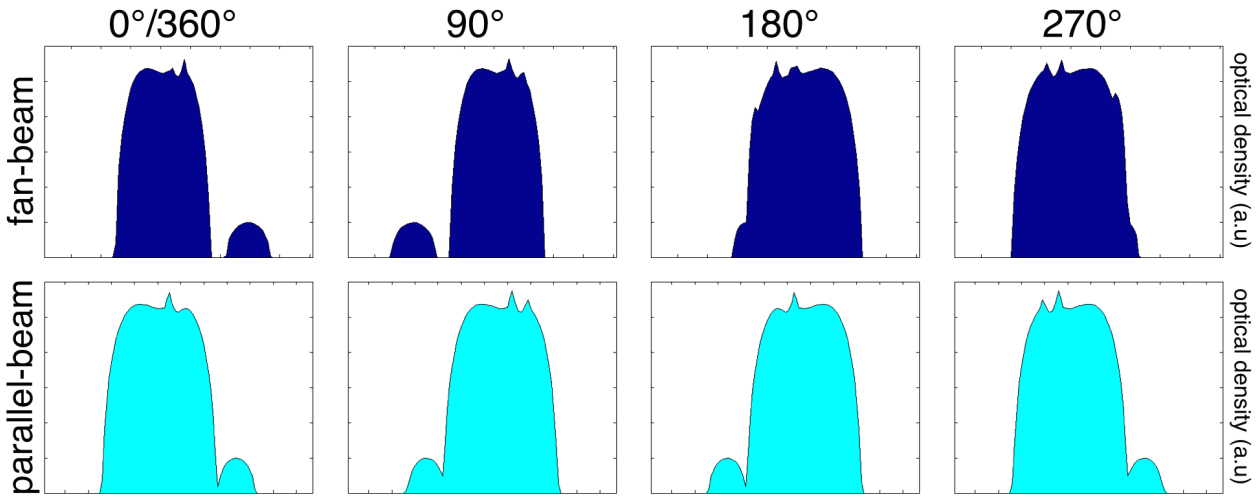

Figure 3.2: By integrating opacity values along each rayline in Figure 3.1, one obtains an OD projection of the object. Here, sample projections are shown of the same object using either a fan-beam geometry or a parallel-beam geometry. Note that the parallel-beam projections at 0° and 90° are respectively mirrored representations of their corresponding projections at 180° and 270°. This redundancy is not seen with a fan-beam geometry.

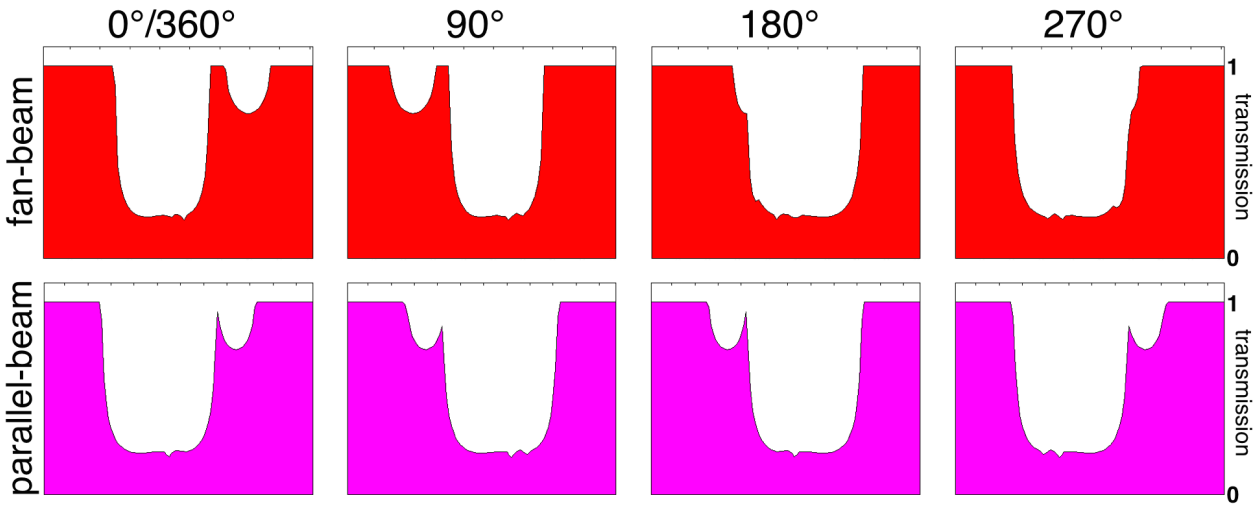

Figure 3.3: The OD projections shown in Figure 3.2 can be calculated after obtaining transmission projections, shown here using either a fan-beam or a parallel-beam geometry. These projections represent the amount of light that will survive the trip through the object. To obtain these projections, measurements of light projections through the object must be compared to reference light values. Typically, when evaluating 3D dosimeters using optical CT, reference light scans of the dosimeter are obtained prior to irradiation.

beam data is essentially slanted compared to parallel-beam data. As such, the value of each ray in a parallel-beam sinogram is determined by sampling the appropriate spot in a fan-beam sinogram. This process is often referred to as "re-binning" [87]. Positions of parallel-beam rays often do not correspond precisely to positions of fan-beam rays, so 2D interpolation is used during the re-binning process.

Once a sinogram of OD data with a parallel-beam geometry has been calculated, an image can be reconstructed using backprojection. As indicated by the name, backprojection essentially smears the intensity of each projection across image space at the same angle the projection was acquired. A rudimentary example in Figure 3.6 shows the reconstruction of a single point using backprojection. As can be seen, the technique of backprojection alone will introduce unwanted noise to the image due to the entry and exit of each projection. To address this unwanted noise, filtered backprojection is used. In filtered backprojection, each projection is convolved with a filter kernel to improve reconstruction accuracy[3] [30, 113]. In Figure 3.7, reconstructions produced by filtered and unfiltered backprojection are shown alongside the original object. A workflow outlining the entire process for a fan-beam geometry is provided in Figure 3.8.

To summarize, one can reconstruct a 2D map of an object's opacity values by measuring transmission values through the object from many different angles. In order to obtain 3D distributions of an object's opacity, measurements are acquired for multiple slices. As will be discussed later in Section 3.3, a variety of different optical CT scanners have been designed with differing geometries. But, fundamentally, they all seek to measure the same thing: transmission sinograms, which can be converted to OD sinograms, which can be used to reconstruct the object.

[3]These filters are applied more quickly via Fourier space.

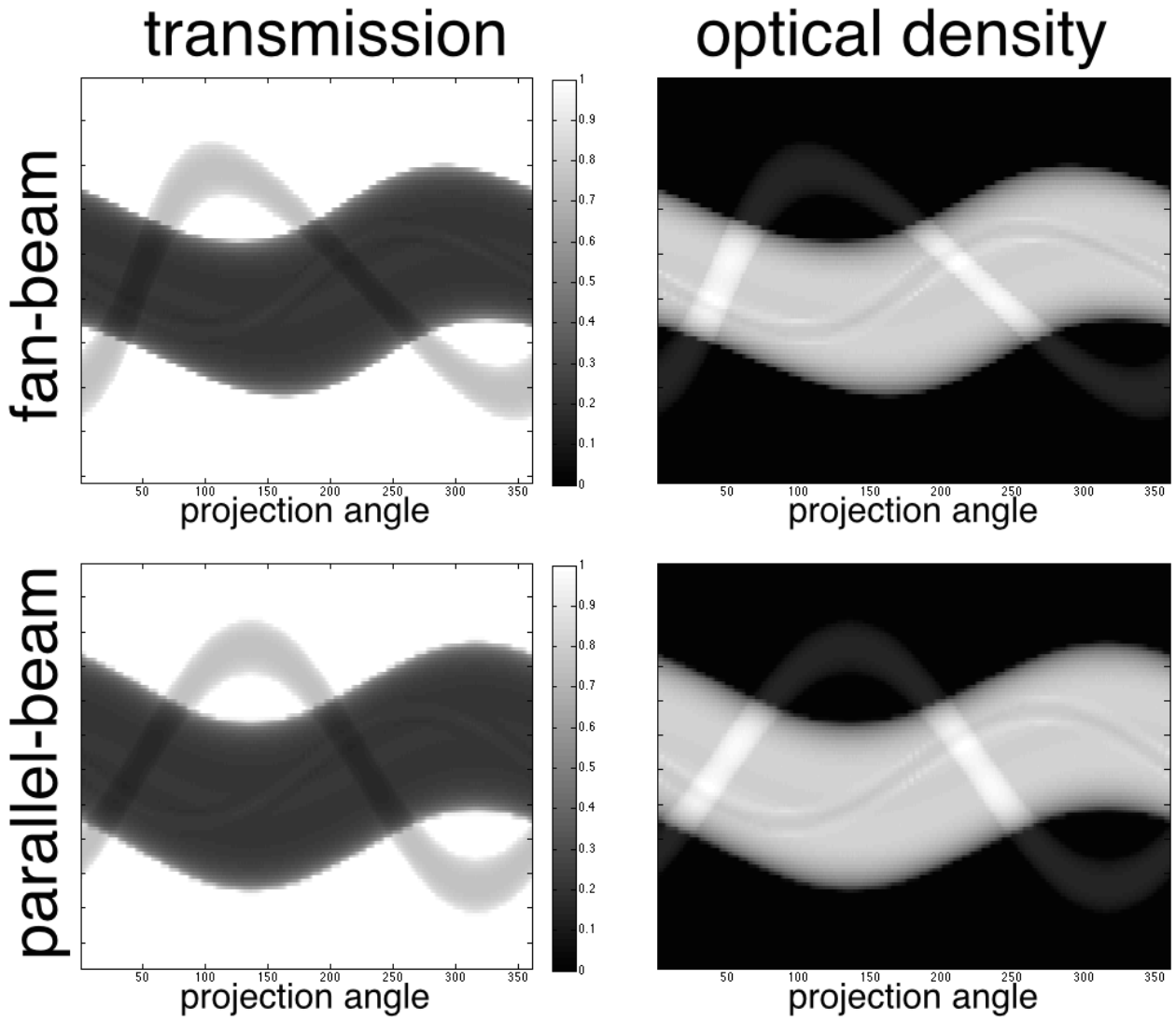

Figure 3.4: In order to reconstruct an image of the test object with reasonable accuracy, many projections are obtained through the object at many different projection angles. A collection of these projections organized by projection angle is referred to as a sinogram. Here, fan-beam and parallel-beam CT geometries were used to collect transmission sinograms of the test object, which can then be used to calculate optical density sinograms. Here, the mirrored redundancy of the front 180° and back 180° of parallel-geometry data is easily recognizable.

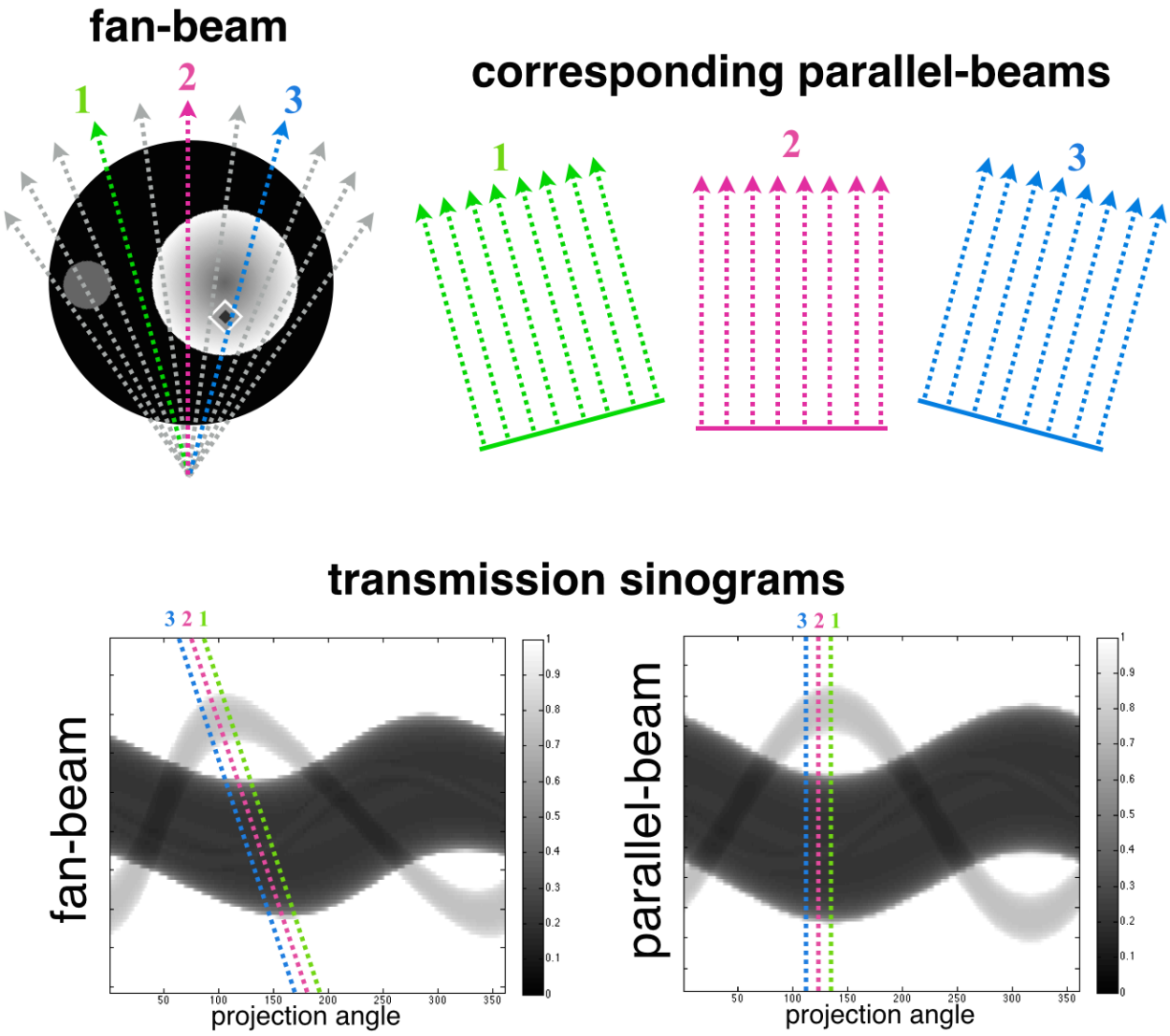

Figure 3.5: Sinogram data collected using a fan-beam geometry can be re-binned into data that matches its equivalent parallel-beam geometry. Top: a set of rays from a fan-beam are shown alongside three sets of parallel rays that match their colour-coded correspondents. Each set of rays in a fan-beam consists of many parallel-beam equivalent rays with differing projection angles. Bottom: the same colour-coded rays are shown overlapping fan-beam and parallel-beam sinograms. Re-binning from fan-beam to parallel-beam geometry is essentially a "de-slanting" of the fan-beam sinogram.

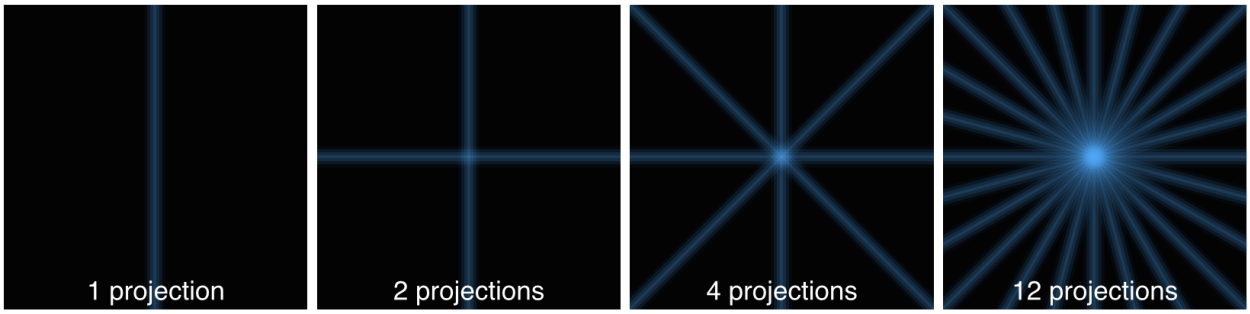

Figure 3.6: Simplified illustration of how backprojection can be used to reconstruct an image of a single point from OD projection data. Note that, in the process of reconstructing the point, unwanted noise is added the image due to the entry and exit of each projection. This noise can be addressed by filtered backprojection (see Figure 3.7.

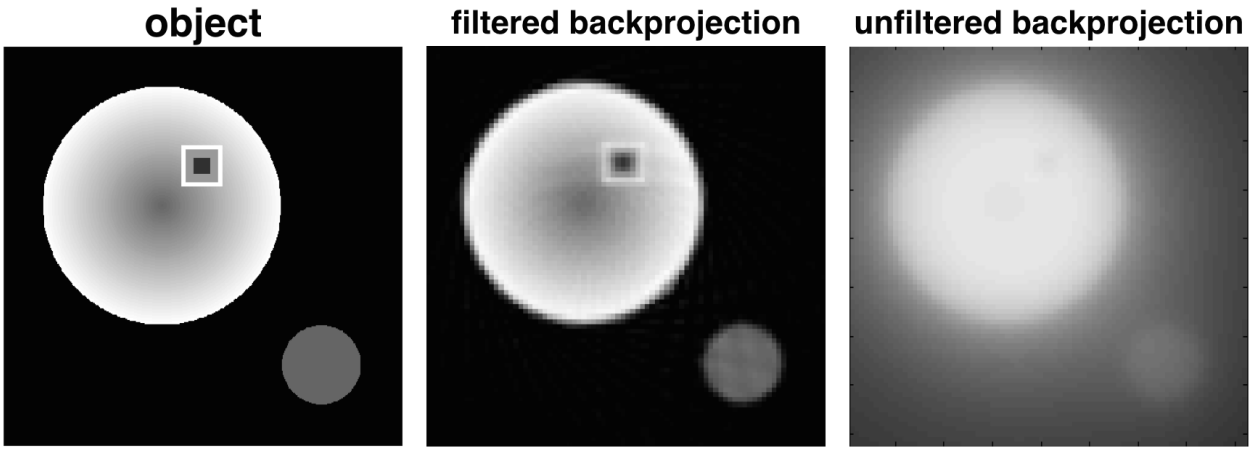

Figure 3.7: Examples of filtered backprojection (ramp filter) and unfiltered backprojection.

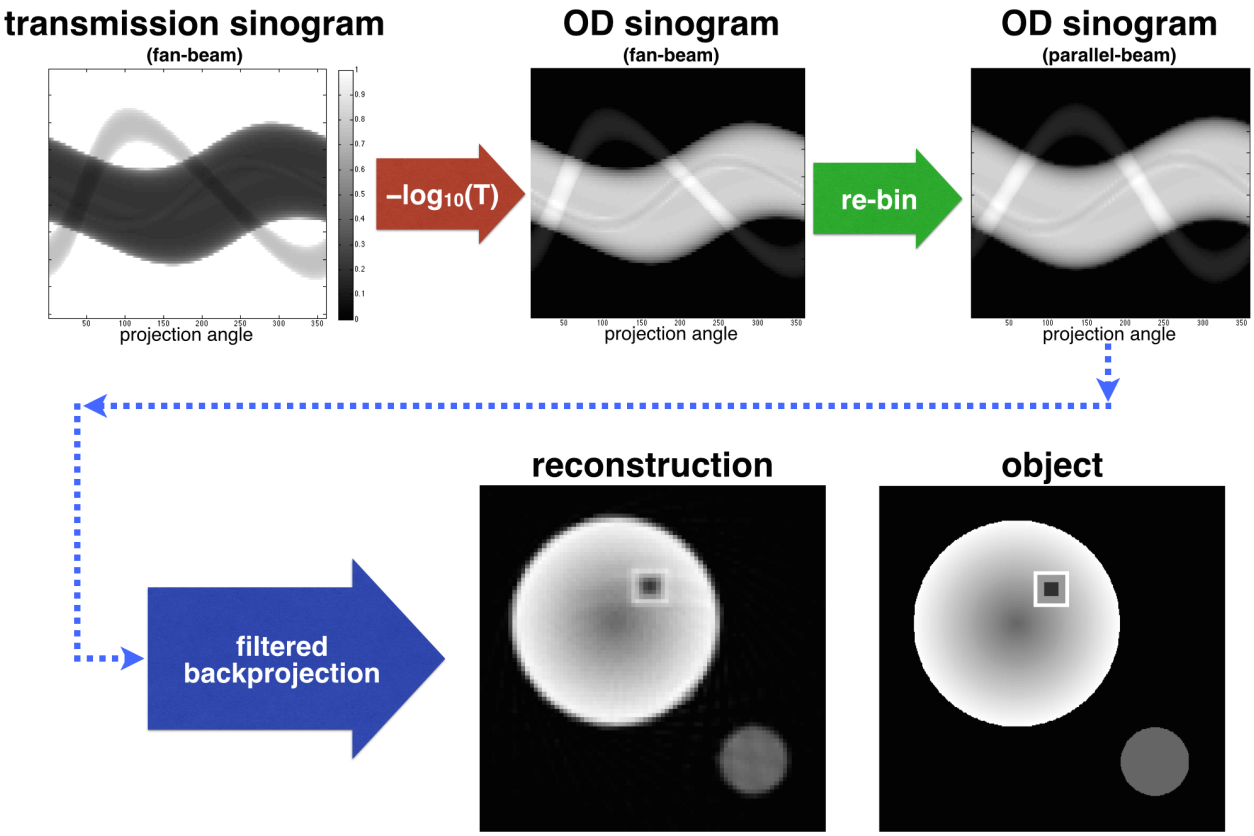

Figure 3.8: Overall workflow of how a fan-beam transmission sinogram becomes a reconstructed image.

3.2 Challenges in Optical CT

With respect to investigative research intent on optimizing performance, optical CT is somewhat playing "catch up" to both MRI and x-ray CT, which have both benefited considerably from years of development due to their uses in healthcare. Due to its analogous nature, the development history of x-ray CT can indeed be taken into consideration when confronting challenges in optical CT. However, the use of visible light in place of x-rays introduces its own unique challenges. The following subsections present issues that are relevant to the optical CT readout of 3D dosimeters.

Streaking Artefacts

Computed tomography allows one to reconstruct images of an object by acquiring many transmission projections through that object at many projection angles. If, within a single projection, an error causes a rayline measurement to either over-represent or under-represent the true transmission value through the object, a streaking artefact will be produced in the reconstructed image. In some instances, these errors are random errors that occur during acquisition (e.g., fluctuations in beam intensity, fluctuations in detector response). In other instances, streaking is caused by aspects of the object being scanned. For instance, in x-ray CT a common source of streaking artefacts are prosthetics or dental fillings which, due to their higher Z-values, attenuate the beam more than tissues of the same density. Over-attenuation by high-Z materials results in beam hardening, scatter, and a lowering of the signal-to-noise ratio [114]. In optical CT, a common source of streaking artefacts are refraction errors (see Figure 3.9, discussed further below).

Ring Artefacts

If a rayline measurement error is limited to a single projection, it will cause a streaking artefact. If rayline measurement errors persist throughout the entire scan, ring artefacts will be produced in the reconstructed image (see Figure 3.9). For both optical CT and x-ray CT, most ring artefacts are caused by response errors in individual detector elements. Although, as was shown with previous investigations using the prototype fan-beam optical CT scanner, some ring artefacts can be caused by reflection [115].

Refraction

When a photon encounters a transition between two materials with two different refractive indexes, it will refract. However, x-rays do not suffer from refraction. This is because refractive indexes vary with respect to wavelength. For x-rays, the refractive index of most materials is 1. For this reason, refraction is an issue that is unique to optical CT. Diagnostic x-rays maintain their trajectory as they traverse a patient in an x-ray CT scanner. However,

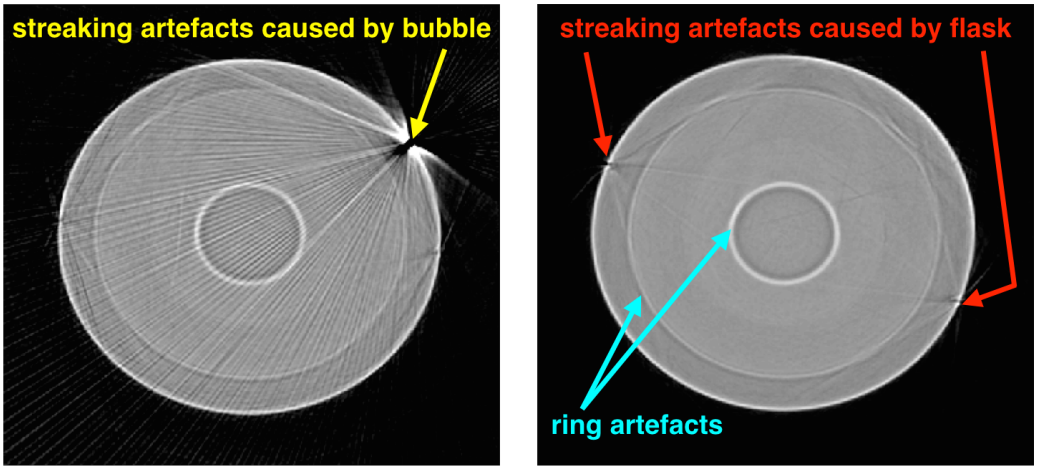

Figure 3.9: Examples of streaking artefacts and ring artefacts in optical CT. On the left, a 1 mm diameter air bubble on the surface of the flask causes widespread streaking artefacts due to refraction errors. On the right, streaking artefacts caused by seams of the flask and ring artefacts caused by corrupted detector elements are more clearly visible.

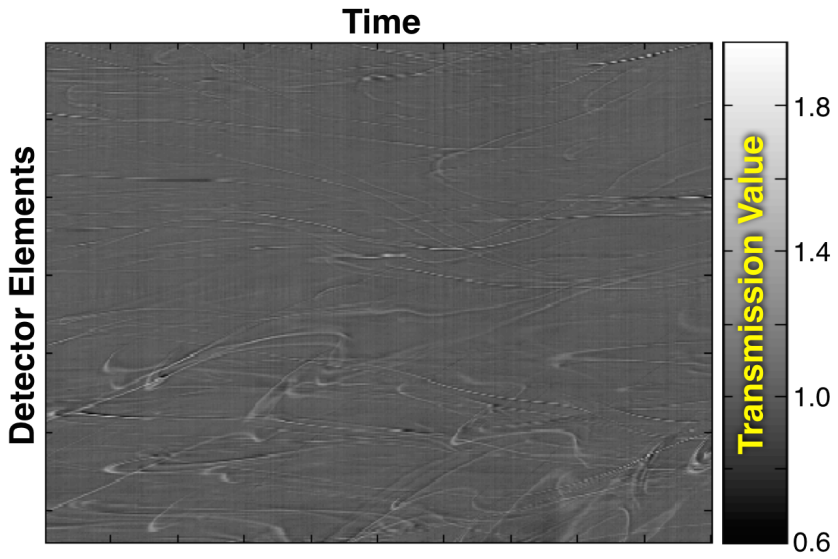

Figure 3.10: Examples of schlieren errors in optical CT. Here, the flow-like errors caused by imperfect dissolution of matching agents in the matching bath are shown in a transmission scan of a recently mixed bath.

the trajectory of visible light can deviate as it traverses materials of varying refractive indexes.

As was shown in Figure 2.4, refraction will occur when photons confront the walls of the dosimeter at non-perpendicular angles. For this reason, nearly all optical CT designs utilize a refractive matching fluid to greatly reduce the size of deviations due to refraction. Some investigators have recently proposed alternatives to matching fluid in order to accommodate in-air or in-water scanning of dosimeters [116–118]. Nevertheless, the majority of optical CT scanner designs that have been reported on in the literature continue to use a matching bath.

The matching bath that is used to reduce refraction errors at the walls of the dosimeter can also be a source of refraction errors. Refractive index inhomogeneities that occur in the bath due to the imperfect dissolution of the matching solute in the matching solution can cause schlieren errors. An example of schlieren errors in a matching bath is shown in Figure 3.10. Flow-like errors are seen in transmission scans of a matching bath that was recently mixed. Schlieren errors are typically minimized by allowing the matching bath to

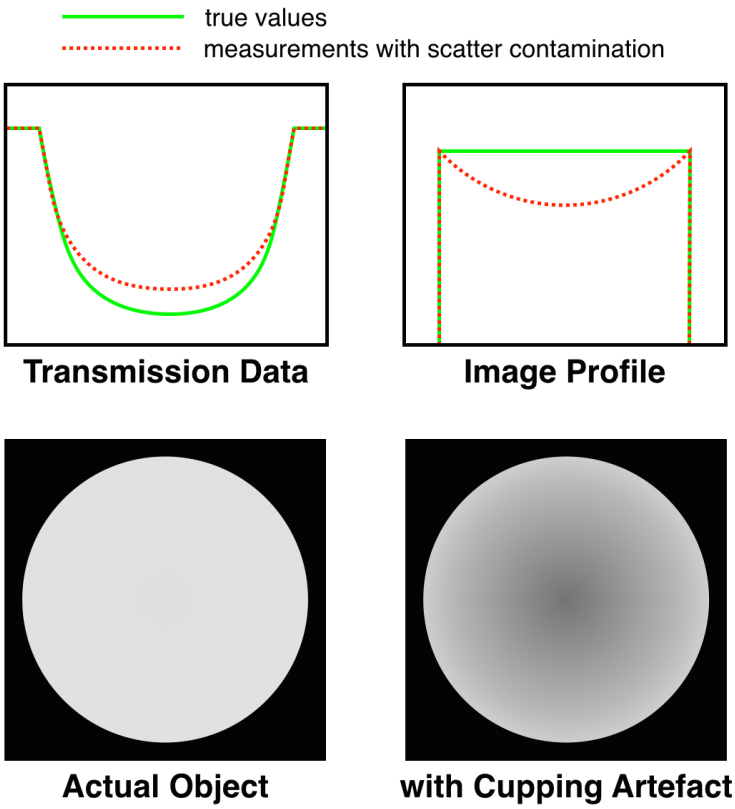

Figure 3.11: Examples of the cupping artefact in optical CT. At the top, transmission projections and profiles of the reconstructed image are used to compare true values against values with scatter contamination. At the bottom, examples of the actual object and the reconstructed image with the cupping artefact are shown.

settle before scanning.

Cupping Artefacts & Scatter Contamination

When imaging a scatter-based attenuator using optical CT, photons that have been scattered out of the primary beam can potentially re-enter the beam via multiple scattering events. As the opacity of a scattering sample increases, the likelihood of multiple scattering events occurring is increased. Therefore, in instances when a more opaque sample is imaged (e.g., imaging a polymer gel dosimeter that was irradiated with higher dose in order to provide a larger optical density signal) beam contamination via multiple scattering events can cause

what is called the cupping artefact. Figure 3.11 shows a depiction of the cupping artefact for a uniform sample. When beam contamination occurs, it is more likely to occur in opaque regions. Beam contamination by scatter causes an over-statement of transmission values, which corresponds to an under-statement of opacity values. As a result, when imaging a highly opaque scatter-based object, reconstructions of the object can exhibit a cup-shaped error [119, 120]. Although the cup-shape is most distinctly observed in a uniform sample, scatter contamination can generally cause widespread under-statements of opacity in a highly scattering object. To prevent such errors from occurring, beam contamination via scatter needs to be avoided.

3.3 Optical CT Scanner Designs

Since the first optical CT scanner was introduced, a number of different scanner designs have been used to evaluate 3D dosimeters. The first two scanner designs were later released as commercial products. Yet, even after commercial options for optical CT were made available, many investigators opted to create their own designs, constructing in-house optical CT scanners from their basic components. In order to provide a frame of reference as to how this work's prototype fan-beam optical CT scanner compares to these other designs, this section describes a variety of different optical CT scanners.

Pencil-Beam Optical CT

The first optical CT scanner, introduced by Gore *et al* in 1996, used a translating pencil beam design, an approach similar to first generation of x-ray CT scanners [61, 121]. A diagram of the first optical CT scanner is shown in Figure 3.12. A pencil-beam laser is translated across the dosimeter (which is submerged in a square matching bath) by translating in unison a pair of mirrors outside the tank. A transmission detector measures the intensity of the

beam after it passes through the tank, and a reference detector paired with a beam splitter monitors the intensity of the beam before it enters the tank. The use of a reference detector allows transmission measurements to be compared against reference measurements while also monitoring fluctuations in the laser's intensity, which can be corrected for. Transmission measurements for the dosimeter are acquired by translating the pencil-beam across the entire sample, rotating the sample slightly, and then repeating beam translation for each projection angle. This type of scanner design was later commercialized as the OCTOPUS^{TM} laser CT scanner (MGS, Inc., Madison, CT, USA) [122]. Because its narrow beam only illuminates a small volume of the dosimeter at any given time, a pencil-beam optical CT scanner does not typically suffer from scatter contamination and is capable of imaging both absorption-based and scatter-based dosimeters [93, 122, 123]. Although its translating geometry causes scan times to be longer than other scanner geometries, the pencil-beam optical CT scanner is considered by some to be the 'gold standard' for optical CT and updated versions of this design continue to be used in recent years [124–126].

Cone-Beam Optical CT

The next optical CT scanner design made a large leap with respect to beam size — from pencil-beam to cone-beam. In 1999, Wolodzko *et al* introduced the design shown in Figure 3.13 [127]. In this design, a diffuse light panel fully illuminates the entire matching bath and dosimeter, all at once. The light that reaches the CCD camera is restricted by using a lens and aperture pair that accepts only a conical beam. In this way, an entire 2D projection of the dosimeter is measured all at once by the CCD camera. Measurements are repeated after the sample is slightly rotated for each projection angle. This design was later commercialized as the Vista^{TM} optical CT scanner (Modus Medical Devices Inc., London, ON, Canada) [128]. Due to the fact that its broad beam illuminates the entire dosimeter simultaneously, this scanner design is susceptible to scatter-related errors [120, 129–131]. Issues related to scatter

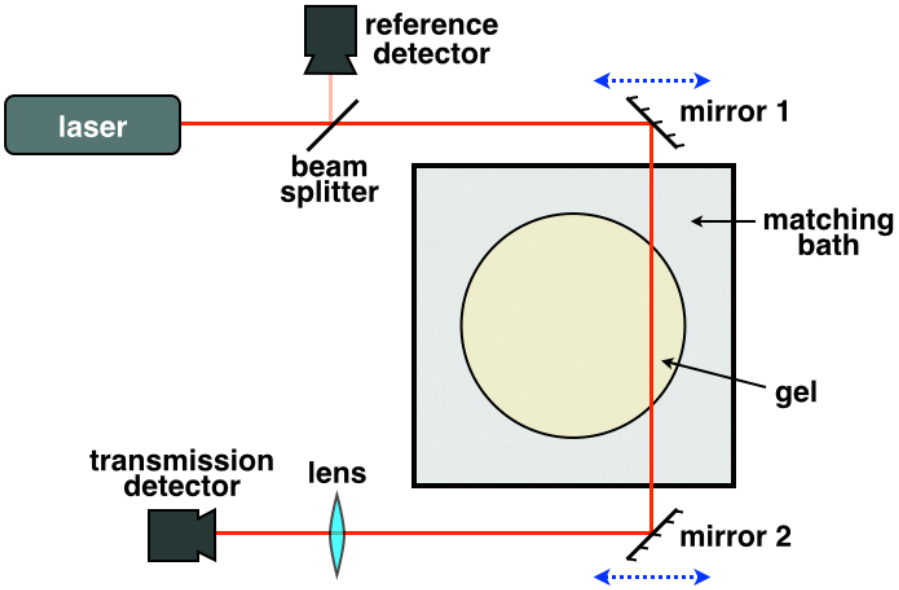

Figure 3.12: Diagram of the first generation pencil-beam optical CT scanner. A pencil-beam is translated across the dosimeter by moving a pair of mirrors. A transmission detector measures the intensity of the transmitted beam, which is then compared to the intensity measured by a reference detector. This scanner design would become the first commercially available optical CT scanner, released as the OCTOPUS^{TM} laser CT scanner.

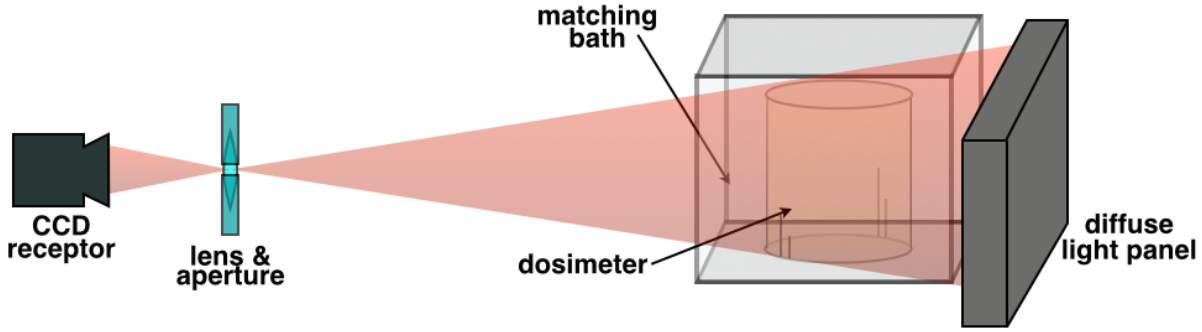

Figure 3.13: Diagram of the cone-beam optical CT scanner. A diffuse light panel is used to fully illuminate the matching bath and dosimeter. Light that reaches the CCD camera is restricted by using a lens and aperture pair that accepts a conical beam. This scanner design would later be released commercially as the Vista^{TM} optical CT scanner.

have motivated most investigators using broad-beam optical CT scanner designs to abandon polymer gel dosimeters for dye-based dosimeters, such as the PRESAGE^{TM} dosimeter and micelle gel dosimeters [110, 132, 133].

Broad Parallel-Beam Optical CT

Alternatively, the use of lenses before and after the tank allowed Krstajić and Doran to create another broad-beam design that used a parallel beam [132, 134]. A diagram depicting this design is shown in Figure 3.14. In this case, a light-emitting diode (LED) is used to illuminate the entire matching bath and dosimeter. Similar to the cone-beam design, a lens and aperture are used to reduce the detection of stray light. An alternative design from Duke University (Durham, NC, USA) used a single diffuse light panel in the place of the first lens, L_1 [125]. However, in recent years, the diffuse light panel design was abandoned by Duke University for the dual lens design. They now perform many of their 3D dosimetry investigations using the PRESAGE^{TM} dosimeter and two broad parallel-beam designs that they refer to as the "Duke Large Optical CT Scanner" and "Duke Midsized Optical CT Scanner" (DLOS and DMOS, respectively) [133, 135–138]. Similarly to cone-beam optical CT scanners, broad parallel-beam optical CT scanners are susceptible to scatter-related errors and are not useful for imaging polymer gel dosimeters.

Fast-Scanning Pencil-beam Optical CT

By utilizing the same dual lens design, some researchers have investigated the possibility of using rotating mirrors to scan the bath with a pencil-beam at higher speeds than would be achievable using translating mirrors [139–141]. A diagram for such a system (here, the 2007 design by Krstajić and Doran) is shown in Figure 3.15 [141]. In this design, apart from the stage that rotates the dosimeter, the only moving parts are the rotating galvanometer mirrors, which deflect the pencil-beam off of a pair of stationary paraboloidal mirrors. While

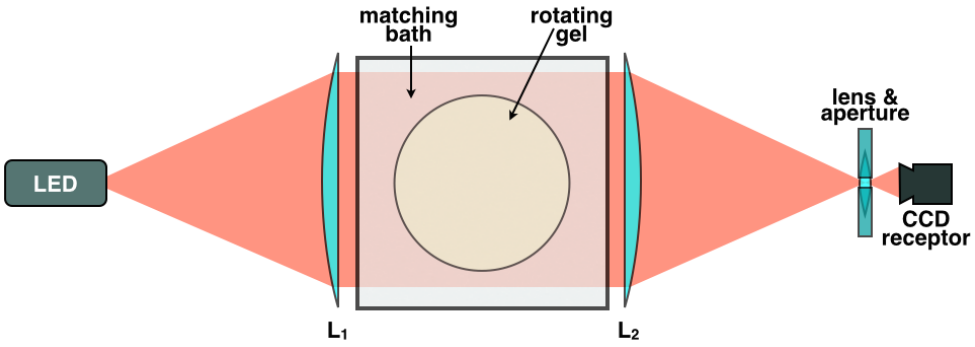

Figure 3.14: Diagram of the broad parallel-beam optical CT scanner. An LED source simultaneously illuminates the entire matching bath and dosimeter. Lenses L_1 and L_2 are used to create parallel raylines through the scanning tank. A lens and aperture is used to restrict light accepted by a CCD camera, which collects an entire 2D projection all at once.

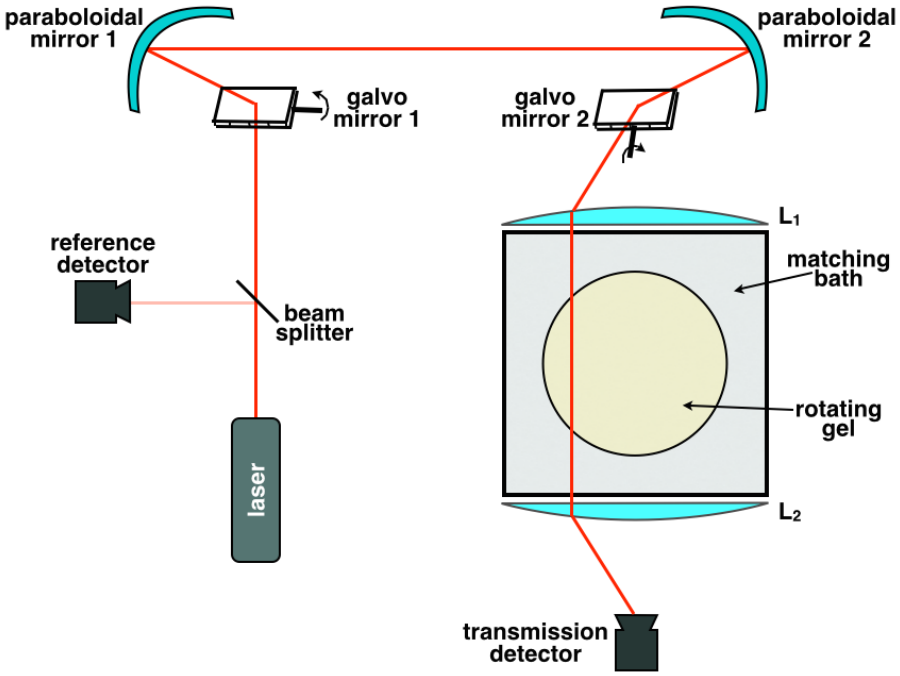

Figure 3.15: Diagram of the fast-scanning parallel-beam optical CT scanner. Similar to the first generation pencil-beam design, a reference detector is used to compare with measurements from a transmission detector. However, rather than using translating mirrors to scan the bath, galvanometer mirrors and paraboloidal mirrors are used to deflect the beam across the bath. Similar to the broad parallel-beam design, lenses L_1 and L_2 are used to create parallel raylines through the scanning tank.

initial characterization and optimization has been performed on this type of optical CT scanner, few dosimetric experiments have been published [142, 143].

Diffused Laser Line Optical CT

In 2011, Papadakis *et al* developed an alternative optical CT scanner design that, much like the fan-beam optical CT scanner that is the focus of this work, used neither a pencil-beam or a broad-beam [144]. A diagram of their scanner is shown in Figure 3.16. Their design used a laser and a cylindrical lens to project a laser line onto a light diffusing panel, creating a planar beam. The orientation of this beam is either vertical or horizontal, depending on the orientation of the cylindrical lens. This laser line is translated side-to-side or up-and-down to collect a full 2D projection. Then, the sample is rotated slightly and transmission data is collected for each projection angle. Scan results they obtained using this diffused line design were shown to be of poorer quality than results they obtained using a wide-field illumination design for the same dosimeter [144]. Followup investigations using this scanner design have yet to be published.

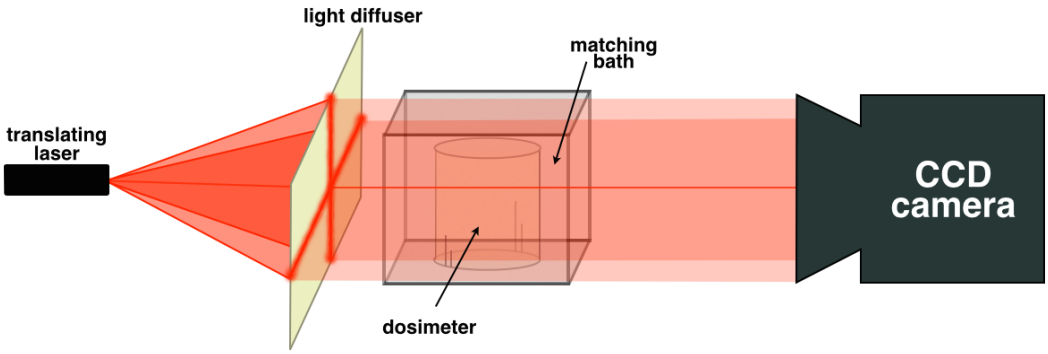

Figure 3.16: Diagram of the diffused laser line optical CT scanner. A laser line is projected onto a light diffusing panel, creating a planar beam that is oriented either vertically or horizontally. The laser line is translated either side-to-side or up-and-down to collect a full 2D projection. The sample is then rotated slightly and transmission data is collected for each projection angle.

3.4 The Prototype Fan-Beam Optical CT Scanner

The optical CT scanner that is main focus of this work is an in-house built scanner with a fan-beam geometry [145, 146]. A diagram representing the scanner as it existed at the start of this PhD work is shown in Figure 3.17. The intensity of a pencil-beam laser is controlled by adjusting the crossing angle of a pair of linear polarizers. A fan-beam is created using a line-generating lens, which is positioned so that its virtual fan vertex resides at the point of concentricity of a semi-circular matching bath. This semi-circular matching tank design ensures that light rays enter and exit the tank at right angles, preventing refraction from altering rayline trajectories. A physical collimator featuring holes that align with the fan vertex is used to limit the detection of stray light. An approximate-arc of 5 linear photodiode arrays forms the detector array.

The intention of this choice of geometry was to use a beam that was broader than a pencil-beam, but not as broad as a cone-beam or broad parallel-beam. The fan-beam acquires a light transmission profile of a full projection for a single slice all at once. As such, it could potentially be capable of performing faster scans than a pencil-beam geometry. Furthermore, by using a physical collimator to eliminate scattered photons of the fan-beam, this prototype scanner would be more capable of scanning scatter-based dosimeters (e.g., polymer gel dosimeters) than an uncollimated system. Broader beam optical CT designs (such as the DLOS, DMOS, and Vista^{TM} scanners) suffer from imaging artefacts caused by scatter contamination when they are used to image polymer gel dosimeters. Therefore, the fan-beam optical CT scanner discussed in this work may be the broadest beam optical CT scanner geometry that is still capable of scanning polymer gel dosimeters.

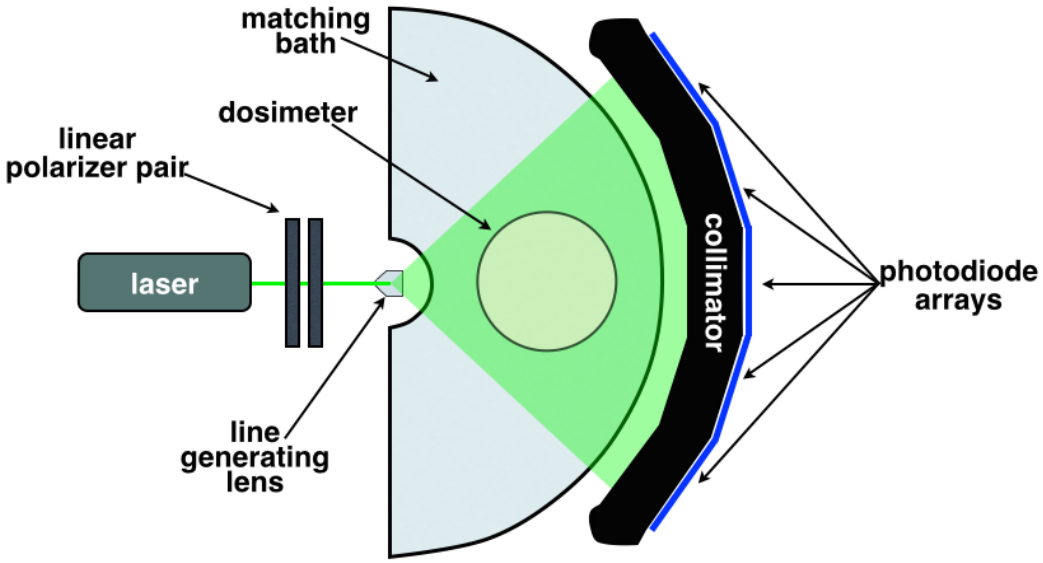

Figure 3.17: Diagram of the prototype fan-beam optical CT scanner. The intensity of a pencil-beam is controlled via the crossing angle of a pair of linear polarizers. A line-generating lens is used to create a fan-beam at the point of concentricity of a semi-circular matching bath. A physical collimator is used to reject stray light before light is detected by an approximate-arc of 5 linear photodiode arrays.

3.4.1 Previous Work

At the beginning of this PhD work, I had already performed a number of investigations with the fan-beam optical CT scanner for my MSc work. The following is an abridged summary that highlights the key findings from those investigations.

A new method of light intensity modulation was created for the optical CT scanner's laser beam. Previously, individual opaque filters with nominal OD values were used to modify the intensity of the pencil-beam that reached the line-generating lens. This meant that every time the light intensity was to be adjusted, these filters needed to be swapped out. When filters were changed, beam alignment would be affected, which meant that the fan-beam would need to be realigned. The new intensity modulation method used the crossing angle of two linear polarizers to allow the fine adjustment of beam intensity without greatly disturbing the alignment of the fan-beam.

Once light intensity could be adjusted without disturbing the alignment of the fan-beam, it was found that the scanner's detector array needed to be characterized. By varying the light intensity striking the detector array and by varying the integration time that detectors accumulated signal, inconsistencies in detector responses were revealed. Investigations ultimately demonstrated that an offset correction was necessary to ensure detector linearity. However, a subset of detector elements in the detector array continued to show inconsistencies even after the offset correction was applied. This led to distinct ring artefacts in scanner reconstructions (as can be seen in Figure 3.9).

Two methods of extending the dynamic range of the scanner were developed. The first method extended the dynamic range by varying detector integration times. By collecting signals for longer times and renormalizing the signal detected, measurements could be made for more opaque samples that could otherwise not be measured. Similarly, the second method extended the dynamic range of the scanner by increasing the intensity of the fan-beam and then renormalizing that signal. Combining these two methods, absorbances as high as 4 could be measured, which corresponds to transmission levels of 0.01%.

After the dynamic range of the scanner was greatly increased via the dynamic range extension methods described above, the effectiveness of the scanner's physical collimators were tested. Two collimators were examined: a single-slot (SS) collimator, and a multi-hole (MH) collimator. When imaging a sample that was primarily absorptive, the MH collimator maintained accurate readout for the entire dynamic range of the scanner, while the SS collimator began to slightly suffer from scatter-contamination for higher absorbances. When imaging a sample that was primarily scattering, the MH collimator still maintained readout accuracy over the entire dynamic range of the scanner, while the SS collimator suffered considerably from scatter-contamination, eventually measuring signals that were 100% scattered light. These tests demonstrated the effectiveness of the multi-hole collimator, which now serves as the default collimator for the scanner.

Tests using scattering solutions as test objects were able to demonstrate the need for proper reference data to compare measurement data against in order to calculate transmission values (i.e., $T = \frac{I}{I_o}$). These tests were performed using a flask with a porthole in its upper portion. Transmission data was collected by scanning a water sample (i.e., I_o), adding a scatterer through the porthole, mixing it, and then scanning the scattering sample (i.e., I). In this fashion, imaging could be performed without disturbing the positioning of the flask in the optical CT scanner. Using a measurement scan of the water-filled flask (i.e., a "blank" sample) was shown to eliminate widespread ringing artefacts — believed to be caused by reflection off of the surface of the flask — that plagued the system. However, reconstructions were shown to be very sensitive to misalignments of flask positioning due to widespread optical imperfections on the surface of the flask. These imperfections were shown to be a significant source of image noise. So, although noise was greatly reduced by comparing the measurement scan to a reference scan of a "blank" sample, slight mismatches in the positioning of these data sets were shown to cause sharp increases in image noise. As a result, accurate positioning was highlighted as an important factor for improving readout.

Finally, following the developments described above, a polymer gel dosimeter was prepared, irradiated, and scanned using the fan-beam optical CT scanner. Because the challenge of accurate flask positioning had yet to be tackled, pre-irradiation and post-irradiation scans of the dosimeter could not be used for reference data and scan data, respectively. To suffice, an unirradiated portion of the dosimeter was scanned to serve as reference data in order to reduce ring artefacts. Reconstructions of the irradiated PGD suffered from considerable amounts of noise, and three main artefacts were highlighted as sources for these errors: (i) streaking caused by refractive inhomogeneities in the dosimeter and two seams that follow down the side of the flask housing the dosimeter, (ii) peak and dip artefacts caused by particulate impurities in the dosimeter, and (iii) ring artefacts caused by data corruption that occurs in specific elements of the detector array.

3.4.2 Unresolved Issues

At the end of my master's thesis, a number of issues were highlighted as priorities for future work. The following is a list of the challenges that remained at that point in time, which served as a starting point for my PhD work.

New Fan-Creation Method

Previously, the intensity of the beam was being adjusted by manually moving the rotational stage of one of the linear polarizers. Preferably, control of beam intensity would be computerizable. Furthermore, an alternative method of fan-creation might be less susceptible to disturbances in alignment. A new fan-creation component that addresses both of these issues is discussed in Section 5.1.

New Matching Tank

The scanner's first matching tank frequently required downtime in order to have warped or cracked entry windows repaired. Additionally, a large volume of the bath goes unused, meaning that more of the RI-matching solution needed to be prepared than is necessary. A new matching tank with less volume and a stable entry window is presented in Section 5.1.

Artefact Removal & Filtering in Sinogram Space

It was suggested that, even after developing a flask registration to allow for better data acquisition, additional efforts could be made to improve reconstruction results by processing data in sinogram space. Specifically, artefact removal techniques could be developed to address ringing and streaking that was still present in scans of a scatter solution sample in a perfectly placed flask. Filtering or data binning could also be performed to suppress any sources of noise that could not be avoided after optimizing flask placement. Section 5.2

presents methods of removing ringing and streaking artefacts in sinogram space, and the majority of Chapter 6 examines the affects that scan parameters and data binning have on noise and accuracy.

Flask Registration

Tests using scattering solutions suggested that large reductions in image noise would be achievable by acquiring pre-irradiation and post-irradiation sinograms of the dosimeter. However, this benefit would be greatest when the dosimeter is perfectly positioned for each scan, allowing for proper comparisons of these two sets of data. So, a top priority for the system was to develop a method of achieving reproducible placements of flasks in the scanner. During my PhD work, a flask registration technique was developed and is presented in Section 5.3.

Moving Acquisitions

At the commencement of this work, scans were being performed using step-and-shoot techniques. That is, whenever the dosimeter was rotated between each projection angle, pauses in data acquisition were inserted to allow for the dosimeter to stop moving before transmission measurements were acquired. In order to speed up scan times, could acquisition be performed while the dosimeter was continually in motion? Section 5.6 presents a time-stamp method was developed to allow for the scanning of continually moving dosimeters.

3.5 Chapter Summary

As can be recognized from the above review, a wide variety of optical CT scanner designs have been developed for the specific purpose of reading out 3D dosimeters. Each scanner is typically designed with the demands of its intended dosimeter in mind. For this work, the prototype fan-beam optical CT scanner was developed to address the largest challenge in the readout of polymer gel dosimeters — scatter. Previous work demonstrated that the prototype's multi-hole collimator is capable of eliminating the effects of scattered light to an impressive level [115]. With the key challenge of scatter addressed, development of the prototype scanner was continued in pursuit of reading out polymer gel dosimeters. The results presented in Chapters 5–7 describe these continued pursuits. Chapter 4 will delineate the materials and methods used to obtain those results.

Chapter 4

Materials & Methods

This chapter describes technical aspects relevant to the three results chapters that follow. Section 4.1 discusses the components of the prototype fan-beam optical CT scanner. Section 4.2 describes two different types of objects imaged in this work: 1) scattering solutions used as test samples, and 2) polymer gel dosimeters. Section 4.3 describes the simulation, treatment planning, and irradiation of the dosimeters used in this work. Section 4.4 describes the data acquisition protocols used for performing scans with the optical CT scanner. Section 4.5 describes how data acquired by the optical CT scanner was processed and used to produce reconstructions. Section 4.6 describes the steps used to align measured dosimeter data with the dose data provided by treatment planning software. Finally, section 4.7 describes methods for refractive matching bath preparation and for rayline tracing.

4.1 Scanner Design

Figure 4.1 shows photographs and a diagram that is representative of the prototype fan-beam optical CT scanner as it existed when this work began. Figure 4.2 shows photographs and a diagram of the scanner as it existed towards the end of this work. Subsequent subsections will

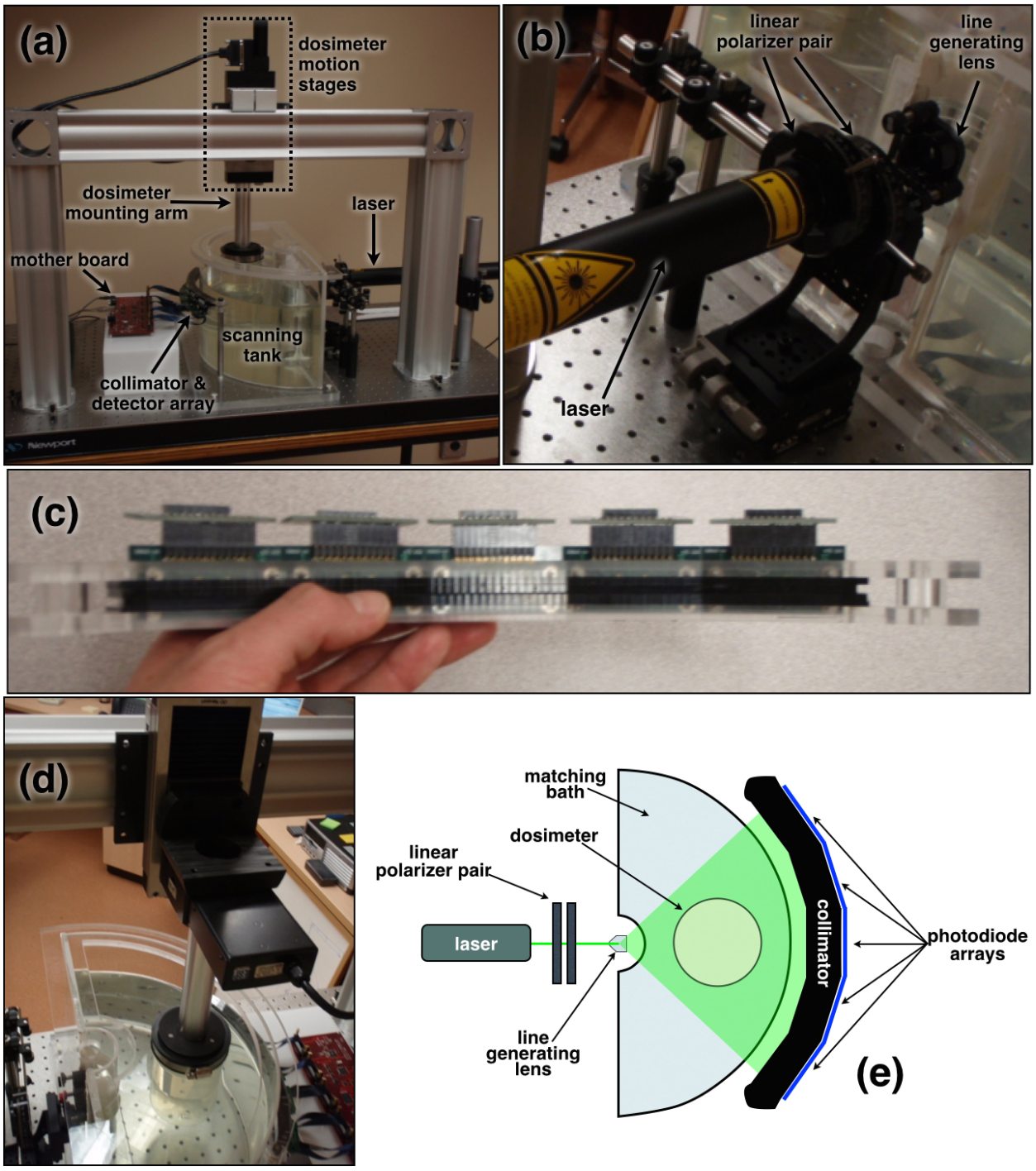

Figure 4.1: Photographs and diagrams of the initial setup for the prototype fan-beam optical CT scanner: (a) the overall setup with main components labelled, (b) a closer look at the fan-creation components, (c) a beam's eye view of the multi-hole collimator detached from the scanner with photodiode arrays and daughterboards still attached, (d) a closer look at the dosimeter motion stages (one rotating stage mounted onto one vertically translating stage), and (e) a schematic diagram of the scanner.

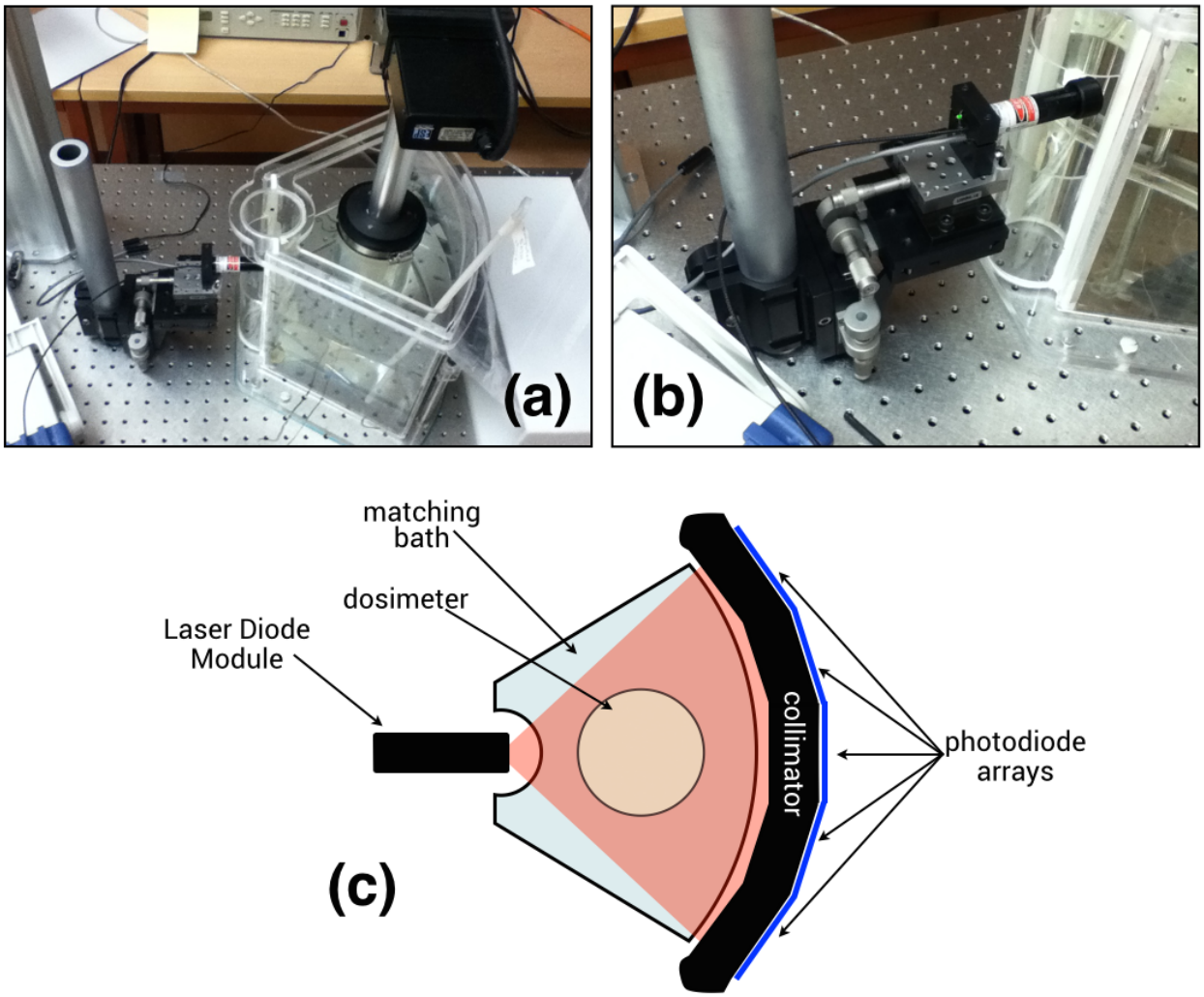

Figure 4.2: Photographs and diagrams of the revised setup for the prototype fan-beam optical CT scanner: (a) the overall setup of the latest implementation of the prototype with two main components changed: a new matching tank, and fan-creation was simplified into a single module, (b) a closer look at the multiple stages used to mount the laser diode module, allowing for fine adjustment of beam positioning, and (c) a schematic diagram of the new scanner setup.

discuss the six main components of the scanner's design: (i) fan-creation, (ii) the matching tank, (iii) photodiode detectors, (iv) the collimator, (v) data-acquisition electronics, and (vi) dosimeter motion stages. Key updates that took place during the course of this work involved fan-creation and the matching tank.

4.1.1 Fan-Creation Methods

The initial method for fan-creation used three components: (i) a green, helium-neon (HeNe) laser light source, (ii) a pair of linear polarizers, and (iii) a line-generating lens. The HeNe laser had a wavelength of 543 nm, 2 mW maximum output, and a circular beam 0.83 mm in diameter with a 0.84 milliradian divergence (Research Electro Optics, Inc.; Boulder, CO, USA). The relative polarization angles of the pair of linear polarizers was used to control the intensity of the HeNe beam according to Malus' Law (Edmund Optics; Barrington, NJ, USA). The line-generating lens was used to created a fan of 60° (Edmund Optics).

The updated method for fan-creation consolidates all three modules above into a single module: a laser diode module (LDM). The LDM creates a 60° fan of red light (635 nm, 3 mW) with a full-width-half-maximum thickness of 1.7 mm (Edmund Optics). Beam intensity of the LDM was controlled using a programmable DC voltage supply (B&K Precision; Yorba Linda, CA, USA).

4.1.2 Matching Tanks

The first version of the matching tank had a semi-circular design and was constructed in the machine shop of the BC Cancer Agency's Vancouver Island Centre. Figure 4.3a includes a to-scale illustration of the top-down view of the tank. The outer curved wall of the tank (acrylic plastic) is 3 mm thick, with an inner radius of 228 mm and an outer radius of 231 mm. The inner curved wall of the tank (polycarbonate plastic) is 3.15 mm thick, with an

inner radius of 31.75 mm and an outer radius of 34.90 mm. The flat wall of the tank (acrylic plastic) is 9.5 mm thick. In order to provide a smooth surface at the tank's entry wall, a portion of the inner curved wall was removed and two different types of plastics were used to form an entry window. The first entry window was made of a 1 mm thick mylar sheet. The second entry window was made of a 1.8 mm thick Lexan polycarbonate resin (SABIC; Riyadh, Saudi Arabia). Both windows suffered from structural issues, as can be seen in Figures 4.3b and 4.3c. The mylar plastic would eventually warp, and the Lexan plastic would eventually crack. The need to remove, replace, and water-tighten the tank would introduce frequent interruptions to research.

A second version of the matching tank was designed: (i) to provide a more reliable entry window, and (ii) to reduce the volume of the tank, thereby reducing the volume of matching fluid necessary for scanning. The new matching tank was designed to have the same radius of curvature for the entry and exit surfaces and was also constructed in the machine shop of the BC Cancer Agency's Vancouver Island Centre. Diagrams illustrating the new tank are shown in Figures 4.3d and 4.3e. Non-curved walls of the new tank were moved to reduce the volume of the tank. The majority of the tank is made of a polycarbonate plastic, with the exception of the entry surface. The inner wall is made of a 3 mm thick glass cylinder with a 35 mm outer radius. The University of Victoria's glassblower cut out a segment of the glass cylinder in order to allow the positioning of the laser diode module at the tank's point of concentricity. The intention of using a glass cylinder at the entry surface was to provide an optically smooth entry window that would not need frequent repairs.

4.1.3 Photodiode Detectors

The detector array is an approximate-arc, consisting of five linear 64-element photodiode arrays (S8865 Series, Hamamatsu; Hamamatsu City, Japan). With a total of 320 photodiode

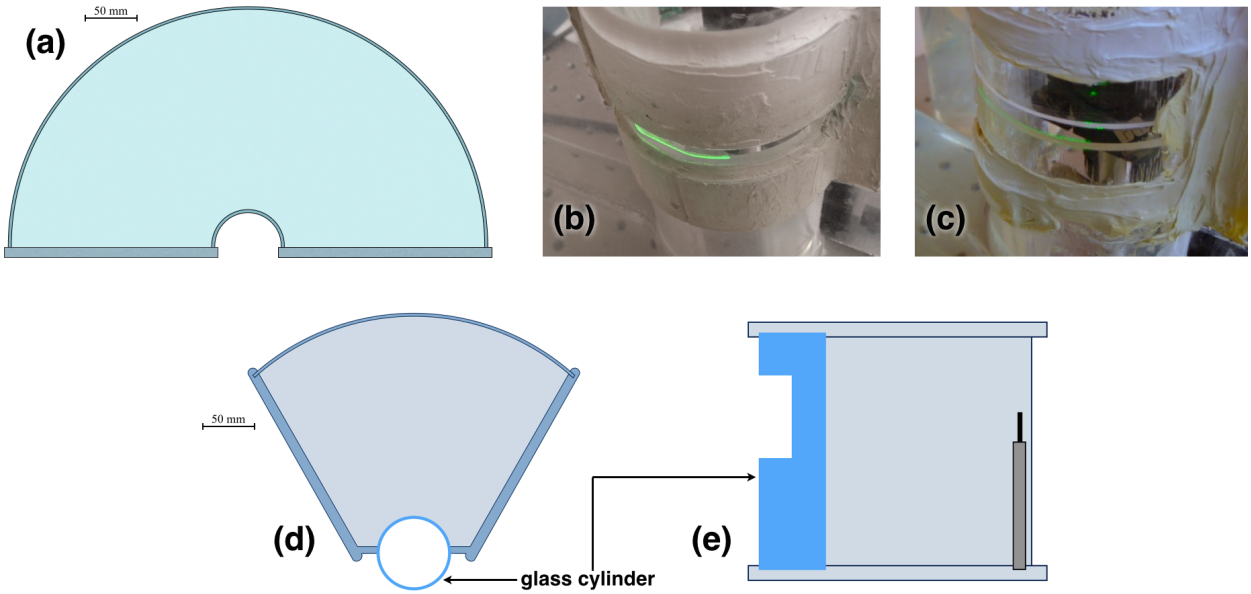

Figure 4.3: The old matching tank (to scale diagram shown in (a)) suffered from issues at the entry window for two different materials: (b) a mylar plastic would eventually become misshapen, and (c) a Lexan polycarbonate resin would eventually crack. A new tank was designed to have a lower tank volume (to scale diagram shown in (d)) and featured a glass cylindrical insert to act as an entry window. A semi-circular portion was cut out of the glass cylinder (see diagram in (e)) so that the fan vertex of the LDM could be positioned at the tank's point of concentricity.

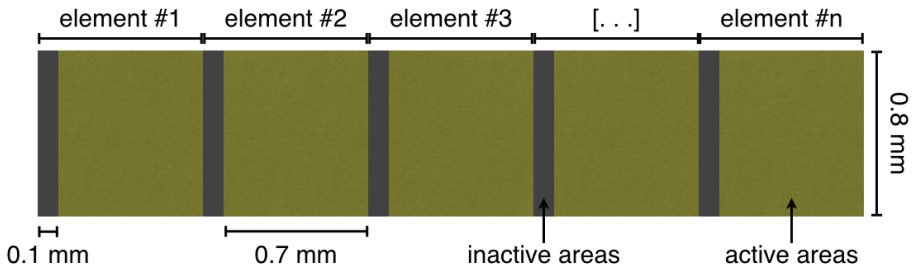

Figure 4.4: Diagram of active and inactive areas in individual detector elements (dexels) of the linear photodiode arrays. The multi-hole collimator was designed so that its septa are positioned over the inactive areas of each element.

elements in the detector array, each detector element (dexel) consists of an active area 0.8 mm in height, 0.7 mm in width, and a pitch of 0.8 mm (see Figure 4.4). These sensors consist of silicon and are operated in photoconductive mode (i.e., reverse biased). As such, they produce an amount of charge that is linear with respect to light intensity. For scanning purposes, the active width of each element is assumed to be representative of the entire dimensions (inactive + active) of each element.

4.1.4 Collimator

Each of the previously described photodiode arrays is mounted directly onto a physical collimator. The collimator is made of black plastic with a 15 mm slot cut for each detector element. The septa (i.e., walls) are 0.1 mm thick and are designed to overlap with the inactive area of each detector element. The design of this multi-hole collimator positions each photodiode array so that its central elements are 260 mm away from the fan vertex. As such, each detector element represents a $0.179° \times 0.8$ mm portion of a 0.8 mm high arc that spans 57.28°. An alternative collimator that consisted of a single slot for the entire array was tested in a previous work. Due to the multi-hole collimator's ability to effectively reject scattered light, it is now the default collimator used for the prototype [115].

4.1.5 Electronics

The data acquisition circuitry necessary for reading out charge values from the detector array was designed, constructed, and programmed in the electronics shop in the University of Victoria's Physics & Astronomy Department. Each photodiode array is mounted directly onto a daughter board, which is then connected to a single motherboard (see Figure 4.5). The placement of the daughter board directly on each photodiode array allows decoupling capacitors to be closely mounted to the array, thereby reducing readout noise. The motherboard features 4 MB of onboard memory, allowing it to store up to 6500 measurements of the entire 320-element detector array. The integration time — the length of time that the motherboard will let detectors collect charge for — can be adjusted between individual scans, ranging from 640 μs to 21.890 ms in increments of 83.33 μs. This allows the sensitivity of the detector array to be adjusted during scanning. Detector measurements are stored as 14-bit binary numbers, ranging from 1 to 16384. For the purpose of ignoring "dark" readout values and "saturated" readout values, it was previously established that detector measurements that are below 50 and above 14500 are assumed to be unreliable.

The motherboard is connected to a personal computer (PC) via Universal Serial Bus (USB), and operation of the motherboard is orchestrated using MATLAB (MathWorks; Natick, MA, USA). Communicating via USB, MATLAB can be used to: (i) change the detector integration time to be used for the next scan, (ii) instruct the motherboard to take a measurement of the entire detector array and store that to its onboard memory, and (iii) transfer all of the data stored on the motherboard's onboard memory to the PC. Communicating via USB, single characters are sent to the motherboard to request that the detector array be scanned ('S') or that stored data be transferred[1] to the PC ('G'). Methods of performing data acquisition during scanning are discussed in Section 4.4.

[1]To aid memorization, the transferring of stored data was colloquially referred to as *getting*.

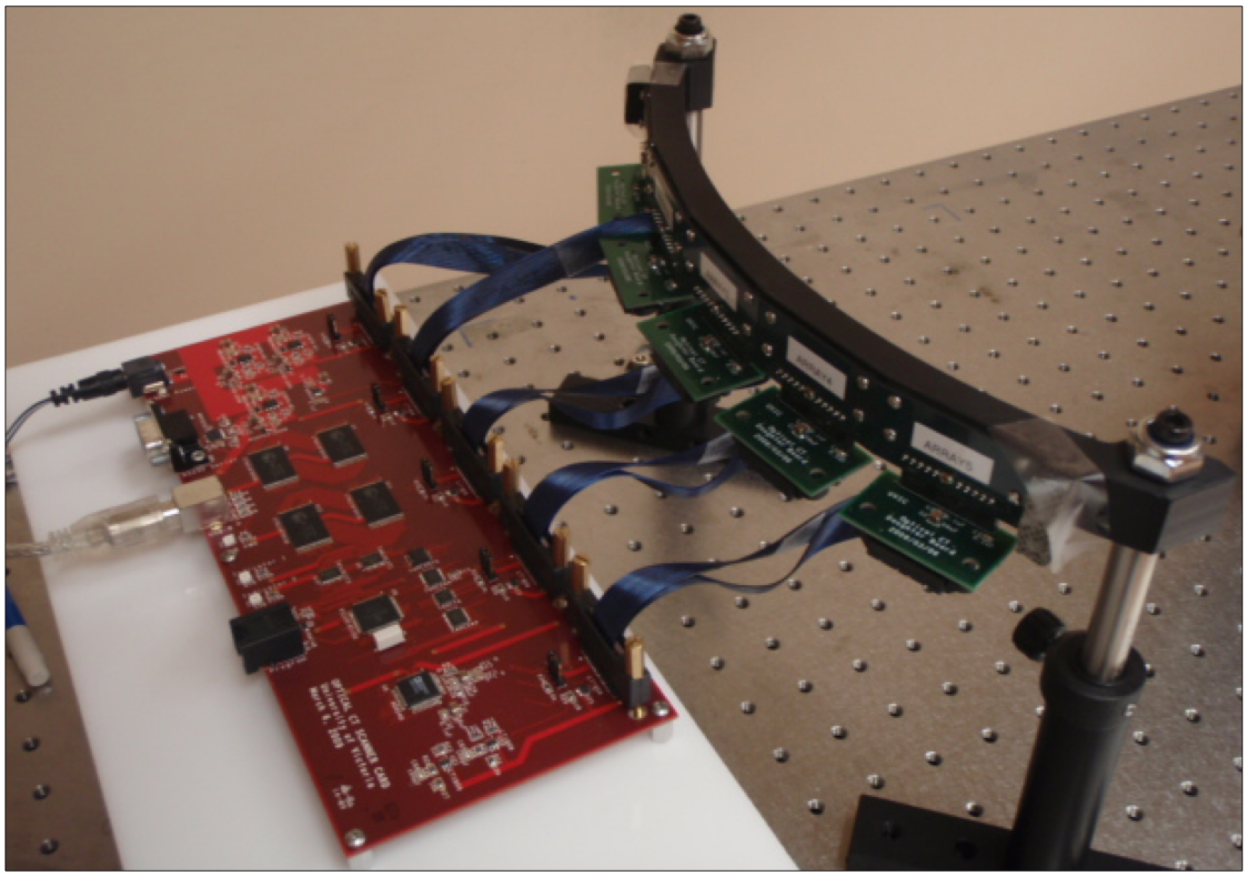

Figure 4.5: Photograph of the motherboard and daughterboards electronics used for data acquisition. Data collection is orchestrated by the motherboard (red) while each of the five daughterboards (green) are directly attached to each linear photodiode array.

4.1.6 Dosimeter Motion Stages

The rotation and the vertical translation of the dosimeter/flask is performed using two stages: one rotating stage and one translating stage (Newport; Irvine, CA, USA). The flask is mounted on an arm that screws into a rotational stage, the rotational stage is mounted onto a translating stage that moves up and down, and the translational stage is suspended over the matching tank on a cross-bar frame. The motion of each stage is directed by a Universal Motion Controller (Newport) and MATLAB is used to send instructions for flask motion to the motion controller via a USB-to-serial dongle. The vertically translating stage has a positional resolution of 1 μm, a maximum velocity of 2.5 $\frac{mm}{s}$, and a maximum acceleration/deceleration of 10 $\frac{mm}{s^2}$. The rotating stage has a positional resolution of 0.0005°, a maximum velocity of 80 $\frac{^\circ}{s}$, and a maximum acceleration/deceleration of 320 $\frac{^\circ}{s^2}$.

4.2 Scattering Solutions & PAGAT Dosimeters

Two types of samples were imaged using the optical CT scanner: (i) scattering solutions, and (ii) polymer gel dosimeters. Both types of samples (shown in Figure 4.6a) were housed in 1 L, 95 mm diameter cylindrical polyethylene terephthalate cylindrical flasks (Modus Medical Devices Inc.; London, ON, Canada). The first type of sample was formulated by adding a concentrated solution of Duramax B-1000 polymer (Rohm and Haas; Philadelphia, PA, USA) to deionized water. The concentrated solution is shown in Figure 4.6b, and tools for imaging these samples without removing the flask from the scanner are shown in Figure 4.6c. A porthole was cut into the upper region of the flask, which allowed concentrated scatterer to be added to the solution using a pipette. In this way: (1) "reference" light (i.e., I_o) could be acquired of a flask filled with deionized water, (2) the concentrated scatterer would then be added and mixed via the porthole, and (3) "measurement" light (i.e., I) could be acquired of the opaque solution.

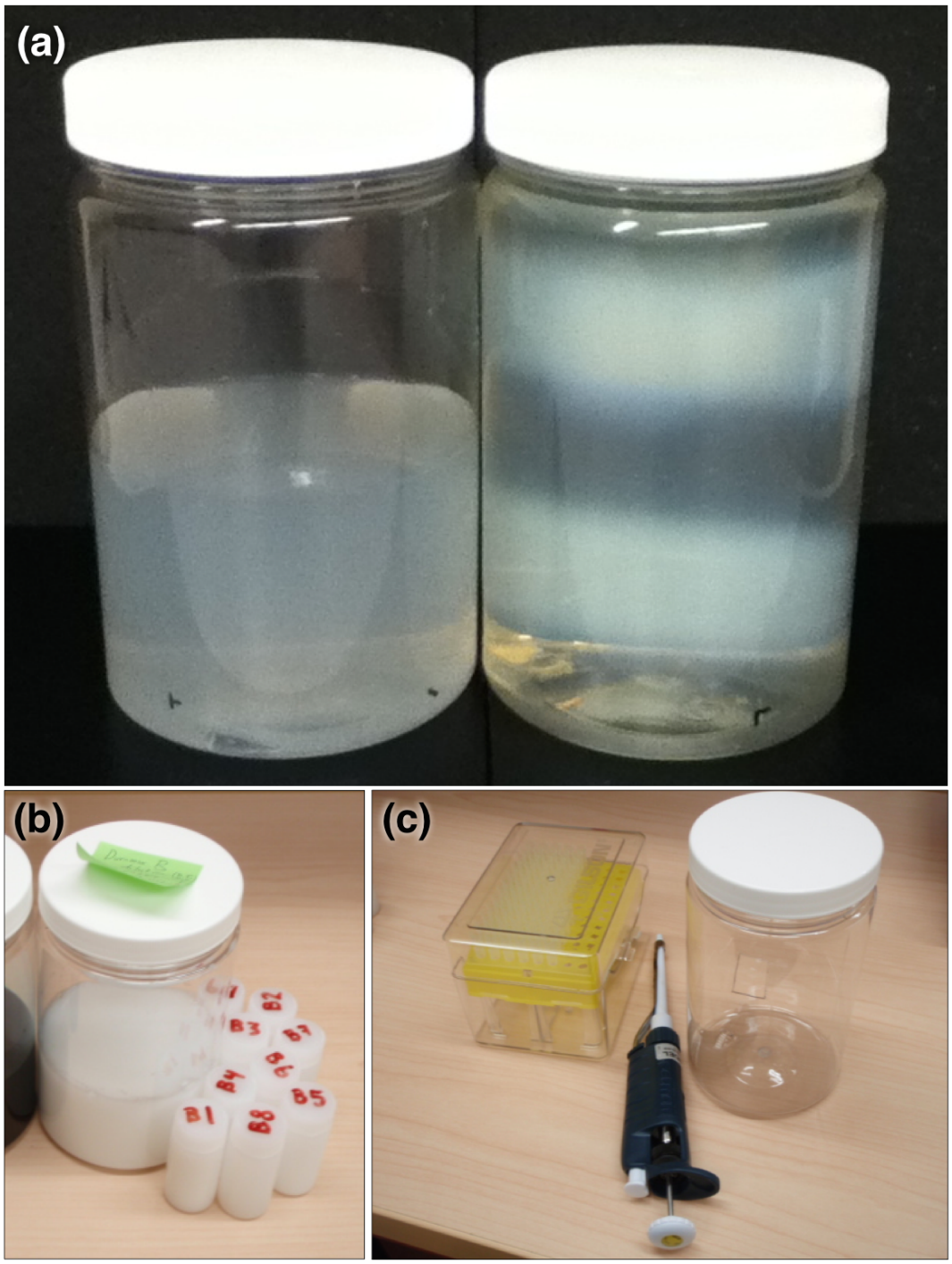

Figure 4.6: Shown in (a) are two types of samples that were imaged in the optical CT scanner: a scattering solution (left) and a PAGAT dosimeter (right). Scattering solutions were prepared by adding concentrated scatterer (b), and scans of scattering solution could be performed without disturbing flask by adding scatterer via a porthole in the upper portion of the flask (c).

The dosimeter investigations in this work use a normoxic polyacrylamide gel dosimeter recipe, which allows dosimeters to be prepared in a laboratory fume hood in the presence of oxygen. These types of dosimeters have been shown to maintain their spatial integrity, not suffering from the diffusion seen in many dye-based gel dosimeters [57, 63, 66, 67, 95]. Furthermore, normoxic polyacrylamide gel dosimeters have been shown not to suffer from significant energy dependence or dose-rate dependence that can affect some dye-based gels [59, 90, 94, 95]. Polyacrylamide gels are also more radiologically water-equivalent than the hard-plastic PRESAGE^{TM} dosimeter [96]. Finally, PGDs can be prepared on-site, whereas the PRESAGE^{TM} dosimeter needs to be ordered and shipped from its manufacturer.

The same recipe — which is similar to other normoxic polymer gel dosimeters studied in the literature — was used consistently throughout the work [96, 130, 147–151]. The chemical composition of all dosimeters were as follows (w/w%): 91.8% deionized water, 4.0% gelatin, 2.0% acrylamide, 2.0% N,N'-methylenebisacrylamide (bis), and 9 mM tetrakis (hydroxymethyl) phosphonium chloride (THPC) (all chemicals from Sigma-Aldrich; Oakville, ON, Canada). Using two acrylamides, gelatine, and THPC, this type of dosimeter recipe is also known as a PAGAT (PolyAcrylamide, Gelatin, And THPC) dosimeter. To prepare a batch of dosimeter gel, a 700 mL portion of water was first heated to 43°C using a magnetically stirring hot plate (Fisher Scientific International Inc.; Hampton, NH, USA). Then, gelatin, bis, and acrylamide were each added and allowed to fully dissolve, one at a time. After these had fully dissolved, the remaining portion of water and THPC (both at room temperature, 21°C) were combined in a separate beaker and then immediately added to the heated solution. The resulting mixture, now complete, was promptly poured into a 1 L flask and sealed. From this point, two different cooling methods were investigated, which is discussed in Section 5.5.

4.3 Treatment Planning & Irradiation

The simulation, treatment planning, and irradiation of PAGAT dosimeters followed a similar workflow that is experienced by a patient when undergoing radiation therapy. First, 3D density information for the dosimeter was acquired using a General Electric HiSpeed FX/i single-slice CT scanner (GE Medical Systems; Milwaukee, WI, USA). Once that data was acquired, it was transferred to the Eclipse^{TM} treatment planning software (TPS) (Varian Medical Systems; Palo Alto, CA, USA). Using Eclipse^{TM}, treatment plans could be designed for the irradiation of dosimeters and the software would calculate the dose expected to be produced in the "body" of the dosimeter (see Figure 4.7). Then, irradiations were performed using either a Varian Clinac 21EX linear accelerator or a Varian TrueBeam^{TM} linear accelerator (Varian Medical Systems). The dosage and photon energies used for dosimeter irradiations varies between investigations, but all irradiations used square 3×3 cm^2 photon

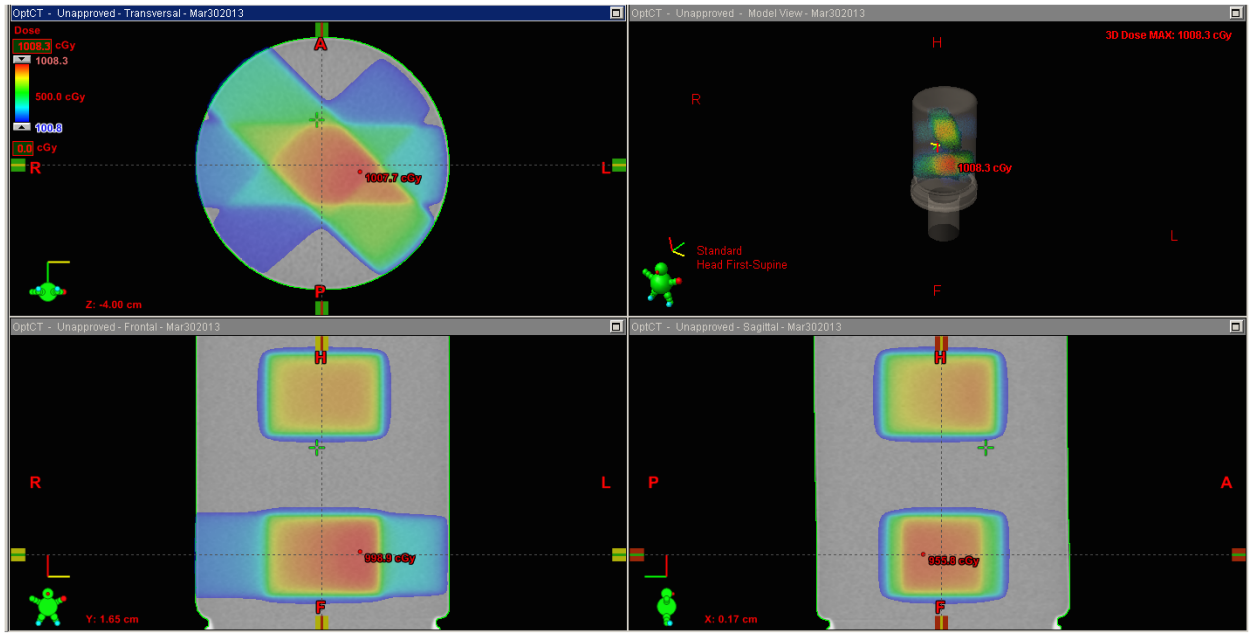

Figure 4.7: Sample screenshot of a dosimeter's treatment plan in the Eclipse^{TM} treatment planning software.

beams, radiation was delivered at a dose rate of 600 monitor units[2] per minute, and dose distributions were calculated using Eclipse^{TM}'s analytic anisotropic dose calculation algorithm (AAA).

Preliminary tests using PAGAT dosimeters (to be discussed in Sections 5.4 and 5.5) were more qualitative in nature. In those instances, the dosimeter was placed on the treatment table, aligned roughly, and irradiated. After these preliminary tests, investigations became more quantitative. As such, for more accurate positioning of PAGAT dosimeters in those subsequent investigations, a specially designed dosimeter mount was used[3] [89]. A photograph of this mount and the more accurate irradiation setup is shown in Figure 4.8.

[2]Monitor units, or MUs, are a measurement of linear accelerator output. MUs are calibrated to introduce a specific value of absorbed dose to a certain location in a specific setup, the definition of which can vary between treatment centres.

[3]This mount also allows for the dosimeter to be positioned within a water-filled anthropomorphic head phantom, but its headless configuration is just as useful for these investigations.

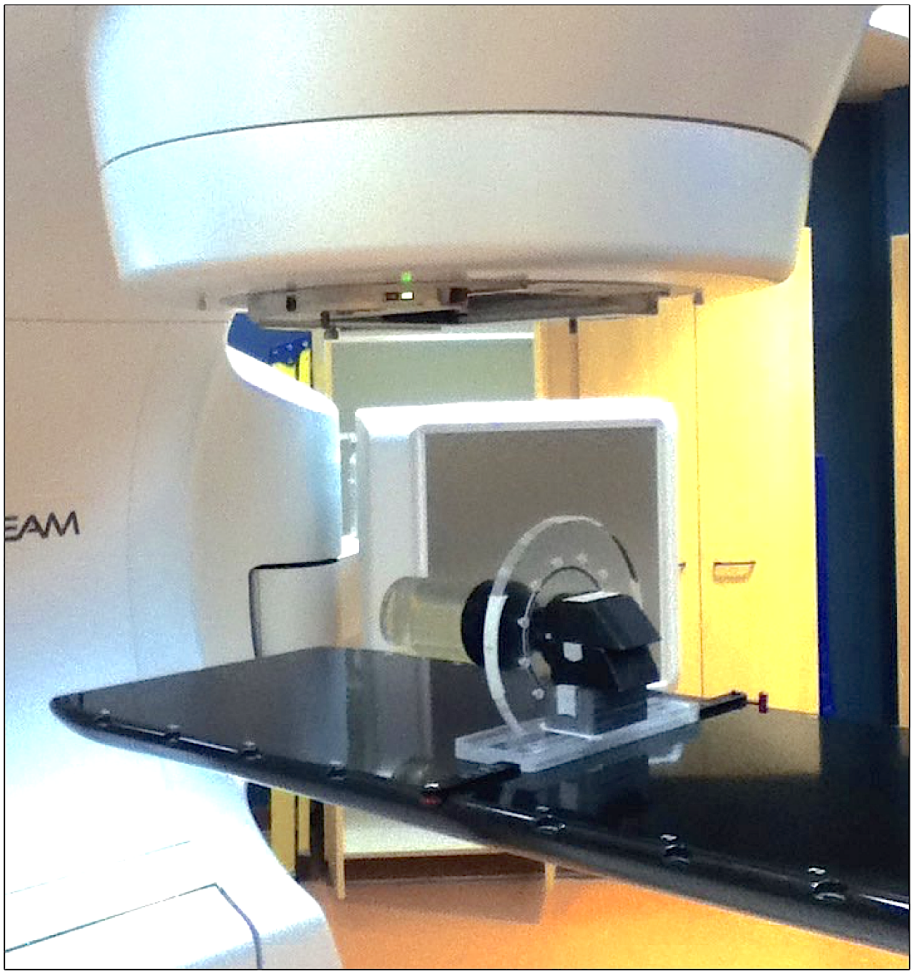

Figure 4.8: Photograph of a polymer gel dosimeter mounted in a specially designed dosimeter mount at the linear accelerator, ready for irradiation.

4.4 Data Acquisition

When using the optical CT scanner to scan an opaque sample, some regions of a light sinogram will typically go below the "dark" readout value of the detector array. In these instances, dynamic range extension needs to be used in order to acquire valid measurements in these dark regions. For this work, dynamic range extension via photodiode integration time was used. As such, two measurements were taken at each projection angle in sinogram space. First, a scan was acquired using a photodiode integration time of 6.06 ms, then a scan was acquired at 21.8 ms. The scan with a longer integration time could then be renormalized to the its shorter scan equivalent by multiplying its measurements by 0.2777. Through these means, a full sinogram of valid light measurements could be stitched together from these short integration time and long integration time scans.

The option to leave detector readout measurements as stored data on the motherboard's onboard memory allows for two possible data acquisition routines. These two acquisition routines were referred to as *'scan, get, scan, get'* and *'scan, scan, scan, get.'* The first routine — scan, get, scan, get — instructs the motherboard to scan the detector array and then transferred that measurement to PC before the detector array is scanned again. This means that each time data is transferred to the PC, it comes in the form of a single 320-element line of detector array readout values. The second routine — scan, scan, scan, get — instructs the motherboard to scan the detector array multiple times, stores those measurements to onboard memory, and then transfers data to the PC once scanning has completed. When multiple scans are collected from onboard memory, it is collected as a a $n\times$320-element line of detector array readout values, where n is the number of scans that was collected. Both of these acquisition routines are illustrated in Figure 4.9. The first acquisition routine cannot scan the detector array as frequently as the second routine because data transfer takes a brief amount of time. On the other hand, the second acquisition routine is limited by

onboard memory, which can only store up to 6500 projections. That much memory is more than enough for a single slice; but, when one considers scanning the volume of an entire dosimeter, this limitation forces the need for intermittent breaks to allow data transfer to take place.

To perform a CT scan of a sample, measurements need to be taken at known projection angles. So, with respect to the optical CT scanning of a sample, there were two different scanning routines. These routines differed according to the motion of the sample being scanned. The two scanning routines were referred to as 'step + shoot' scanning and 'continuous rotation' scanning. As might be evident from their naming, the step and shoot routine allows the sample to move and come to a complete stop between each incremental rotation of the sample, and the continuous rotation routine instructs the sample to fully rotate at a constant speed while multiple scans are acquired of the moving sample. These two different scanning routines are illustrated in Figure 4.10.

Preliminary scanning used the step and shoot routine due to its more reliable positioning accuracy. Although, this accuracy comes with the cost of longer scan times. This is due to the necessary pause in the data acquisition routine in order to wait for motion to complete. In the interest of speeding up scans, the continuous rotation scanning routine was considered. Additionally, with continuous rotation scanning, the 'scan, scan, scan, get' acquisition would be more appropriate, because it would delay data transfer until the sample has fully rotated. This would allow projection measurements to be acquired more frequently while the sample is rotating. However, in order for continuous rotation scanning to work, dosimeter rotation and scan acquisition timing both need to be consistent. Issues that arise with continuous rotation and methods of resolving those issues are discussed in Section 5.6.

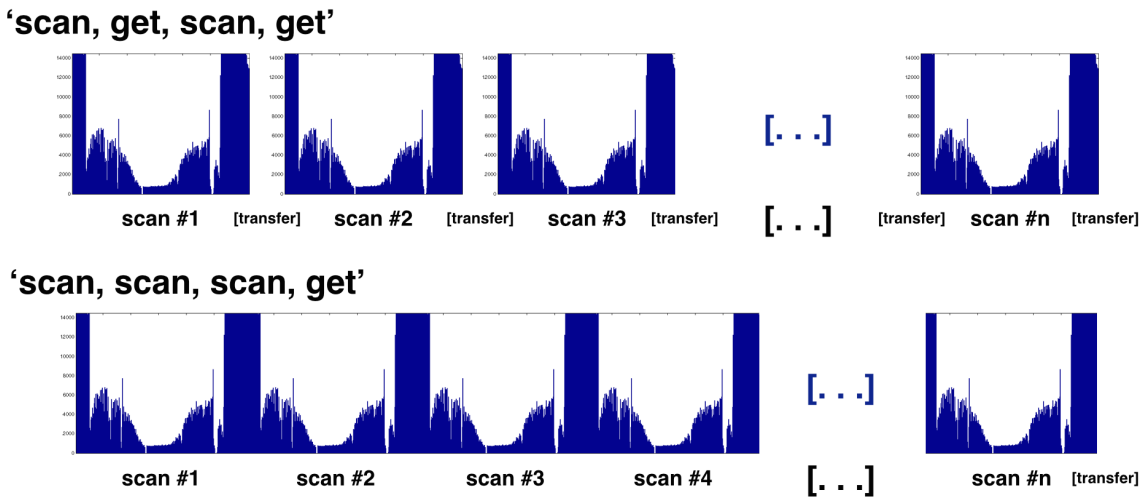

Figure 4.9: Readout of the detector array can be performed using two different routines. The first routine — scan, get, scan, get — tells the motherboard to scan the detector array and then transfers measured data from motherboard memory to the PC before requesting another scan. The second routine — scan, scan, scan, get — tells the motherboard to scan the detector array multiple times and stores measured data on the motherboard's memory before being transferred to the PC.

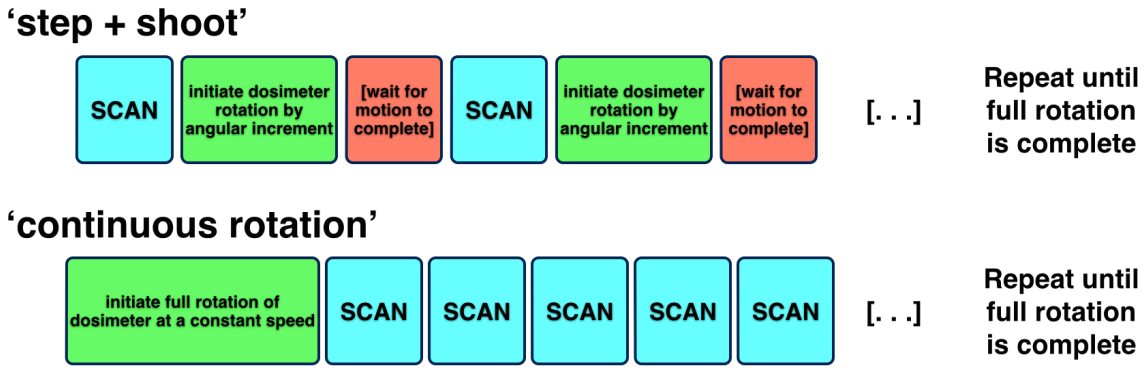

Figure 4.10: When CT scanning a dosimeter, measurements need to be taken at known projection angles. The 'step + shoot' method acquires scans while the dosimeter is motionless, with dosimeter motion taking place between each projection scan. This ensures accurate dosimeter positioning, but forces a necessary pause to be included in the data acquisition routine while the dosimeter is in motion. The 'continuous rotation' method initiates a full rotation of the dosimeter at a constant speed, and then scans the dosimeter while in motion. Although, for this second method to work, dosimeter rotation and scan acquisition timing need to be reliable.

4.5 Data Processing & Image Reconstruction

Data acquired by the optical CT scanner's electronics needs to be processed before it can be used reliably. The first step involves tagging all "dark" or "saturated" readout values (<50 or >14500, respectively) as unreliable. This is done by setting these values to -1, a nonsensical value[4]. Next, a detector offset correction, which was uncovered during previous investigations, is applied. Shown in Figure 4.11, the detector array exhibits a zero-value offset shape that must be subtracted from readout data in order for photodiode measurements to accurately represent the light they are measuring. Once the offset correction is applied, corrected light data can be used reliably. Finally, reliable measurements that were acquired using short and long photodiode integration times are stitched together into a single light measurement.

Two types of light measurements are acquired in order to scan an object: "reference" light (i.e., I_o), and "measurement" light (i.e., I). Dividing measurement light values by reference light values provides a transmission measurement, and this transmission measurement allows for the calculation of optical density. Using a polymer gel dosimeter, examples of all four types of profiles are shown in Figure 4.12. These profiles are acquired at many different projection angles in order to reconstruct an image of the sample.

After a reference scan and a measurement scan are acquired for a full-rotation of the sample, an optical density sinogram can be calculated. At this point, data in the sinogram has a fan-beam geometry. In order to reconstruct an image of opacity attenuation values from a fan-beam sinogram of OD values, one must first convert the fan-beam sinogram into a parallel-beam sinogram. MATLAB has a function that purports to perform this in one line of code — *ifanbeam*. However, previous work demonstrated that this function does not perform as documented and, in reality, ignores the latter half of the fan-beam sinogram.

[4]The detector array does not return values < 0.

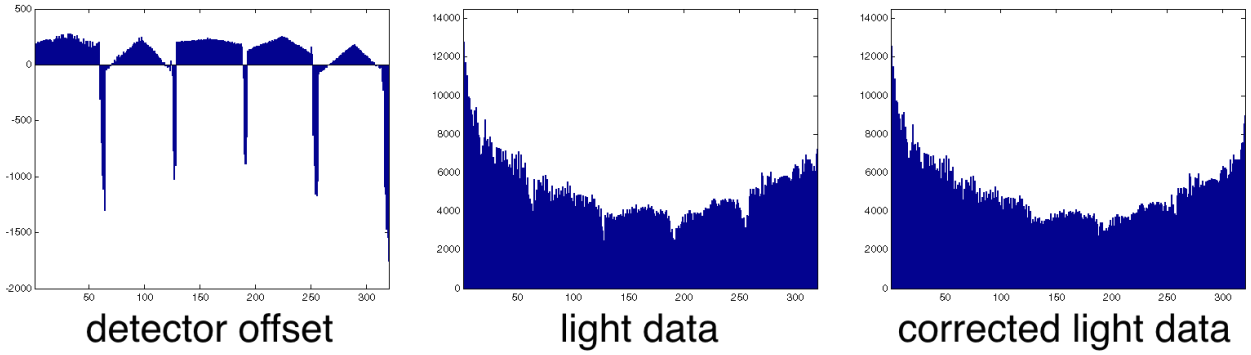

Figure 4.11: Previous work indicated that an offset correction needed to be applied to raw light data in order to accurately represent the light intensities being measured. Here, plots show the detector offset, and an example of raw light data and corrected light data.

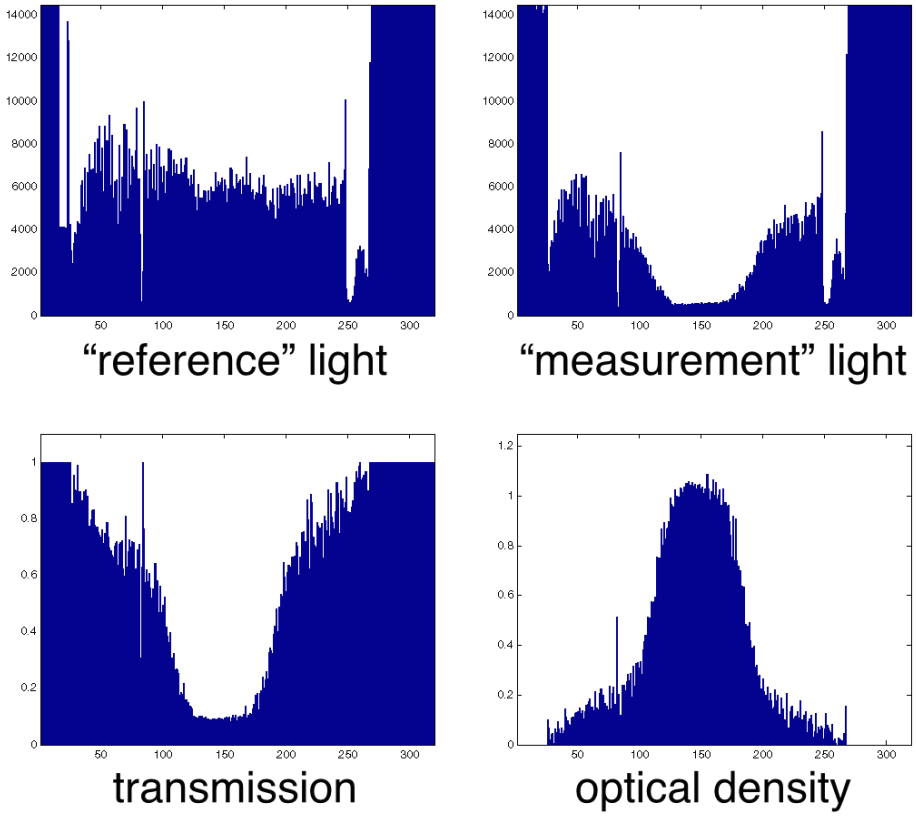

Figure 4.12: As an example, four different plots are shown for a single projection of a dosimeter: reference light (i.e., pre-irradiation, I_o), measurement light (i.e., post-irradiation, I), transmission, and optical density.

Although a bug report was filed and acknowledged by MathWorks, the function continues to perform sub-optimally at the time of this writing. As a result, a work around method was developed to convert fan-beam data into parallel-beam data without ignoring the latter half of the fan-beam sinogram. This method is illustrated in Figure 4.13. Essentially, the 360° sinogram of fan-beam data is converted into two semi-redundant[5] 180° sinograms of parallel-beam data. These two sinograms are then averaged ray-by-ray to produce a single 180° sinogram of parallel-beam data that takes full advantage of the entire fan-beam sinogram. From this, an image is reconstructed using filtered backprojection (linear interpolation, ramp-Hamming filter, 512×512 images with pixel sizes of 0.25×0.25 mm^2).

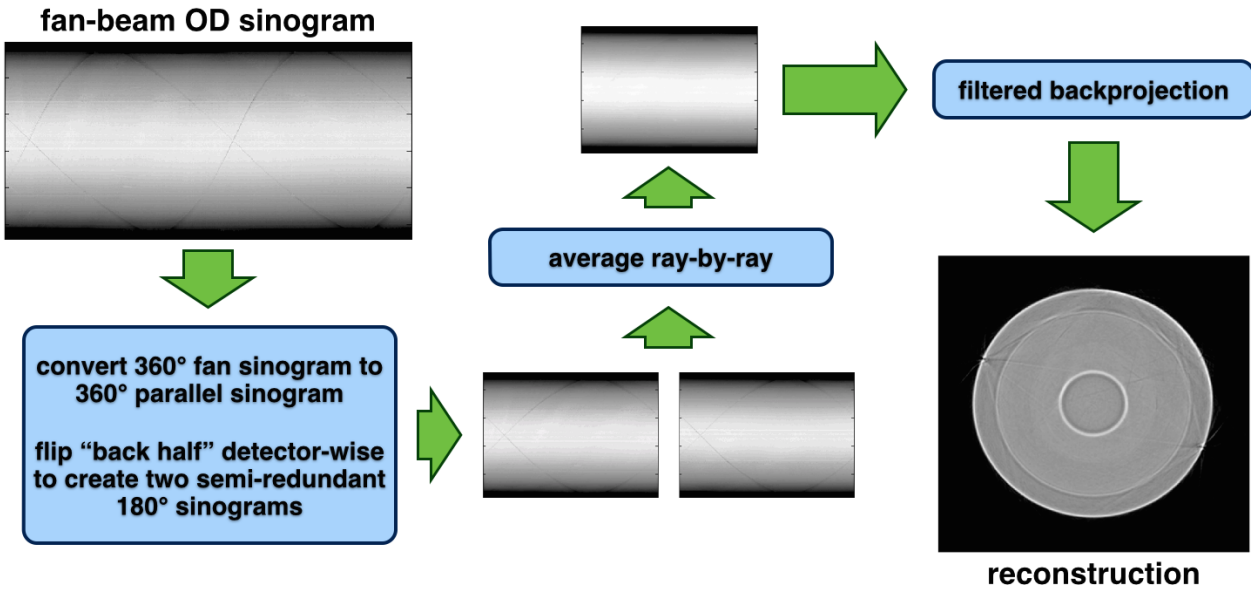

Figure 4.13: Workflow diagram illustrating the data processing steps necessary to obtain a reconstructed image from a fan-beam OD sinogram. Fan-beam to parallel-beam re-binning uses linear interpolation.

[5] "Semi-redundant" because they should theoretically represent the same data. But, each ray from these sinograms — in reality — traversed the sample in opposite directions.

4.6 Co-Registration of Measured Opacity Data & TPS Dose Data

The pixels in a reconstructed image of a dosimeter represent the opacity of the dosimeter at that position. Opacity at a given position can be quantitatively represented by an opacity attenuation coefficient, which is of arbitrary units. In order to convert a dosimeter's opacity image into a dose image, a relationship must be established between opacity attenuation coefficients and absorbed dose. To establish this relationship, opacity images need to be spatially registered with dose images calculated by the treatment planning system. So, a routine was established to aligns these two datasets. The routine is illustrated in Figure 4.14 and is performed as follows:

1. Align both images onto a grid of equally sized pixels.
2. Assuming a linear relationship between opacity and dose, convert the gel opacity image to a dose image using an initial opacity-to-dose scaling constant.
3. Calculate the center of gravity for each image and align that with the center of the image matrix.
4. Seeking to minimize the sum of squared pixel differences, perform fine adjustments to...
   (a) ...the XY positioning of the gel image.
   (b) ...the opacity-to-dose scaling constant.
   (c) ...the rotational positioning of the gel image.
5. Repeat fine adjustments once.
6. Divide the gel image by the opacity-to-dose conversion constant.

At the end of this routine, the gel image has been returned to its original opacity scale, only with its positioning aligned with TPS dose data. The grid size used for this work was

512×512 pixels, each pixel being 0.25×0.25 mm^2. As such, interpolation was used to re-grid TPS dose data, which was originally calculated with 1×1 mm^2 pixel sizes. The starting opacity-to-dose scaling constant used in this work was 236,000[6]. While the assumption of a linear relationship between opacity and dose serves as a useful approximation for this co-registration technique, the relationship between opacity and dose is examined more closely in Section 5.7.

The alignment routine described above was meant to minimize the positional differences between these two datasets in order to investigate the readout of the dosimeter itself. It is not meant for investigations that look into the actual dosimetric measurement of a radiotherapy treatment technique. If one sought to use a dosimeter to evaluate a radiation treatment technique, a different data alignment routine would need to be used. For example, a treatment error could see the radiation treatment miss the target by a significant distance or by a significant dosage. The alignment routine described above would easily miss such errors. Nevertheless, this alignment routine is sufficient for the investigations in this work.

4.7 Matching Bath Preparation & Rayline Tracing

At times, it can be useful to obtain information regarding the trajectory of rays in the fan-beam. For instance, the purpose of the refractive matching bath is so that rays maintain a straight trajectory through the dosimeter. As such, after the matching bath has been properly prepared, the trajectory of rays passing through the bath should be unchanged when the dosimeter is placed in the scanner. In order to examine rayline trajectories, a "combed" fan-beam is used.

By placing a line-pair pattern on the entry window of the optical CT scanner (see Figure 4.15), the fan-beam becomes modulated into a set of teeth and gaps. Taking a measurement

[6]Determined empirically.

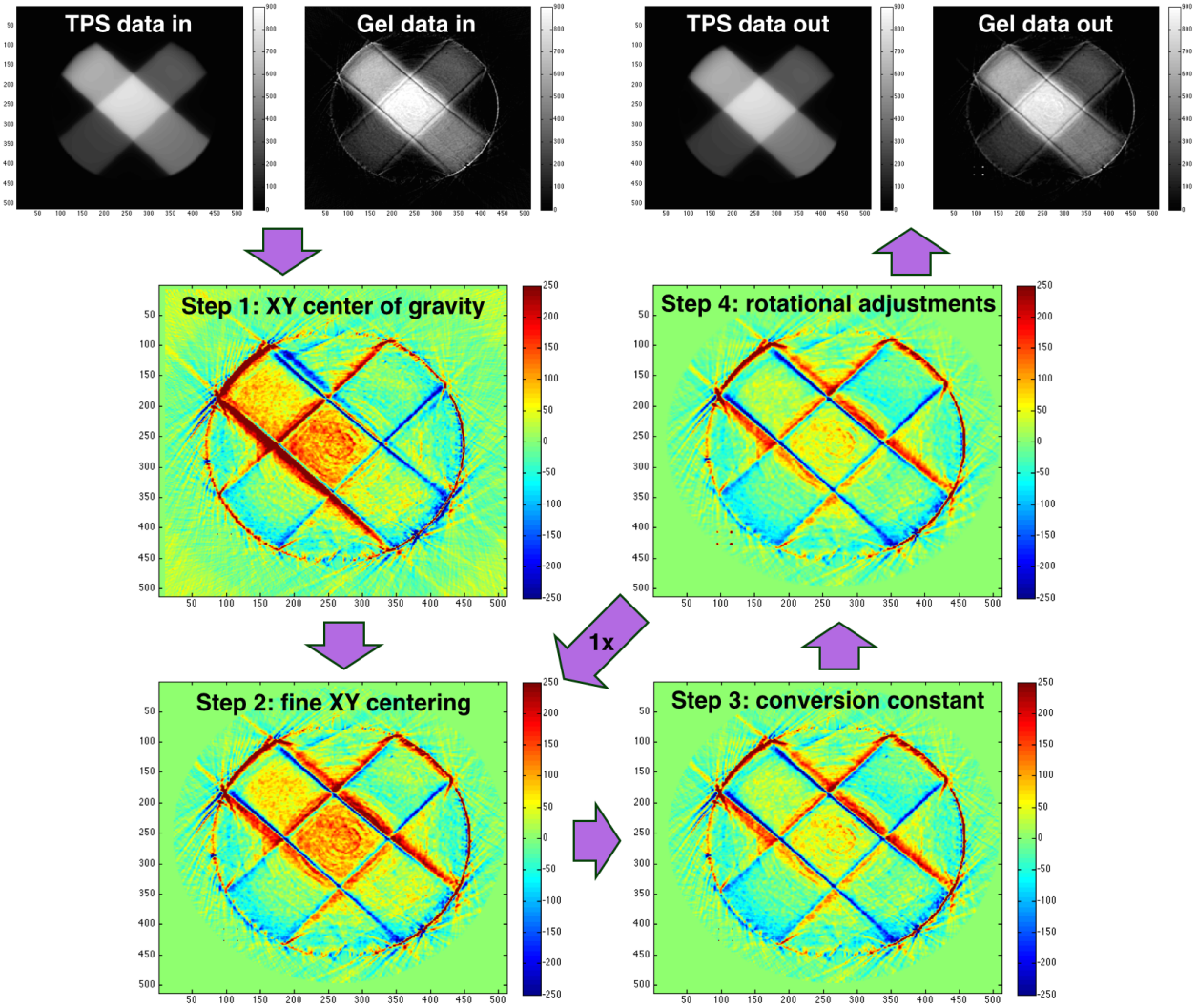

Figure 4.14: Once TPS dose data and scaled gel data are positioned on a matrix of equal pixel size, steps are taken to align the two images. Here, difference images (gel − TPS) are shown after the implementation of each step. Minimization of the sum squared difference for all pixels in the two images is used to guide alignment. Step 1: the "center of gravity" of dose for each image is aligned on the central pixel of the grid. Step 2: fine XY positional adjustments are made on gel data. Step 3: the scaling constant applied to gel data is adjusted. Step 4: rotational adjustments are made to gel data. Finally, steps 2–4 are repeated once. All images are in units of cGy.

of this combed fan-beam in a water bath establishes the shape of the ideal trajectory to aim for with a properly matched bath. Glycerol (Sigma Aldrich) was used as a refractive agent. After a dosimeter was placed in the scanner with a water bath, noticeable trajectory errors are seen as a distortion of the combed pattern. The matching bath was empirically formulated by adding glycerol (n = 1.47) to the water bath (n_{H_2O} = 1.33) until the comb pattern traversing the dosimeter aligns with the original pattern. The bath is matched on a dosimeter by dosimeter basis and has a refractive index of approximately 1.34, slightly higher than water.

Similarly, this combed fan-beam approach to trajectory measurements can be useful to detect rayline errors after the bath has already been prepared to match the refractive index of the dosimeter. For instance, a sinogram acquired using a combed fan-beam can provide a rayline tracing sinogram (see Figure 4.16a). A rayline tracing sinogram shows how much raylines can deviate throughout the course of a scan. By monitoring the position of each tooth and gap in the rayline tracing sinogram, one can quantify how much raylines can deviate from their average position (see Figures 4.16b and 4.16c). The errors apparent in Figure 4.16 cause severe refraction artefacts, which are the main topic of Chapter 7.

4.8 Chapter Summary

The components and configuration of the prototype fan-beam optical CT scanner evolved throughout the course of the work presented in Chapters 5–7. Similarly, the methods used (e.g., gel fabrication, measurement protocols) were also continually modified, as new results often indicated alternative approaches for attaining better results. The details included above provide a good basis for interpreting the results that follow. In the remainder of this thesis, wherever pertinent, specific details or methods are incorporated into the discussion.

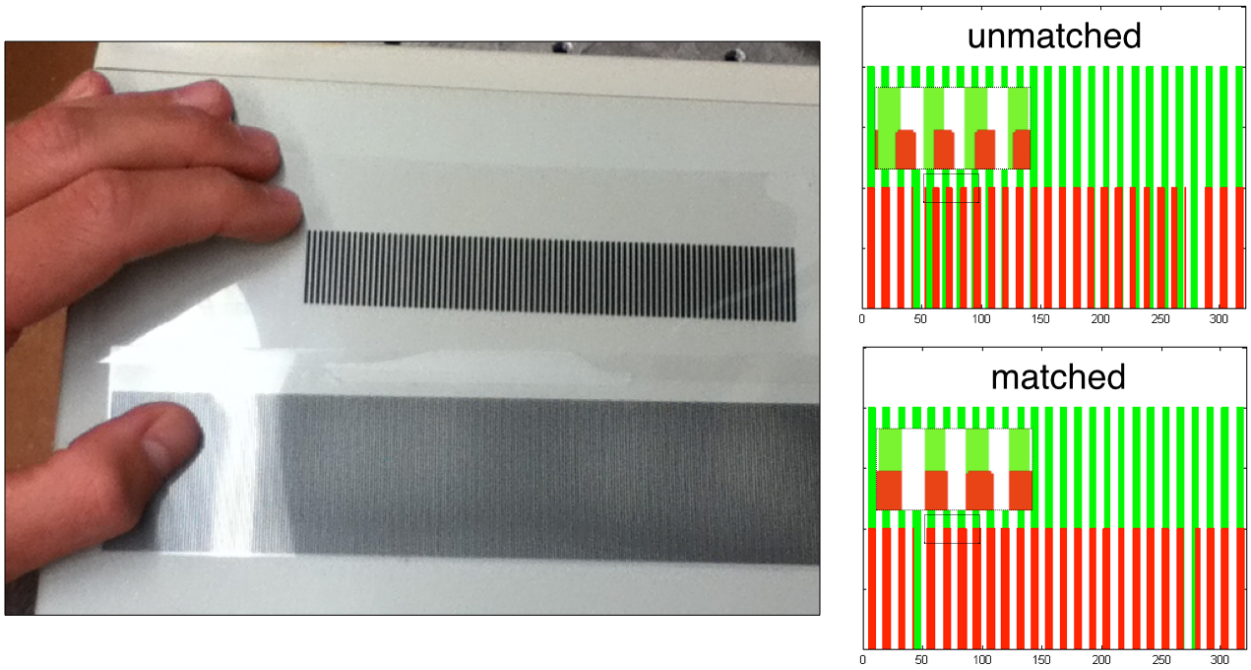

Figure 4.15: On the left, two examples of line-pair patterns used for rayline tracing are shown. By placing such a pattern on the entry window of the matching tank, one can create a "combed" fan-beam. Monitoring the teeth and gaps of the combed fan-beam allows one to empirically formulate the matching bath by ensuring that raylines align with one another when the dosimeter is in place and when the dosimeter is absent.

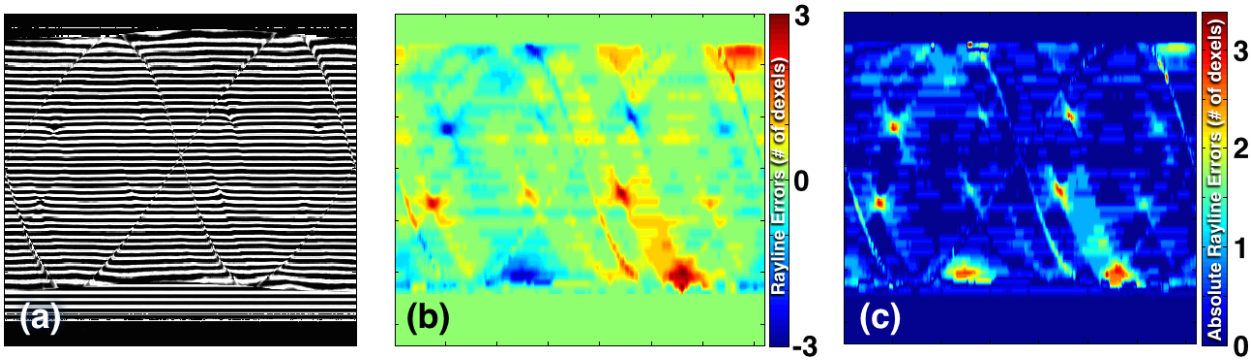

Figure 4.16: Using a combed fan-beam, one can obtain (a) rayline tracing sinograms, which can be used to calculate (b) rayline error sinograms, and (c) absolute rayline error sinograms. These sinograms were acquired for an irradiated PAGAT dosimeter.

Chapter 5

Results & Discussion I: Development of the Optical CT Dosimetry System

The work presented in this chapter investigates topics related to the continued development of the optical CT dosimetry system. Section 5.1 examines two new scanner components: a new fan-creation method, and a new matching tank. Section 5.2 presents artefact removal techniques that were developed to remove flask seam artefacts and ring artefacts in sinogram space. Section 5.3 introduces a flask registration technique to allow for the reproducible placement of flasks in the optical CT scanner. Using this flask registration technique, Section 5.4 illustrates the benefits gained by comparing post-irradiation scans of a dosimeter to pre-irradiation scans. Section 5.5 compares scanning results of a PAGAT dosimeter that was cooled quickly after fabrication and one that was cooled slowly. Section 5.6 examines errors that arise during continuous rotation acquisition and the steps necessary for correcting these errors. Finally, section 5.7 investigates calibration techniques for the PAGAT dosimeter.

5.1 Scanner Updates

5.1.1 New Fan-Creation Method

The red laser diode module that replaced the old fan-creation components (HeNe laser, pair of linear polarizers, and a line-generating lens) was superior in multiple ways. First, the LDM exhibits lower beam intensity fluctuations than the HeNe setup (relative standard deviations of ∼0.8% versus ∼2%, respectively). Additionally, intensity fluctuations tended to be exhibited uniformly across the entire beam, whereas intensity fluctuations in the HeNe setup often occurred unevenly across the beam. Also, the LDM is more suitable for imaging the commonly used PRESAGE^{TM} dosimeter because its wavelength matches the relevant dose-response peak for the PRESAGE^{TM}. Furthermore, the ability to control the intensity of the LDM remotely via voltage control is more desirable than the HeNe setup, which requires adjustments to the crossing-angle of the polarizer pair to modulate intensity. Finally, the fact that the LDM is a single module means that it can be easily mounted onto a set of stages, allowing for fine adjustments to be made to its positioning. This greatly simplifies alignment of the fan-beam while also allowing for useful out-of-plane rayline error detection, which will be discussed in Chapter 7.

5.1.2 New Matching Tank

There were two main motivations for designing the new matching tank. First and foremost, the cylindrical glass entry window was chosen to eliminate the need for the frequent interruptions that arose each time the entry window needed to be replaced. These repairs — performed by the BCCA Vancouver Island Centre's machine shop — involved removing the old window, cleaning the mounting surface, cutting the new window to shape, sealing it in place, waterproofing the seal, and testing to ensure that waterproofing was effective.

Then, the scanner needed to be reassembled, including the time consuming realignment of the fan-beam.

Secondary to those concerns regarding the entry window, the new matching tank was designed to have a smaller volume. At the time that the LDM was being selected for fan-creation and the new tank was being designed, the intent was to explore how well the fan-beam scanner could image the PRESAGE™ dosimeter. However, because its refractive index is higher than polymer gels, the PRESAGE™ dosimeter requires a special refractive matching fluid. A smaller tank would reduce the amount of matching fluid necessary to perform a scan.

Regarding the entry window of the glass cylinder, difficulties arose with the new matching tank. As can be seen in Figure 5.1a and Figure 5.1b, cracks occurred spontaneously, weeks after the tank was constructed and had been working as intended. These cracks caused the matching bath to gradually leak out. Fortunately, these cracks did not occur in the region of the cylinder where the fan-beam enters the tank, and it was possible to seal them using waterproof glue (see Figure 5.1c). It is believed that the occurrence of these cracks resulted from stress on the glass cylinder that accompanied the binding of the cylinder into its plastic surroundings. At the time of this writing, no further cracking of the glass cylinder has occurred[1].

Regarding the special matching fluid intended for the PRESAGE™ dosimeter, two containers of the fluid were acquired. Specifically, the fluid suggested by the manufacturer is, by volume: 91% octyl salicylate, 9% octyl-p-methoxy cinnamate (Modus Medical Devices Inc.). In conversations with the manufacturer of the PRESAGE™, they cautioned that this fluid might not be compatible with certain types of plastics. Heeding this warning, a portion of the matching fluid was tested on the old matching tank. It would appear that the matching fluid is not compatible with the previous tank (see Figure 5.1d and Figure 5.1e). Severe and

[1] *knock on wood*

widespread cracking of the old tank occurred following its exposure to the special matching fluid. Due to the fact that the new tank has been performing reliably enough to allow for investigations with PAGAT dosimeters to continue, the matching fluid has not yet been tested on the new tank and investigations into the scanning of PRESAGE^{TM} dosimeters were halted.

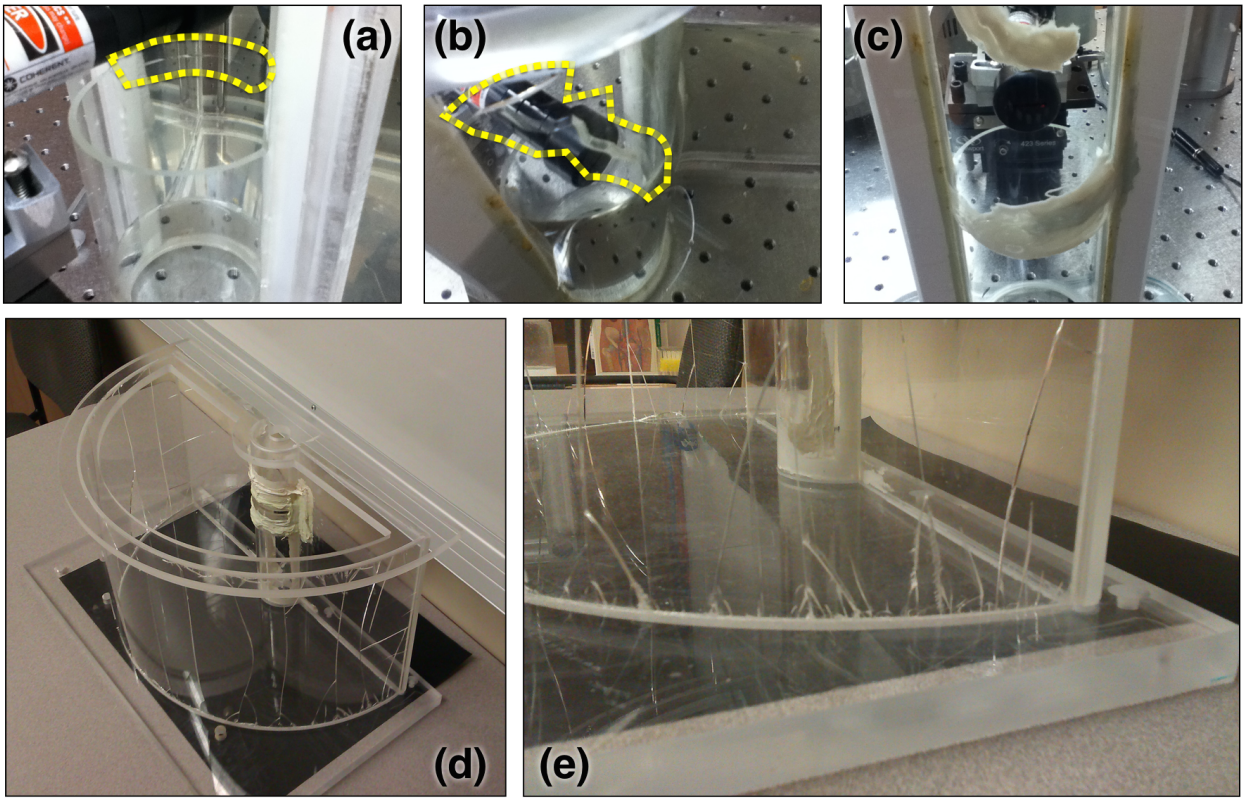

Figure 5.1: The glass cylinder insert for the second matching tank cracked weeks after construction. Two major cracks are shown in (a) and (b), indicated by the dashed yellow line. In (c), water-proof glue was used to seal these cracks, which fortunately did not obstruct the entry region of the fan-beam. Cracking of the first tank is shown in (d) and (e), which occurred after the tank was exposed to a small amount of the PRESAGE^{TM} refractive matching fluid.

5.2 Artefact Removal Techniques

At the beginning of this PhD work, two imaging artefacts persisted in reconstructions: flask seam artefacts and ring artefacts. Examples of these artefacts are shown in Figure 5.2 in a reconstruction of a scattering solution. First, the flask seam artefacts shown in Figure 5.2 are streaking artefacts caused by, as the name implies, two seams that run vertically down the sides of the flasks used to house scattering solutions and PAGAT dosimeters. Due to refraction, these seams cause rayline errors that introduce streaks to reconstructions.

Second, the ring artefacts seen in this image arise from data corruption that occurs on edge-elements in the photodiode arrays. As the entire detector arc is read, each linear photodiode array is turned on one at a time. As each photodiode array is initiated, the first few elements in the array return unreliable data. Attempts to resolve this issue by slowing down data acquisition via adjustments to the motherboard's firmware proved to be unsuccessful and ring artefacts persisted. Both types of artefacts — rings and seams — are tackled by segmenting and cutting "bad" data from sinogram space and using interpolation

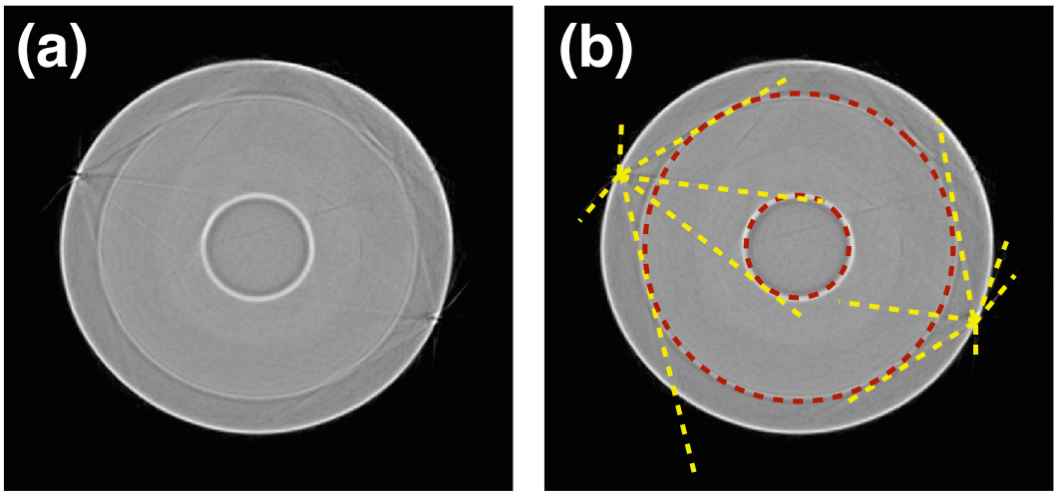

Figure 5.2: Examples of flask seam artefacts and ring artefacts can be seen in (a) on a reconstructed image of a scattering solution. Artefacts are highlighted in (b) by dashed lines.

to calculate replacement values. This is a method similar to those used to tackle metal artefacts[2] in x-ray CT [114, 152, 153].

5.2.1 Flask Seam Artefacts

In order to highlight the positions of flask seams in sinogram space, fan-beam OD data was first converted to its parallel-beam equivalent. This simplifies things greatly, as the mask used to highlight flask seam pixels in sinogram space will follow a sinusoidal curve in a parallel-beam sinogram. As such, the amplitude of the sinusoidal (roughly the radius of the flask) and the phases of the two seams were manually modified to adjust the positioning of the flask seam mask until it overlapped with the seam artefacts (see Figure 5.3). Once pixels were cut from sinogram space, a replacement method used a linear interpolation of the nearest pair of valid pixels in sinogram space to calculate new values for masked pixels. These steps alone could be used to tackle flask seam artefacts, but a similar removal technique is also implemented for corrupted data elements that cause ring artefacts.

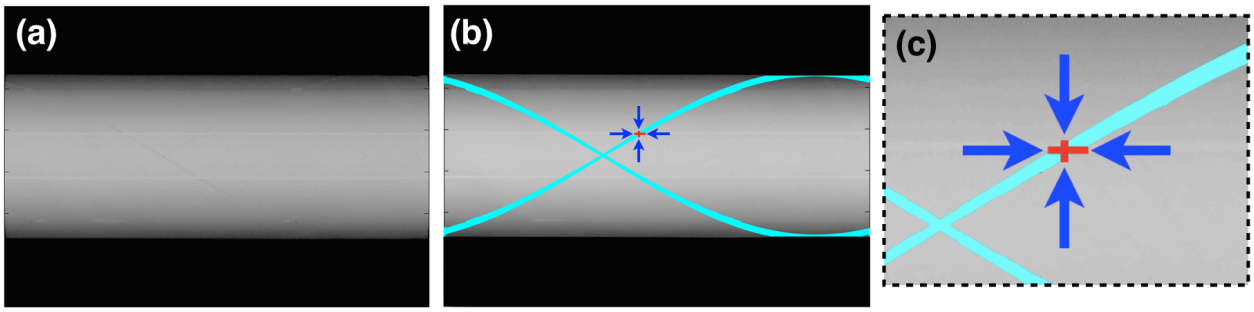

Figure 5.3: The seam artefact removal technique. In (a), raw sinogram data (parallel geometry) of a scattering solution is shown. In a parallel geometry, flask seam positions follow a sinusoidal curve. Phase and amplitude, which describe the positions of each curve, were manually adjusted so that a cut mask (seen in (b)) overlaps with both seams. The nearest pair of valid pixels (either detector-wise or projection-wise) were used to interpolate replacement values for each masked pixel, illustrated by the zoomed inset in (c).

[2]Streaking caused by the high-Z materials of dental fillings, pacemakers, and other implants.

5.2.2 Ring Artefacts

The positions of corrupted detector elements in the detector array are roughly symmetrical across the entire detector arc, which is also roughly centered on the rotational axis of the dosimeter/flask. As such, when viewed in sinogram space, corrupted data from the front half and back half of a full rotation sinogram overlap with one another (see Figure 5.4a). In order to avoid this overlap, the rotational axis of the scanner was shifted laterally 7.5 mm so that the flask was slightly off-centre with respect to the detector array (see Figure 5.4b). This way, when a 360° fan-beam sinogram is converted to a 360° parallel-beam sinogram and the latter half is flipped for redundancy, corrupted detector elements no longer overlap. With the new asymmetrical setup, regions of the sinogram that are corrupted in the front half of the sinogram are measured reliably by the back half of the sinogram, and vice versa (see Figures 5.4c and 5.4d). In order to suppress the influence of these bad pixels, measurements obtained by corrupted detector elements are masked and replacement values are calculated using linear detector-wise interpolation.

A modified workflow diagram is shown in Figure 5.5 to illustrate how these artefact removal techniques were implemented. Data obtained by the scanner first needs to be cropped detector-wise to center sinogram data on the scanner's rotational axis. The detector element that corresponds to the rotational axis can be located by finding the element that is halfway between the two locations where flask seams cross in sinogram space. Then, a pair of redundant 180° parallel-beam sinograms are calculated. Flask seams are cut from both sinograms and interpolation is used to calculate their replacement values. Corrupted detector elements are then cut from both sinograms and interpolation is used for their replacement. The resulting two 180° sinograms are averaged ray-by-ray to provide a single 180° parallel-beam sinogram, which is then used for reconstruction.

Results of these artefact removal techniques are shown in Figure 5.6 for an image of a

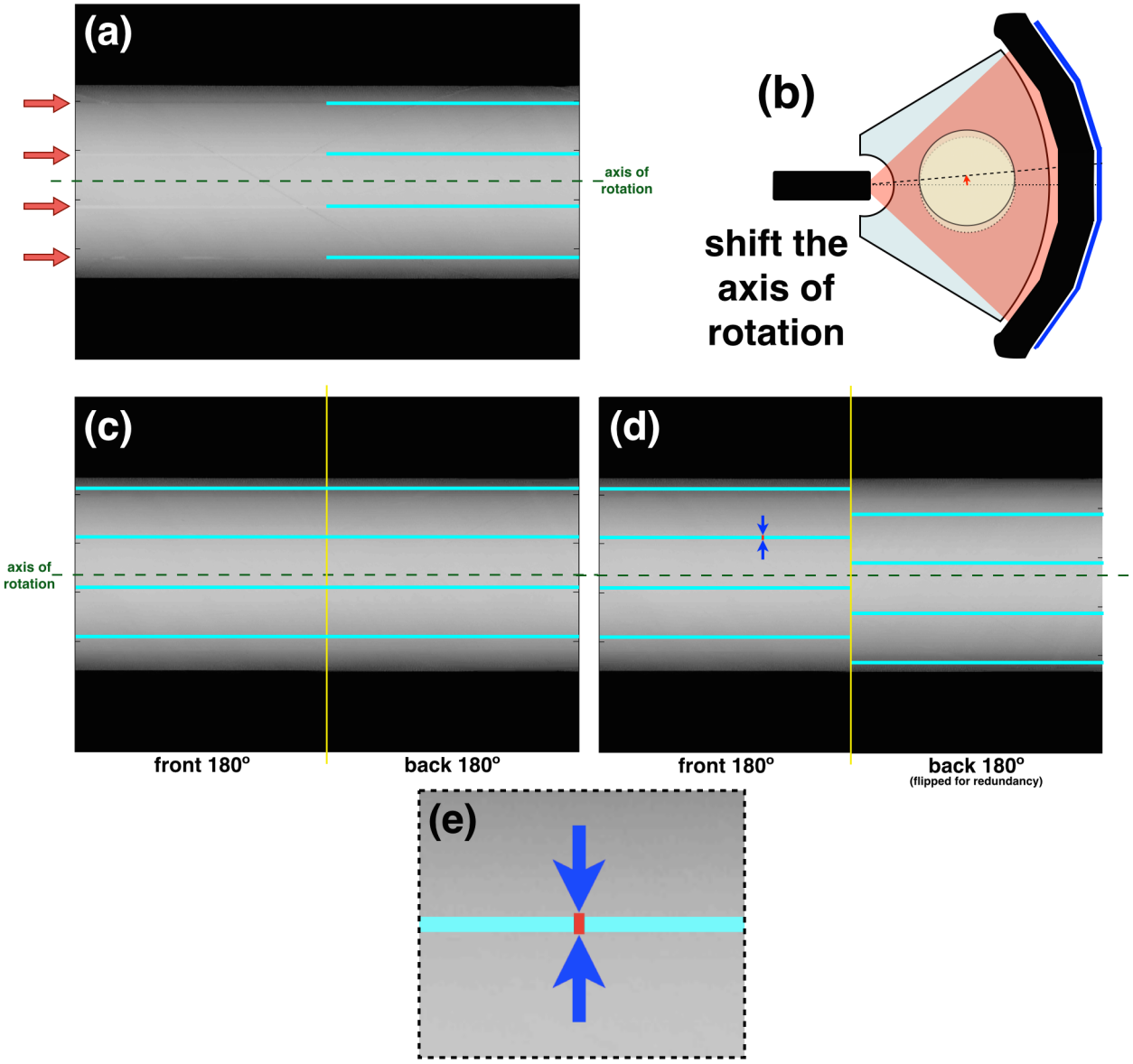

Figure 5.4: The ring artefact removal technique. In (a), the position of corrupted detector elements are roughly symmetrical across the axis of rotation of the scanner (here, cyan lines are used in the back half of the sinogram to indicate the position of corrupted elements). A slight shift in the scanner's axis of rotation is shown in (b). In (c), after shifting the axis of rotation, corrupted detector elements no longer occur symmetrically across the axis of rotation. In (d), after flipping the back half of the parallel geometry sinogram to provide a semi-redundant representation of the front half, corrupted detector elements no longer overlap. As a result, each half collects valid data wherever data is corrupted in the other half. Detector-wise interpolation for corrupted elements are applied, illustrated by the zoomed inset in (e), before averaging the front and back halves.

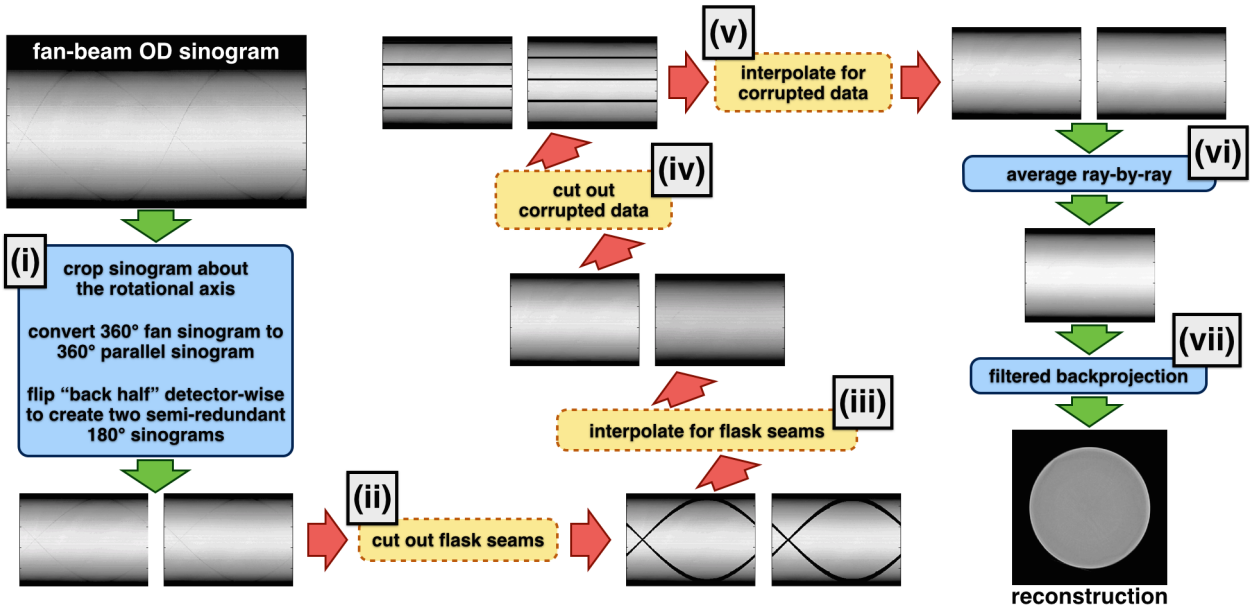

Figure 5.5: Workflow diagram for artefact removal and image reconstruction, starting with a 360° asymmetrical fan-beam OD sinogram in the upper left: (i) sinogram data is cropped symmetrically across the scanner's axis of rotation, the fan-beam sinogram is rebinned into a parallel-beam geometry, and the back 180° of sinogram data is flipped detector-wise, resulting in two semi-redundant 180° sinograms. If artefact removal techniques are implemented, steps in the middle of the diagram occur: (ii) flask seams are cut from each sinogram, (iii) interpolation is used to replace cut rays, (iv) corrupted detector elements are cut from each sinogram, and (v) interpolation is again used to replace cut rays. In all cases: (vi) the two 180° sinograms are averaged, ray-by-ray, and (vii) filtered backprojection is used to reconstruct the final image.

scattering solution and an image of an irradiated polymer gel dosimeter. For the scattering solution, the artefact removal technique reduced ring artefacts as large as 40%. Also, using two regions of interest (ROIs) near flask seams for evaluation, noise in those two regions reduced from 3.0% and 2.9% to 2.3% and 1.9%, respectively. For the polymer gel dosimeter, opacity data has already been converted into its dose equivalent (calibration to be discussed later in Section 5.7). The difference image shown in Figure 5.6 is in units cGy, and shows the change introduced by the artefact removal technique. Ring artefacts removed were on the order of 1 Gy, whereas flask seam artefacts were much more substantial, introducing positive and negative errors greater than 5 Gy in magnitude.

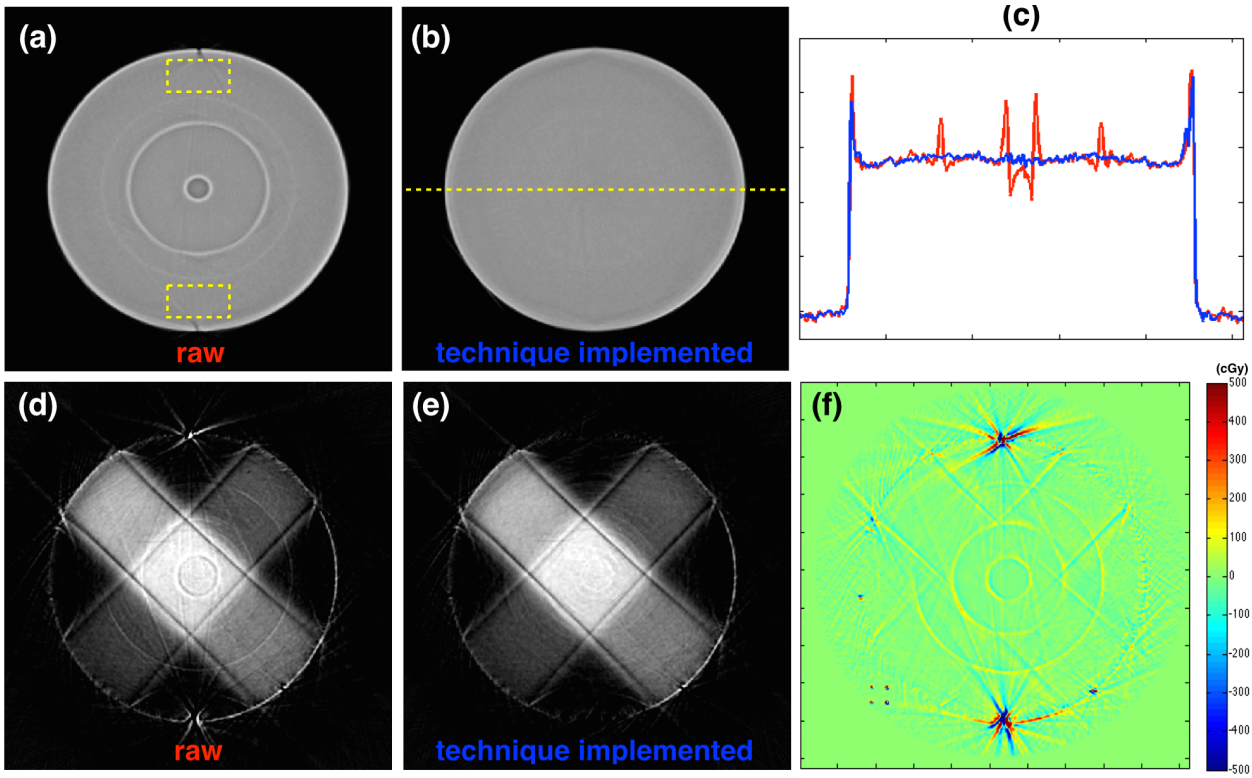

Figure 5.6: Artefact removal results. In (a), flask seam artefacts and ring artefacts are seen in a raw reconstruction of a scattering solution. Two ROIs in (a) were used to sample noise values near flask seams. In (b), a reconstruction of the same solution is shown using the artefact removal techniques described in this section. In (c), cross-sections through (a) and (b) are plotted alongside each other, with their position indicated by the dashed yellow line in (b). Similar data is shown for reconstructions of a polymer gel dosimeter in (d), (e), and a difference image with units of cGy is shown in (f). Image pairs (a) & (b) and (d) & (f) are identically windowed and levelled.

5.3 Flask Registration

Previous investigations that involved the optical CT scanning of scattering solutions revealed that random imperfections on the surface of the flask were a significant source of image noise. If accurate positioning could be maintained, this noise could be avoided. However, slight shifts in flask positioning would introduce noise to transmission scans due to a mismatch in these random imperfections.

In addition to the imperfections that exist on the surface of the flask, one would expect additional imperfections to result as the gel sets. Due to various inhomogeneities that will arise in the bulk of the dosimeter, imperfections will occur both on the surface of the flask and throughout the slice being examined. Ultimately, the goal is to perform a pre-irradiation scan (reference, I_o), a post-irradiation scan (measurement, I), and compare those two scans for optimal readout (transmission, T). In order to ensure the accurate positioning of these two scans, it was necessary to develop a method of reproducing flask placement in the optical CT scanner.

The random imperfections that cause so much noise when position errors occur were the key to developing the flask registration technique that follows. To begin, an opaque mark is placed on the flask that allows for the rough placement of the flask, angularly and vertically. Then, the flask is shifted a specific vertical distance so that the fan-beam is traversing a region of the flask that will go unirradiated. At this point, a light profile is acquired through the flask and saved for later scans (see Figure 5.7a). This position is now designated as the "zero" position for flask placement, and the light profile that was acquired and saved will be the "key" for returning to this position. The key light profile is essentially a snapshot through the zero position, which is a unique position on the flask with its own unique imperfections. From here, scan shifts during the "reference" scan need to be documented so that they may be identically repeated when the "measurement" scan is to be acquired. After scanning is

complete, the flask may be fully removed from the scanner.

When the flask needs to be placed back into the scanner, the same rough alignment takes place via the opaque mark on the flask and the specific vertical shift to the unirradiated region of the flask. At this point, the flask in roughly in the vicinity of the zero position from before. Here, a survey of many different light profiles are taken after implementing a range of slight angular and vertical shifts to the position of the flask (see Figure 5.7b). If the survey is large enough, the zero position will be contained within this range of flask positions.

Next, each light profile in the survey is divided by the key light profile that was saved from the initial scan. This division converts each light profile in the survey into a transmission profile, with the key light profile serving as the reference profile. Ideally, if one of the profiles acquired in the survey was at the zero position, it would be the least noisy transmission profile. And, as can be seen in Figure 5.8, other profiles will become noisier and noisier as they deviate from that position. As such, the relative standard deviation (σ/μ) of each transmission profile in the survey became the quantity used for flask registration.

A sampling of noise values found in a typical survey for a water-filled flask is shown in Figure 5.9. As can be seen, much more noise is introduced by angular mismatches than by vertical mismatches, but both directions show a noise minimum at the zero position. Noise at the zero position is typically be around 3%, whereas maximum noise in the survey can be greater than 150%. In Figure 5.9, the zero position is already at the center of the survey. This typically will not be the case in the first survey acquired. Nevertheless, wherever the noise minimum occurs in the survey informs the necessary angular and vertical shifts that will position the least noisy position in the center of the survey. These shifts are performed, and then another survey is acquired. Once the least noisy profile is centered in the survey, the flask has been returned to the zero position.

In order to demonstrate the efficacy of the flask registration technique, Figure 5.10 com-

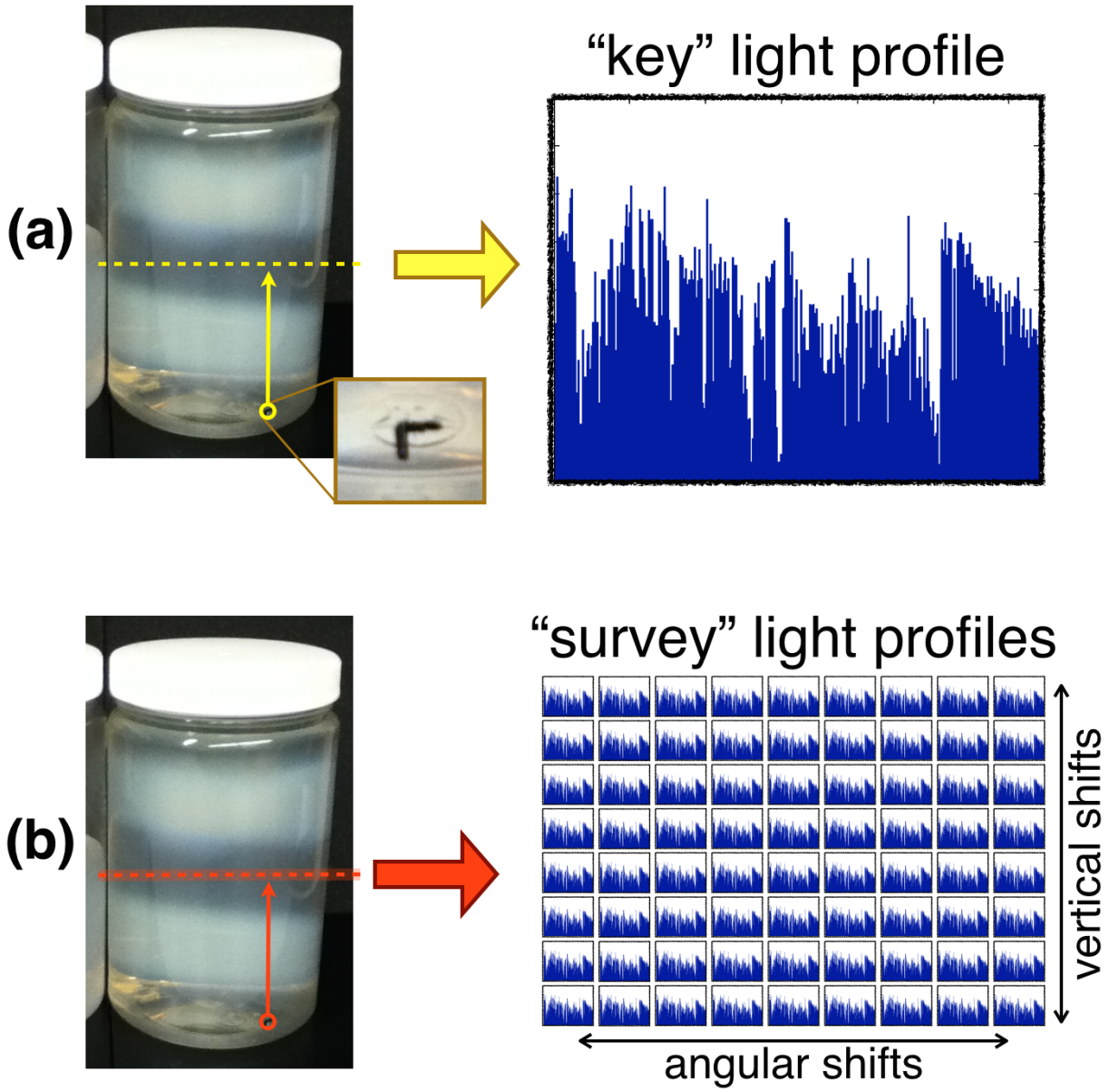

Figure 5.7: Illustration of the data collected for the flask registration technique. In (a), during the reference scan, an opaque mark in an unused portion of the flask (indicated by the zoomed inset) is used for rough positioning, vertically and angularly. Then, a specific vertical shift moves to a portion of the flask that will go unirradiated. There, a single light projection is acquired and saved. In (b), when positioning of the flask needs to be reproduced, the same opaque mark is used for rough positioning, and the same specific vertical shift is implemented. At this point, the flask is roughly in the vicinity of the reference scan position. Here, a survey is used to acquire multiple light projections with a range of slight positional shifts, both angularly and vertically.

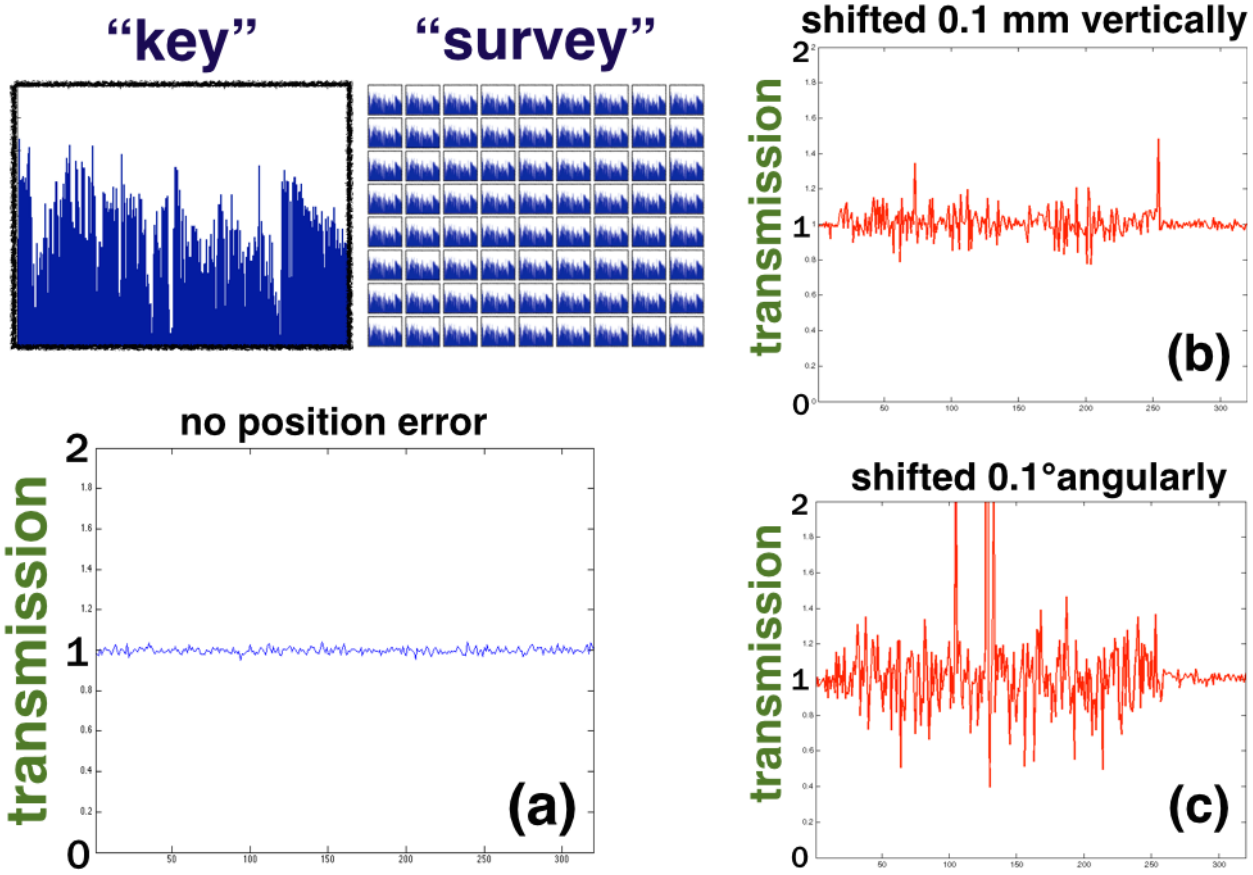

Figure 5.8: Illustration of the data analysis used for the flask registration technique. Using the same "key" projection, transmission profiles are calculated for each projection in the "survey" of projections. In (a), assuming the ideal placement of the flask, the resulting transmission profile would equal 1. Positional mismatches will introduce noise to this profile. The transmission profile for a 0.1 mm vertical mismatch is shown in (b). The transmission profile for a 0.1° angular mismatch is shown in (c). Relative noise values of "survey" transmission values are used to evaluate placement accuracy.

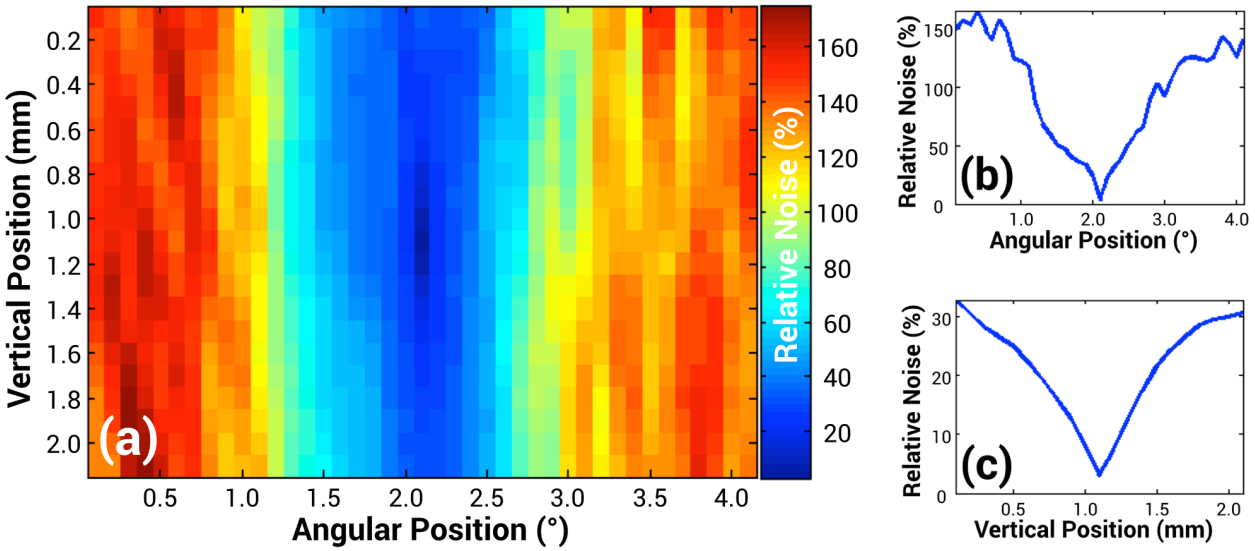

Figure 5.9: Relative noise values ($\sigma/\mu\%$) for "survey" transmission profiles, with various combinations of vertical and angular positioning, are shown in (a). The zero position occurs at the central pixel of the survey. In (b), relative noise values with respect to angular positioning errors are shown for a flask that is accurately place, vertically. In (c), relative noise values with respect to vertical positioning errors are shown for a flask that is accurately placed, angularly.

pares four %-difference images of a scattering solution (i.e., [image] $-\ \mu_{ROI}$). The first image, in Figure 5.10a, came from comparing a reference sinogram of a water-filled flask and a measurement sinogram after a concentrated scatterer was added, both sinograms having been acquired without disturbing the positioning of the flask. The images in Figure 5.10b and Figure 5.10c have respectively had their reference sinogram deliberately mispositioned by 1 mm vertically or by 1° angularly. The last image, in Figure 5.10d, was acquired after fully removing the flask between acquisition of the reference sinogram and the measurement sinogram. The ROI in Figure 5.10a was used to quantify the noise in each image. Examining the absolute percent difference in the same ROI for each image, mean and standard deviations were found to be: 2.2±1.9% in the unmoved case, 4.0±3.1% in the vertically displaced case, 8.4±8.6% in the angularly displaced case, and 3.5±2.7% in the fully removed and replaced case. For the fully removed and replaced case, any errors that remained after registration,

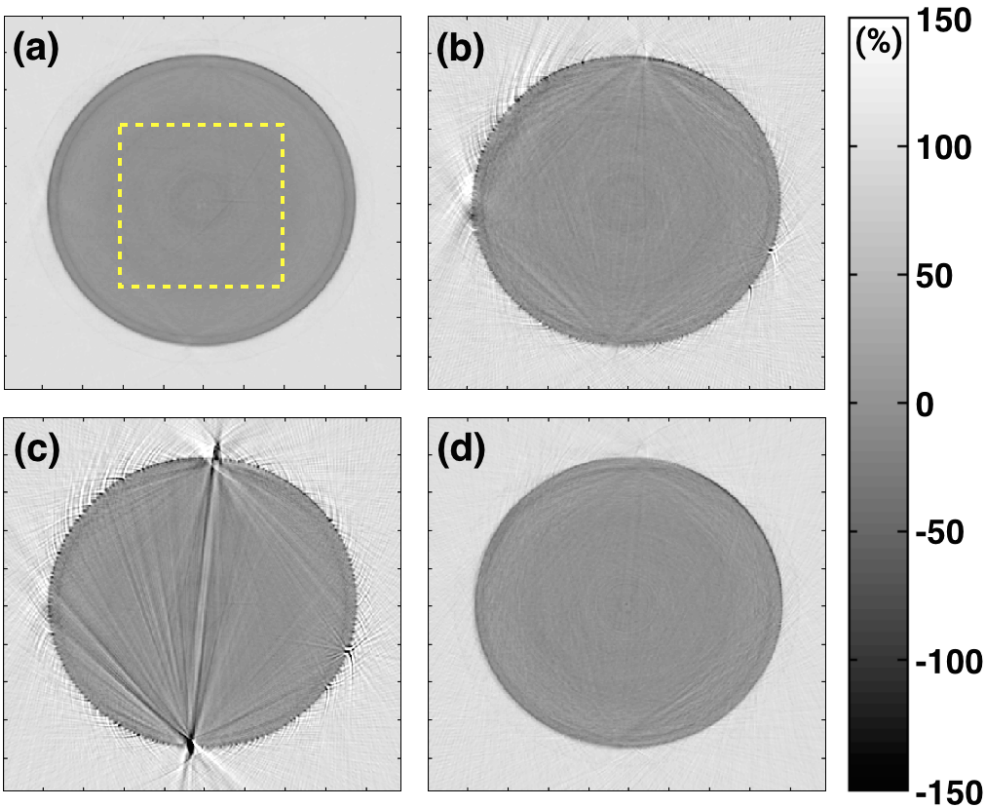

Figure 5.10: Reconstructions of scattering solutions were used to demonstrate the efficacy of the flask registration technique. Here, %-difference images are shown (i.e., [image] $-\ \mu_{ROI}$). In (a), reference and measurement scans were acquired without disturbing the placement of the flask. In (b), reference and measurement data were deliberately mismated by 1 mm vertically. In (c) reference and measurement data were deliberately mismatched 1° angularly. In (d), the registration techniques was used to fully remove and replace the flask between reference and measurements scans. The ROI indicated in (a) was used to quantify absolute differences.

both angular and vertical, will contribute to the noise in this image. As such, the flask registration technique is shown to successfully reproduce flask placement with sub-millimetre and sub-degree accuracy.

It is worth noting that this registration technique only allows for angular or vertical repositioning of the flask. Positioning errors with respect to the axial tilt of the flask could still result. Such errors can be reduced if one takes added care in the placement of the flask in the scanner's mounting arm. Additionally, one could use dual registration marks to

reproduce axial positioning. However, such errors have not yet shown themselves to be of obvious concern.

5.4 Pre-Irradiation/Post-Irradiation Scanning of PAGAT Dosimeters

Once the flask registration technique was developed, pre-irradiation and post-irradiation scanning of PAGAT dosimeters became feasible. So, a dosimeter was fabricated. During fabrication, after the gel solution was prepared (as described in Section 4.2), the sealed flask was immediately placed in a refrigerated water bath (∼5 °C) to ensure that it set quickly. Approximately 6 hours later, the dosimeter was removed from the fridge and scanned using the optical CT scanner (at the time of this scan, the green HeNe laser setup was still being used for fan-creation). Including flask registration and scanning time, the dosimeter was in the room temperature (∼21 °C) matching bath for ∼45 minutes. After this pre-irradiation scan, the dosimeter was irradiated. Square 3×3 cm^2 beams of 6 MV photons were used to irradiate a dosimeter with a simple cross pattern with a maximum dose of 4.4 Gy. Once irradiated, the dosimeter was returned to the cold bath and given time to fully polymerize. Approximately 24 hours later, the dosimeter was removed from the fridge and a post-irradiation scan was acquired.

From the data acquired, two images were reconstructed (see Figure 5.11). The first image compared a post-irradiation scan of an irradiated slice of the dosimeter to a post-irradiation scan of an unirradiated slice of the dosimeter. The second image compared a post-irradiation scan of an irradiated slice of the dosimeter to a pre-irradiation scan of the same slice. Both reconstructions used the same measurement light sinogram, but different reference light sinograms.

As is evident, the pre-irradiation and post-irradiation comparison avoids a considerable amount of noise. I attribute this noise to refractive inhomogeneities that occur randomly in the gel. Using a pre-irradiation and post-irradiation comparison can partly accommodate such imperfections. Furthermore, in the case where the post-irradiation scan is compared against the scan of an unirradiated portion of the dosimeter, imperfections from both slices will be compounded rather than accommodated. Due to the potential for temporal variations in the dosimeter and in the fan-beam, it is worth acknowledging that the pre-irradiation and post-irradiation scans were acquired 24 hours apart, whereas the post-irradiation scan and the scan of an unirradiated slice were acquired only minutes apart. Despite this, the pre/post comparison still outperformed the alternative.

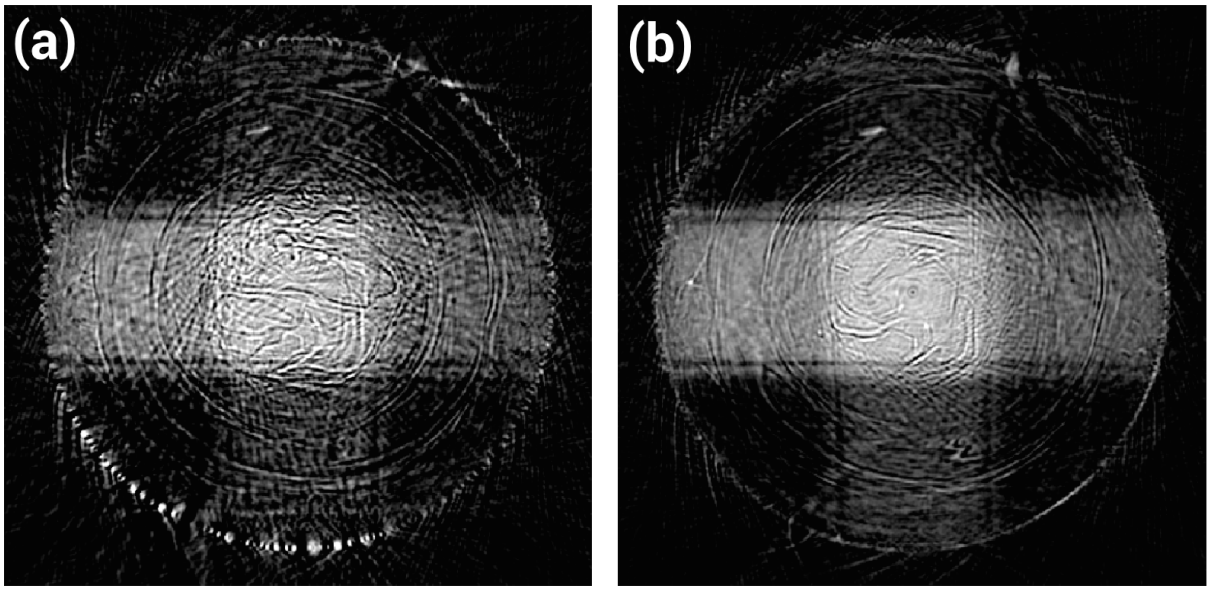

Figure 5.11: The same measurement scan of a polymer gel dosimeter was used to reconstruct two images using two different sources of reference data. In (a), reference data was a light sinogram that was acquired in an unirradiated slice of the dosimeter. In (b), reference data and scan data were light sinograms acquired on the same slice of the dosimeter before and after being irradiated, respectively. Images are identically windowed and levelled.

5.5 Effects of Cooling Rate in PAGAT Dosimeter Fabrication

Results obtained using pre-irradiation and post-irradiation scan comparisons proved to be qualitatively better than comparing post-irradiation scans to an unirradiated slice of the dosimeter. However, errors still present in the pre-/post-irradiation reconstruction raised two concerns with respect to the temperature of the gel (see Figure 5.11b). First, it was suspected that cooling the gel in a refrigerated bath induced convection currents within the dosimeter, potentially causing severe RI inhomogeneities. Second, after removing the dosimeter from the cold bath and being placed in the room temperature matching bath of the optical CT scanner, it will begin to warm. As such, it was also suspected that the gel may be physically shifting as it warms unevenly during the scan. The ability of pre-/post-irradiation scans to fully accommodate random RI inhomogeneities in the dosimeter might be thwarted if the sample is shifting as its temperature adjusts during each scan. Additionally, variations in dosimeter opacity have previously been observed with variations in gel temperature [154]. Upon examining these points, a new protocol was devised.

A new dosimeter was fabricated in an identical fashion to those fabricated previously, with the exception of the cooling of the dosimeter after fabrication. After the dosimeter was prepared and sealed in its flask, it was placed in a room temperature bath and given time to slowly cool. Roughly 24 hours later, a pre-irradiation scan of the dosimeter was acquired, the dosimeter was irradiated, and then it was returned to the room temperature bath. After giving the dosimeter another 24 hours to fully polymerize, the post-irradiation scan was acquired.

A comparison of two irradiated PAGAT dosimeters, one that was cooled quickly and one that was cooled slowly, are shown in Figure 5.12. As is evident from these images, the dosimeter that was cooled slowly avoids a considerable amount of the inhomogeneity errors

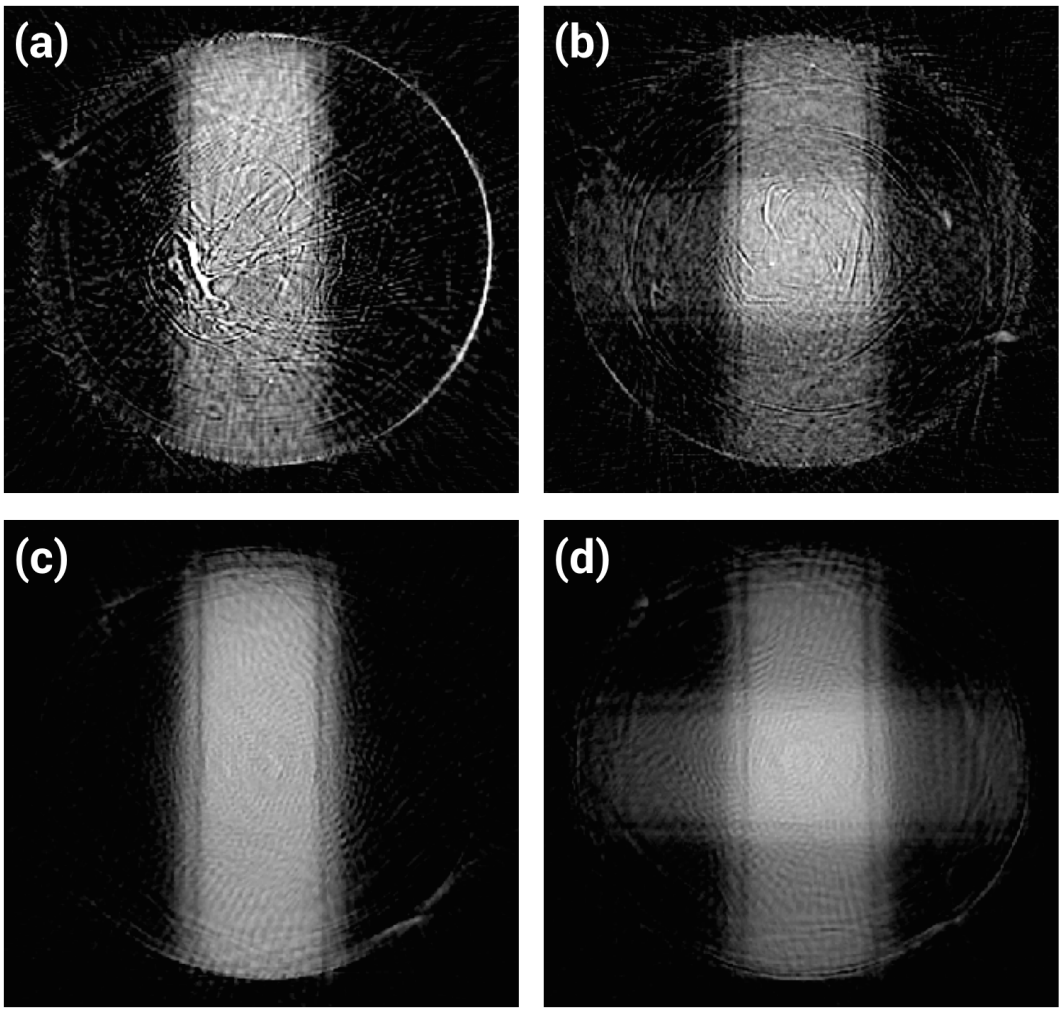

Figure 5.12: Images illustrating the effects of gel cooling rate on polymer gel dosimeter reconstructions. In (a) and (b), flasks filled with liquid gel were placed into a cold bath in a refrigerator in order to speed up cooling of the dosimeter. In (c) and (d), flasks filled with liquid gel were placed in a room temperature bath and 24 hours to cool. All images used pre-irradiation and post-irradiation scans for their reference and measurement scans, respectively. All images are identically windowed and levelled.

observed with the quickly cooled dosimeter. However, it must be acknowledged that, by the time that this dosimeter was scanned, a few variables other than gel cooling rate were also changed: (i) the new LDM was adopted for fan-creation (green light instead of red light), (ii) the dosage delivered to the dosimeter was increased (from central dosages of 3.7 Gy and 4.4 Gy with the quickly cooled dosimeter to 8.7 Gy and 10.0 Gy with the slowly cooled dosimeter), and (iii) a different energy of photons was used for irradiation (18 MV with the slowly cooled dosimeter instead of 6 MV).

The first two points — wavelength and dosage — are interconnected. Red light is attenuated less by scatterers than green light. As such, the increase in dose was specifically made so that the maximum optical densities measured by the scanner would be roughly equivalent. Regarding the last point, it has been shown that PAGAT dosimeters do not exhibit a significant energy dependence [155]. For these reasons, slowing down the cooling rate was suspected to be responsible for improving dosimeter readout, and the slow cooling procedure was adopted for subsequent PAGAT dosimeters.

5.6 Continuous Rotation Data Acquisition

Previous experiments that examined scattering solutions demonstrated that image noise was reduced by increasing the number of projection angles that are sampled throughout the optical CT scan (similar experiments were performed using a PAGAT dosimeter in Section 6.3). However, high projection number scans that use the 'step + shoot' acquisition routine are time consuming. A plot of acquisition time versus the number of projection angles in a single rotation is shown in Figure 5.13[3]. These times include the acquisition of two profiles per projection angle using two different photodiode integration times for dynamic

[3]Note that, if one were to image 100 slices of a 10 cm tall cylindrical dosimeter, a 900 second per slice scan time would require 25 hours to scan the entire dosimeter. That is 50 hours total to perform the pre-irradiation and post-irradiation scans.

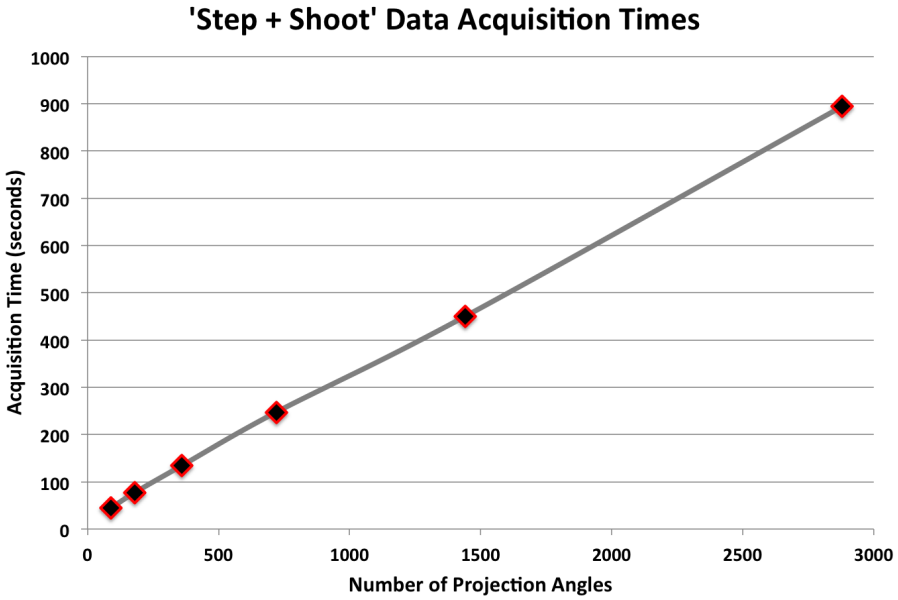

Figure 5.13: Plot of 'step+shoot' data acquisition times with respect to number of projection angles for a single slice.

range extension. In an effort to obtain a higher number of projection angles in a shorter acquisition time, continuous rotation data acquisition was explored.

Tests examining continuous rotation data acquisition began with scanning a water-filled flask. The water-filled flask was instructed to rotate 360° at a constant velocity ($3.27\frac{^\circ}{s}$) while the 'scan, scan, scan, get' acquisition routine was used to obtain light profiles in quick succession. Once this scan was complete and the set of profiles was transferred from motherboard memory to the PC, another scan was requested using the exact same block of code. If dosimeter rotation and data acquisition performed ideally, the two sinograms returned by these scans should be identical, with the exception of fluctuations in LDM output and particulates in the bath. Unfortunately, there were inconsistencies between these two scans. The two light sinograms and their corresponding transmission sinogram are shown in Figure 5.14. Positioning errors are apparent, and mismatches in positioning cause severe readout errors, most notably due to mismatches of the flask seams.

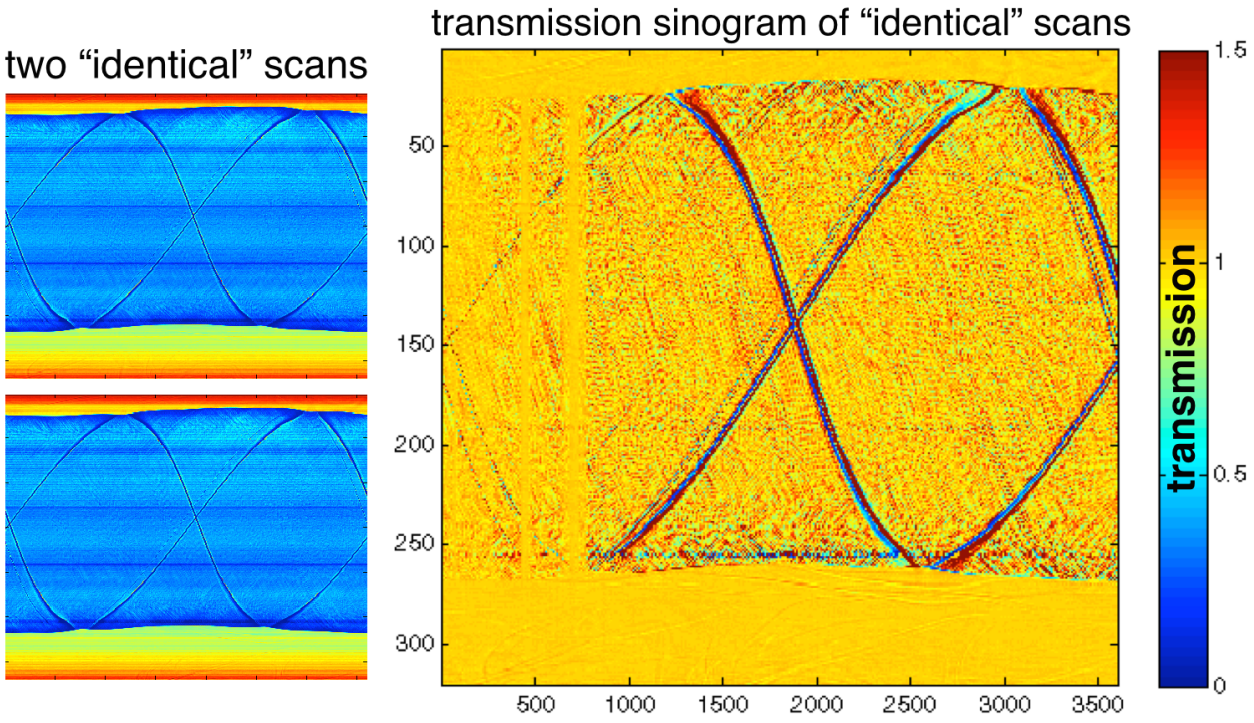

Figure 5.14: Two “identical” scans of a water-filled flask were acquired using a continuous rotation acquisition. A transmission sinogram calculated by using these two scans would ideally provide a sinogram of rays equalling 1. Errors shown here indicate positional mismatches between the two scans.

The rotational stage was not believed to be at fault for these errors due to the impressive levels of accuracy in its specifications (positional resolution of 0.0005°). As such, the timing of detector array measurements were believed to be at fault. So, three “identical” scans were performed in a similar fashion as those above, only with an additional line of code that recorded a timestamp when each profile was acquired. Plots of scan timing are shown in Figure 5.15. At this scale, it would appear that timing is relatively consistent. However, subtracting these time plots from one another reveals inconsistencies between scans. Figure 5.15 also shows the timing errors between scans and their corresponding transmission sinograms. Larger timing errors correspond to larger errors in sinogram space. This is not surprising, as a 1 second error for a flask rotating at $3.27\frac{^\circ}{s}$ would correspond to a 3.27° positioning mismatch.

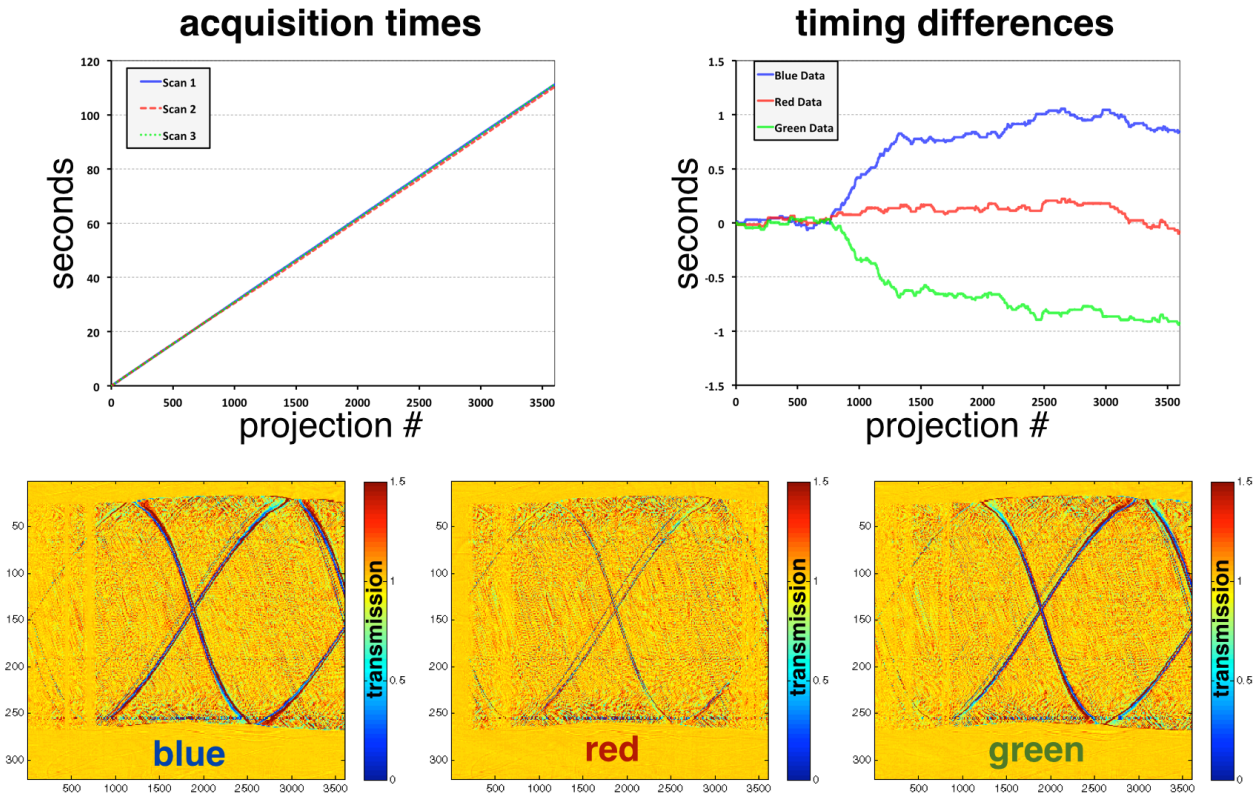

Figure 5.15: For three seemingly "identical" scans, plots are shown for their acquisition times and the timing differences between the three scans. Comparisons of timing difference plots and their transmission sinograms (blue, red, and green) show that larger timing errors correspond with larger transmission errors.

A method for correcting these timing errors was developed with the assumption that the rotational stage performs ideally. Assuming that the flask rotates at a constant speed, timestamp data were converted into angular position data by multiplying timestamp data by the flask's rotational velocity. Then, profiles were binned accordingly into equally sized angular increments. For the 3600 projections acquired in each of the three sinograms, these projections were binned into corrected sinograms that had angular increments of 0.25° (i.e., 1400 projections for 360°). The results of using corrected sinograms for transmission comparisons are shown in Figure 5.16. As is evident, errors are reduced significantly by implementing these timing corrections. Note that the tail end of each comparison shows cutoffs related to some data not being acquired for the complete rotation in each sinogram. Not includ-

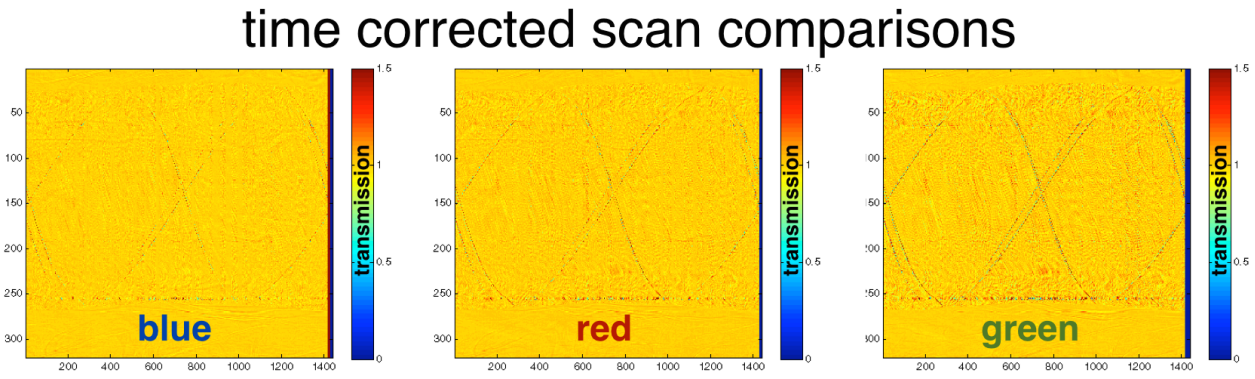

Figure 5.16: Transmission sinograms for three "identical" scans are shown after timestamps were used to calculate angular positions for all projections.

ing these tail ends, mean and standard deviation values of transmission and OD for these sinograms, corrected and uncorrected, are provided in Table 5.1. Values for a step + shoot acquisition are also provided for comparison.

In order to examine continuous acquisition in practice, an irradiated dosimeter was scanned using two methods: (i) a step + shoot acquisition that took 247 seconds to acquire a 720 projection sinogram, and (ii) a continuous rotation acquisition that took 141 seconds (including data transfer time) to acquire a sinogram of ∼1600 projections. Both of these acquisitions used dynamic range extension via photodiode integration time, so two profiles (one short integration time, one long integration time) were acquired for each projection (i.e., 1440 total acquisitions for step + shoot, and 3200 total acquisitions for continuous rotation). Also, for the continuous rotation acquisition, the flask was instructed to rotate 365° to ensure that a full 360° sinogram was acquired. Then, the flask was reversed 5° to return it to its zero position.

Results of a step+shoot scan and a time-corrected continuous rotation scan are shown in Figure 5.17. As is evident, the continuous rotation acquisition provides a superior readout than the step + shoot acquisition method that took nearly double the time to acquire. The effects that the number of projection angles used in a sinogram has on image quality will be

explored quantifiably in Chapter 6. However, it would appear that, by acquiring timestamp data during the scan, continuous rotation acquisition will prove to be faster and provide better results than step+shoot acquisition.

	Timing Corrected		Uncorrected		Step + Shoot	
Transmission	**μ**	**σ**	**μ**	**σ**	**μ**	**σ**
Blue Data Set	1.003	0.049	1.074	1.167		
Red Data Set	1.008	0.064	1.037	0.768	1.006	0.037
Green Data Set	1.008	0.097	1.081	1.267		
Optical Density	**μ**	**σ**	**μ**	**σ**	**μ**	**σ**
Blue Data Set	0.0011	0.0206	0.0310	0.336		
Red Data Set	0.0034	0.0269	0.0156	0.247	0.0024	0.0158
Green Data Set	0.0035	0.0198	0.0337	0.356		

Table 5.1: Mean and standard deviation values of transmission and optical density for timestamp-corrected and uncorrected light sinograms. For reference, values obtained by using a step + shoot acquisition are also provided. "Blue, red, and green" refers to the blue, red, and green data sets shown in Figure 5.15.

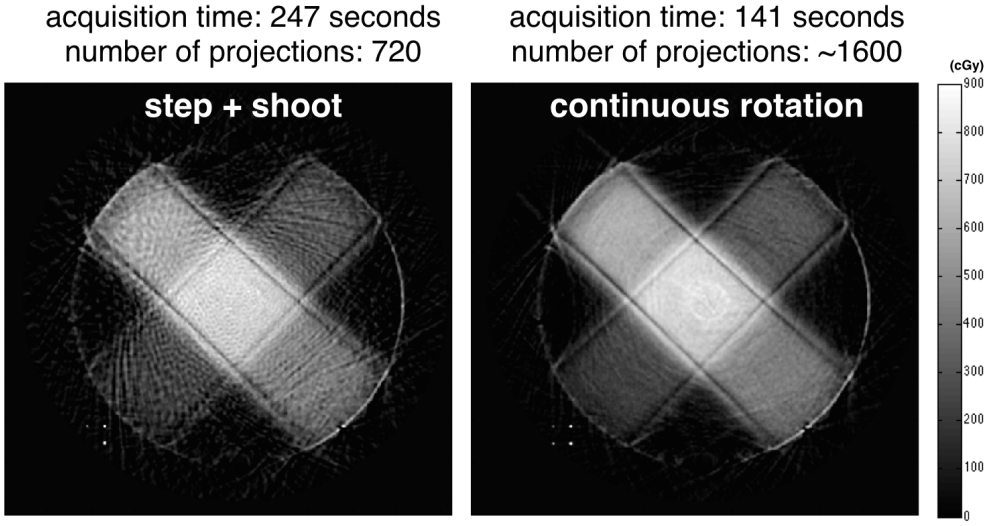

Figure 5.17: Reconstructions of the same dosimeter using either a step + shoot acquisition or a timestamp-corrected continuous rotation acquisition. The continuous rotation acquisition performs as desired, obtaining visibly better results in nearly half the acquisition time. Both images are identically windowed and levelled.

5.7 PAGAT Dosimeter Calibration

Chapter 6 will examine the effects that scan parameters have on reconstruction quality for PAGAT dosimeters. In that chapter, accuracy and precision of dosimeter readout will be evaluated by observing readout errors and image noise. However, in order to compare reconstructions of dosimeter opacity to expected dose distributions provided by TPS, the dosimeter first needs to be calibrated. This section examines the calibration of PAGAT dosimeters.

Two PAGAT dosimeters were irradiated with a total of four irradiation patterns (two each, see Figure 5.18). Each dosimeter was irradiated with two different dose distributions in their upper and lower regions. In the upper region of both gels, an identical "Calibration" dose distribution was delivered with a maximum dosage just over 8 Gy. In the lower region of each gel, a similar "Cross" dose distribution was delivered, but at two dosage levels —

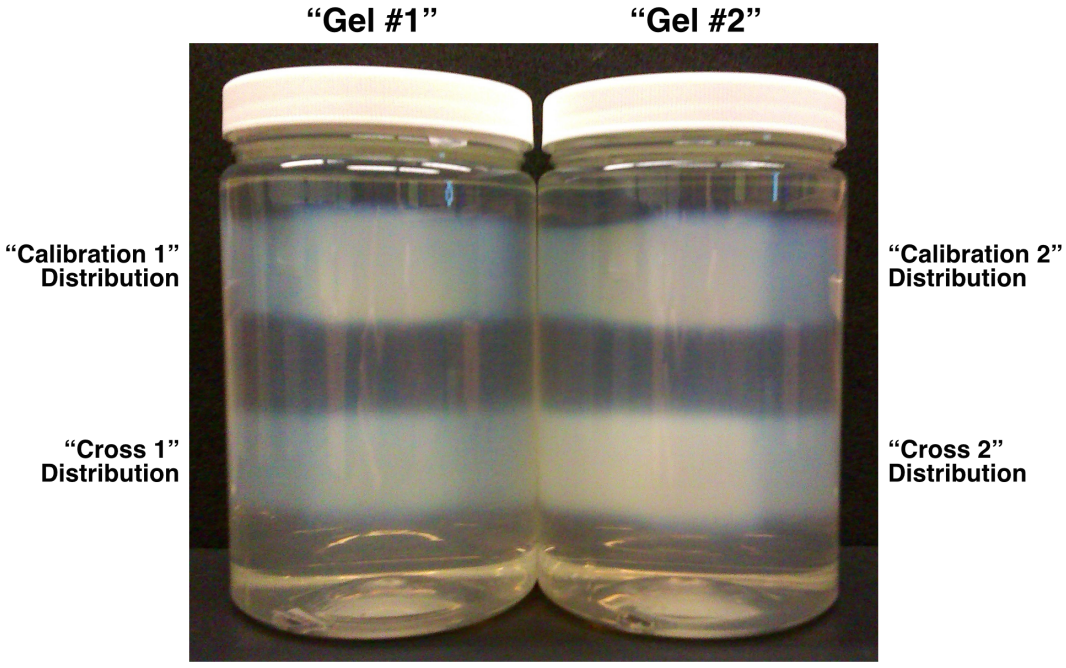

Figure 5.18: Photo of two PAGAT dosimeters. Each dosimeter was irradiated with two irradiation patterns. Both feature the same "Calibration" pattern in the upper region, and similar "Cross" patterns at two different dosages in the lower region.

Cross 1 receiving a maximum dosage of 4 Gy, and a maximum dosage of 8 Gy for Cross 2. The TPS-calculated dose distributions for these irradiation patterns, which used 3×3 cm^2 6 MV photon beams, are shown in Figure 5.19. Both gels were prepared using the "slow cooling" procedure, and scans were acquired using a continuous rotation acquisition routine that collected data for 1600 projection angles in $\sim$140 seconds. The co-registration method described in Section 4.6 was used to align TPS dose data with gel measurements.

For two reasons, only low dose gradient regions (<5 cGy/mm) of TPS-calculated dose distributions were used for calibration purposes. First, this avoids the potential for alignment errors that can occur on steep dose gradients. Second, by cutting away regions with high dose gradients, distinct streaking artefacts (which are the topic of Chapter 7) are also avoided. Figure 5.20 illustrates the areas that are removed from consideration by not including high dose gradient regions. Although high dose gradient regions were not used for the calculation of any calibration curves, later analyses will evaluate the impact of calibration factors on: (i) data with gradients ignored, and (ii) data with gradients included.

Plotting opacity versus dose, Figure 5.21 shows all data points (gradients included) for all four irradiation patterns. In order to help visualize where many points lie atop one another, plot markers are 95% transparent. The same plots with gradients ignored are shown in Figure 5.22. Comparing these two figures, one can appreciate how much variation is removed by cutting away steep gradients. Additionally, the distinct streaking artefacts that are avoided when dose gradients are ignored seem to appear as structured errors in the calibration curves that include dose gradients.

Previous works that have evaluated polymer gel dosimeters with optical CT used linear fits when calculating opacity-to-dose calibration curves [61, 122, 123]. However, recent investigations that evaluated polymer gel dosimeters using x-ray CT showed that, when examining an approximate range of 0 Gy to 30 Gy, the dose-response curve takes on a sigmoidal shape [89]. Although the polymer gel recipe used for that work is quite a bit different from the

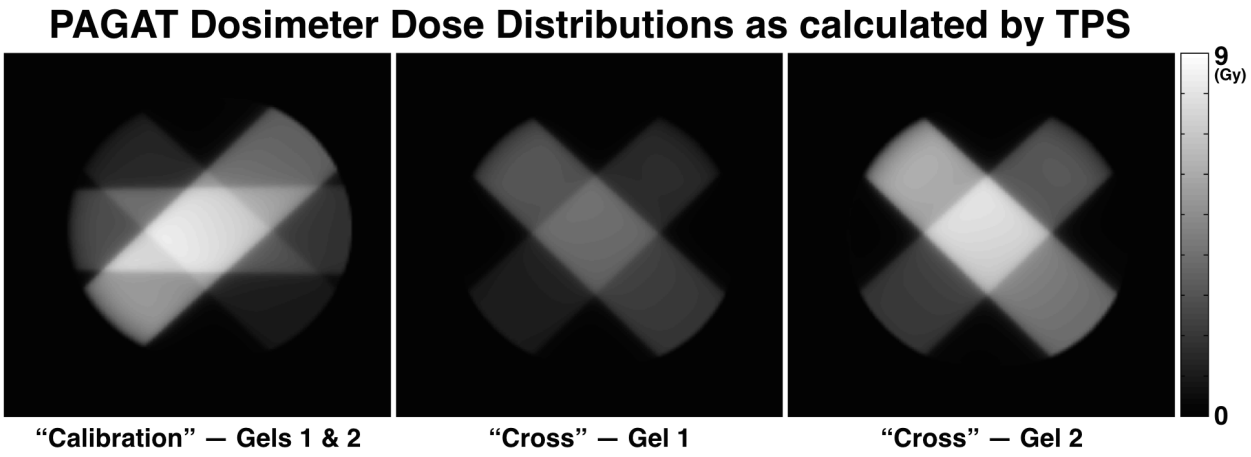

Figure 5.19: Dose distributions as calculated by treatment planning software for the “Calibration” and “Cross” irradiation patterns.

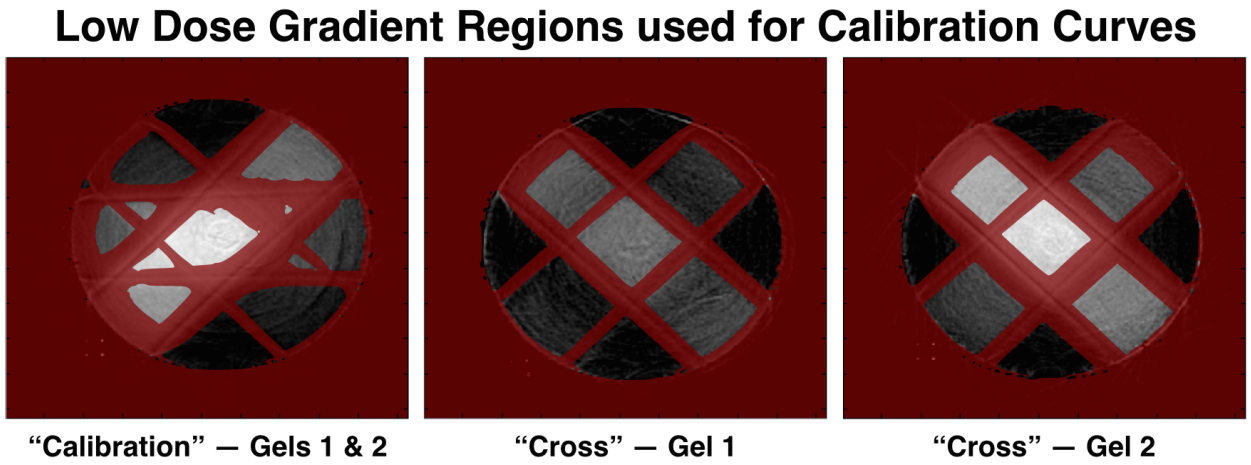

Figure 5.20: Dose distributions for the “Calibration” and “Cross” irradiation patterns with steep dose gradients cut in order to calculate calibration curves. Regions in red were not included for calibration curve calculations.

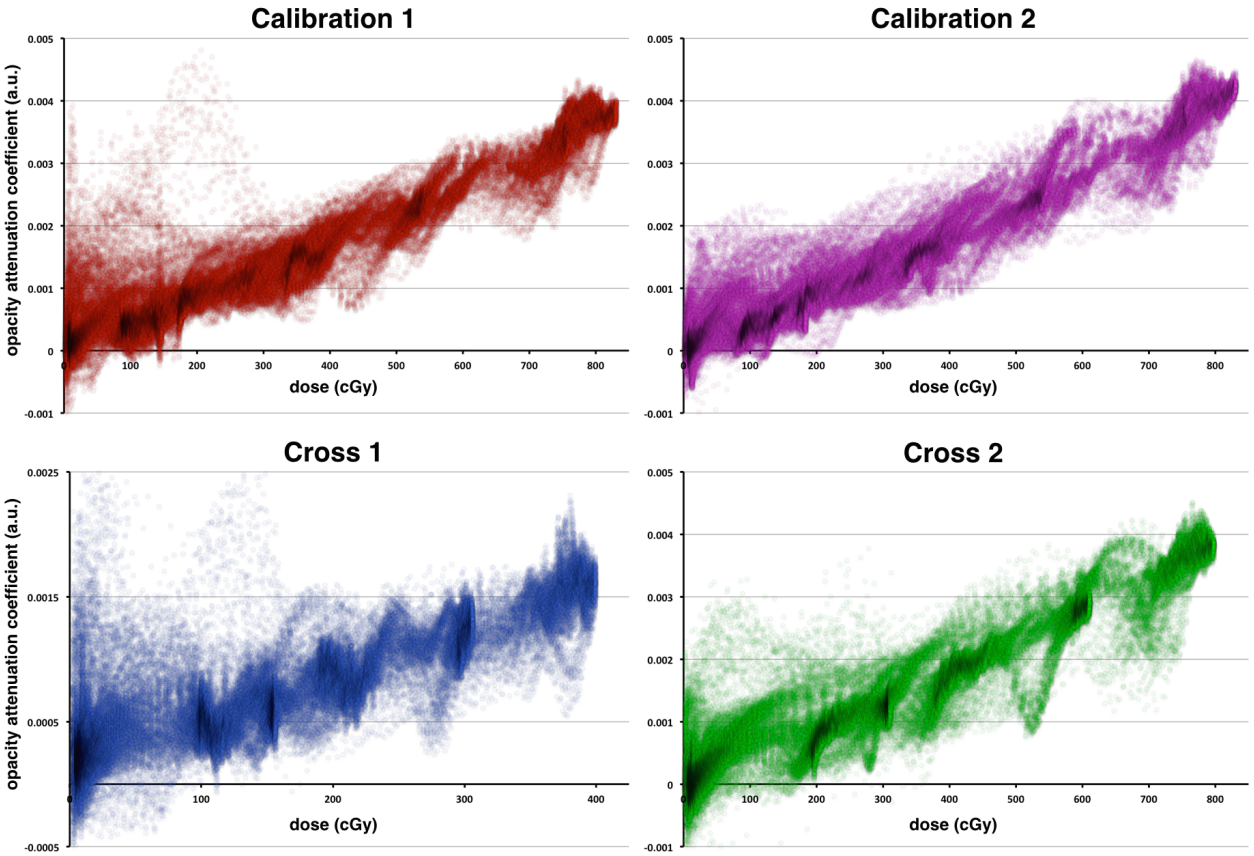

Figure 5.21: Plots of PAGAT opacity attenuation coefficients versus TPS-calculated dose for all data points in four irradiation patterns.

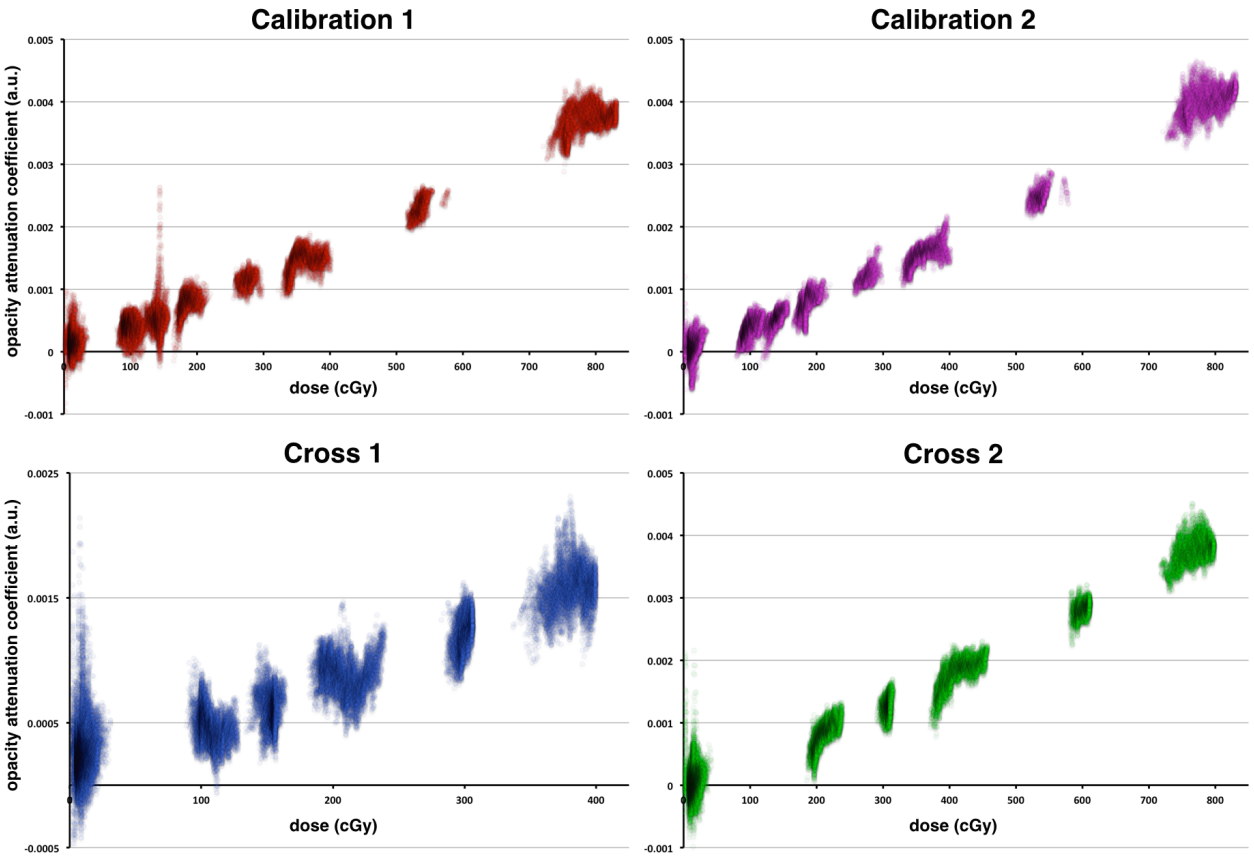

Figure 5.22: Plots of PAGAT opacity attenuation coefficients versus TPS-calculated dose in four irradiation patterns, ignoring data points with dose gradients >5 cGy/mm.

recipe used in this work and the dosages used here are not in the same range, it is possible that a similar shape might emerge as larger dose ranges were to be explored. The ostensible suitability of a linear fit, as was seen previously, could be due to exploring too small of a range of the overall dose-response curve. Therefore, it was worth examining whether or not a higher order polynomial would be more suitable for calibrating dose-response curves.

Linear, quadratic, and cubic curves were considered for calibration curves. Using data with dose gradients ignored, bulk data as consolidated by taking the median values of 100 data points at a time, sorted with respect to the TPS-calculated dose axis. This provided 476 data points for both Calibration distributions, 707 for Cross #1, and 549 for Cross #2. Then, these consolidated data sets were used to calculate calibration curves using 1^{st}, 2^{nd}, and 3^{rd} order polynomials. Plots of these consolidated data sets and their corresponding calibration curves are shown in Figure 5.23.

In order to determine whether or not higher order polynomials were necessary for calibration curves, residuals were examined for each calibration curve in all four irradiation patterns. Each type of calibration curve was used to convert its corresponding irradiation pattern from opacity to dose. Due to the fact that each irradiation pattern's own data points were used to calculate its own calibration curve, this is referred to as "self calibration." Then, readout errors were calculated pixel-by-pixel and sorted along the TPS-calculated dose axis in dose bins 25 cGy wide. Plots of median readout errors with respect to TPS-calculated dose are shown in Figure 5.24. Trendlines are also included, and error bars indicate the range of $\mu-\sigma$ to $\mu+\sigma$ within each bin. Residuals for cubic and quadratic calibration curves were so similar that, in order to avoid clutter, cubic data points were not plotted. Rather, only the trendline for cubic data was plotted (dotted green line).

The curvature of residuals for the linear calibration curve would suggest that a higher order polynomial might be more suitable for calibrating PAGAT dose-response. In order to determine quantifiably how much of a benefit a higher order polynomial would have on

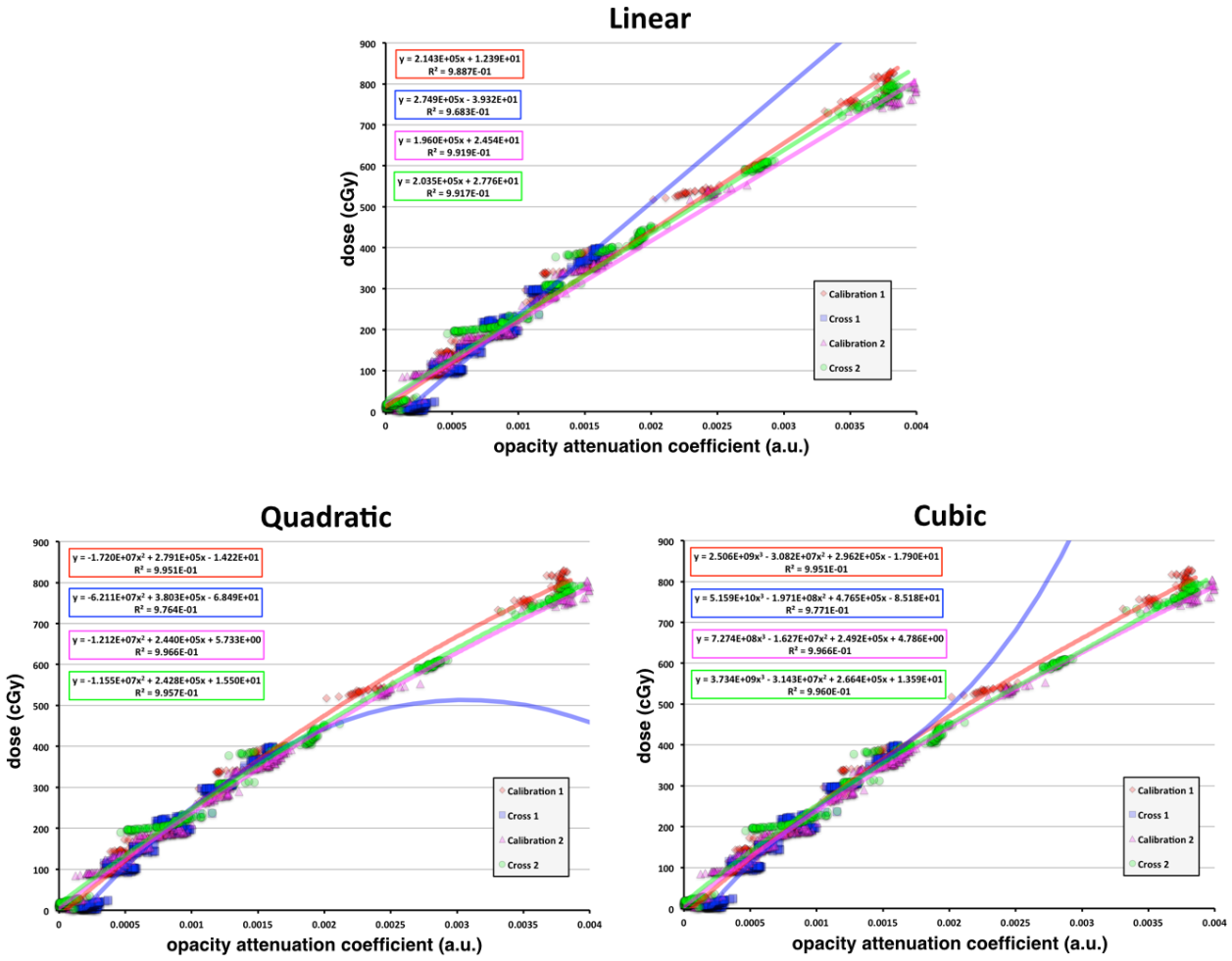

Figure 5.23: Plots of PAGAT dosimeter calibration curves for four irradiation patterns using either linear, quadratic, or cubic fits. Note: for 'Cross 1' fits, curve values for dosages >4 Gy are shown simply to illustrate the unreliability of extrapolating dose-response values beyond the calibrated dose range.

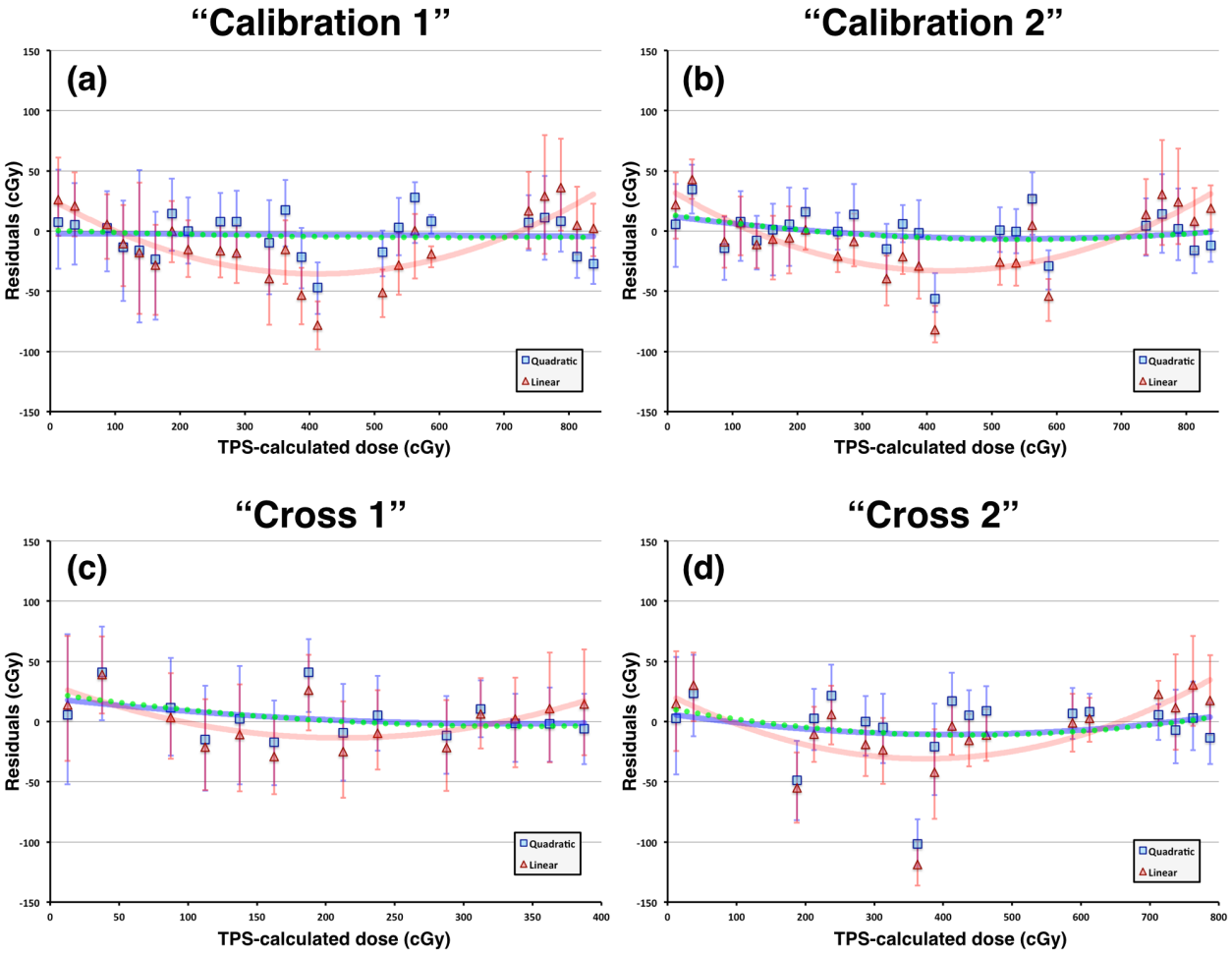

Figure 5.24: Readout residuals for four irradiation patterns using either quadratic (blue squares) or linear (red triangles) calibration curves. Trendlines for these residuals are shown respectively in blue and red, and trendlines for cubic residuals are shown as a dotted green line. The curvature of residuals for linear calibration curves would suggest that a higher order polynomial might be more suitable. Portions of the dose axis where data points are missing correspond to regions of each dose distribution that featured high dose gradients.

readout, average absolute residuals were calculated for each irradiation pattern. Furthermore, in addition to examining self-calibrated data, intra-gel and inter-gel calibrations were examined. For intra-gel calibration, each irradiation pattern is converted to dose by the calibration curve of the other irradiation pattern in the dosimeter (e.g., using the "Calibration 1" calibration curve to calculate the dose equivalent of the opacity seen in "Cross 1"). For inter-gel calibration, an irradiation pattern is converted to dose by a calibration curve obtained from another dosimeter (e.g., using the "Calibration 1" calibration curve to calculate the dose equivalent of the opacity seen in "Cross 2"). In order for a calibration curve to be suitable to calibrate another irradiation pattern, it should cover the full dose range of that irradiation pattern. Therefore, the calibration curve obtained from "Cross 1" was not used to calibrate any other pattern due to the fact that it only covers half the dose range of the other dose distributions.

With high dose gradients ignored, Table 5.2 provides the mean absolute residuals for each irradiation pattern using either linear, quadratic, or cubic calibration curves, and using either self, intra-gel, or inter-gel calibration. The same data with high dose gradients included is provided in Table 5.3. Note that intra-gel calibration was not available for "Calibration 1" because its partner irradiation pattern only covers half of its dose range.

First, to examine the effect that polynomial order has on calibration curve residuals, average absolute residuals for cubic and quadratic calibration curves were compared to linear values for each irradiation pattern. These comparisons are summarized in Table 5.4. Regardless of whether or not high dose gradients were ignored, both cubic and quadratic calibration curves showed smaller residuals than the linear calibration curve. By using either a quadratic or a cubic fit, residuals were reduced by 17% when high dose gradients are ignored, and by 6% when high dose gradients are included. It is also worth noting that there is no statistically significant benefit in choosing a cubic calibration curve over a quadratic calibration curve. As such, the quadratic calibration curve outperforms the linear calibration

Mean Absolute Residuals (cGy)	Calibration Curve Type (gradients ignored)		
"Calibration 1"	Linear	Quadratic	Cubic
Self Calibrated	30.1	24.4	24.2
Intra-Gel Calibrated	-	-	-
Inter-Gel Calibrated	42.2	32.6	33.4
"Cross 1"	Linear	Quadratic	Cubic
Self Calibrated	27.9	25.6	25.9
Intra-Gel Calibrated	27.1	24.4	24.6
Inter-Gel Calibrated	31.8	24.3	24.2
"Calibration 2"	Linear	Quadratic	Cubic
Self Calibrated	27.1	20.0	20.1
Intra-Gel Calibrated	29.4	21.0	24.4
Inter-Gel Calibrated	36.3	29.8	30.9
"Cross 2"	Linear	Quadratic	Cubic
Self Calibrated	30.1	25.7	25.2
Intra-Gel Calibrated	36.3	27.1	27.3
Inter-Gel Calibrated	36.5	33.6	31.9

Table 5.2: Mean absolute residuals for four irradiation patterns using linear, quadratic, or cubic calibration curves, and self-calibration, intra-gel calibration, or inter-gel calibration (dose gradients > 5 cGy/mm ignored).

Mean Absolute Residuals (cGy)	Calibration Curve Type (gradients included)		
"Calibration 1"	Linear	Quadratic	Cubic
Self Calibrated	37.5	36.3	36.5
Intra-Gel Calibrated	-	-	-
Inter-Gel Calibrated	49.1	42.7	43.5
"Cross 1"	Linear	Quadratic	Cubic
Self Calibrated	32.4	29.7	29.8
Intra-Gel Calibrated	30.8	28.7	28.7
Inter-Gel Calibrated	34.8	28.0	27.9
"Calibration 2"	Linear	Quadratic	Cubic
Self Calibrated	37.0	32.6	32.8
Intra-Gel Calibrated	36.9	32.7	34.6
Inter-Gel Calibrated	42.6	40.7	40.4
"Cross 2"	Linear	Quadratic	Cubic
Self Calibrated	48.7	48.2	48.2
Intra-Gel Calibrated	51.7	48.0	48.1
Inter-Gel Calibrated	53.4	56.3	55.0

Table 5.3: Mean absolute residuals for four irradiation patterns using linear, quadratic, or cubic calibration curves, and self-calibration, intra-gel calibration, or inter-gel calibration (dose gradients > 5 cGy/mm included).

curve, but the cubic calibration curve does not outperform the quadratic calibration curve.

Second, to examine the accuracy that can be expected depending on how an irradiation pattern is calibrated, average absolute residuals for intra-gel calibration and inter-gel calibration were compared to self calibration values for each irradiation pattern. These comparisons used quadratic calibration curves, and are summarized in Table 5.5. From these comparisons, it would appear that intra-gel calibration does not perform any worse than self calibration, indicating that the dose-response of a given gel is consistent throughout the individual dosimeter. However, inter-gel calibration does exhibit larger residuals than self calibration. By using inter-gel calibration, residuals were increased by 27% for data points that ignore high dose gradients, and by 13% for data points that include high dose gradients. This indicates that the dose-responses of these two gels were not consistent with one another. Consistency between dosimeters could possibly be improved by improving the reproducibility of dosimeter fabrication. Nevertheless, due to the consistency of intra-gel calibration, it is apparent that using a calibration irradiation pattern in the upper region of the dosimeter to calibrate for a measurement irradiation pattern in the lower region of the dosimeter is a reliable approach.

A summary of the effects that calibration curve type and calibration method have on absolute residuals are provided in Table 5.6. For best results, one should use self calibration, with a 2^{nd} order polynomial for calibration curve fitting. Nevertheless, within error, intra-gel calibration does not perform any worse than self-calibration. Alongside these measurements of residuals, a summary of the effects that calibration curve type and calibration method have on readout noise is provided in Table 5.7. As can be seen, calibration method and calibration curve type do not significantly influence readout noise. Rather, readout noise is more effectively reduced by optimizing scan parameters. Chapter 6 will examine the effects that changing scan parameters can have on absolute residuals and readout noise.

Relative Residual Comparisons	(gradients ignored)		(gradients included)	
Irradiation Pattern	**Cubic/ Linear**	**Quadratic/ Linear**	**Cubic/ Linear**	**Quadratic/ Linear**
"Calibration 1"	0.803	0.809	0.973	0.968
"Cross 1"	0.927	0.915	0.919	0.916
"Calibration 2"	0.741	0.736	0.886	0.881
"Cross 2"	0.839	0.856	0.991	0.989
	0.827±0.077	**0.829±0.076**	**0.942±0.048**	**0.939±0.049**

Table 5.4: Using self calibration, relative residual comparisons of four irradiation patterns are shown, comparing residuals of cubic and quadratic calibration curves against residuals of a linear calibration curve.

Relative Residual Comparisons	(gradients ignored)		(gradients included)	
Irradiation Pattern	**Intra-Gel/ Self**	**Inter-Gel/ Self**	**Intra-Gel/ Self**	**Inter-Gel/ Self**
"Calibration 1"	-	1.339	-	1.178
"Cross 1"	0.956	0.950	0.964	0.941
"Calibration 2"	1.054	1.494	1.003	1.250
"Cross 2"	1.054	1.307	0.995	1.167
	1.021±0.056	**1.272±0.230**	**0.987±0.021**	**1.134±0.134**

Table 5.5: Relative residual comparisons of four irradiation patterns, comparing residuals of intra-gel calibration and inter-gel calibration against residuals of self-calibration. Recall that intra-gel calibration was not attempted for the "Calibration 1" pattern due to its intra-gel irradiation pattern covering only half of its dose range.

Average Absolute Residuals (cGy)	Calibration Curve Type		
Gradients Ignored	**Linear**	**Quadratic**	**Cubic**
Self Calibrated	28.8±1.5	23.9±2.7	23.8±2.6
Intra-Dosimeter Calibrated	30.9±4.7	24.2±3.0	25.4±1.6
Inter-Dosimeter Calibrated	36.7±4.3	30.1±4.2	30.1±4.1
Gradients Included	**Linear**	**Quadratic**	**Cubic**
Self Calibrated	38.9±6.9	36.7±8.1	36.8±8.1
Intra-Dosimeter Calibrated	39.8±10.8	36.4±10.1	37.1±9.9
Inter-Dosimeter Calibrated	45.0±8.1	41.9±11.6	41.7±11.2

Table 5.6: Average absolute residuals across all four irradiation patterns are for self-calibration, intra-gel calibration or inter-gel calibration, and for linear, quadratic, or cubic calibration curves.

Average Readout Noise (cGy)	Calibration Curve Type		
Gradients Ignored	**Linear**	**Quadratic**	**Cubic**
Self Calibrated	29.1±6.0	27.5±5.0	28.2±5.4
Intra-Dosimeter Calibrated	26.4±2.6	26.9±5.5	27.3±4.8
Inter-Dosimeter Calibrated	26.7±0.8	26.7±2.4	27.0±2.0
Gradients Included	**Linear**	**Quadratic**	**Cubic**
Self Calibrated	63.5±9.7	60.5±10.4	60.5±9.8
Intra-Dosimeter Calibrated	59.0±15.6	59.5±13.0	59.5±13.0
Inter-Dosimeter Calibrated	60.5±17.1	60.2±14.8	60.0±14.7

Table 5.7: Average readout noise across all four irradiation patterns are for self-calibration, intra-gel calibration or inter-gel calibration, and for linear, quadratic, or cubic calibration curves.

5.8 Chapter Summary

A number of topics presented in this chapter were presented in a talk at the International Conference on 3D Dosimetry in Sydney, Australia in November of 2012 [156]. Findings were also later published as an article for Medical Physics — *"A prototype fan-beam optical CT scanner for 3D dosimetry"* [115].

This chapter describes a number of developments in the optical CT dosimetry system. A new fan-creation method and a new matching tank were shown to be improvements compared to the scanner components they replaced. Artefact removal techniques were developed to remove flask seam artefacts and ring artefacts from sinogram space, respectively reducing errors in reconstructions on the order of >5 Gy and ∼1 Gy. A flask registration technique was developed to allow for the reproducible placement of flasks in the optical CT scanner, and was it demonstrated to reproduce flask placement with sub-millimetre and sub-degree accuracy. This flask registration technique allowed for the comparison of pre-irradiation and post-irradiation scans, which provided visibly apparent improvements in dose reconstruction quality. Modifications to the dosimeter fabrication routine appeared to further improve dose reconstructions by allowing the dosimeter to cool slowly in a room temperature bath rather than cooling it quickly in a refrigerated bath. Investigations that examined continuous rotation data acquisition revealed that timestamp data acquired for each light profile must be used to calculate each profile's angular position. Using timestamp-corrected data, continuous rotation acquisition was shown to provide better results than a step + shoot acquisition that took nearly twice as long to acquire. Finally, PAGAT dosimeter calibration was examined, with analyses indicating that a 2^{nd} order polynomial should be used for calibration curve fits. Although self calibration provided the best results, intra-gel calibration did not perform any worse, within error. However, inter-gel calibration did show a statistically significant increase in absolute residuals. Neither calibration curve type nor calibration method were

shown to have any significant influence on readout noise. Readout noise can more effectively be reduced by optimizing scan parameters, which are examined in the following chapter.

Chapter 6

Results & Discussion II: Scanning Parameters & Image Quality in Fan-beam Optical CT Readout

The work presented in this chapter examines the role that some key parameters of the scanning protocol have on dose reconstructions for PAGAT dosimeters. To that end, in each section a single scan parameter was intentionally varied in order to assess the influence it had on reconstruction quality. Specifically, "quality" here was considered to be the precision and accuracy of the optical CT scanner's readout when compared against TPS-calculated dose distributions. To evaluate precision and accuracy, respectively, readout noise and readout errors were observed in the following investigations. Imaging benefits were evaluated based on these two factors.

Section 6.1 examines two PAGAT dosimeters that were irradiated with an identical irradiation pattern, only with one dosimeter receiving half the dosage of the other. Section 6.2 examines the effects of acquiring and averaging multiple light profile samples at each projection angle during the scan. Section 6.3 examines the effects of varying the number of

projection angles sampled in a full 360° rotation. Section 6.4 examines the effects of binning the profiles of a sinogram that sampled many projection angles into sinograms with fewer projections. Section 6.5 examines the effects of binning sinogram data to simulate larger detector elements. Section 6.6 examines the effects of binning image data into pixels of larger sizes. Section 6.8 combines the findings from all sections to establish a "best protocol" and to reconstruct an optimal image of a PAGAT dosimeter. "Best protocol" results are intended to demonstrate the current performance of the dosimeter & fan-beam optical CT system. Finally, the chapter summary in Section 6.8 highlights what are believed to be a new type of optical CT imaging artefact, which is the topic of Chapter 7.

All of the following sections examine single slices in the central region of the "Cross" irradiation patterns, which were previously examined in Section 5.7. The artefact removal techniques described in Section 5.2 were used to remove flask seam artefacts and ring artefacts. In Section 6.1, an identical continuous rotation data acquisition routine was used to scan both dosimeters. All other sections used a step+shoot acquisition routine. Self-calibrating quadratic calibration curves were used to convert opacity images into dose images for each irradiation pattern. In each section of this chapter, noise and error analyses were performed twice — with and without dose gradients included. The dose gradient masks used to distinguish these regions are shown in Figure 5.20.

6.1 Dose

This section examines the effects that the amount of radiation dose delivered to a dosimeter has on readout quality. Two different dosimeters were treated using the same "Cross" irradiation pattern, with one receiving a maximum dose of 400 cGy (henceforth referred to as "half" dose) and the other receiving a maximum dose of 800 cGy (henceforth referred to as "full" dose). Reconstructed PAGAT dose distributions, along with their corresponding

relative error images, are shown in Figure 6.1. These reconstructions were produced using an identical continuous rotation acquisition routine that acquired ∼1600 projections over a full 360° rotation (as described in Section 5.6).

Visual comparisons of relative error maps indicate that there is some benefit to increasing the dosage level used for dosimeter irradiation. Ideally, these maps would be uniformly green (i.e., readout errors = 0). As can be seen in Figure 6.1, the "half" dose reconstruction deviates from such values to a larger extent than the "full" dose reconstruction. To better understand the benefits of doubling dose, relative readout noise and relative readout errors (with and without dose gradients included) were plotted versus their relative TPS-calculated dose values (see Figure 6.2).

Noise and error values for all sections in this chapter were calculated in a similar fashion. To begin, a difference image was calculated by subtracting the TPS-calculated dose image from the PAGAT dose image (i.e., PAGAT − TPS). Then, difference image pixel values were sorted into bins with respect to their corresponding TPS-calculated dose value. Bins 12.5 cGy wide and 25 cGy wide for the "half" dose image and the "full" dose image, respectively. Readout noise for each bin was represented by its standard deviation (σ), and readout noise for each bin was represented by its average (μ). In Figure 6.1, relative noise and relative errors were calculated with respect to the value of each TPS dose bin, and relative TPS-calculated dose values (i.e., position along the horizontal axis) were calculated with respect to each irradiation pattern's maximum dose value.

As is evident from relative error plots, there appears to be no accuracy benefit gained from doubling the dosage delivered to the dosimeter. The relative magnitude of errors are not appreciably reduced when dosage is doubled. The benefit of doubling dosage came in reductions of noise. Plots of relative noise roughly illustrate that doubling the dosage to the dosimeter will double the signal-to-noise ratio. Relative comparisons of the relative noise in each image (i.e., [relative noise in the "full" dose image]/[relative noise in the "half"

dose image]) indicate that doubling dosage reduces noise: median (first quartile, third quartile) values of 0.57 (0.48, 0.70) with gradients included and 0.37 (0.31, 0.43) with gradients ignored.

In order to evaluate the lowest readout noise that can be achieved with the current system, the "full" dose irradiation pattern was used to examine remaining scan parameters.

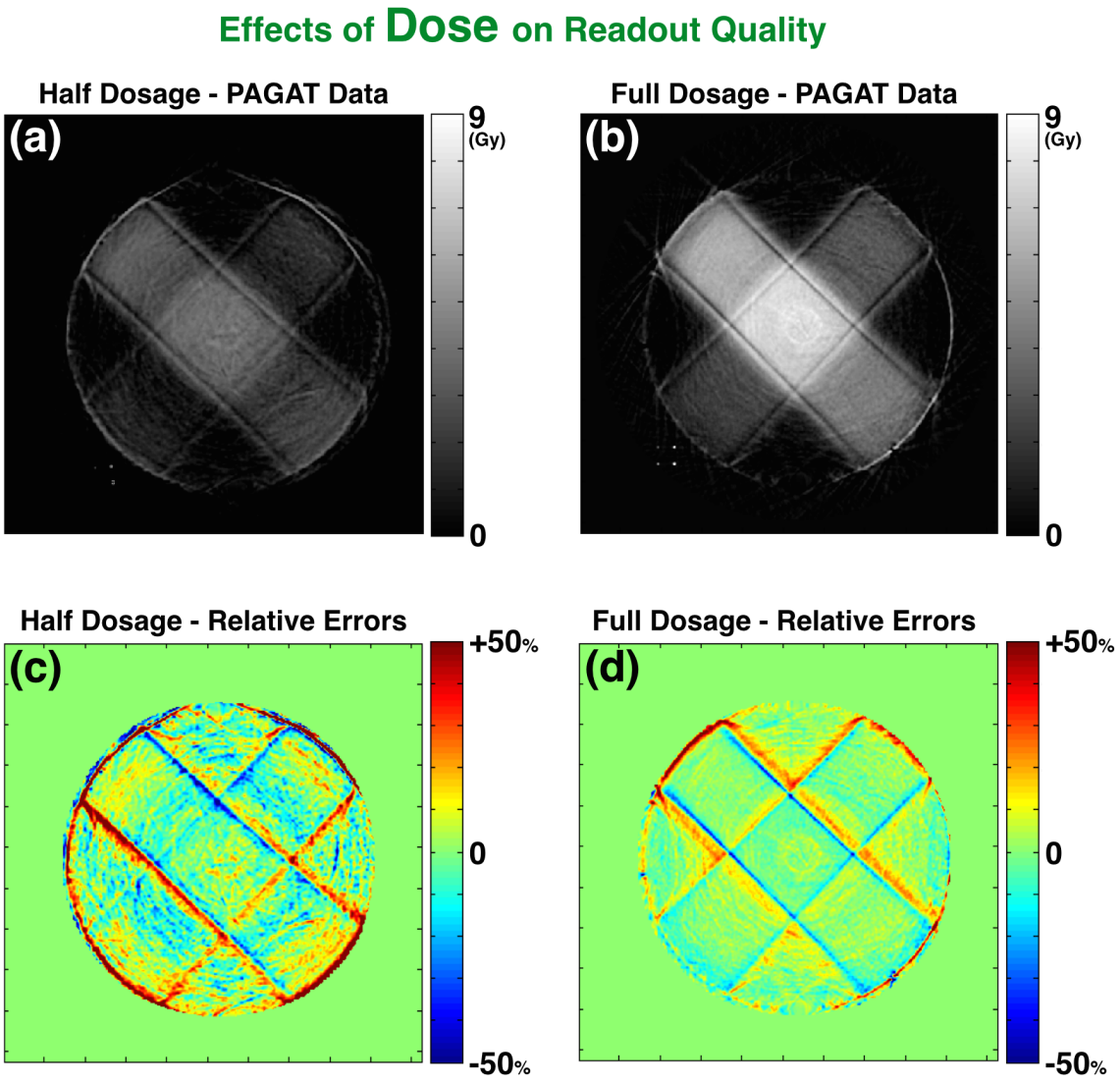

Figure 6.1: Shown are reconstructed PAGAT dose distributions of the cross irradiation pattern (a) at "half" dose, (b) at "full" dose, and their corresponding readout error maps are shown in (c) and (d), respectively. For better visual comparison, relative errors in (c) and (d) are scaled relative to each irradiation pattern's maximum dose value.

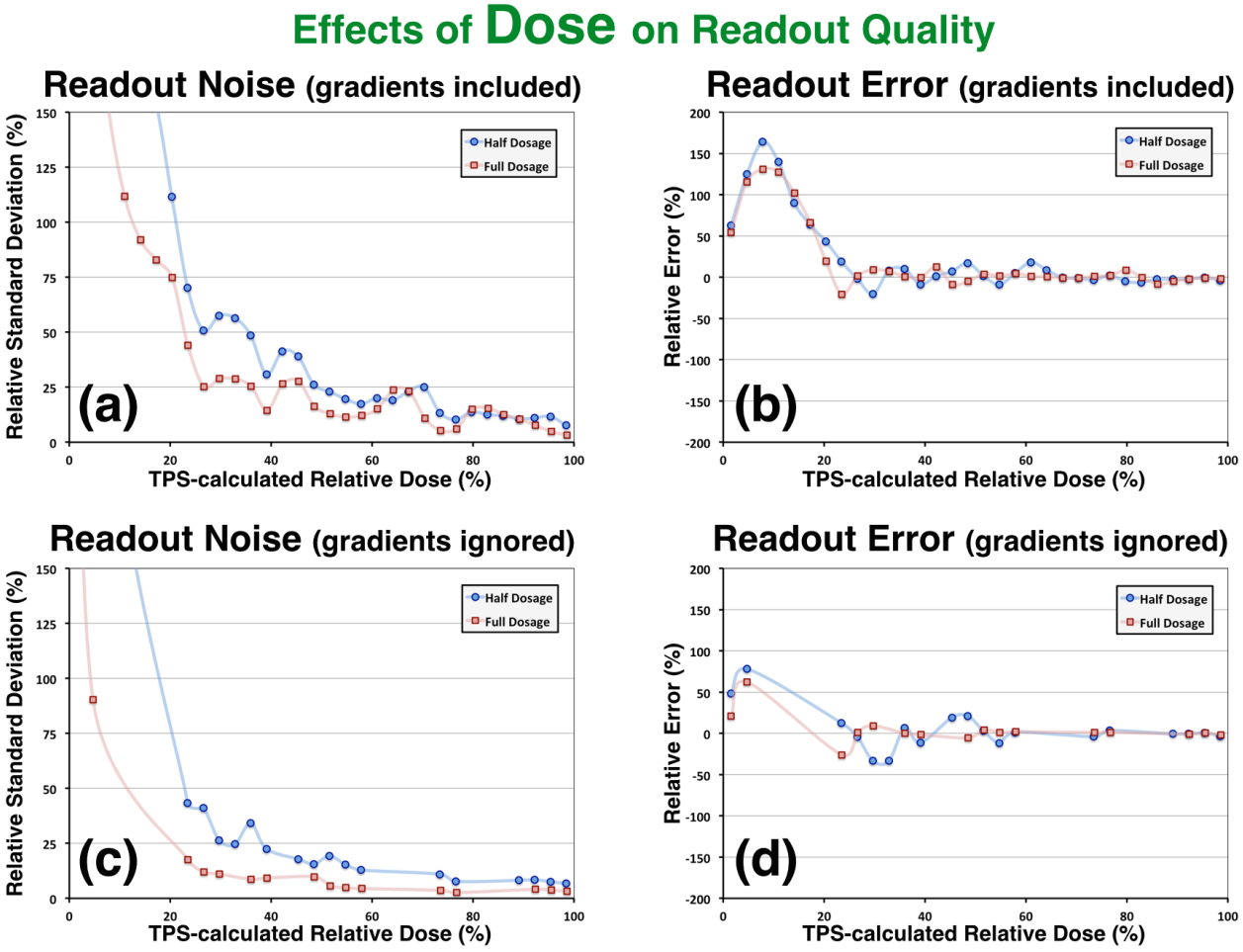

Figure 6.2: Plots of PAGAT (a) relative readout noise and (b) relative readout errors with dose gradients included, and (c) relative readout noise and (d) relative readout errors with dose gradients ignored. Relative errors and relative noise were calculated relative to their local dose value and *not* relative to the irradiation pattern's maximum dose. The horizontal axis (TPS-calculated relative dose) was normalized to the maximum dose for each irradiation pattern.

6.2 Light Profile Sampling

This section examines the effects that the number of light profile samples acquired and averaged at each projection angle has on readout quality. Essentially, the question being entertained here was: *"Will improving measurements of light profiles translate to improvements in reconstructions?"*

For these tests, the "full" dose cross irradiation pattern was scanned at 360 unique projection angles over a full 360° rotation (i.e., a rotational increment of 1° between each projection). At each projection angle, 5 light profile samples were collected. From these 1800 samples, 5 sinograms were calculated by averaging 1 to 5 of the samples collected at each projection angle. From these 5 sinograms, 5 different images were produced.

Dose reconstructions and relative error images for the "1 sample" case and the "5 samples" case are shown in Figure 6.3. Plots of readout noise and readout errors for all 5 cases are provided in Figure 6.4. Plots a–d in Figure 6.4 present noise and errors with and without steep dose gradients included. Furthermore, to gain a better sense of how changing the parameter in question (i.e., the number of samples) affects readout noise and readout errors, normalized noise trends and error trends are plotted in 6.4e and 6.4f, respectively.

To calculate normalized noise trends, noise values in each bin along the TPS-calculated dose axis were normalized by the "1 sample" case. Then, these normalized values were observed as the number of samples averaged was increased. Normalizing with respect to the "1 sample" case provides an indicator for how beneficial additional scans will be for reducing image noise. For error trends, error values over the entire dose range were observed. Plots in 6.4e and 6.4f show median, first quartile and third quartile values. These values are summarized in Table 6.1. For the sake of consistency, and to allow for easier comparisons of the relative importance of various scan parameters, identical analyses were performed in subsequent sections (i.e., for number of projection angles, projection angle binning, detector

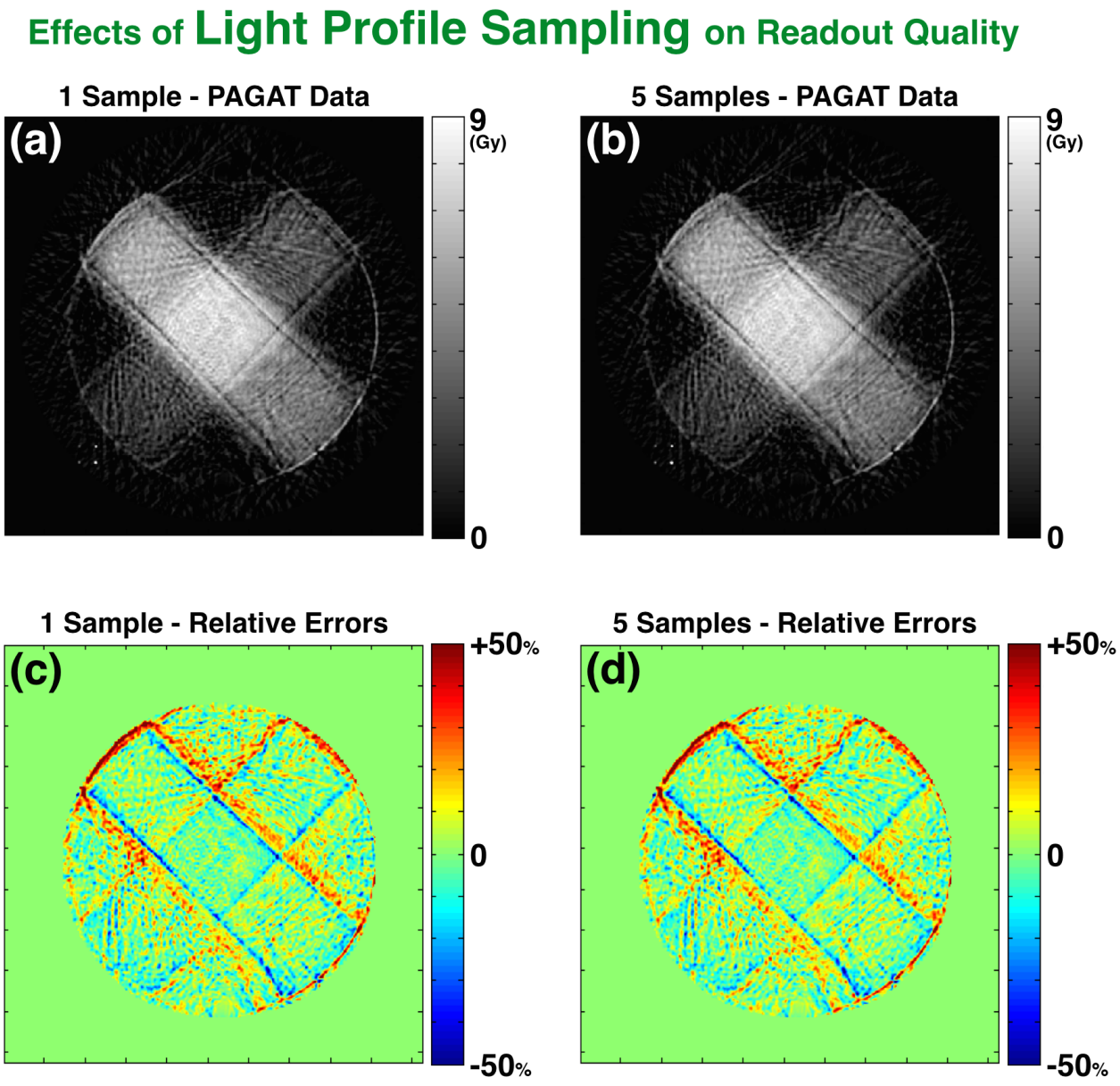

Figure 6.3: Using 360 projection angles over a full rotation, 5 light profiles were acquired at each angle. Reconstructed PAGAT dose distributions were calculated using (a) 1 light profile and (b) 5 light profiles averaged at each projection angle, and their corresponding readout error maps are shown in (c) and (d), respectively. For better visual comparison, relative errors in (c) and (d) are scaled relative to the irradiation pattern's maximum dose value.

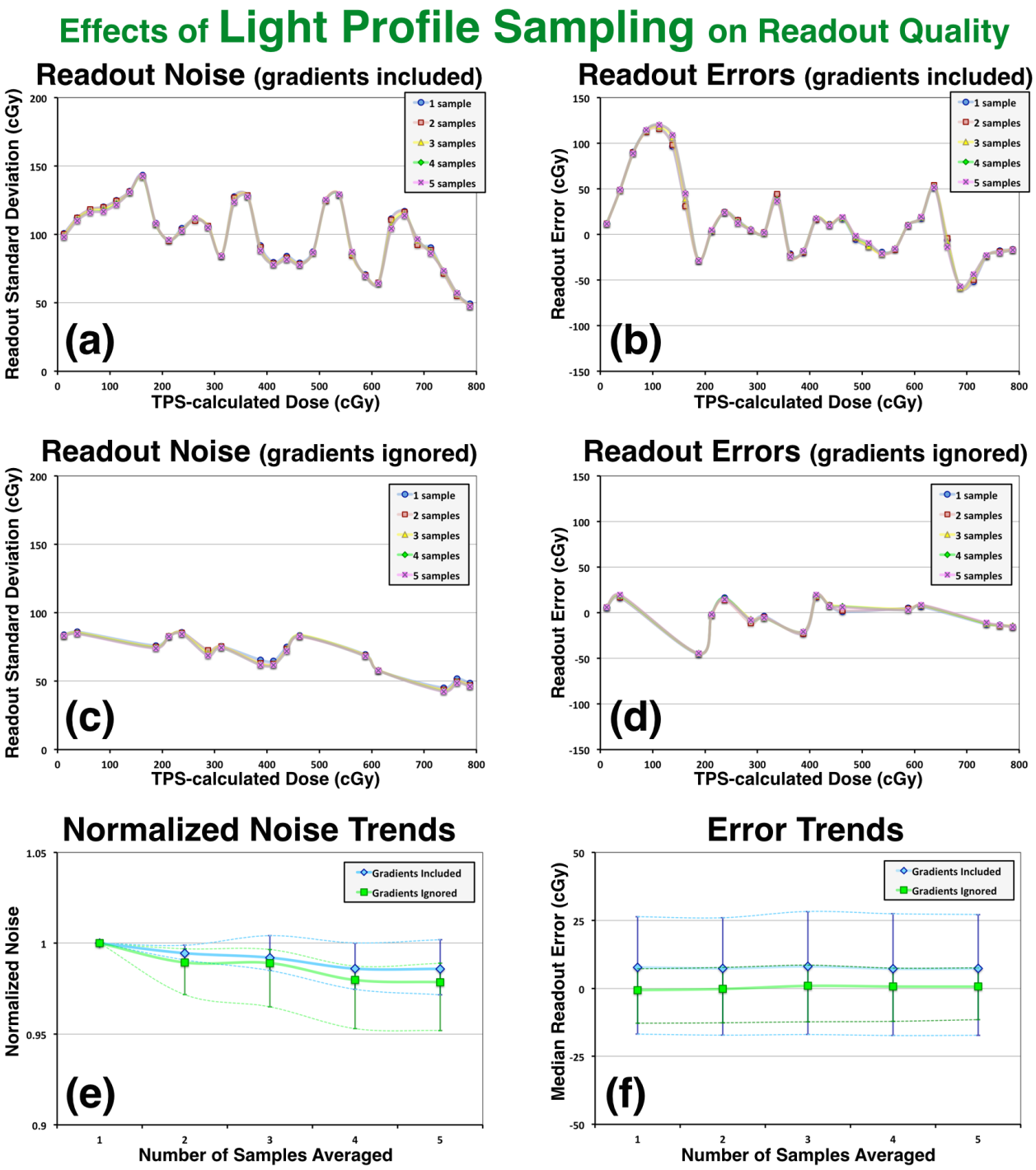

Figure 6.4: Using 360 projection angles over a full rotation, 5 light profile samples were acquired at each angle. With 1–5 samples being averaged per projection angle, plots are shown for: (a) readout noise and (b) readout errors with dose gradients included, (c) readout noise and (d) readout errors with dose gradients ignored, (e) normalized noise trends, and (f) error trends. Noise values were normalized using the reconstruction that used 1 sample per projection angle.

element binning, and pixel binning).

There appears to be no visible benefit gained from acquiring additional light profile samples at each projection angle. Though, upon examining error and noise plots in Figure 6.4e, a slight decrease in readout noise is achieved by acquiring additional samples. For the n=5 case, a modest 2% reduction in readout noise is observed when steep dose gradients are ignored, and this reduction in readout noise drops to 1% when gradients are included. It is believed that these reductions in image noise are related to noise in light profiles caused by turbulence in the matching bath. Similar analyses that examined a scattering solution in a water bath showed no reduction in noise when the number of light profiles sampled was increased. Here, a matching bath of water+glycerol was used to match the refractive index of the gel. By acquiring and averaging additional light profile samples, the effects of optical turbulence in the bath can be reduced.

Increased sampling of light profiles had no significant influence on readout errors. As will be seen throughout the rest of this chapter, changes to scanning protocol have little effect on readout errors, particularly the streaks that run along the sides of each photon beam. These streaks remain the largest source of readout errors and are the main topic of Chapter 7.

	Number of Samples Averaged				
Normalized Noise	**n = 1***	**n = 2**	**n = 3**	**n = 4**	**n = 5**
Gradients Ignored	**1**	**0.989** (0.972, 0.997)	**0.989** (0.965, 0.997)	**0.980** (0.953, 0.987)	**0.979** (0.952, 0.989)
Gradients Included	**1**	**0.995** (0.991, 0.999)	**0.992** (0.985, 1.004)	**0.986** (0.975, 1.000)	**0.986** (0.972, 1.002)
Readout Errors (cGy)	**n = 1**	**n = 2**	**n = 3**	**n = 4**	**n = 5**
Gradients Ignored	**-0.6** (-12.8, 7.2)	**-0.2** (-12.7, 7.7)	**0.9** (-12.3, 8.5)	**0.7** (-12.1, 7.5)	**0.7** (-11.5, 7.5)
Gradients Included	**7.7** (-16.8, 26.4)	**7.4** (-17.2, 26.0)	**8.1** (-17.0, 28.3)	**7.2** (-17.3, 27.4)	**7.3** (-17.3, 27.2)

Table 6.1: Normalized noise and readout error values for reconstructions of a PAGAT dosimeter with a varying number of light profile samples taken at each projection angle. Boldfaced values are medians, and error ranges (shown in parentheses) indicate the first and third quartiles. *Noise values were normalized using the reconstruction that used 1 sample per projection angle.

6.3 Number of Projections

This section examines the effects that the number of projection angles sampled has on readout quality. The previous section illustrated that acquiring additional light profiles at each projection angle had only a weak influence on subsequent image noise. Here, the question posited was: *"Will acquiring additional light profile samples from more projection angles improve reconstructions?"*

For these tests, the same irradiation pattern was scanned at 2880 unique projection angles over a full 360° rotation. A single light profile sample was acquired at each projection angle. From this sinogram of 2880 unique projections, 5 additional sinograms were created, each one sampling fewer and fewer of the original sinogram's projections — 2880, 1440, 720, 360, 180, and 90 projections. As a result, incremental spacing between projections in these sinograms ranged from 4° to 0.125° between projections. From these 6 sinograms, 6 different images were produced. Dose reconstructions and relative error images for the "90 projection" case and the "2880 projection" case are shown in Figure 6.5. Plots of readout noise and readout errors for all 6 cases are provided in Figure 6.6. Noise trends and error trends shown in Figures 6.6e and 6.6f are summarized in Table 6.2. For normalized noise trends, noise values were normalized with respect to the 360 projection angle case.

It is very evident from these images that increasing the number of unique projection angles used in a scan can reduce noise substantially. The 90-projection image suffers from excessive levels of noise, while the 2880-projection image features a much smoother measured dose distribution. When considering readout noise normalized with respect to the 360 projection case, there was a significant benefit in increasing the number of projections and a significant detriment in decreasing the number of projections. Compared to the 360 projection case, the 2880 projection case saw 68% less noise when dose gradients were ignored, and 24% less noise when dose gradients were included. On the other hand, the 90 projection case saw

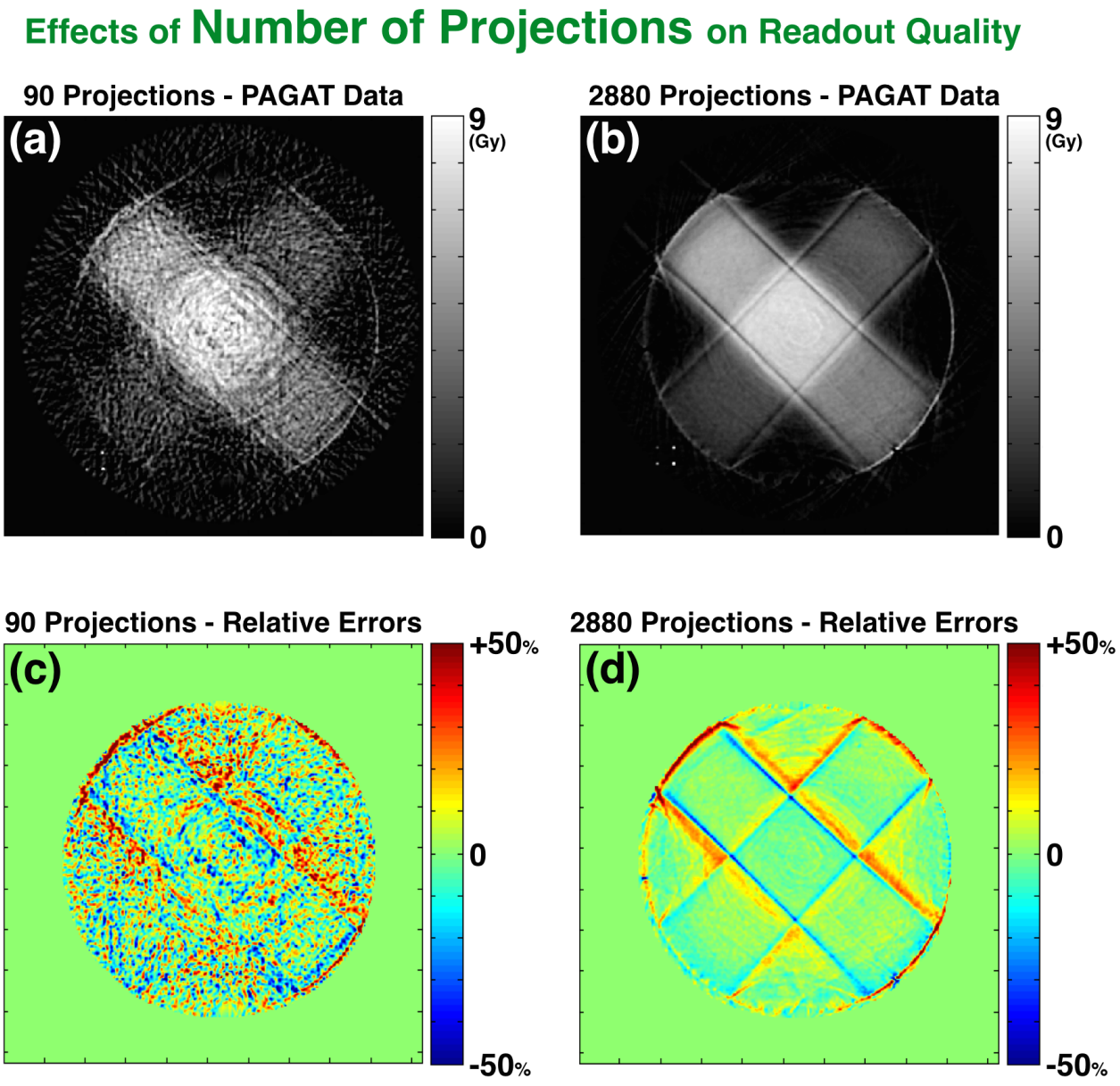

Figure 6.5: Acquiring a single light profile at each projection angle, a varying number of projection angles were sampled over a full 360° rotation. Reconstructed PAGAT dose distributions were calculated by sampling (a) 90 projection angles and (b) 2880 projection angles, and their corresponding readout error maps are shown in (c) and (d), respectively. For better visual comparison, relative errors in (c) and (d) are scaled relative to the irradiation pattern's maximum dose value.

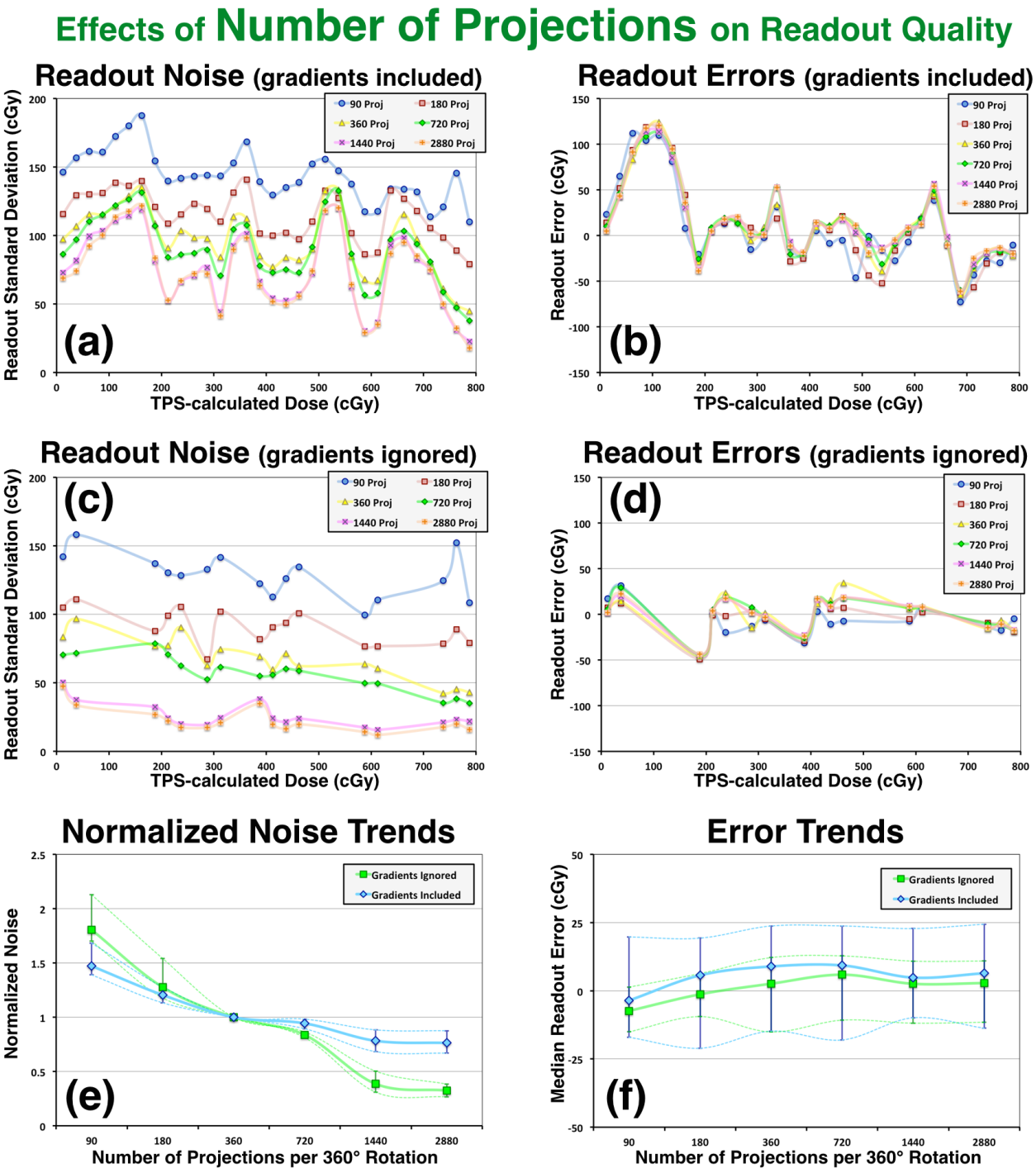

Figure 6.6: Using a single light profile at each projection angle, a varying number of projection angles were sampled evenly over a full 360° rotation. With a varying number of projection angles sampled, plots are shown for: (a) readout noise and (b) readout errors with dose gradients included, (c) readout noise and (d) readout errors with dose gradients ignored, (e) normalized noise trends, and (f) error trends. Noise values were normalized using the reconstruction that sampled 360 projection angles.

81% more noise when dose gradients were ignored, and 47% more noise when dose gradients were included.

With respect to readout accuracy, increasing the number of projection angles did not have a clear influence on the magnitude of readout errors. As is shown in Figure 6.6f and Table 6.2, there is no clear trend in readout errors with respect to the number of projection angles sampled.

	Number of Projections					
Normalized Noise	**90**	**180**	**360***	**720**	**1440**	**2880**
Gradients Ignored	**1.81** (1.70, 2.13)	**1.28** (1.18, 1.54)	**1**	**0.837** (0.812, 0.864)	**0.386** (0.310, 0.503)	**0.325** (0.266, 0.384)
Gradients Included	**1.47** (1.39, 1.68)	**1.20** (1.13, 1.28)	**1**	**0.943** (0.894, 0.983)	**0.783** (0.683, 0.883)	**0.763** (0.669, 0.876)
Readout Errors (cGy)	**90**	**180**	**360**	**720**	**1440**	**2880**
Gradients Ignored	**-7.4** (-15.0, 1.3)	**-1.3** (-9.5, 6.3)	**2.6** (-15.1, 12.2)	**5.9** (-10.8, 12.8)	**2.6** (-11.9, 10.9)	**2.8** (-11.5, 10.9)
Gradients Included	**-3.6** (-17.0, 19.7)	**5.7** (-21.1, 19.3)	**8.9** (-14.8, 23.8)	**9.3** (-18.0, 23.8)	**4.8** (-9.9, 22.8)	**6.4** (-13.7, 24.4)

Table 6.2: Normalized noise and readout error values for reconstructions of a PAGAT dosimeter that sampled a varying number of unique projection angles over a full 360° rotation. Boldfaced values are medians, and error ranges (shown in parentheses) indicate the first and third quartiles. *Noise values were normalized using the reconstruction that sampled 360 projection angles.

6.4 Projection Angle Binning

This section examines the effects that projection angle binning has on readout quality. The previous section demonstrated that a significant reduction in image noise can be obtained by increasing the number of projection angles sampled. However, sinograms with a higher number of projections take longer to reconstruct. For example, using filtered backprojection, an image can be reconstructed from a 90-projection sinogram in 1.03 seconds, but it takes 32.1 seconds to reconstruct an image from a 2880-projection sinogram[1]. Half of a minute may not seem too bothersome, but if a 10 cm vertical range of a cylindrical dosimeter were to be imaged with 1 mm pitch between slices, that half of a minute turns into nearly an hour. In the end, the question was raised: *"If a sinogram that sampled many projection angles was encapsulated by binning it into a sinogram of fewer projections, would the benefits of noise reduction still remain?"*

For these tests, the sinogram that sampled 2880 unique projection angles in the previous section served as a starting point to create 5 additional sinograms with fewer and fewer projections. However, all projections from the 2880-projection sinogram were used to calculate profile values for each sinogram (i.e., instead of skipping over profiles as was done in Section 6.3, profiles were averaged together here). This provided 6 sinograms varying by number of projections data was binned into — 90, 180, 360, 720, 1440, and 2880 (i.e., no binning). From these 6 different sinograms, 6 different images were produced. Dose reconstructions and relative error images for the "90 projection" case and the "2880 projection" case are shown in Figure 6.7. Plots of readout noise and readout errors for all 6 cases are provided in Figure 6.8. Noise trends and error trends shown in Figures 6.8e and 6.8f are summarized in Table 6.3. For normalized noise trends, noise values were normalized with respect to the case that used no binning.

[1]Performed on a personal computer (Intel® Core™2 Duo E8400) using MATLAB's *iradon* function (linear interpolation, ramp-Hamming filter).

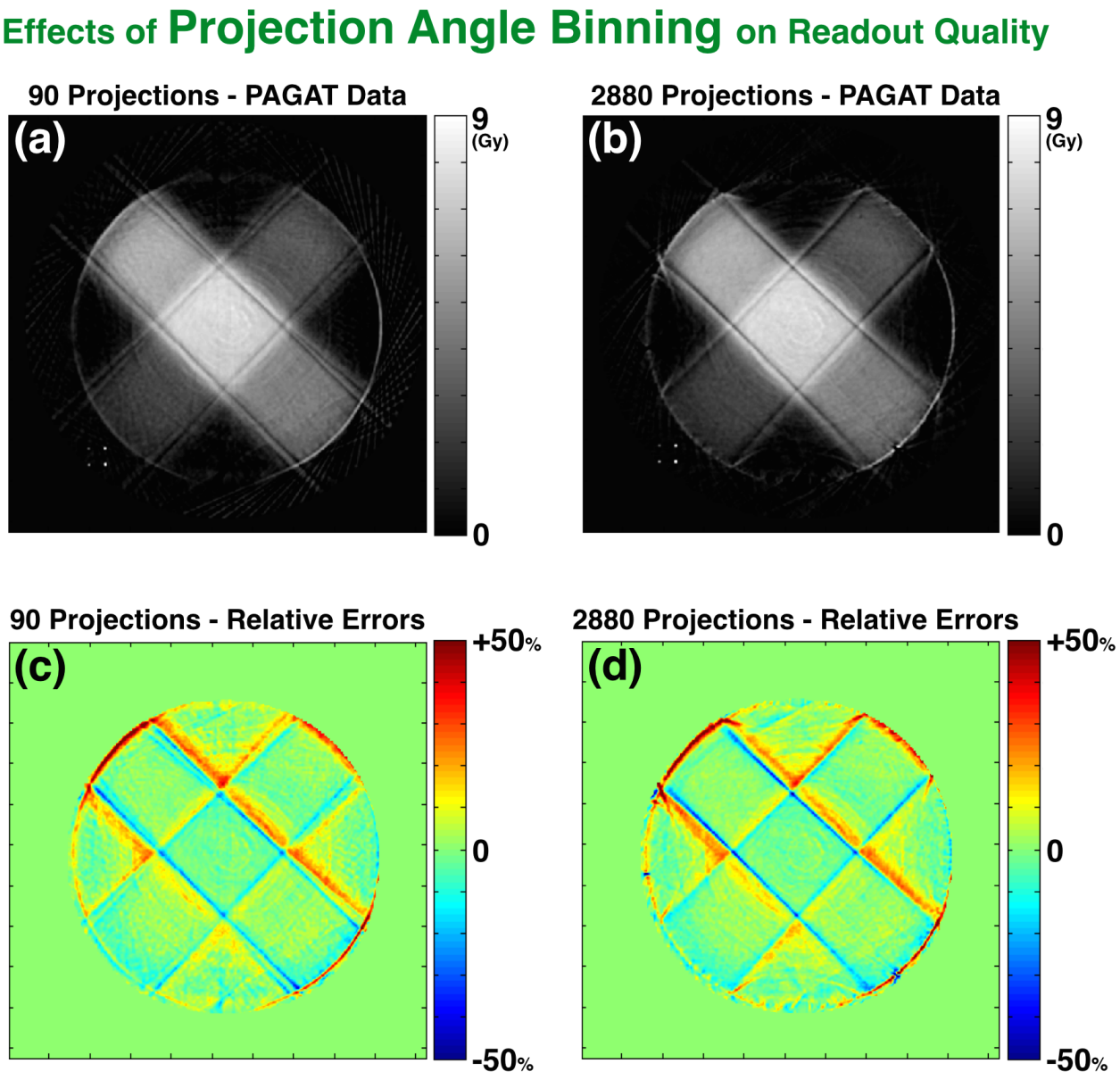

Figure 6.7: Starting with the same 2880-projection sinogram, projections were averaged into sinograms with a varying number of projection angle bins over a full 360° rotation. Reconstructed PAGAT dose distributions were calculated using (a) 90 projection angle bins and (b) 2880 projection angle bins (i.e., no binning), and their corresponding readout error maps are shown in (c) and (d), respectively. For better visual comparison, relative errors in (c) and (d) are scaled relative to the irradiation pattern's maximum dose value.

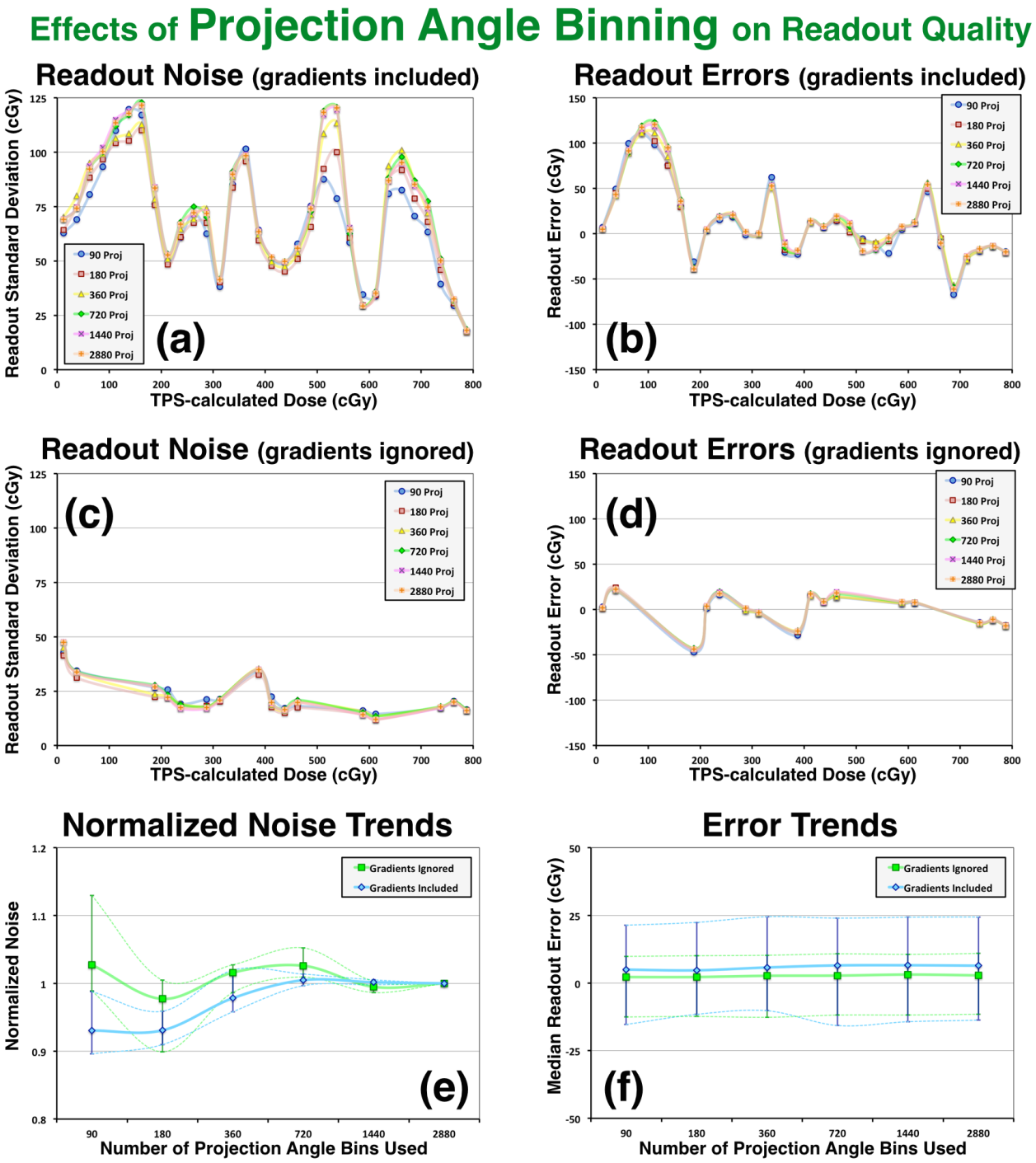

Figure 6.8: Starting with the same 2880-projection sinogram, projections were averaged into sinograms with a varying number of projection angle bins over a full 360° rotation. With a varying number of projection angle bins used, plots are shown for: (a) readout noise and (b) readout errors with dose gradients included, (c) readout noise and (d) readout errors with dose gradients ignored, (e) normalized noise trends, and (f) error trends. Noise values were normalized using the reconstruction that used no binning.

Two main observations can be made from these results. First, the bold streaks that follow along the sides of each radiation beam in the 2880-projection image are duplicated and subdued in the 90-projection image. It would appear that, in the 90-projection image, pairs of narrower streaks of smaller magnitude are reconstructed in the place of each of the broader streaks that appear in the 2880-projection image. The pair of narrow streaks illustrate the 4° angular step that was taken between two projections in the binned sinogram. As was stated previously, these streaking artefacts will be investigated in more detail in Chapter 7. Although it might seem that projection angle binning could potentially be exploited to remove these artefacts, the physical cause of these artefacts ends up causing much more severe errors in other instances[2].

Second, normalized noise trends indicate that the noise reduction benefit seen previously when more projections were sampled was not lost when those projections are encapsulated into sinograms with fewer projections. Although no clear trend emerges, noise values for the 90-projection case were either slightly higher or slightly lower, depending on whether or not dose gradients were ignored or included, respectively. It is believed that these differences are related to having too few projections in the 90-projection case. When dose gradients are included, normalized noise values reflect how the angular spacing of 4° between projections has subdued the streaking artefacts that run alongside each photon beam. When dose gradients are ignored these artefacts are also ignored, and one can see slight rippling beginning to occur in low dose gradient regions (most notably in regions distant from the center of the reconstruction), which is due to having too few projections. In order to avoid such rippling, it is recommended that projection angle binning be used with no fewer than 360 projections per full rotation (i.e., 1° rotational increments between projections).

[2]To be discussed in Chapter 7

	Projection Angle Binning					
Normalized Noise	**90**	**180**	**360**	**720**	**1440**	**2880***
Gradients Ignored	**1.03** (0.989, 1.13)	**0.977** (0.899, 1.00)	**1.02** (0.987, 1.03)	**1.03** (1.01, 1.05)	**0.995** (0.986, 1.00)	**1**
Gradients Included	**0.931** (0.896, 0.988)	**0.931** (0.910, 0.959)	**0.978** (0.958, 1.02)	**1.00** (0.997, 1.01)	**1.00** (0.998, 1.01)	**1**
Readout Errors (cGy)	**90**	**180**	**360**	**720**	**1440**	**2880**
Gradients Ignored	**2.2** (-12.5, 9.9)	**2.2** (-12.3, 10.1)	**2.7** (-12.6, 10.3)	**2.7** (-11.9, 10.8)	**3.1** (-11.8, 10.6)	**2.8** (-11.5, 10.9)
Gradients Included	**4.9** (-15.3, 21.3)	**4.7** (-11.6, 22.4)	**5.8** (-10.2, 24.5)	**6.5** (-15.7, 24.0)	**6.6** (-14.3, 24.3)	**6.4** (-13.7, 24.4)

Table 6.3: Normalized noise and readout error values for reconstructions of a PAGAT dosimeter that used a varying number of projection angle bins for the same 2880-projection sinogram. Boldfaced values are medians, and error ranges (shown in parentheses) indicate the first and third quartiles. *Noise values were normalized using the reconstruction that used no binning.

6.5 Detector Element Binning

This section examines the effects that detector element binning in sinogram space has on readout quality. The size of the scanner's detector elements project a rayline width of 0.4 mm at the axis of rotation. However, typical TPS-calculated dose distributions use voxel sizes $\geq 2\times2\times2$ mm^3. If the goal is to compare dosimeter measurements against typical TPS dose distributions, the scanner's detector elements are smaller than necessary. So, this section posited the question: *"How much noise reduction can be realized by simulating larger detector elements?"*

For these tests, one 720-projection sinogram was used as a starting point to create 4 additional sinograms, each imposing a different level of detector element binning. Light profiles were binned detector-wise by averaging varying numbers of detector elements together — 1 (i.e., no binning), 2, 3, 4, and 5 detector elements binned together. Through this binning, the detector axis of each sinogram effectively became 320, 160, 106, 80, and 64 elements wide, which respectively corresponds to projected rayline widths at the axis of rotation equalling 0.4 mm, 0.8 mm, 1.2 mm, 1.6 mm, and 2.0 mm. From these 5 sinograms, 5 different images were produced. Dose reconstructions and relative error images for the "no binning" case and the "5 elements binned" case are shown in Figure 6.9. Plots of readout noise and readout errors for all 5 cases are provided in Figure 6.10. Noise trends and error trends shown in Figures 6.10e and 6.10f are summarized in Table 6.4. For normalized noise trends, noise values were normalized with respect to the case that used no binning.

As one might expect, detector element binning had a large effect on readout noise. As can be seen in Figure 6.10e, normalized noise values in the "5 elements binned" case were reduced by 62% when dose gradients were ignored and by 32% when dose gradients were included. Detector element binning was not shown to have any effect on readout errors. One concern that exists when one reduces the resolution of the detector array would be a loss

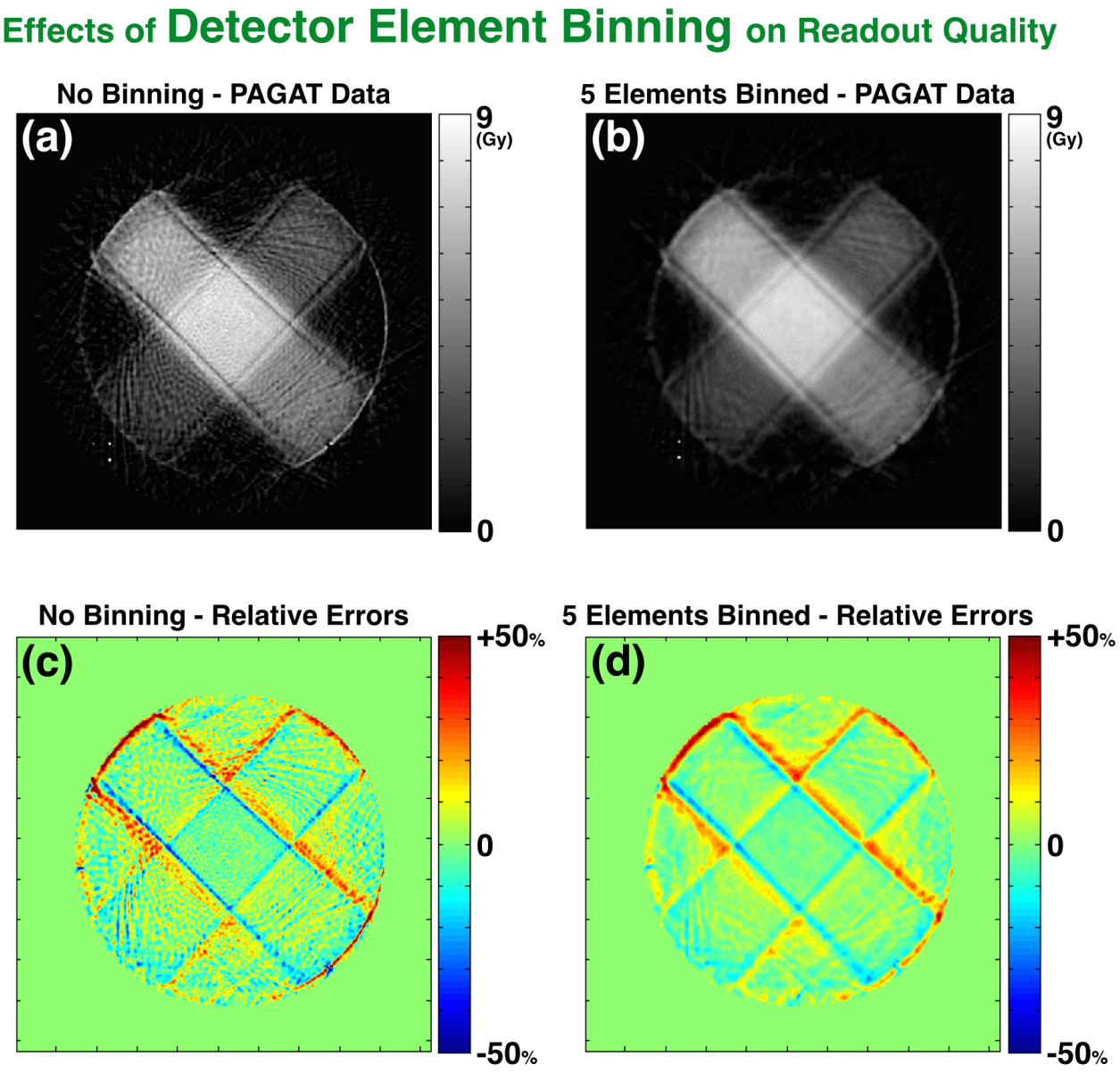

Figure 6.9: Starting with the same 720-projection sinogram, data was binned to simulate larger detector elements. Reconstructed PAGAT dose distributions were calculated using (a) no binning and (b) binning 5 elements wide, and their corresponding readout error maps are shown in (c) and (d), respectively. For better visual comparison, relative errors in (c) and (d) are scaled relative to the irradiation pattern's maximum dose value.

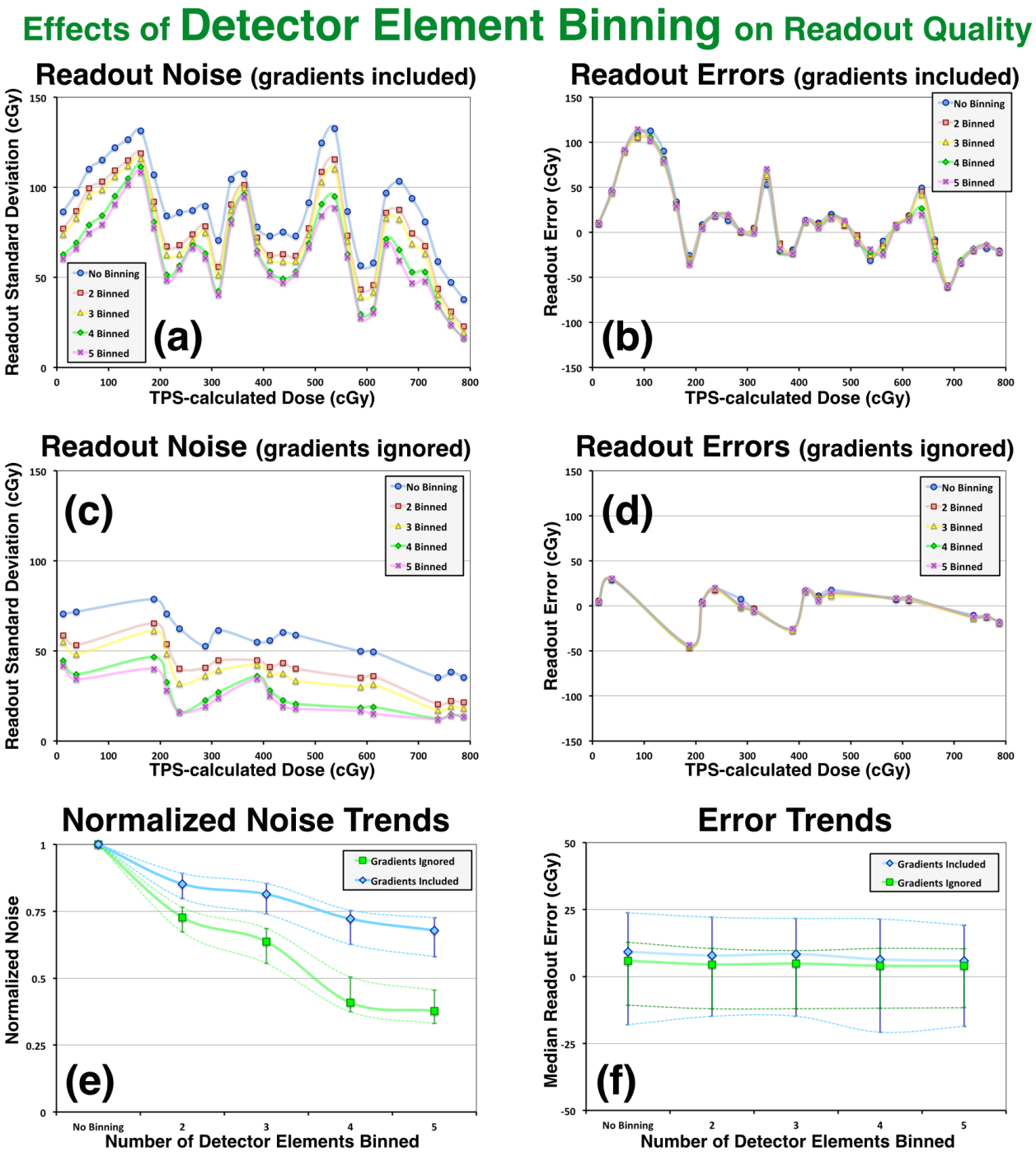

Figure 6.10: Starting with the same 720-projection sinogram, data was binned to simulate larger detector elements. With a varying levels of detector element binning, plots are shown for: (a) readout noise and (b) readout errors with dose gradients included, (c) readout noise and (d) readout errors with dose gradients ignored, (e) normalized noise trends, and (f) error trends. Noise values were normalized using the reconstruction that used no binning.

in image resolution causing readout errors. However, with the amount of noise that exists in images reconstructed with this scanner, one can appreciate the compromise of *potentially* sacrificing resolution in order to *actually* attain reductions in noise. It would be safe to assume that readout errors caused by the detector element binning used here would only manifest for a dose distribution with higher spatial modulation.

	Number of Detector Elements Binned				
Normalized Noise	**No Binning***	**2**	**3**	**4**	**5**
Gradients Ignored	**1**	**0.728** (0.673, 0.765)	**0.636** (0.555, 0.686)	**0.409** (0.374, 0.505)	**0.378** (0.331, 0.456)
Gradients Included	**1**	**0.852** (0.798, 0.892)	**0.814** (0.739, 0.854)	**0.722** (0.627, 0.754)	**0.679** (0.580, 0.726)
Readout Errors (cGy)	**No Binning**	**2**	**3**	**4**	**5**
Gradients Ignored	**5.9** (-10.8, 12.8)	**4.5** (-12.1, 10.4)	**4.8** (-12.0, 9.7)	**4.0** (-11.8, 10.5)	**3.9** (-11.6, 10.4)
Gradients Included	**9.3** (-18.0, 23.8)	**7.8** (-14.9, 22.1)	**8.4** (-14.8, 21.7)	**6.4** (-20.8, 21.5)	**5.9** (-18.6, 19.2)

Table 6.4: Normalized noise and readout error values for reconstructions of a PAGAT dosimeter that used varying levels of detector element binning. Boldfaced values are medians, and error ranges (shown in parentheses) indicate the first and third quartiles. *Noise values were normalized using the reconstruction that used no binning.

6.6 Pixel Binning

This section examines the effects that pixel binning in image space has on readout quality. The intent of this examination is along the same vein as the previous section. Current reconstructions have been produced using pixels 0.25×0.25 mm^2 in size, but these are to be compared against TPS dose images that typically use pixels $\geq$ 2×2 mm^2 in size. So, the question was posited: *"How much noise reduction can be realized by compromising resolution in image space?"*

For these tests, the same 720-projection sinogram that was used in Section 6.5 was used (without detector element binning) to produce one image that served as a starting point. From that image, 3 additional images were produced, providing 4 images with differing levels of pixel binning — no binning, and binning using 2×2, 4×4, and 8×8 binning windows. These correspond to pixel sizes of 0.25 mm, 0.5 mm, 1.0 mm, and 2.0 mm squared, respectively. Pixels were binned by taking the mean value of all pixels within the binning window. For comparison purposes, TPS-calculated dose distributions were similarly binned. Dose reconstructions and relative error images for the "no binning" case and the "8×8 binning window" case are shown in Figure 6.11. Plots of readout noise and readout errors for all 4 cases are provided in Figure 6.12. Noise trends and error trends shown in Figures 6.12e and 6.12f are summarized in Table 6.5. For normalized noise trends, noise values were normalized with respect to the case that used no binning.

Once again, the sacrifice of resolution comes with the benefit of noise reduction. As can be seen in Figure 6.12e, normalized noise values in the "8×8 binning window" case were reduced by 66% when dose gradients were ignored and by 37% when dose gradients were included. These levels of noise reduction are similar to the levels of noise reduction seen with detector element binning for a similar loss in resolution (i.e., 2 mm pixel size here, and 2 mm projected rayline width in Section 6.5). Also, as was the case with detector element binning,

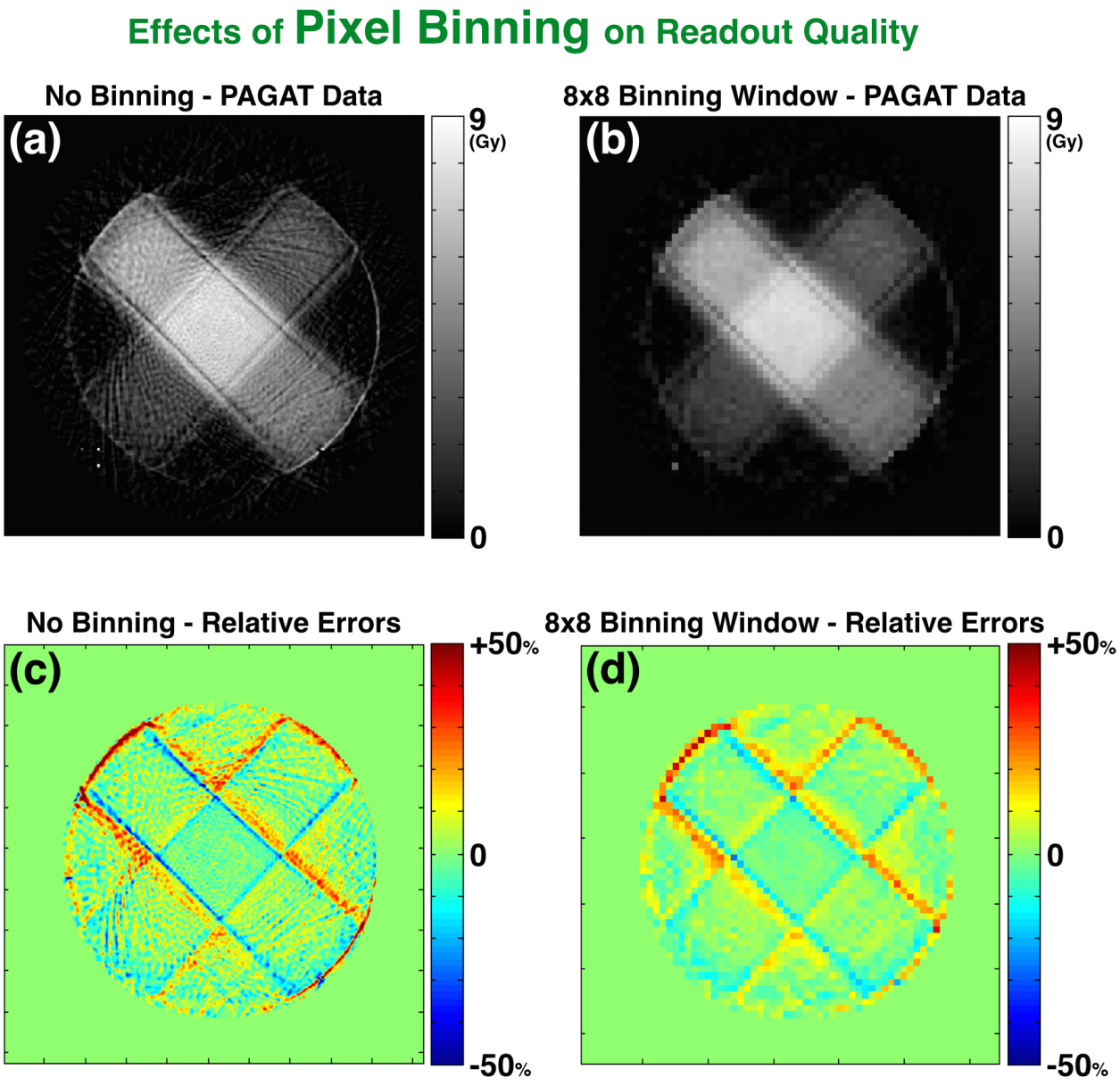

Figure 6.11: Starting with the same reconstruction produced by a 720-projection sinogram, pixels were binned into larger pixels using square binning windows. Reconstructed PAGAT dose distributions were calculated using (a) no binning and (b) an 8×8 binning window, and their corresponding readout error maps are shown in (c) and (d), respectively. For better visual comparison, relative errors in (c) and (d) are scaled relative to the irradiation pattern's maximum dose value.

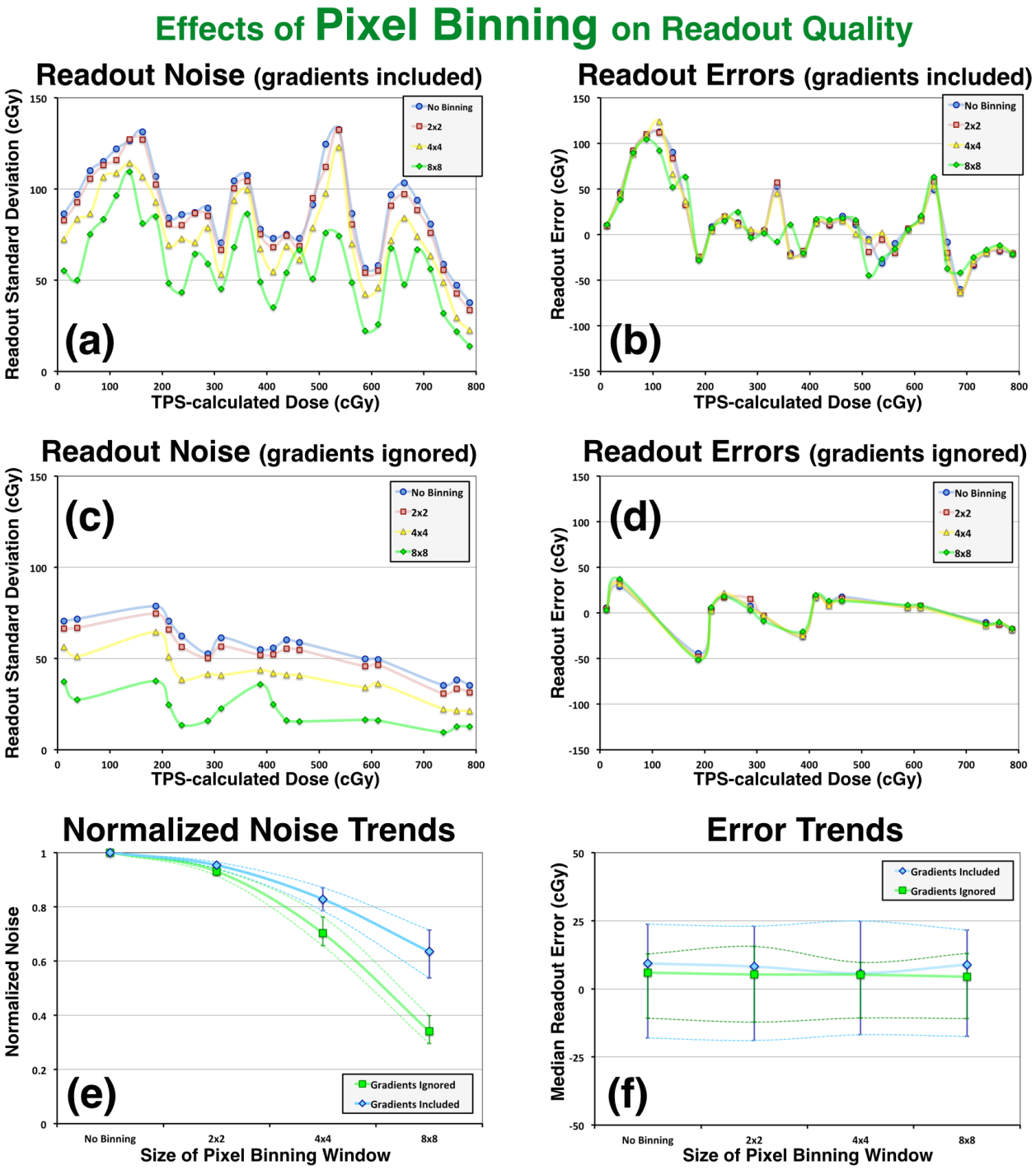

Figure 6.12: Starting with the same reconstruction produced by a 720-projection sinogram, pixels were binned into larger pixels using square binning windows. With a varying levels of pixel binning, plots are shown for: (a) readout noise and (b) readout errors with dose gradients included, (c) readout noise and (d) readout errors with dose gradients ignored, (e) normalized noise trends, and (f) error trends. Noise values were normalized using the reconstruction that used no binning.

pixel binning did not have a significant effect on readout errors. However, it is worth noting in the readout error plot in Figure 6.12b that an error of ∼50 cGy (near the 350 cGy point of the x-axis) is largely suppressed in the 8×8 binned cased. These types of suppression are likely representative of errors — discernible by using higher resolution — being smeared away when binning is implemented.

Based on these findings, one can appreciate that, in order to minimize readout noise, the width of detector elements projected at the axis of rotation and the size of image pixels should be no smaller than the TPS dose grid against which measurements will be compared. If one were to examine dose distributions with higher modulation, requiring higher resolution readout, one would need to use alternative methods of combatting image noise (e.g., increasing unique projection angles, increasing dosage).

	Pixel Binning Window Size			
Normalized Noise	**No Binning***	**2x2**	**4x4**	**8x8**
Gradients Ignored	**1**	**0.931** (0.915, 0.940)	**0.703** (0.657, 0.763)	**0.341** (0.295, 0.399)
Gradients Included	**1**	**0.954** (0.941, 0.965)	**0.828** (0.786, 0.871)	**0.635** (0.538, 0.715)
Readout Errors (cGy)	**No Binning**	**2x2**	**4x4**	**8x8**
Gradients Ignored	**5.9** (-10.8, 12.8)	**5.3** (-12.2, 15.6)	**5.2** (-10.7, 9.7)	**4.5** (-10.9, 13.0)
Gradients Included	**9.3** (-18.0, 23.8)	**8.2** (-19.0, 23.0)	**5.7** (-16.8, 24.9)	**8.9** (-17.5, 21.6)

Table 6.5: Normalized noise and readout error values for reconstructions of a PAGAT dosimeter that used varying levels of pixel binning. Boldfaced values are medians, and error ranges (shown in parentheses) indicate the first and third quartiles. *Noise values were normalized using the reconstruction that used no binning.

6.7 Best Practices

Results from Sections 6.1–6.6 answer a number of questions revolving around the "best practices" for PAGAT readout using the prototype fan-beam optical CT scanner. It is possible that many of these findings could be equally beneficial if they were to be applied with other scanner geometries and other dosimeter types. Findings from previous sections were able to inform protocol choices on six key points, which are summarized in Table 6.6.

Using these findings, an image was reconstructed using the "best protocol" achievable with the current system. The "full dose" cross irradiation pattern was scanned by sampling 2880 projection angles. Once transmission sinograms were calculated, artefact removal techniques (described in Section 5.2) were implemented to remove flask seam artefacts and ring artefacts. Then, projection angle binning (360 projection bins) and detector element binning (5 detector elements) were both implemented in sinogram space. Finally, an 8×8 pixel binning window was used to provide an opacity reconstruction that combines the best approaches of each section in this chapter. The resulting opacity image was self-calibrated using a quadratic calibration curve. The final dose image, readout error map, profile comparisons, and difference profiles are shown in Figure 6.13. Readout noise and readout errors (with and without dose gradients included) are shown in Figure 6.14. Across the entire TPS-calculated dose range, median (first quartile, third quartile) readout noise values were calculated: 6.8 cGy (5.5 cGy, 10.4 cGy) when dose gradients were ignored, and 31.5 cGy (26.4 cGy, 44.9 cGy) when dose gradients were included. Readout error values were 5.8 cGy (-11.5 cGy, 8.3 cGy) when dose gradients were ignored, and 6.1 cGy (-17.9 cGy, 18.0 cGy) when dose gradients were included.

Scan Parameter	Recommendations
Dose	A reduction in relative readout noise can be achieved by increasing the dose delivered to the dosimeter. Doubling dose (while avoiding saturation) will double the signal-to-noise ratio, but will have no effect on relative readout errors.
Light Profile Sampling	Only modest (if any) reductions in readout noise were obtained by acquiring and averaging multiple light profiles at each projection angle. Better use of scan time should instead be spent sampling a higher number of projection angles. No effect on readout accuracy.
Number of Projections	Substantial reductions in readout noise are achieved by increasing the number of unique projection angles sampled during a scan. Increasing projection numbers had no effect on readout accuracy.
Projection Angle Binning	The noise reduction benefit that is gained by sampling a higher number of projection angles is not lost when those projections are binned into a sinogram with fewer projections. To avoid noise related to too few projections, ensure that $n_{ProjBin} \geq 360$. No effect on readout accuracy.
Detector Element Binning	Substantial reductions in readout noise are seen by implementing detector element binning in sinogram space. To the level of binning implemented here, there have been no adverse effects on readout accuracy.
Pixel Binning	Similar to detector element binning, large reductions in readout noise are seen when pixel binning is implemented in image space. Both types of binning compromise resolution to attain reductions in noise. To the level of binning implemented here, there have been no adverse effects on readout accuracy.

Table 6.6: Summary of six key aspects of scanning protocol and their influence on readout quality.

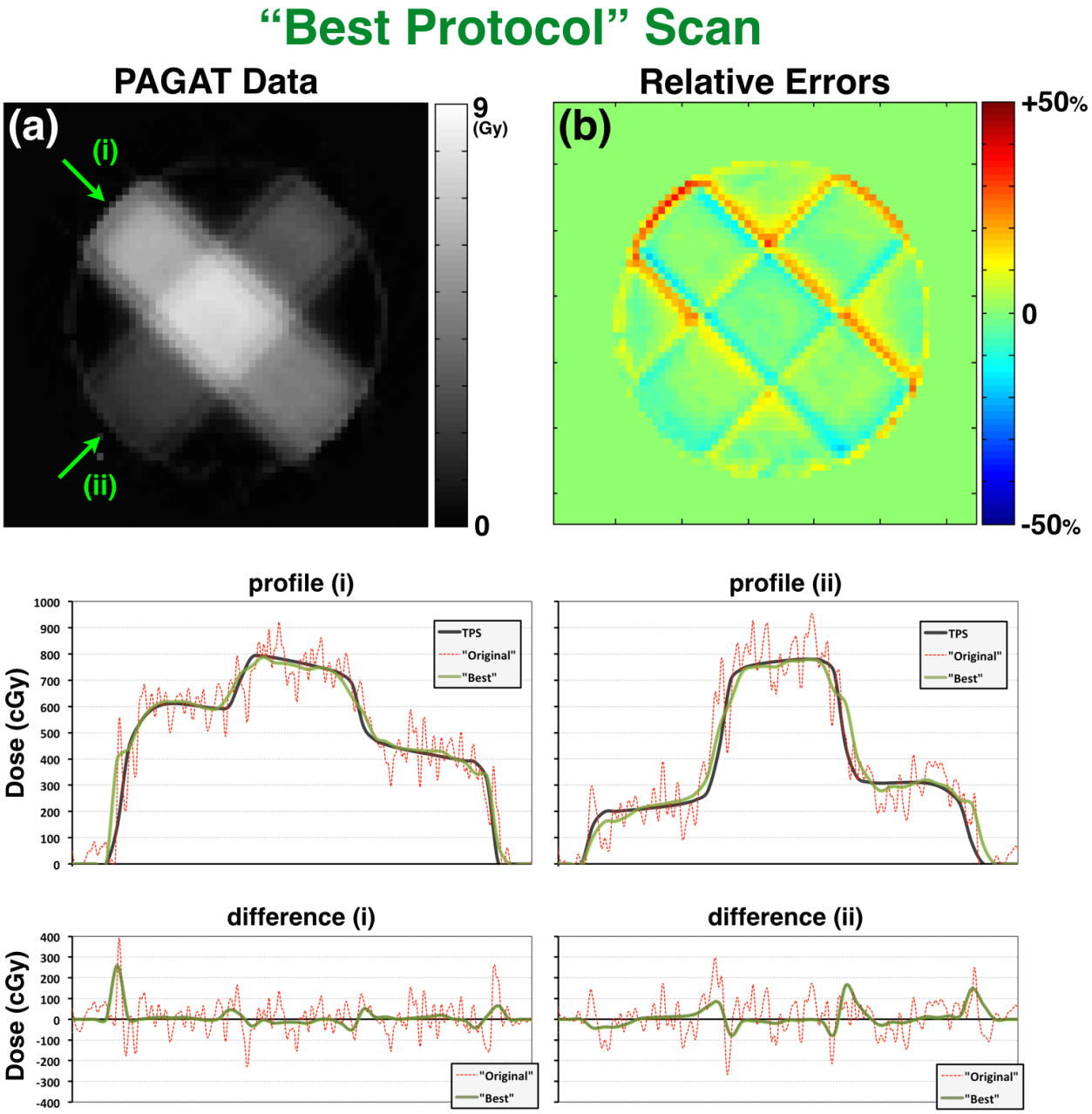

Figure 6.13: Using a "best protocol" scan as informed by results from this chapter, shown are: (a) PAGAT dose reconstruction, (b) relative error map, profile comparisons, and difference profiles. Profiles of the same irradiation pattern obtained using the "original" protocol (n_{sample}=1, n_{proj}=360, no artefact removal, no binning, linear calibration curve) are shown for comparison. Positions of profiles (i) and (ii) are indicated in (a).

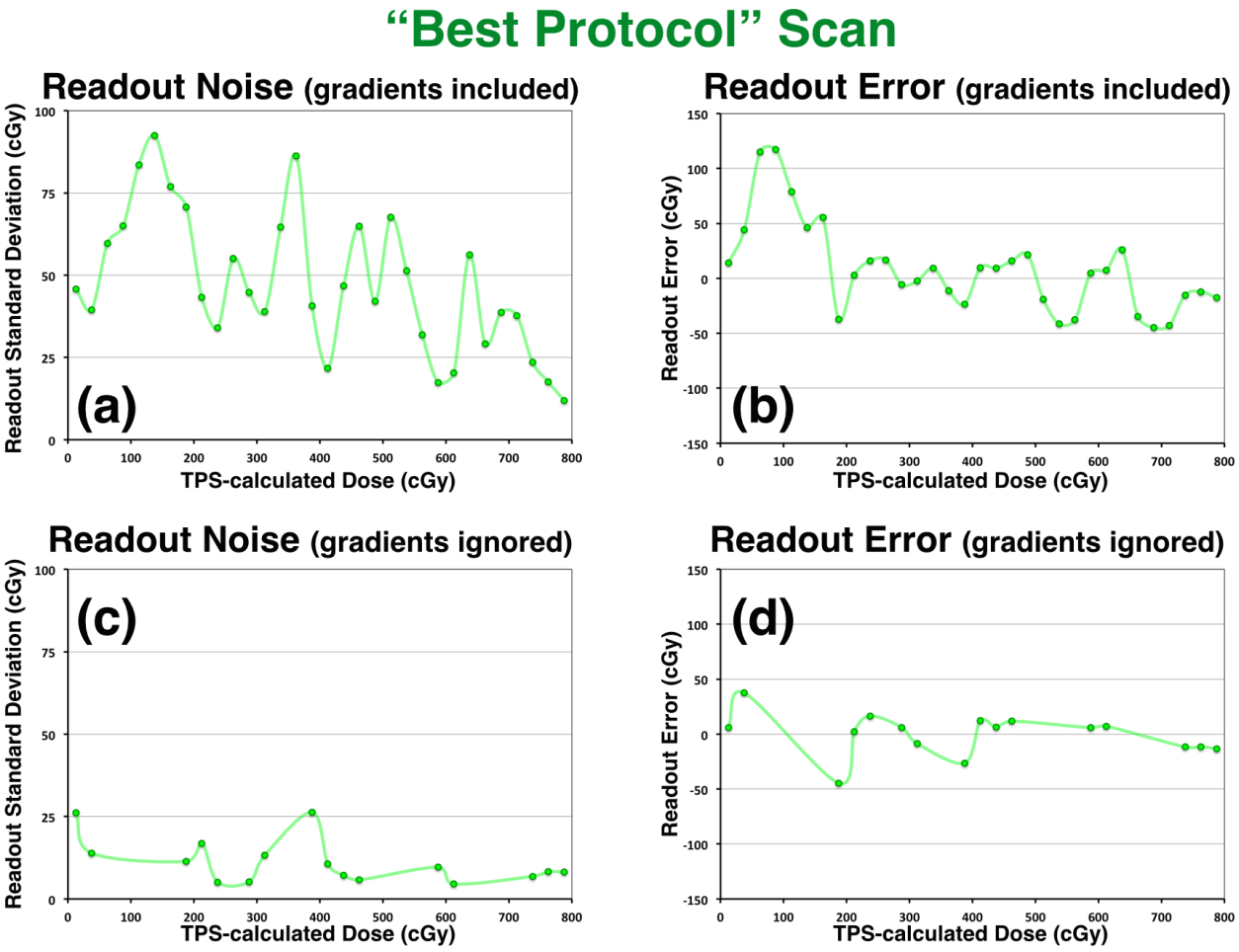

Figure 6.14: Using a "best protocol" scan as informed by results from this chapter, plots are shown for: (a) readout noise and (b) readout errors with dose gradients included, and (c) readout noise and (d) readout errors with dose gradients ignored.

6.8 Chapter Summary

An article reporting the findings from this chapter is currently being drafted. These results clarify the influence of a number of key scanning parameters for the prototype fan-beam optical CT scanner. The most significant quality benefits that were gained by improving scan protocols came in reductions of readout noise (precision). Adjustments to the scan parameters that were examined in this chapter had little effect on readout errors (accuracy). Readout errors continue to be evident in the "best protocol" image (see Figure 6.13). Despite using optimal scan parameters, the streaking artefacts that follow along the sides of each photon beam remain. These streaking artefacts are seen in the reconstructed image, in the readout error map, in profile comparisons, and in difference profiles. In regions just outside of each photon beam, we see overestimates of dose. In regions just within each photon beam, we see underestimates of dose.

Ultimately, it was hypothesized that these streaks were a refraction artefact caused by radiation-induced refractive index changes in polyacrylamide gels. This hypothesis is the main topic of investigation for Chapter 7.

Chapter 7

Results & Discussion III: Radiation-Induced Refraction Artefacts in the Optical CT Readout of PAGAT Dosimeters

The efforts described in Chapter 5 and Chapter 6 — intended to improve the scanning protocol and reduce readout noise and readout errors — ultimately revealed a new type of imaging artefact. When PAGAT dosimeters were treated with square, 3×3 cm^2 photon beams, distinct streaking errors appeared along the sides of irradiated regions in optical CT reconstructions. Just inside of irradiated regions, streaking errors showed underestimations of the expected dose value. Just outside of irradiated regions, streaking errors showed overestimations of the expected dose value. After scanning parameters were optimized, these streaks remain as a large source of readout error in optical CT reconstructions (see Figure 6.13). These types of imaging artefacts have not been reported on, thus far, in the field of

optical CT[1].

At first, it was thought that these streaks might be caused by an error in the alignment of the optical CT scanner's fan-beam, or by a mismatch in the refractive index value of the matching bath. However, repeated re-alignments of the scanner's fan-beam and repeated adjustments to the matching bath's formulation were unable to eliminate these artefacts. Eventually, it was posited that these artefacts might be caused by radiation-induced refractive index (RI) changes, which are known to occur in polyacrylamide gels.

In 1996, Maryañski *et al* examined the optical properties of polyacrylamide gels for the purposes of 3D gel dosimetry [62]. In addition to observing the increases in opacity that occurred upon irradiation, they also observed a slight increase in refractive index. Over a range from 0–14 Gy, refractive index increased by $\sim$0.6%. At the time, they predicted that such a small increase in RI would not be significant enough to cause distortion errors in optical CT readout of polymer gel dosimeters.

In the years since that initial work, investigators have widely ignored radiation-induced RI changes. In a review of the literature, only one work was found that attempted to investigate the effects radiation-induced RI changes. In 2004, Oldham & Kim sought to reveal any geometric distortion that might be caused by this increase in RI [91]. In their work, they inserted fully opaque needles into polyacrylamide gel dosimeters and measured the positions of these needles pre-irradiation and post-irradiation. They observed no difference between pre-irradiation and post-irradiation needle positions, concluding that geometric distortion was non-existent. They attributed streaking artefacts that appeared in their images to the fact that the needles they used for their experiment were non-transmitting and reflective. Nevertheless, that work was performed using an optical CT scanner with a different geometry than the one used in this work, and artefacts related to radiation-induced refractive index changes are likely dependent on scanner geometry.

[1]Nor the field of x-ray CT, for that matter.

This chapter reveals the impact that radiation-induced refractive index changes can have on the fan-beam optical CT readout of polyacrylamide gel dosimeters. It will be shown that refraction caused by radiation-induced RI changes only occurs when a dose gradient — therein, an RI gradient — occurs perpendicular to the trajectory of rays in the beam of the optical CT scanner. This is compatible with the results from Oldham & Kim, which showed no change on the pre-irradiation and post-irradiation positions of needles in a PAGAT dosimeter. Although some rays in certain light projections would be susceptible refraction errors, the ultimate positions of needles in image space would be largely unaffected by brief displacements in sinogram space due to refraction errors. Also, streaking caused by refraction artefacts and streaking caused by fully opaque needles would be difficult to distinguish from one another.

To start, Section 7.1 describes refraction behaviour that could hypothetically occur in a PAGAT dosimeter by briefly illustrating the differences between refraction at an abrupt RI transition and refraction at an RI gradient. Then, Section 7.2 presents the artefacts in question, including those believed to be caused by rayline errors that occur within the plane of the fan-beam and others believed to be caused by rayline errors that occur perpendicular to the plane of the fan-beam. Section 7.3 describes investigative scans that were performed in order to detect radiation-induced rayline errors. Section 7.4 shows the results of these investigative scans. Section 7.5 offers two attempts to use filtering to remove these artefacts in sinogram space and shows their effects in sinogram space. Section 7.6 presents filtering results in image space. Section 7.7 examines artefacts and rayline errors in three different dosimeter irradiations. Section 7.8 offers some discussion revolving around these artefacts and the challenges that need to be faced in addressing them. Finally, Section 7.9 summarizes this chapter's results.

7.1 GRIN Refraction

The work from Maryañski *et al* — which examined a BANG gel dosimeter — measured an increase in RI from n=1.355 to n=1.363 over a dose range from 0 Gy to 14 Gy [62]. According to Snell's Law, if one were to model an abrupt transition between these two values at, a 45° angle of incidence, a 44.7° angle of refraction would result. The resulting displacement error that would result in an optical CT scanner due to this abrupt transition would ultimately depend on the scanner's geometry. With the prototype examined in this work, assuming this transition occurred half way between the beam vertex and the detector array, the ultimate displacement error would be 0.68 mm. This is small when compared to the size of the scanner's detector elements (0.8×0.8 mm^2).

However, radiation-induced refractive index changes in a PAGAT dosimeter would not be able to produce an abrupt transition between two distinct RI values. Scattered dose from x-ray interactions will always ensure the presence of a dose gradient. Therefore, Snell's Law is less useful in this instance. To better understand refraction that occurs at an RI gradient, one should consider refraction as it is described by Huygens' principle — *each point of a propagating wavefront acts as a spherical source of secondary wavelets, and the resulting wavefront is an envelope of these wavelets.* For instance, consider Figure 7.1, which illustrates refraction using Huygens' principle. Here, changes in phase velocity are expressed by changes in wavelet radius. The simplest examples in Figures 7.1a and 7.1b demonstrate the commonly understood behaviour of refraction between two homogenous media; rayline bending only occurs when the angle of incidence is less than 90°.

Examples in Figures 7.1c and 7.1d demonstrate the type of refraction that occurs when a wave confronts an RI gradient. In Figure 7.1c, the direction of the wave goes unaltered because the gradient occurs parallel with the wave's trajectory. In this case, all portions of the wave experience a common decrease in phase velocity. However, in Figure 7.1d, the

RI gradient occurs perpendicular to the trajectory of the wave. Portions of the wave on the right side experience larger decreases in phase velocity than portions of the wave on the left side. As a result, the trajectory of the wave begins to bend toward the right. Thus, refraction due to an RI gradient is to be expected only when a component of the gradient runs perpendicular to the trajectory of the wave. When such a gradient is encountered, light will tend to bend toward the side of the gradient with a higher RI (i.e., toward regions of higher dose in the case of the PAGAT dosimeter). This type of light behaviour is known as GRIN optics (Gradient Refractive INdex optics, or GRadient INdex optics), and is used in the design of GRIN lenses [157].

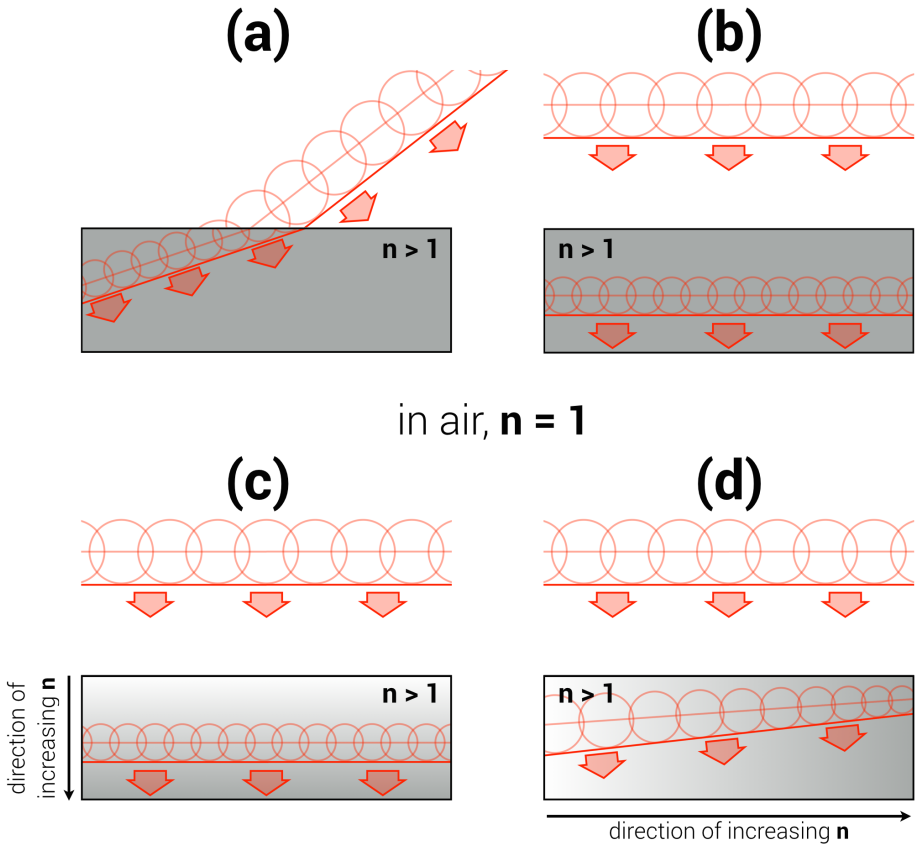

Figure 7.1: Refraction illustrated using Huygens' principle. Wavelets and wavefronts are shown encountering abrupt RI transitions in (a) and (b), and materials featuring RI gradients in (c) and (d). Changes in phase velocity are conveyed using changes in wavelet radius (i.e., smaller wavelets indicate a lower phase velocity).

7.2 Refraction Artefacts in Reconstructions

The PAGAT dosimeter that was irradiated with the "full cross" irradiation pattern was used for the main investigations in this chapter. Using a continuous rotation "scan, scan, scan, get" data acquisition, a sinogram of 1600 projections was collected. In order to solely examine the artefacts we believed to be caused by radiation-induced RI changes, artefact removal techniques (i.e., ring and flask seam) and data binning techniques (i.e., detector element and pixel) were not implemented in this chapter. Reconstructions shown in Figure

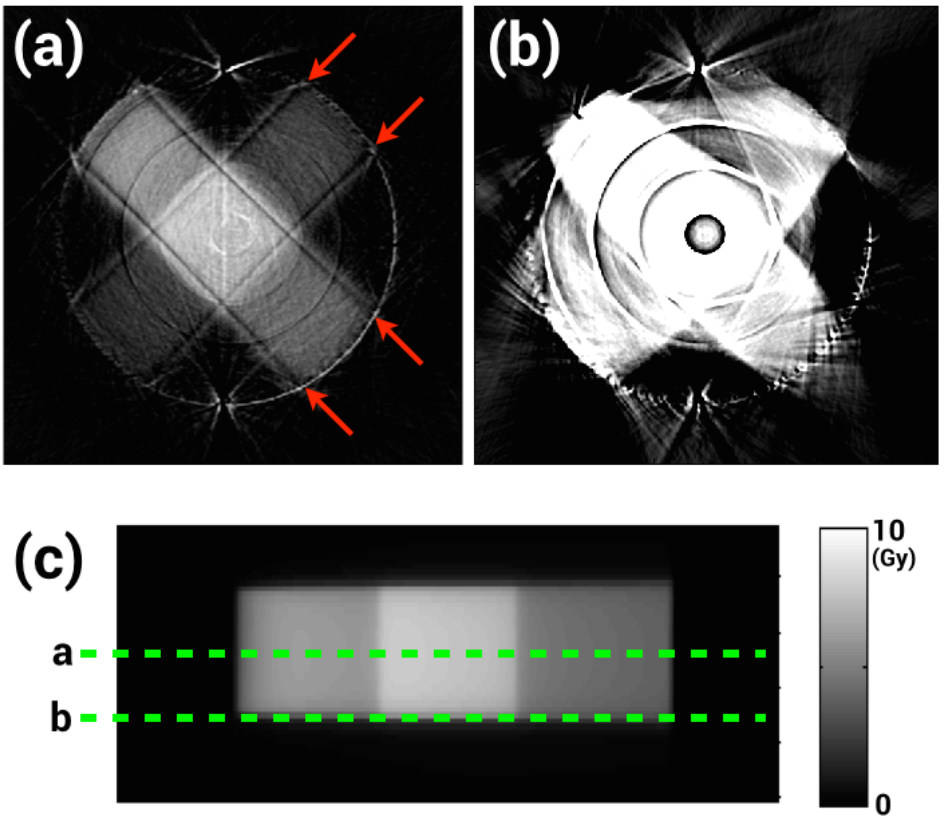

Figure 7.2: Examples of imaging artefacts believed to be caused by radiation-induced refraction errors. Streaks indicated by red arrows in (a) underestimate dose values and are believed to be caused by rayline errors that occur within the plane of the fan-beam. Widespread errors that overestimate dose values are shown in (b). In (c) the positions of slices sampled for (a) and (b) are shown overlaying a transverse image of the "full cross" irradiation pattern's TPS-calculated dose distribution.

7.2 illustrate two distinct symptoms that are believed to be caused by radiation-induced refractive index changes in polyacrylamide gels. In Figure 7.2a, bold streaking artefacts just inside of each beam in the irradiation pattern (as indicated by red arrows) underestimate the expected dose values at those points. Just outside of each beam in the irradiated region of Figure 7.2a, streaks overestimate expected dose values.

Due to the fact that these streaks occur parallel to steep dose gradients, it was postulated that the RI gradients introduced by each beam may be to blame for these artefacts. Yet, if RI gradients were to blame for these artefacts, one should expect to also see artefacts when the upper and lower edges of the irradiation pattern (with respect to the vertical position in the flask) are scanned.

Scanning the lower edge of the irradiation pattern, we see the errors in Figure 7.2b, which are more severe and more widespread. Figure 7.2c illustrates where the slices in 7.2a and 7.2b were acquired with respect to a transverse image of the irradiation pattern's TPS-calculated dose distribution. In the upper and lower edge of the irradiation pattern, dose gradients occur perpendicular to the plane of the fan-beam. Here, where dose should be tapering off ($\sim$50 cGy), dose measurements as high as 14.5 Gy are observed; this is almost double the maximum dose in the central region of the irradiation pattern (8 Gy). The perception of high dose values would be expected if rays were to be bent out of the detector plane. Light missing the detector array would correspond to overestimations of opacity.

7.3 Investigative Scanning

Our hypothesis assumes that the artefacts presented in Figure 7.2 are caused by rayline errors near steep dose gradients that bend towards high dose regions. Therefore, in order to evaluate this assumption, scans need to be able to demonstrate that this type of rayline bending occurs near these gradients. To that end, after post-irradiation transmission data

was acquired, two types of investigative scans were performed.

The first type of investigative scan used a line-pair pattern insert (see Figure 7.3a) to create a combed fan-beam. As was described previously, scanning with a combed fan-beam provides a ray-tracing sinogram of teeth and gaps. By monitoring the positions of these teeth and gaps, we can calculate a rayline error sinogram that illustrates rayline bending that occurs within the plane of the fan-beam. The second type of investigative scan imposed vertical shifts in the position of the dosimeter and the optical CT scanner's laser diode module (see Figure 7.3b–e). Two different scans were acquired — one where the dosimeter and the fan-beam were shifted upward 2 mm, the other where they were shifted downward 2 mm. Respectively, these scans were used to detect light that had bent downward and upward out of the plane of the fan-beam.

7.4 Rayline Errors in Sinogram Space

Results from investigative scans indicate that, as predicted, rayline errors are present in regions on transmission scans that correspond to the artefacts in question. These rayline errors demonstrate that light from the fan-beam bends towards high-dose regions when a steep dose gradient is encountered. This suggests that both types of artefacts shown in Figure 7.2 are due to rayline errors caused by radiation-induced RI changes in polyacrylamide gels. Figure 7.4 illustrates rayline bending within the plane of the fan-beam. Sinograms are shown for the central slice of the irradiation pattern (slice 'a' in Figure 7.2c), including transmission data, combed data, and absolute rayline error data. Zoomed insets are also included for a region of interest. As can be seen, refraction occurs near each of the four steep dose gradients in the central region of the irradiation pattern. These occurrences correspond to each portion of the sinogram where rays of the fan-beam confront a sustained RI gradient that is perpendicular to their trajectory, yet still within the fan-beam plane. In these instances,

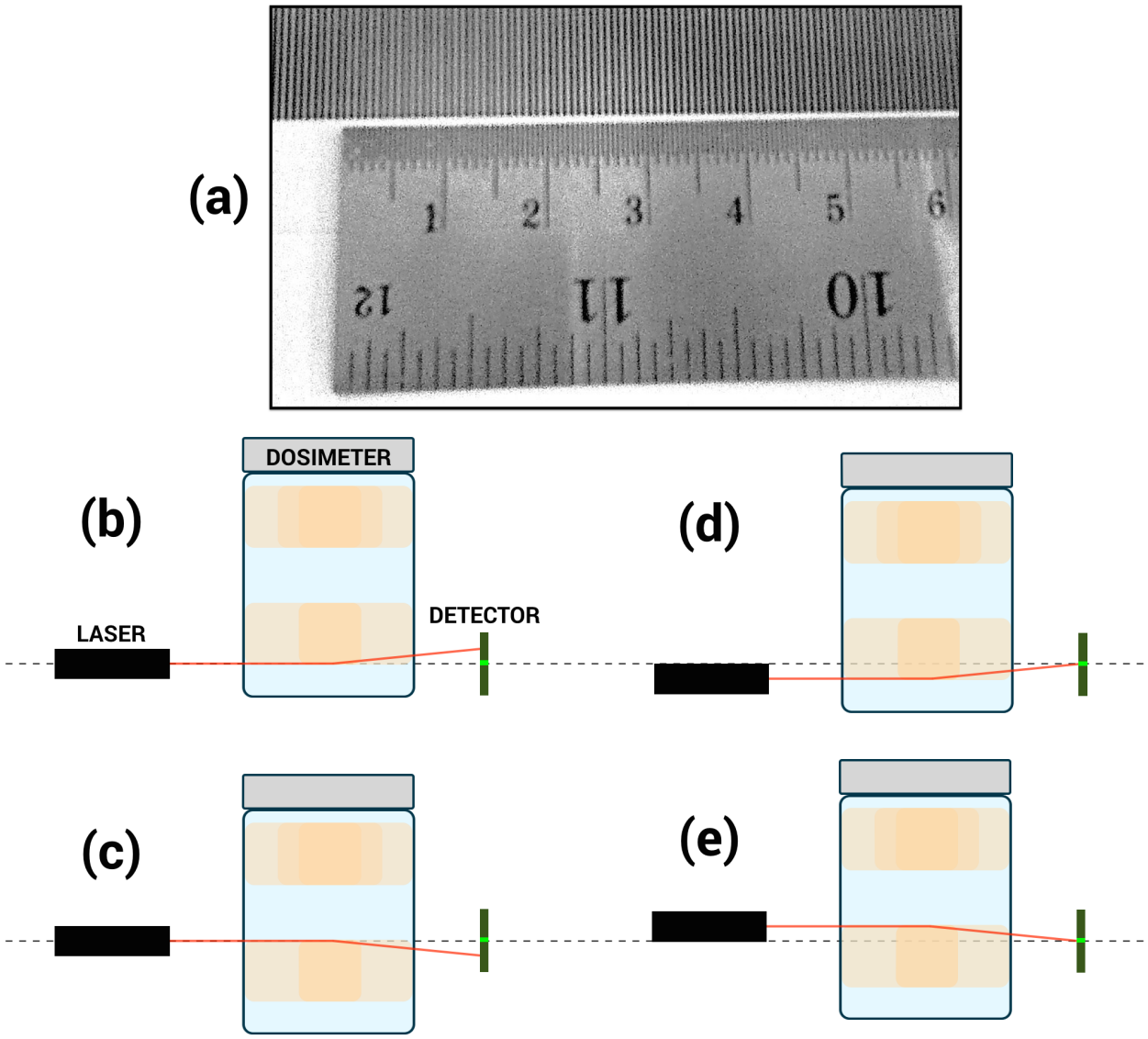

Figure 7.3: Investigative scans to evaluate in-plane rayline bending were performed using a combed fan-beam, produced by (a) a line-pair pattern printed on a sheet of transparency. Scans to evaluate out-of-plane rayline bending were performed by imposing vertical shifts to the laser diode module and the dosimeter. In (b) and (c), steep dose gradients that run perpendicular to the fan-beam would result in light bending out of the plane of the fan-beam. By shifting the laser and dosimeter in unison, as shown in (d) and (e), scans would be able to detect out-of-plane rayline errors

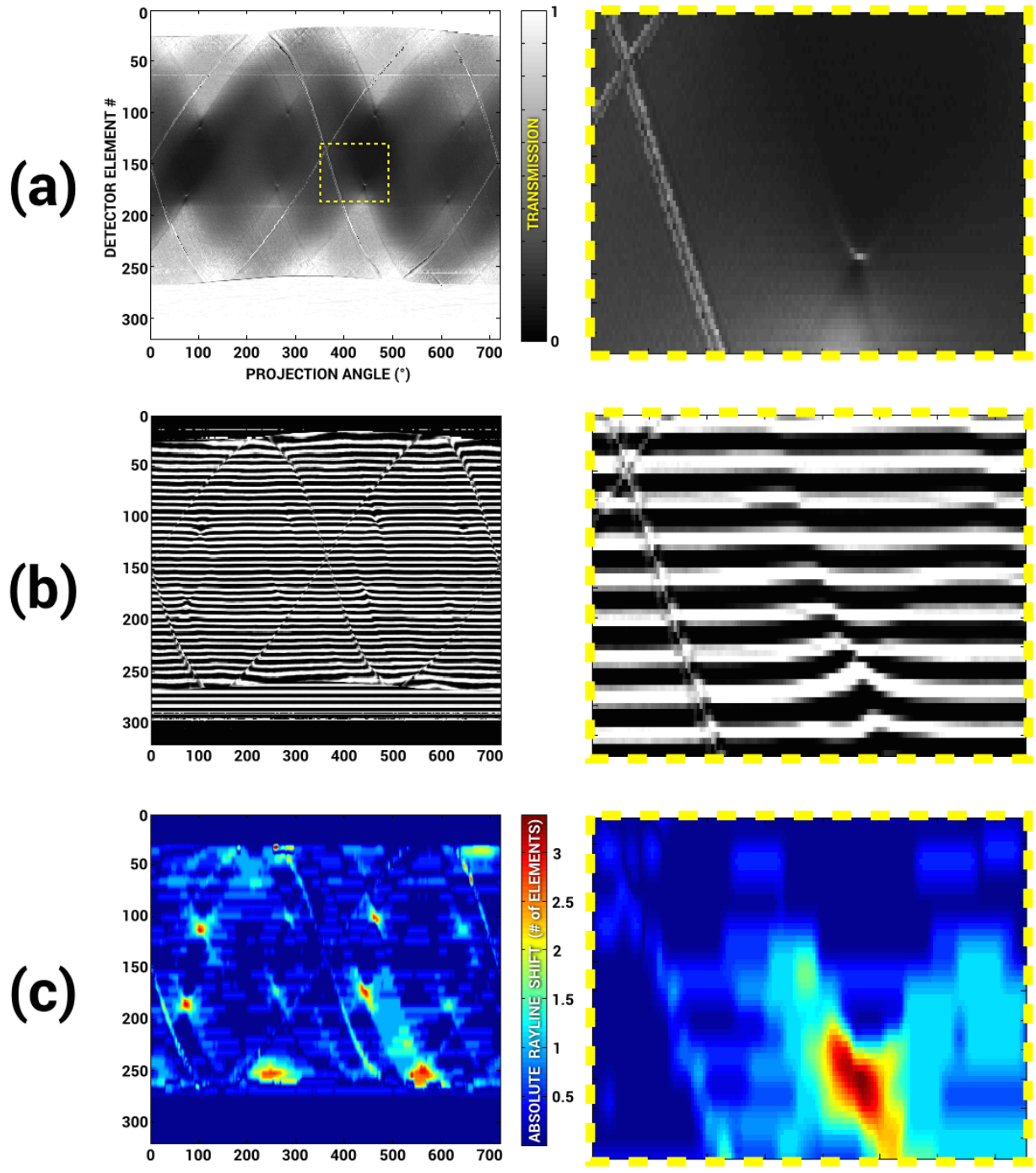

Figure 7.4: Rayline bending that occurs within the plane of the fan-beam are shown in (a) transmission, (b) combed light, and (c) absolute rayline error sinograms. Insets of a ROI are shown on the right for each data type. The position of this ROI is indicated by the dashed yellow box in (a).

rays are shown bending towards high-dose regions. As a result, higher intensity light rays from less opaque regions of the dosimeter are refracted into more opaque regions of the dosimeter. These cases of refraction contribute to overestimations of light, which equates to underestimations of opacity. Ultimately, this type of rayline error in sinogram space results in distinct streaking in image space that underestimates the actual opacity of the dosimeter. Additionally, when light refracts out of these less opaque regions, this leads to underestimation of light. This results in the overestimation of dose just outside of the treated region of the dosimeter that was seen in the previous chapter.

Examples of out-of-plane rayline bending are provided in Figure 7.5. In Figure 7.5a, 50 slices of transmission data are shown for a single projection angle. At the same projection angle, scans in Figure 7.5b and 7.5c show light data that was collected after the detector array was effectively shifted 2 mm downward and 2 mm upward, respectively. As can be seen in the transmission data, severe overestimations of opacity are observed on the upper and lower edges of the dose distribution. Data from the shifted scans supports the postulation that these overestimations in opacity are due to rays bending out of the detector plane. For overestimations that occur on the upper edge of the dose distribution, rays would bend downward, towards the higher dose region; this light is shown in Figure 7.5b in the downward-shifted scan. Overestimations on the lower edge of the dose distribution would similarly bend upward, which is shown in Figure 7.5c in the upward-shifted scan.

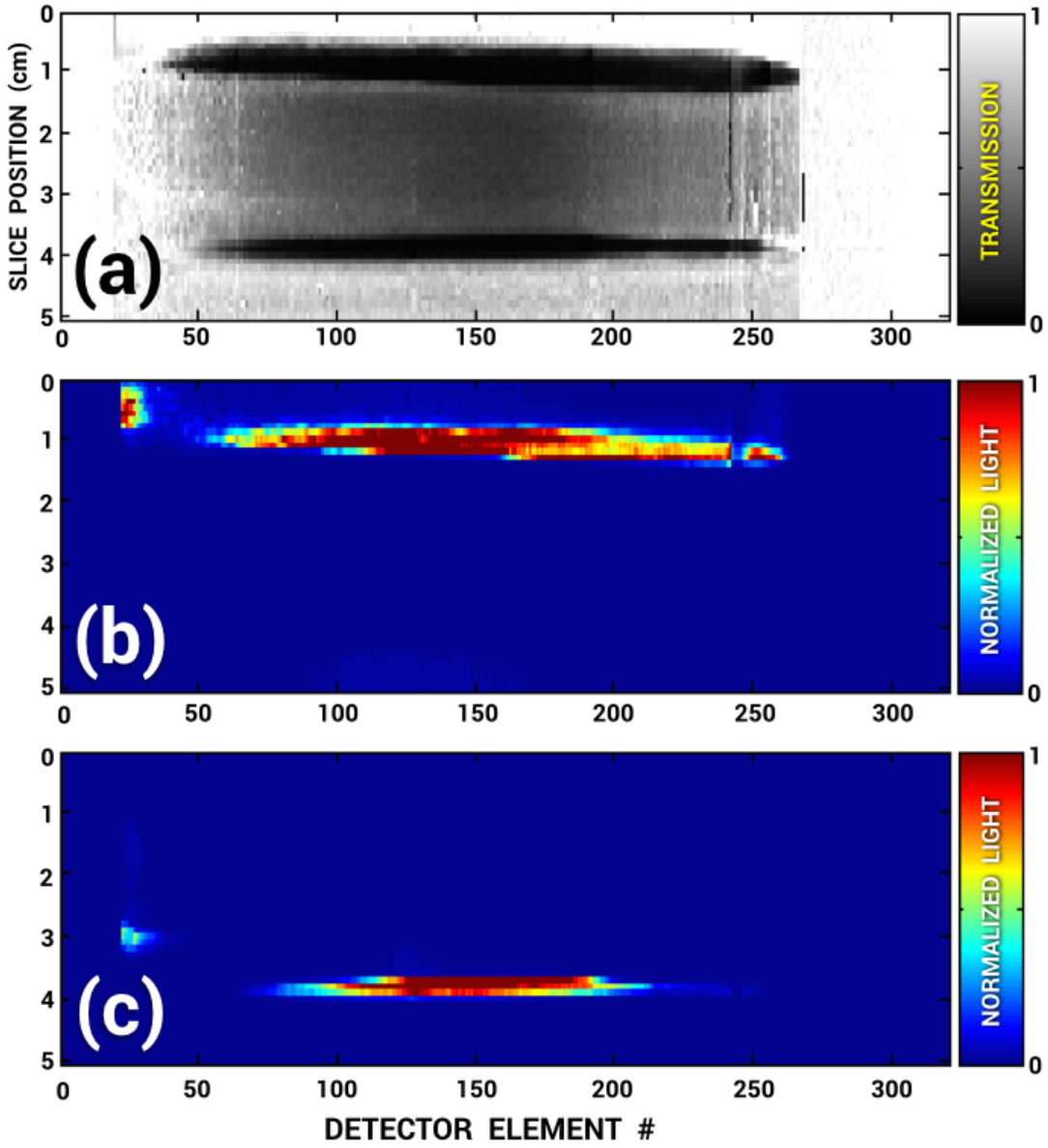

Figure 7.5: Rayline errors that cause light to bend out of the plane of the fan-beam are shown in projections of (a) normal transmission data, (b) light that has shifted downward, and (c) light that has shifted upward.

7.5 Sinogram Filtering

Various methods of addressing the artefacts in question were considered. For in-plane rayline errors, one possible technique involved "de-distorting" the sinogram that has been distorted by rayline errors. After all, *"if we can perform an investigative scan that indicates where light has bent out of place and by how much, might we be able to put light back into its place?"* Nevertheless, attempts to do so were unsuccessful. Streaks related to rayline errors were simply displaced by a distance of a few detector elements. It would appear that the current ray-tracing technique does not provide rayline error data at high enough spatial resolution (detector-wise) to allow for the precise re-distribution of light in sinogram space. This is most notably appreciated when one considers the ray-tracing inset in Figure 7.4b. There, a broad tooth of the combed fan-beam can be seen being "pinched" by the refraction events at the steep dose gradient. Additionally, light replacement was not a viable option for addressing out-of-plane rayline errors because scans using a single vertical shift of the fan-beam can only measure the intensity of light that has bent a certain distance out of the typical scan plane. A scan using a single vertical shift does not necessarily indicate the size of vertical displacement. It is possible that multiple scans that impose a range of vertical shift sizes could be used to indicate this displacement, but such techniques would be very time consuming.

Alternatively, a technique that first cut "bad" data points (those shown to be affected by rayline errors) from sinogram space and then interpolated new replacement values for those data points were considered. These techniques were previously demonstrated to mitigate ring artefacts and flask seam artefacts in Section 5.2. Unfortunately, the distribution of rayline error magnitudes throughout sinogram space made it difficult to distinguish "bad" data from "good" data by simply considering the sizes of rayline errors. Various rayline error threshold values were used in an attempt to isolate and remove data that caused

readout errors. But, before all readout errors could be highlighted by thresholding, excessive proportions of "good" data would also be selected. By closely inspecting Figures 7.4 and 7.5, one realizes that rayline errors do not always result in errors in transmission data.

Ultimately, a filtering routine was developed to filter transmission data in sinogram space. The method is similar to another filtering routine that Jirasek *et al* have used to remove structured noise from x-ray CT reconstructions of polymer gel dosimeters [72]. The filter developed here — the iterative Savitzky-Golay filter — smooths data along one dimension, and its implementation is described as follows: **(i)** each pixel in a 1D line of data is examined alongside a symmetrical range of pixels on either side, **(ii)** considering only pixels in this range, a polynomial fit of these points is used to calculate a temporary "filtered" value for the central pixel, **(iii)** the absolute relative difference of the filtered value and the original value (i.e., $|\text{"original"} - \text{"filtered"}|/\text{"filtered"}$) is calculated for the central pixel, **(iv)** the window of pixels examined is scanned across the dataset to calculate "filtered" values for all pixels, **(v)** once "filtered" values have been calculated for all pixels in the dataset, a top percentile of pixels with the largest relative differences between their filtered value and their original value are highlighted (e.g., the top 1%), **(vi)** highlighted pixels keep their "filtered" value and all other pixels revert to their "original" value, **(vii)** each subsequent iteration repeats steps i–vi using the updated dataset.

Essentially, the filter described above gradually replaces pixels that deviate the most from a polynomial fit, and all other pixels are left unchanged in each given iteration. The performance of the filter can be adjusted by modifying the degree of the polynomial, the number of pixels included in the symmetrical range (i.e., window size), the percentile of pixels whose original value is swapped for the filtered value in each iteration, and the total number of iterations. To speed up implementation of this routine, the Savitzky-Golay filter was used. The Savitzky-Golay filter is capable of speedily performing polynomial smoothing of a 1D dataset provided that the points in that dataset are spaced an equal distance apart

[158]. Hence, the name of the filter: iterative Savitzky-Golay (ISG).

For comparison, an adaptive mean (AM) filter was alternatively used to filter 2D transmission projections (MATLAB function *wiener2*, 5×5 window). Hilts *et al* previously used a 2D AM filter in image space to reduce noise in polymer gel dose distributions measured using x-ray CT [71]. The AM filter smooths data variably across the entire image using a 2D scanning filter window[2]. The strength of the filter adjusts throughout the image depending on a relative comparison of the overall variance of the entire image (σ_O^2) to the window's local variance (σ_L^2). Filter output for each pixel is calculated according to the following function:

$$f(x,y) = g(x,y) - \frac{\sigma_O^2}{\sigma_L^2}[g(x,y) - \mu_L] \tag{7.1}$$

where f(x,y) are filtered output pixel values, g(x,y) are unfiltered input pixel values, and μ_L is the window's local mean. For the present investigations, AM and ISG filters were implemented in sinogram space. It has previously been shown in x-ray CT that filtering in sinogram space prior to filtered backprojection can improve reconstruction quality [159, 160]. Hence, due to the accessibility of sinogram space data for the fan-beam optical CT scanner, sinogram space filtering was implemented rather than image space filtering[3].

The ISG filtering routine used for optical CT data filtered each 2D projection in the transmission sinogram individually. Each of the 720 projections in the sinogram were 50×320 (i.e, 50 slices high, 320 detector elements wide). For a given iteration of the ISG filter, each 2D projection was filtered one direction at a time (i.e., first horizontally to address in-plane rayline errors, then vertically to address out-of-plane rayline errors). Projections were one-padded on all sides by a distance equal to half the size of the Savitzky-Golay filter window along each axis. The routine was implemented using MATLAB as follows:

[2]A square or rectangular range of pixels.

[3]Sinogram space data for commercial x-ray CT scanners is not readily available to users.

1. **In-plane rayline errors**

   (a) Save a temporary version of the 2D projection, "TEMP"

   (b) Calculate a filtered version of the 2D projection, "FILT," by filtering each pixel horizontally (i.e., across the detector array) using a 1D Savitzky-Golay filter: *sgolayfilt*(data, degree, window)

   (c) Calculate a 2D absolute relative difference map, "DIFF" = *abs*[(TEMP - FILT)./FILT]

   (d) "CUT"% of pixels with the largest DIFF values have their TEMP values replaced by their FILT values

   (e) The updated version of TEMP carries forward

2. **Out-of-plane rayline errors**

   (a) Save a temporary version of TEMP

   (b) Calculate FILT again, this time filtering each pixel vertically (i.e., between slices for a given detector element)

   (c) Calculate DIFF again

   (d) CUT% of pixels with the largest DIFF values have their TEMP values replaced by their FILT values

   (e) The updated version of TEMP carries forward

3. **Repeat n times for each projection**

Again, the ISG routine specifically targets outlier data. The choice of *degree* and *window* values in the function *sgolayfilt* can be varied to adjust the aggressiveness of the smoothing filter. *CUT* and n values can be varied to fine-tune how gradually the routine is executed.

Results of the ISG filtering routine in sinogram space are shown in Figure 7.6. Out-of-plane rayline errors required more aggressive filtering than in-plane rayline errors. This is

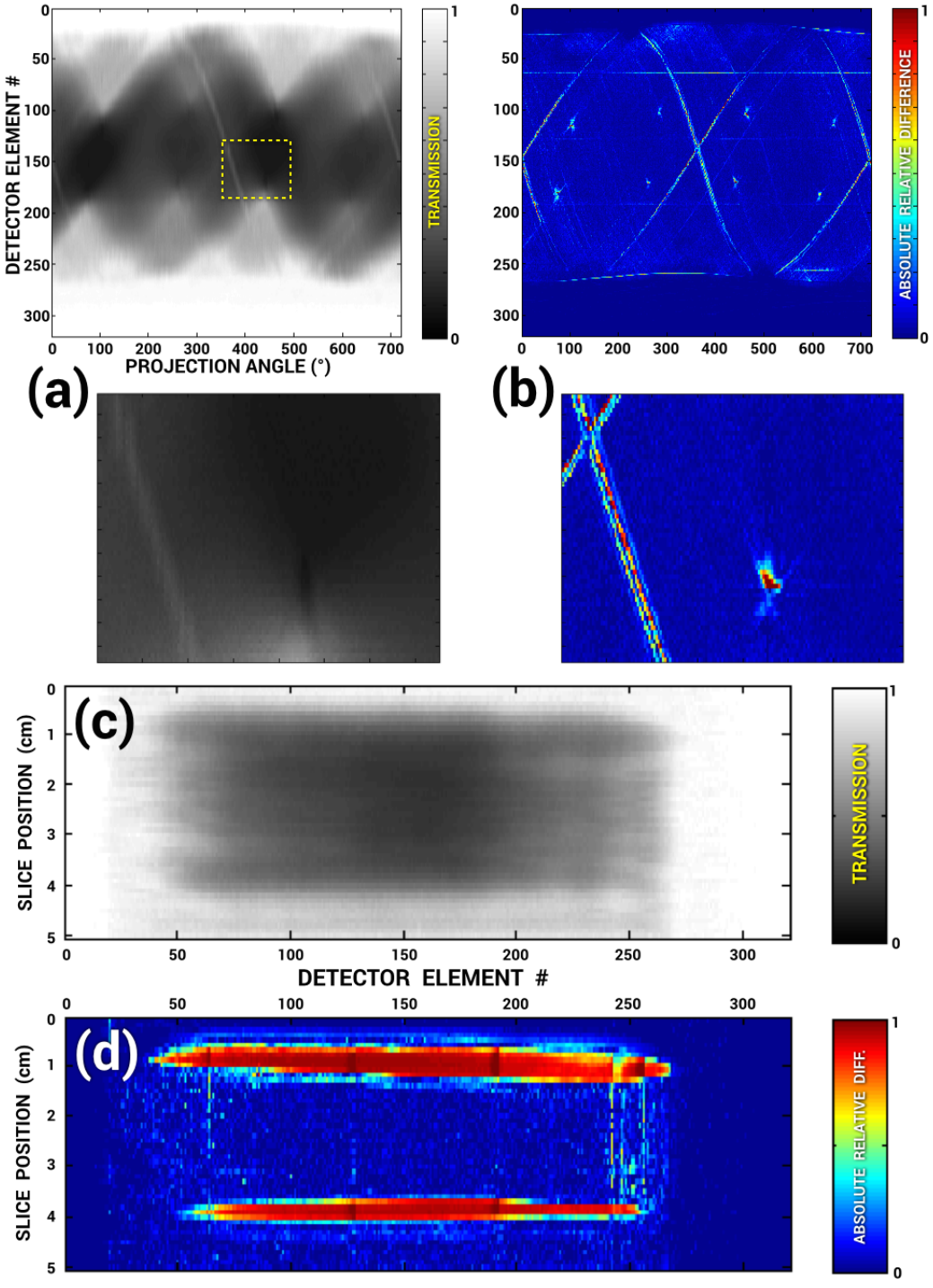

Figure 7.6: Sinogram space effects of the ISG filtering technique. For a mid-beam slice: (a) transmission data after ISG, and (b) absolute relative difference data (i.e. $|Raw - ISG|/ISG$); position of zoomed insets indicated by dashed box in (a). For a 2D projection of all 50 slices at a single projection angle: (c) transmission data after ISG, and (d) absolute relative difference.

reflected by the different values of degree and window that were used in the ISG filtering routine. For in-plane corrections, a degree value of 8 (i.e., smoothing with an 8^{th} degree polynomial) and a window value of 61 ($\approx 11^{\circ}$ of the fan-beam) were used. For out-of-plane corrections, a degree value of 1 (i.e., linear smoothing) and a window value of 5 (5 mm of the dosimeter perpendicular to the plane of the fan-beam) were used. For both types of corrections, a CUT value of 2.5% and an n value of 25 were used to filter 720 projections over a full rotation of the dosimeter. Using these values, the ISG routine took 25 minutes to process on a desktop personal computer (Intel® Core^{TM} 2 Duo, 3 GHz). For comparison, the adaptive-mean filter took less than 2 seconds to process the same amount of data. To decrease processing times, CUT and n values can be adjusted (increase CUT, decrease n). However, such adjustments will affect the aggressiveness of the filter.

7.6 Corrected Reconstructions

Optical CT reconstructions produced from unfiltered readout data ("Raw"), AM filtered data, and ISG filtered data were compared against TPS dose distributions. Image comparisons in three planes and profile comparisons along three lines are shown in Figure 7.7. Both the ISG filter and the AM filter were able to remove considerable amounts of noise seen in the unfiltered reconstruction. However, the AM filter was less capable than the ISG filter in mitigating the well-structured artefacts caused by radiation-induced RI changes. For example, in the case of in-plane rayline errors, the largest streaking artefact seen in the irradiated region (i.e., dose $>$ 7 Gy, see Figure 7.7b) had a magnitude of 49% in unfiltered data. This streak was suppressed to 14% by the AM filter, and to 6% by the ISG filter. Although errors related to out-of-plane rayline errors were much more severe and could not be fully removed from reconstructions, the ISG routine was able to considerably reduce these errors. In a low-dose region (i.e., dose $\sim$50 cGy, see Figure 7.7c), dose overestimations of 13 Gy,

10 Gy, and 3.1 Gy were seen for unfiltered, AM filtered, and ISG filtered data, respectively. Additionally, the ISG filter suppressed unrelated ring and streaking artefacts that previously required manual removal from sinogram space. On the other hand, the ISG filtering routine caused considerable amounts of blurring to the measured dose distribution, particularly in the direction perpendicular to the plane of the fan-beam.

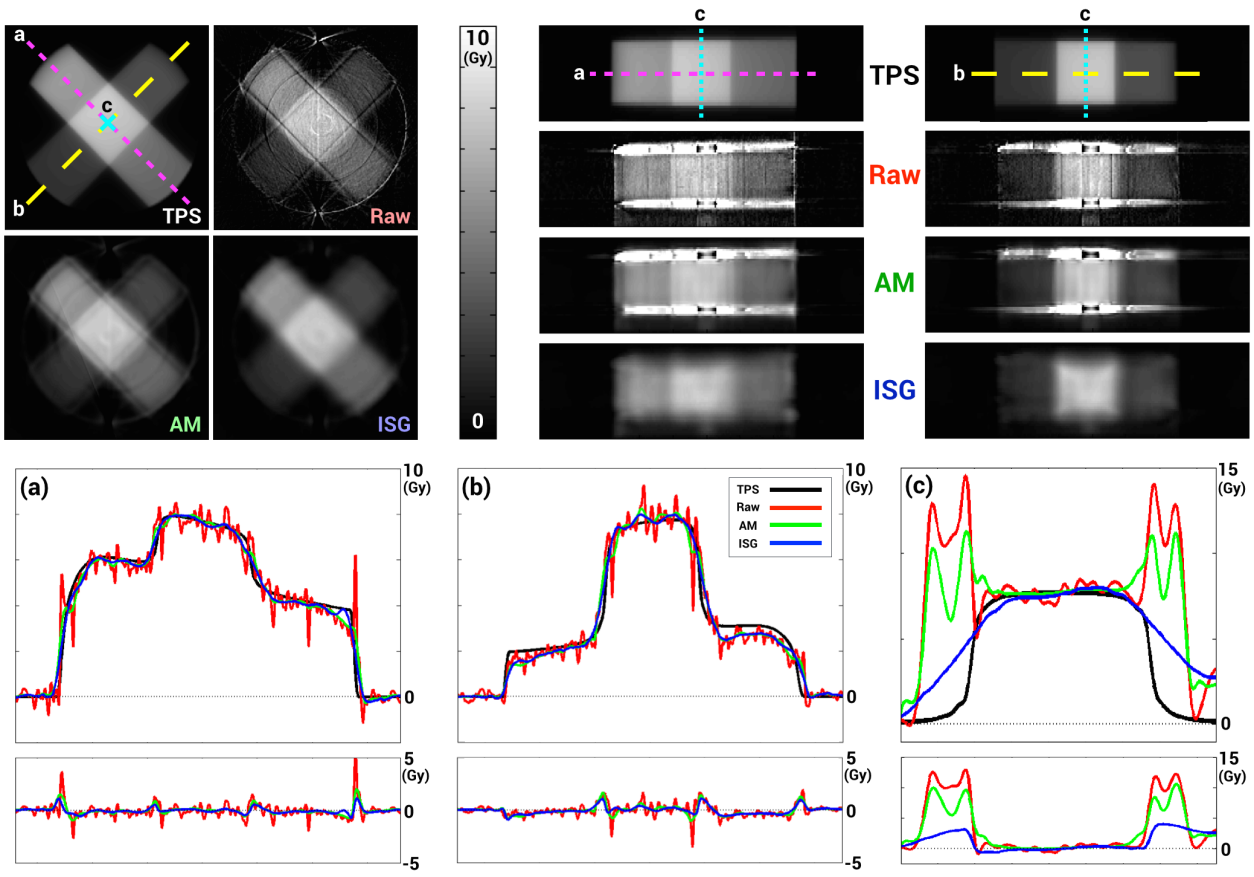

Figure 7.7: Image space results: treatment planning system (TPS), unfiltered (Raw), adaptive mean filtered (AM), and iterative Savitzky-Golay filtered (ISG). Dashed lines overlaying TPS data indicate the positions of the three planes shown, as well as the profile comparisons and difference profiles in (a), (b), and (c). The errors seen near the edge of the dosimeter (most notable in (a)) are not uncommon, caused by refraction that occurs at the wall of the flask housing the dosimeter. All images are equally windowed and levelled on a scale from 0–10 Gy.

7.7 Radiation-Induced Refraction Artefacts in Different Irradiation Patterns

In order to gain some sense of the consistency of these errors, one can consider the three different irradiation patterns that were examined in the previous chapter. Figure 7.8 shows reconstructions, rayline error sinograms, and images of back-projected rayline errors for the mid-beam regions of the calibration irradiation pattern and the two dosages of the cross irradiation pattern. It is worth noting that reconstructions show distinct streaks related to radiation-induced RI changes on each beam in all three irradiation patterns. This is somewhat perplexing. Beams delivering lower dosages to the dosimeter will introduce smaller dose gradients to the dosimeter. Therefore, one might have expected that a beam delivering less radiation would be less susceptible to refraction artefacts, and eventually a low enough dosage would avoid these artefacts altogether.

It is equally worth noting that, for beams delivering lower dosages, the size of rayline errors in sinogram space are smaller. Upon closer examination of all three reconstructions, one will notice that the pair of dark streaks that follow along the sides of each beam occur closer together for higher dosage beams. It would seem that the size of rayline errors has an influence on the positioning of these refraction artefacts but not necessarily their magnitude. Nevertheless, artefacts still appear for the lowest weighted beams of the half-dose cross and calibration irradiation patterns. For lower dosage beams, streak artefacts remain even though rayline errors and back-projected rayline errors are not significantly noticeable relative to rayline errors seen throughout the rest of the dosimeter. This could indicate that reducing the dose delivered to the dosimeter may not provide a simple method of avoiding these artefacts. Still, it is possible that a lower dose range may exist that could produce RI gradients small enough to avoid refraction artefacts.

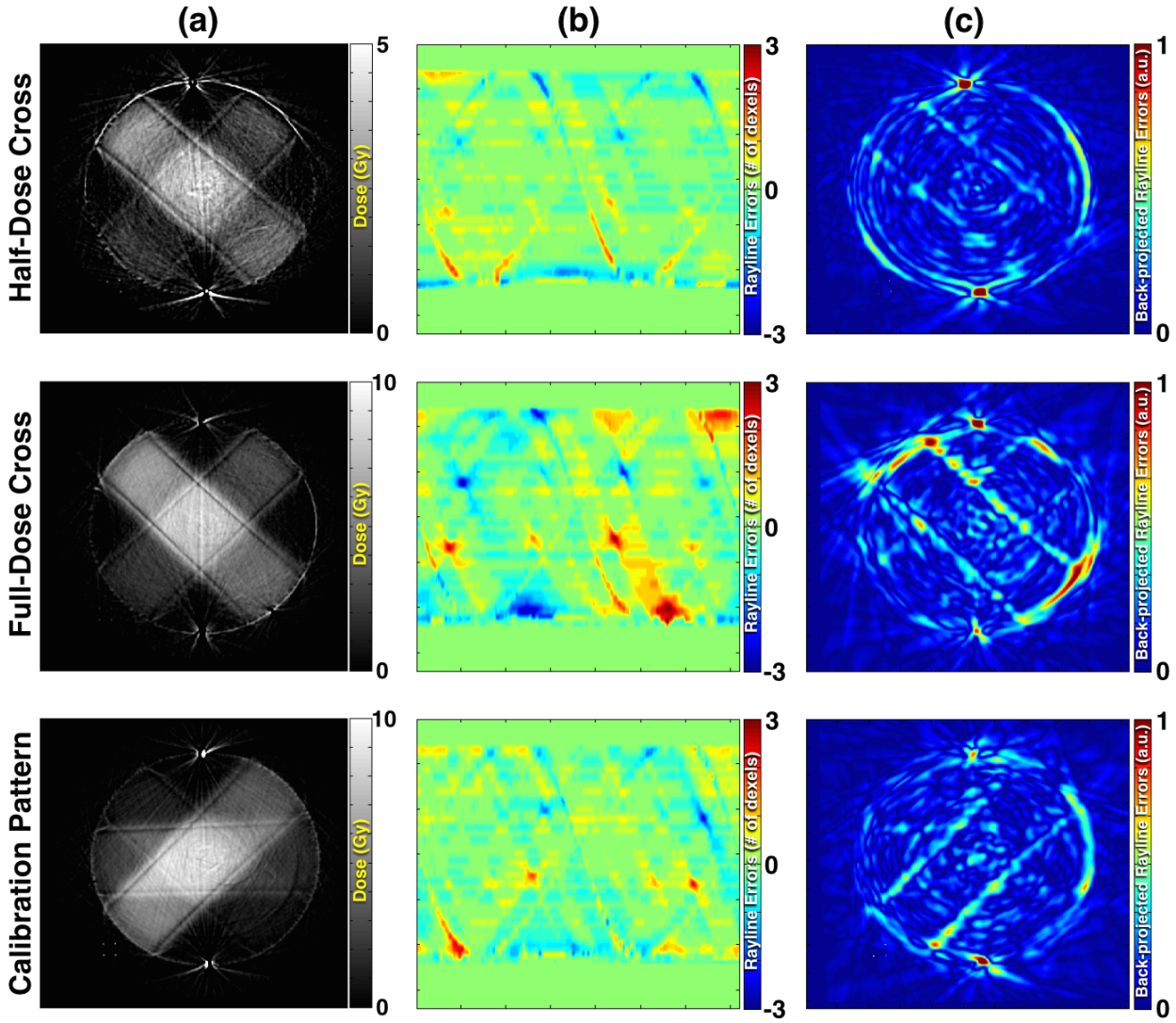

Figure 7.8: Radiation-induced refraction artefacts (a) in reconstructions, (b) in rayline error sinograms, and (c) images of back-projected rayline errors for the half-dose cross, full-dose cross, and calibration irradiation patterns. For better visualization and comparison, back-projected rayline errors for all three images in (c) were normalized to a common value.

7.8 Discussion

The results in this chapter present distinct indicators that a given dosimeter may be suffering from radiation-induced RI changes. Using these indicators, researchers can now recognize radiation-induced rayline errors, whether they be due to (i) issues in their scanner's geometry, or (ii) an unexpected RI-dose relationship in their dosimeter.

To the first point, one could argue that the intended resolution of our prototype scanner is more precise than necessary. For instance, the detector array would be less susceptible to out-of-plane rayline errors if it were thicker. Also, detector elements may be unnecessarily small (0.4 mm projected width at the axis of rotation) when one considers the dimensions of dose grids typically used in treatment planning software (1×1 mm^2 to 2.5×2.5 mm^2). The ability of a detector system to discern a rayline error is dependent on the size of its individual detector elements, with smaller elements capable of (i.e., more sensitive to) detecting smaller rayline errors. As such, larger detector elements might be less sensitive to radiation-induced refraction errors and other dosimeter inhomogeneities. The dimensions of our scanner could explain how radiation-induced refraction errors went unobserved for so long. If this were the case, one might ask: *why did detector element binning in the previous chapter not eliminate these artefacts?*. Unfortunately, due to the strict acceptance angles of our scanner's physical multi-hole collimator, simply re-binning data to simulate larger detector size would not produce the exact same result as having larger detector elements. Portions of the beam that bend and deviate from the acceptance angle of the collimator will be eliminated by the collimator's septa. At the moment, it is not clear whether the multi-hole collimator plays a beneficial or detrimental role with respect to radiation-induced refraction errors.

To the second point, it has not been established that radiation-induced RI changes are an issue unique to polyacrylamide gels. While the RI-dose relationship for polyacrylamide gel dosimeters was shown long ago, a variety of new optically scanned 3D dosimeters have been

introduced over the years without any report on how dose affects their RI[63, 64, 66, 110]. It is possible that the radiation-induced refraction artefacts seen in this work could occur with other types of 3D dosimeters.

It is worth noting that, although the irradiation pattern used here features high dose gradients that were useful in revealing radiation-induced refraction artefacts, the treatment plan was rather basic. Typical treatment plans are more elaborate, and the appeal of 3D dosimeters is driven by a desire to properly verify *complex*, next-generation radiation therapy treatments. Nevertheless, some treatment plans will feature high dose gradients, such as those where the planning target volume is closely situated to an organ at risk. It is currently unclear how frequently radiation-induced refraction artefacts would present themselves in typical treatment plans.

The aggressiveness of the ISG routine must also be considered. Although the ISG routine was able to reduce the magnitude of the artefacts in question, it could not fully eliminate them before introducing considerable amounts of blurring to the measured distribution, particularly in the direction perpendicular to the plane of the fan-beam. It should be noted that such losses in spatial resolution are directly related to filter parameter values — degree, window, CUT, and n. These parameters essentially put constraints on the level of modulation in the dose distribution that the ISG routine deems permissible. If the parameter values used for the dosimeter in this work were used for another dosimeter that did no exhibit these artefacts, filtering of this severity would in fact produce errors (i.e., smoothing of steep dose gradients). With such a dosimeter, one could select a less aggressive set of filter parameter values. In that case, the ISG routine could reduce structured noise without significantly impacting spatial resolution. Yet, in such a case, one might also expect better results from an adaptive-mean filter. Therefore, it should be noted that the ISG filtering routine is not the most elegant solution to radiation-induced refraction artefacts. Avoiding radiation-induced RI changes altogether would be more ideal.

There are a number of ways that radiation-induced RI changes might be reduced in polyacrylamide gel dosimeters. It would be worthwhile to examine the effects that different ingredients in the gel's recipe have on the RI-dose relationship. For instance, when they examined the chemical polymerization of acrylamide and the chemical polymerization of bisacrylamide, Maryañski *et al* showed that bisacrylamide exhibits a larger increase in RI than acrylamide [62]. It is possible that recipe modifications (e.g., lowering the amount of bisacrylamide in the recipe) could lessen RI changes. Additionally, one could consider greatly lowering the dose that the dosimeter received. Although the previous section showed that refraction artefacts remained present in all of the dosimeters irradiated in this work, it is possible that a treatment with low enough dosage would result in a low enough RI gradient to avoid these rayline errors. Unfortunately, this would come at a great cost to the signal-to-noise ratio. However, in the absence of radiation-induced refraction artefacts, a less aggressive ISG filter or an AM filter might perform well.

7.9 Chapter Summary

Preliminary investigations into the artefacts discussed in this chapter were presented in a talk at the International Conference on 3D Dosimetry in Sydney, Australia in November of 2012 [161]. More refined investigations were later presented at the Canadian Organization of Medical Physicist's Annual Scientific Meeting in Banff, Alberta in July of 2014. Findings were ultimately published as an article for Medical Physics — *"Radiation-induced refraction artifacts in the optical CT readout of polymer gel dosimeters"* [162].

Results from this chapter reveal a new category of imaging artefacts that can affect the optical CT readout of polyacrylamide gel dosimeters. Investigative scans support the hypothesis that radiation-induced RI changes cause significant rayline errors when rays confront a prolonged dose gradient that runs perpendicular to their trajectory. These errors manifested

themselves in two ways: (i) distinct streaking artefacts along beam edges caused by in-plane rayline bending, and (ii) severe overestimations of opacity caused by rays bending out of the fan-beam plane and missing the detector array. Optical CT reconstructions were provided to illustrate the signs of each type of rayline error. A filtering routine (ISG) was designed to address these errors and its results were shown. Although the ISG routine was able to suppress these artefacts better than an adaptive-mean filter, it significantly blurred the measured dose distribution, particularly in the direction perpendicular to the plane of the fan-beam. These findings provide useful insight for those intending to evaluate polyacrylamide gel dosimeters using optical CT. Additionally, these results provide recognizable signs to indicate that a given 3D dosimeter is exhibiting radiation-induced RI changes large enough to be of concern. At the moment, radiation-induced refraction artefacts are the largest challenge faced by the "PAGAT dosimeter/fan-beam optical CT" dosimetry system presented in this work.

Chapter 8

Thesis Summary

The work presented in this doctoral thesis examined the performance of a prototype fan-beam optical CT scanner for its intended purpose — the readout of polymer gel dosimeters. Below, conclusions are summarized and suggestions for future work are offered.

8.1 Conclusions

Modifications to two key components provided improvements to the optical CT scanner. A new fan-creation device (laser diode module) replaced the previous fan-creation components; in addition to exhibiting lower fluctuations in beam intensity, the laser diode module could be mounted onto a set of finely translating stages, allowing for investigative scans to be performed to evaluate out-of-plane rayline bending. A new matching tank was constructed that featured a cylindrical glass entry window and a lower bath volume. Although a pair of stress-related cracks occurred on the glass cylinder, these cracks were easily repaired and did not occlude the relevant portion of the entry wall (i.e., where the fan-beam enters the tank).

Artefact removal techniques were developed to address two imaging artefacts — flask seam artefacts and ring artefacts. These artefacts were removed by segmenting problematic

rays in sinogram space, and using interpolation with nearby rays to calculate replacement values for segmented rays. For reconstructions of an irradiated PAGAT dosimeter with a maximum dose of 8 Gy, ring artefacts and flask seam artefacts, respectively on the order of 1 Gy and 5 Gy, were removed.

A flask registration technique was developed to allow for the reproducible placement of flasks in the optical CT scanner. This registration technique exploited the noise caused by random flask imperfections in order to reproduce the flasks position. By acquiring a key light profile during the initial scan, subsequent placements compare the key light profile to a survey of light profiles in order to locate the original placement by minimizing the relative noise seen in key/survey transmission comparisons. The registration technique was shown to achieve sub-millimetre and sub-degree placement accuracy.

Once the flask registration technique was developed, pre-irradiation/post-irradiation scan comparisons of dosimeters were possible. As such, pre-irradiation and post-irradiation scans were acquired for a PAGAT dosimeter. Compared to a scan that used a blank region of the dosimeter as a reference, pre-irradiation/post-irradiation comparisons were shown to provide noticeable improvements in readout quality.

A modification was made to the PAGAT dosimeter fabrication/scanning routine. Rather than cooling dosimeters quickly in a refrigerated water bath and then scanning in the room temperature matching bath of the scanner, dosimeters were cooled slowly in a room temperature water bath and then scanned in the room temperature matching bath. This modification in the fabrication/scanning routine provided considerable improvements in readout quality. It is believed that this modification reduces RI inhomogeneities in the dosimeter, and also limits mid-scanning changes that may occur in the dosimeter while it warms unevenly to room temperature.

In an effort to improve scanning speed, a continuous rotation data acquisition technique was tested. Tests revealed that considerable errors arose due to slight deviations in data

acquisition timing. By acquiring timestamp data for each light profile, errors could effectively be eliminated. In comparison to a slower step+shoot data acquisition technique, the timing-corrected continuous rotation acquisition technique was able to provide better PAGAT readout in roughly half the time.

To examine dosimeter calibration, two PAGAT dosimeters were irradiated with a total of four irradiation patterns and scanned using the fan-beam optical CT scanner. Three types of polynomial calibration curves were evaluated: linear, quadratic, and cubic. Examination of residuals from these three curves revealed that a linear calibration curve insufficiently described the PAGAT dose-response; negligible differences between quadratic and cubic residuals were observed. Using quadratic calibration curves, calibration tests also examined self calibration, intra-gel calibration, and inter-gel calibration. Relative to the self calibrated case, statistically significant relative increases in residual errors arose when a separate dosimeter's calibration curve was used. However, there was no significant difference between the self calibrated and intra-gel calibrated cases.

Key parameters of the scanning protocol were evaluated for their effect on readout noise and readout errors. Increasing the dose delivered to a PAGAT dosimeter was shown to effectively double the signal-to-noise ratio in dose reconstructions. Acquiring and averaging additional light profiles at each projection angle was shown to provide only modest reductions in readout noise. More substantial reductions in readout noise were achieved by increasing the number of projection angles sampled during a scan. The reductions in noise achieved by sampling more projection angles was not lost when that data was encapsulated into sinograms with fewer projections, although streaking did arise when fewer than 360 projections were used. Detector element binning in sinogram space indicated that reductions in noise might be achieved if larger detector elements were used. Pixel binning in image space demonstrated that noise reduction can be achieved by reducing image resolution. All of these findings were combined to acquire a "best protocol" scan of a cross irradiation pattern:

pre-irradiation/post-irradiation scan comparisons, slow cooling during fabrication, 800 cGy maximum dose, projections = 2880, projection bins = 360, detector elements binned = 5, pixel size = 2×2 mm^2, self-calibrated, quadratic calibration curve. Respectively for low dose gradient regions and the overall distribution, median (1^{st} quartile, 3^{rd} quartile) readout noise values were 6.8 cGy (5.5 cGy, 10.4 cGy) and 31.5 cGy (26.4 cGy, 44.9 cGy), and readout error values were 5.8 cGy (-11.5 cGy, 8.3 cGy) and 6.1 cGy (-17.9 cGy, 18.0 cGy).

In all reconstructions of PAGAT dosimeters, distinctly recognizable streaking artefacts gradually became more apparent as readout noise was reduced. It was ultimately hypothesized that these streaking artefacts were caused by radiation-induced refractive index changes in the PAGAT dosimeter. If this were the case, dose gradients in the dosimeter would also represent RI gradients, which could cause refraction errors during optical CT scans. When confronting these dose gradients, visible light would tend to refract towards high dose regions.

Investigative scans were used to demonstrate that radiation-induced refraction errors were indeed causing the artefacts observed in PAGAT reconstructions. A line-pair pattern was inserted in the entry window of the optical CT scanner to create a combed fan-beam, which could reveal in-plane rayline bending in sinogram space. Also, using an uncombed fan-beam, vertical shifts to the laser diode module were used to examine out-of-plane rayline bending in sinogram space. Both types of investigative scans demonstrated that, near steep dose gradients, raylines bend towards high dose regions. The locations of these rayline bending events in sinogram space corresponded to the locations of artefacts in image space. These results — artefacts seen in PAGAT reconstructions and rayline errors seen in investigative scans — introduce a new type of imaging artefact that is unique to optical CT: radiation-induced refraction (RIR) artefacts.

A sinogram space filtering routine was developed in an attempt to remove RIR artefacts. The iterative Savitzky-Golay (ISG) filter was designed to gradually remove outlier pixels in 2D transmission projections. Results of the ISG routine were shown to specifically target

regions in sinogram space that corresponded to RIR artefacts. The ISG routine was also shown to significantly reduce RIR artefacts in image space. However, artefact reductions in image space were accompanied by significant blurring of dose distributions. ISG results were compared alongside an alternative, an adaptive mean filter, which was unable to reduce RIR artefacts.

RIR artefacts and in-plane rayline tracings were examined in three different PAGAT irradiations. These examinations revealed that rayline errors consistently occurred near steep dose gradients, and higher dose gradients resulted in larger rayline errors. However, the observance of smaller rayline errors in sinogram space did not correspond to a reduction of RIR artefacts in image space. Rather, variations in rayline error size merely corresponded to variations in the locations where RIR artefacts occurred with respect to the dose gradient. As such, reducing the dose delivered to the dosimeter, which would thereby reduce the size of radiation-induced RI changes, would likely not eliminate RIR artefacts. The issue of RIR artefacts remains the largest challenge currently faced by the "polymer gel dosimeters & fan-beam optical CT scanner" dosimetry system.

8.2 Future Work

If the fan-beam optical CT scanner is to be used for the readout of PAGAT dosimeters, the issue of RIR artefacts must be addressed. One way of alleviating these artefacts would be to reduce or eliminate the radiation-induced RI changes that occur in the gel. This would most likely be achieved by modifying the PAGAT recipe. It is possible that changes to the amount of each ingredient — gelatin, acrylamide, bisacrylamide, or THPC — would have an effect on radiation-induced RI changes. For instance, Maryañski *et al* showed that chemically polymerized bisacrylamide exhibited a larger increase in RI than acrylamide [62]. Could reducing the amount of bisacrylamide in the recipe alleviate RIR artefacts? Possibly.

Alterations to the PAGAT recipe are worth examining.

On the other hand, I can envision a scenario where the PAGAT dosimeter & fan-beam optical CT system moves forward in spite of the hindrance of RIR artefacts. Indeed, the removal of RIR artefacts using the ISG filtering technique was shown to greatly blur the measured dose distribution. However, the irradiation patterns used in this work were basic patterns specifically designed to observe a large range of dose in order to evaluate the fan-beam optical CT scanner's readout performance. Typical clinical treatments aim for uniform doses to a specific target volume. It is possible that RIR artefacts could manifest differently, or less severely, for more clinically-relevant dose distributions.

Furthermore, one should consider the types of investigations that could be performed using the current system. For example, I can imagine the system providing useful information for evaluating a 4D radiation treatment technique. If the question being asked is: *"Can we hit a moving target?"*, then one might not be as concerned with whether or not the ISG filtering routine blurs portions of the dose distribution. One might be more interested in observing the volumes that contain >50%, >80%, and >90% of the maximum dose, and how treatment of a moving target compares to a control (static target).

The work in this thesis has provided significant improvements to the fan-beam optical CT scanner and its ability to readout polymer gel dosimeters. Despite such improvements, the system is currently hindered somewhat by the issue of RIR artefacts. Nevertheless, while in the midst of pursuing advanced dosimetric tools, one must occasionally take a step back and ask: *"What can we **do** with what we have?"* In my opinion, a useful direction for future work would involve testing the system's performance for evaluating 4D RT treatments[1].

[1] Alongside continued development of the scanner and its intended dosimeters, of course.

Bibliography

[1] Statistics Canada. "Leading causes of death, by sex (both sexes)". *StatCan.gc.ca*, January 2014. [Online: `http://www.statcan.gc.ca/tables-tableaux/sum-som/l01/cst01/hlth36a-eng.htm`; posted 28-Jan-2014].

[2] Canadian Cancer Society's Advisory Committee on Cancer Statistics. *Canadian Cancer Society 2014 Statistics*. Canadian Cancer Society, Toronto, ON, Canada, 2014.

[3] A. L. Potosky, J. Legler, P. C. Albertsen, J. L. Stanford, F. D. Gilliland, A. S. Hamilton, J. W. Eley, R. A. Stephenson, and L. C. Harlan. Health outcomes after prostatectomy or radiotherapy for prostate cancer: results from the Prostate Cancer Outcomes Study. *Journal of the National Cancer Institute*, 92(19):1582–1592, October 2000.

[4] S. Mukherjee. *The Emperor of All Maladies: A Biography of Cancer*. Scribner, New York, NY, 2010.

[5] A. Stanton. Wilhelm Conrad Röntgen – On A New Kind of Rays: translation of a paper read before the Würzburg Physical and Medical Society, 1895. *Nature*, 53(1896):274–276, 1896.

[6] A. Clark. The Effect of the Roentgen Rays in a Case of Chronic Carcinoma of the Breast. *British Medical Journal*, 1(2110):1398–1399, June 1901.

[7] British Columbia Cancer Agency. "Radiation Therapy". *BCCancer.BC.ca*, Jan 2013. [Online: `http://www.bccancer.bc.ca/PPI/CancerTreatment/RadiationTherapy/default.htm`; posted Jan-2013].

[8] F. M. Khan. *The Physics of Radiation Therapy.* Lippincott Williams & Wilkins, Baltimore, MD, 3rd edition, 2003.

[9] F. M. Khan, J. Gibbons, D. Mihailidis, and H. Alkhatib. *Khan's Lectures: Handbook of the Physics of Radiation Therapy.* Lippincott Williams & Wilkins, Baltimore, MD, 2011.

[10] R. L. Warters and K. G. Hofer. Radionuclide toxicity in cultured mammalian cells. Elucidation of the primary site for radiation-induced division delay. *Radiation Research*, 69(2):348–358, February 1977.

[11] M. Joiner and A. van der Kogel. *Basic Clinical Radiobiology.* Hodder Arnold, London, England, 4th edition, 2009.

[12] L. Sundbom. Individually designed filters in cobalt 60 teletherapy. *Acta Radiologica: Therapy, Physics, Biology*, 2:189–208, June 1964.

[13] P. Källman, B. Lind, A. Eklöf, and A. Brahme. Shaping of arbitrary dose distributions by dynamic multileaf collimation. *Physics in Medicine and Biology*, 33(11):1291–1300, November 1988.

[14] B. S. Teh, S. Y. Woo, and E. B. Butler. Intensity modulated radiation therapy (IMRT): a new promising technology in radiation oncology. *The Oncologist*, 4(6):433–442, 1999.

[15] K. Otto. Volumetric modulated arc therapy: IMRT in a single gantry arc. *Medical Physics*, 35:310–317, 2008.

[16] A. Bel, M. Van Herk, H. Bartelink, and J. V. Lebesque. A verification procedure to improve patient set-up accuracy using portal images. *Radiotherapy and Oncology*, 29(2):253–260, 1993.

[17] M. Chan and Y. Song. A systematic approach to 4D radiation therapy–integration of 4D medical imaging into 4D radiation therapy. *Proceedings of the 51st Annual Meeting of the ISSS*, 51(2), 2007.

[18] F.H. Attix. *Introduction to Radiological Physics and Radiation Dosimetry*. John Wiley and Sons, New York, NY, 1986.

[19] R. P. Rao, M. de Murcia, and J. Gasiot. Optically stimulated luminescence dosimetry. *Radiation protection dosimetry*, 6(1-4):64–66, 1983.

[20] S. W. S. McKeever. Optically stimulated luminescence dosimetry. *Nuclear Instruments and Methods in Physics Research B*, 184:29–54, 2001.

[21] P. Scalchi and P. Francescon. Calibration of a mosfet detection system for 6-MV in vivo dosimetry. *International Journal of Radiation Oncology, Biology, Physics*, 40(4):987–993, March 1998.

[22] S. Ramkumar, C. M. Buttar, J. Conway, A. J. Whitehead, R. S. Sussman, G. Hill, and S. Walker. An assessment of radiotherapy dosimeters based on CVD grown diamond. *Nuclear Instruments and Methods in Physics Research A*, 460:401–411, 2001.

[23] M. Bucciolini, F. B. Buonamici, S. Mazzocchi, C. De Angelis, S. Onori, and G. A. P. Cirrone. Diamond detector versus silicon diode and ion chamber in photon beams of different energy and field size. *Medical Physics*, 30(8):2149–2154, August 2003.

[24] M. Rodriguez, S. Griffin, L. DeWerd, and R. Jeraj. Characterization of the ADII-33 diamond detector. *Medical Physics*, 34(1):215–220, 2007.

[25] W. L. McLaughlin, A. Miller, S. Fidan, K. Pejtersen, and W. Batsberg Pedersen. Radiochromic plastic films for accurate measurement of radiation absorbed dose and dose distributions. *Radiation Physics and Chemistry (1977)*, 10(2):119–127, 1977.

[26] Y. Zhu, A. S. Kirov, V. Mishra, A. S. Meigooni, and J. F. Williamson. Quantitative evaluation of radiochromic film response for two-dimensional dosimetry. *Medical Physics*, 24(2):223–231, February 1997.

[27] W. Ansbacher. Three-dimensional portal image-based dose reconstruction in a virtual phantom for rapid evaluation of IMRT plans. *Medical Physics*, 33(9):3369–3382, 2006.

[28] R. J. W. Louwe, L. N. McDermott, J. J. Sonke, R. Tielenburg, M. Wendling, M. B. van Herk, and B. J. Mijnheer. The long-term stability of amorphous silicon flat panel imaging devices for dosimetry purposes. *Medical Physics*, 31(11):2989–2995, 2004.

[29] B. M. C. McCurdy and P. B. Greer. Dosimetric properties of an amorphous-silicon EPID used in continuous acquisition mode for application to dynamic and arc IMRT. *Medical Physics*, 36(7):3028–3039, July 2009.

[30] J.T. Bushberg, J.A. Seibert, E.M. Leidholt, and J.M. Boone. *The Essential Physics of Medical Imaging*. Lippincott Williams & Wilkins, New York, NY, 2nd edition, 2002.

[31] W. van Elmpt, L. McDermott, S. Nijsten, M. Wendling, P. Lambin, and B. Mijnheer. A literature review of electronic portal imaging for radiotherapy dosimetry. *Radiotherapy and Oncology*, 88(3):289–309, September 2008.

[32] N. Suchowerska, P. Hoban, M. Butson, A. Davison, and P. Metcalfe. Directional dependence in film dosimetry: radiographic and radiochromic film. *Physics in Medicine and Biology*, 46(5):1391–1397, May 2001.

[33] V. Feygelman, G. Zhang, C. Stevens, and B. E. Nelms. Evaluation of a new VMAT QA device, or the "X" and "O" array geometries. *Journal of Applied Clinical Medical Physics*, 12(2):146–168, 2011.

[34] J. L. Bedford, Y. K. Lee, P. Wai, C. P. South, and A. P. Warrington. Evaluation of the Delta4 phantom for IMRT and VMAT verification. *Physics in Medicine and Biology*, 54(9):N167–76, May 2009.

[35] A. L. Petoukhova, J. van Egmond, M. G. C. Eenink, R. G. J. Wiggenraad, and J. P. C. van Santvoort. The ArcCHECK diode array for dosimetric verification of HybridArc. *Physics in Medicine and Biology*, 56(16):5411–5428, August 2011.

[36] B. E. Nelms, D. Opp, J. Robinson, T. K. Wolf, G. Zhang, E. Moros, and V. Feygelman. VMAT QA: measurement-guided 4D dose reconstruction on a patient. *Medical Physics*, 39(7):4228–4238, July 2012.

[37] M. Wendling, L. N. McDermott, A. Mans, J. J. Sonke, M. Van Herk, and B. J. Mijnheer. A simple backprojection algorithm for 3D in vivo EPID dosimetry of IMRT treatments. *Medical Physics*, 36(7):3310–3321, July 2009.

[38] A. Jemal, W. D. Travis, R. E. Tarone, L. Travis, and S. S. Devesa. Lung cancer rates convergence in young men and women in the United States: analysis by birth cohort and histologic type. *International Journal of Cancer*, 105:101–107, May 2003.

[39] R. Peto, S. Darby, H. Deo, P. Silcocks, E. Whitley, and R. Doll. Smoking, smoking cessation, and lung cancer in the UK since 1950: combination of national statistics with two case-control studies. *British Medical Journal*, 321:323–329, August 2000.

[40] R. Govindan, N. Page, D. Morgensztern, W. Read, R. Tierney, A. Vlahiotis, E. L. Spitznagel, and J. Piccirillo. Changing epidemiology of small-cell lung cancer in the

United States over the last 30 years: analysis of the surveillance, epidemiologic, and end results database. *Journal of Clinical Oncology*, 24(28):4539–4544, October 2006.

[41] Tami Freeman. "Safety in radiotherapy: help or hindrance?". *MedicalPhysicsWeb.org*, May 2014. [Online: `http://medicalphysicsweb.org/cws/article/opinion/57093`; posted 06-May-2014].

[42] D. N. Margalit, Y. Chen, P. J. Catalano, K. Heckman, T. Vivenzio, K. Nissen, L. D. Wolfsberger, R. A. Cormack, P. Mauch, and A. K. Ng. Technological advancements and error rates in radiation therapy delivery. *International Journal of Radiation Oncology, Biology, Physics*, 81(4):e673–e679, November 2011.

[43] J. Nénot. Radiation accidents over the last 60 years. *Journal of Radiological Protection*, 29:301–320, September 2009.

[44] Zosia Chustecka. "Docs in prison after radiation overdose in prostate cancer". *Medscape.com*, Feb 2013. [Online: `http://www.medscape.com/viewarticle/778862`; posted 06-Feb-2013].

[45] P. R. Almond, P. J. Biggs, B. M. Coursey, W. F. Hanson, M. S. Huq, R. Nath, and D. W. Rogers. AAPM's TG-51 protocol for clinical reference dosimetry of high-energy photon and electron beams. *Medical Physics*, 26(9):1847–1870, September 1999.

[46] H. Fricke and S. Morse. The chemical action of Roentgen rays on dilute ferrous sulphate solutions as a measure of radiation dose. *American Journal of Roentgenology, Radium Therapy and Nuclear Medicine*, 18:430–432, 1927.

[47] H. Fricke and E. R. Brownscombe. The Reduction of Chromate Solutions by x-Rays. *Journal of the American Chemical Society*, 55:2358–2363, June 1933.

[48] M. J. Day and G. Stein. Chemical effects of ionizing radiation in some gels. *Nature*, 166(4212):146–147, July 1950.

[49] P. Alexander, A. Charlesby, and M. Ross. The degradation of solid polymethylmethacrylate by ionizing radiation. *Proceedings of the Royal Society of London. Series A. Mathematical and Physical Sciences*, 223(1154):392–404, 1954.

[50] H. L. Andrews, R. E. Murphy, and E. J. LeBrun. Gel dosimeter for depth-dose measurements. *The Review of Scientific Instruments*, 28(5):329–332, 1957.

[51] F. E. Hoecker and I. W. Watkins. Radiation polymerization dosimetry. *The International Journal of Applied Radiation and Isotopes*, 3:31–35, 1958.

[52] A. L. Boni. A polyacrylamide gamma dosimeter. *Radiation Research*, 14:374–380, 1961.

[53] J. C. Gore, Y. S. Kang, and R. J. Schulz. Measurement of radiation dose distributions by nuclear magnetic resonance (NMR) imaging. *Physics in Medicine and Biology*, 29(10):1189–1197, October 1984.

[54] A. Appleby, E. A. Christman, and A. Leghrouz. Imaging of spatial radiation dose distribution in agarose gels using magnetic resonance. *Medical Physics*, 14(3):382–384, May 1987.

[55] L. E. Olsson, B. A. Westrin, A. Fransson, and B. Nordell. Diffusion of ferric ions in agarose dosimeter gels. *Physics in Medicine and Biology*, 37(12):2243–2252, 1992.

[56] M. J. Maryañski, J. C. Gore, R. P. Kennan, and R. J. Schulz. NMR relaxation enhancement in gels polymerized and cross-linked by ionizing radiation: a new approach to 3D dosimetry by MRI. *Magnetic Resonance Imaging*, 11(2):253–258, 1993.

[57] C. Baldock, Y. De Deene, S. Doran, G. Ibbott, A. Jirasek, M. Lepage, K. B. McAuley, M. Oldham, and L. J. Schreiner. Polymer gel dosimetry. *Physics in Medicine and Biology*, 55:R1–R63, February 2010.

[58] M. J. Maryañski, R. J. Schulz, G. S. Ibbott, J. C. Gatenby, J. Xie, D. Horton, and J. C. Gore. Magnetic resonance imaging of radiation dose distributions using a polymer-gel dosimeter. *Physics in Medicine and Biology*, 39:1437–1455, September 1994.

[59] J. Novotny Jr., V. Spevacek, P. Dvorak, J. Novotny, and T. Cechak. Energy and dose rate dependence of BANG-2 polymer-gel dosimeter. *Medical Physics*, 28(11):2379–2386, November 2001.

[60] Y. Xu, C. Wuu, and M. J. Maryañski. Sensitivity calibration procedures in optical-CT scanning of BANG®3 polymer gel dosimeters. *Medical Physics*, 37(2):861–868, 2010.

[61] J. C. Gore, M. Ranade, M. J. Maryañski, and R. J. Schulz. Radiation dose distributions in three dimensions from tomographic optical density scanning of polymer gels: I. Development of an optical scanner. *Physics in Medicine and Biology*, 41:2695–2704, December 1996.

[62] M. J. Maryañski, Y. Z. Zastavker, and J. C. Gore. Radiation dose distributions in three dimensions from tomographic optical density scanning of polymer gels: II. Optical properties of the BANG polymer gel. *Physics in Medicine and Biology*, 41:2705–2717, December 1996.

[63] R. G. Kelly, K. J. Jordan, and J. J. Battista. Optical CT reconstruction of 3D dose distributions using the ferrous-benzoic-xylenol (FBX) gel dosimeter. *Medical Physics*, 25(9):1741–1750, September 1998.

[64] J. Adamovics and M. J. Maryañski. A new approach to radiochromic three-dimensional dosimetry-polyurethane. *Journal of Physics: Conference Series*, 3:172–175, 2004.

[65] N. Krstajić, P. Wai, J. Adamovics, and S. Doran. Spectrophotometry of PRESAGE^{TM} polyurethane dosimeters. *Journal of Physics: Conference Series*, 3:244–247, 2004.

[66] K. Jordan and N. Avvakumov. Radiochromic leuco dye micelle hydrogels: I. Initial investigation. *Physics in Medicine and Biology*, 54:6773–6789, November 2009.

[67] S. Babic, J. Battista, and K. Jordan. Radiochromic leuco dye micelle hydrogels: II. Low diffusion rate leuco crystal violet gel. *Physics in Medicine and Biology*, 54:6791–6808, November 2009.

[68] A. T. Nasr, T. Olding, L. J. Schreiner, and K. B. McAuley. Evaluation of the potential for diacetylenes as reporter molecules in 3D micelle gel dosimetry. *Physics in Medicine and Biology*, 58:787–805, February 2013.

[69] M. Hilts, C. Audet, C. Duzenli, and A. Jirasek. Polymer gel dosimetry using x-ray computed tomography: a feasibility study. *Physics in Medicine and Biology*, 45:2559–2571, September 2000.

[70] C. Audet, M. Hilts, A. Jirasek, and C. Duzenli. CT gel dosimetry technique: comparison of a planned and measured 3D stereotactic dose volume. *Journal of Applied Clinical Medical Physics*, 3(2):110–118, 2002.

[71] M. Hilts and A. Jirasek. Adaptive mean filtering for noise reduction in CT polymer gel dosimetry. *Medical Physics*, 35(1):344–355, January 2007.

[72] A. Jirasek, J. Carrick, and M. Hilts. An x-ray CT polymer gel dosimetry prototype: I. Remnant artefact removal. *Physics in Medicine and Biology*, 57:3137–3153, May 2012.

[73] A. Jirasek, M. Hilts, and K. B. McAuley. Polymer gel dosimeters with enhanced sensitivity for use in x-ray CT polymer gel dosimetry. *Physics in Medicine and Biology*, 55:5269–5281, September 2010.

[74] J. N. M. Chain, A. Jirasek, L. J. Schreiner, and K. B. McAuley. Cosolvent-free polymer gel dosimeters with improved dose sensitivity and resolution for x-ray CT dose response. *Physics in Medicine and Biology*, 56:2091–2102, March 2011.

[75] C. Baldock, R. P. Burford, N. Billingham, G. S. Wagner, S. Patval, R. D. Badawi, and S. F. Keevil. Experimental procedure for the manufacture and calibration of polyacrylamide gel (PAG) for magnetic resonance imaging (MRI) radiation dosimetry. *Physics in Medicine and Biology*, 43:695–702, March 1998.

[76] Y. De Deene, C. De Wagter, B. Van Duyse, S. Derycke, W. De Neve, and E. Achten. Three-dimensional dosimetry using polymer gel and magnetic resonance imaging applied to the verification of conformal radiation therapy in head-and-neck cancer. *Radiotherapy and Oncology*, 48:283–291, September 1998.

[77] P. M. Fong, D. C. Keil, M. D. Does, and J. C. Gore. Polymer gels for magnetic resonance imaging of radiation dose distributions at normal room atmosphere. *Physics in Medicine and Biology*, 46:3105–3113, December 2001.

[78] Y. De Deene, C. Hurley, A. Venning, K. Vergote, M. Mather, B. J. Healy, and C. Baldock. A basic study of some normoxic polymer gel dosimeters. *Physics in Medicine and Biology*, 47:3441–3463, October 2002.

[79] M. L. Mather, A. K. Whittaker, and C. Baldock. Ultrasound evaluation of polymer gel dosimeters. *Physics in Medicine and Biology*, 47:1449–1458, May 2002.

[80] M. L. Mather and C. Baldock. Ultrasound tomography imaging of radiation dose distributions in polymer gel dosimeters: Preliminary study. *Medical Physics*, 30(8):2140–2148, 2003.

[81] S. Khoei, J. V. Trapp, and C. M. Langton. Ultrasound attenuation computed tomography assessment of PAGAT gel dose. *Physics in Medicine and Biology*, 59:N129–N137, August 2014.

[82] C. Westbrook, C. K. Roth, and J. Talbot. *MRI in Practice*. Wiley-Blackwell, Oxford, UK, 4th edition, 2011.

[83] J. Vandecasteele and Y. De Deene. On the validity of 3D polymer gel dosimetry: I. Reproducibility study. *Physics in Medicine and Biology*, 58:19–42, December 2012.

[84] J. Vandecasteele and Y. De Deene. On the validity of 3D polymer gel dosimetry: II. Physico-chemical effects. *Physics in Medicine and Biology*, 58:43–61, December 2012.

[85] J. Vandecasteele and Y. De Deene. On the validity of 3D polymer gel dosimetry: III. MRI-related error sources. *Physics in Medicine and Biology*, 58:63–85, December 2012.

[86] G. J. Salomons, Y. S. Park, K. B. McAuley, and L. J. Schreiner. Temperature increases associated with polymerization of irradiated PAG dosimeters. *Physics in Medicine and Biology*, 47:1435–1448, May 2002.

[87] J. Hsieh. *Computed Tomography: Principles, Design, Artifacts, and Recent Advances*. Wiley-Interscience, Bellingham, WA, 2nd edition, 2009.

[88] P. C. Parks. Johann Radon – On the determination of functions from their integral values along certain manifolds (Translated from original German text). *IEEE Transactions on Medical Imaging*, 5(4):170–176, December 1986.

[89] H. Johnston, M. Hilts, J. Carrick, and A. Jirasek. An x-ray CT polymer gel dosimetry prototype: II. Gel characterization and clinical application. *Physics in Medicine and Biology*, 57:3155–3175, May 2012.

[90] Y. De Deene, K. Vergote, C. Claeys, and C. De Wagter. The fundamental radiation properties of normoxic polymer gel dosimeters: a comparison between a methacrylic acid based gel and acrylamide based gels. *Physics in Medicine and Biology*, 51:653–673, February 2006.

[91] M. Oldham and L. Kim. Optical-CT gel-dosimetry II: Optical artifacts and geometrical distortion. *Medical Physics*, 31(5):1093–1104, May 2004.

[92] L. V. Wang and H-I. Wu. *Biomedical Optics: Principles and Imaging*. Wiley-Interscience, Hoboken, NJ, 2007.

[93] P. Guo, J. Adamovics, and M. Oldham. A practical three-dimensional dosimetry system for radiation therapy. *Medical Physics*, 33(10):3962–3972, 2006.

[94] J. Vandecasteele, S. Ghysel, S. H. Baete, and Y. De Deene. Radio-physical properties of micelle leucodye 3D integrating gel dosimeters. *Physics in Medicine and Biology*, 56:627–651, January 2011.

[95] J. Vandecasteele and Y. De Deene. Evaluation of radiochromic gel dosimetry and polymer gel dosimetry in a clinical dose verification. *Physics in Medicine and Biology*, 58:6241–6262, August 2013.

[96] S. Brown, A. Venning, Y. De Deene, P. Vial, L. Oliver, J. Adamovics, and C. Baldock. Radiological properties of the PRESAGE and PAGAT polymer dosimeters. *Applied Radiation and Isotopes*, 66:1970–1974, 2008.

[97] M. Oldham, I. Baustert, C. Lord, T. A. Smith, M. McJury, A. P. Warrington, M. O. Leach, and S. Webb. An investigation into the dosimetry of a nine-field tomotherapy irradiation using BANG-gel dosimetry. *Physics in Medicine and Biology*, 43:1113–1132, 1998.

[98] A. R. Farajollahi, D. E. Bonnett, A. J. Ratcliffe, R. J. Aukett, and J. A. Mills. An investigation into the use of polymer gel dosimetry in low dose rate brachytherapy. *The British Journal of Radiology*, 72(863):1085–1092, November 1999.

[99] V. P. Cosgrove, P. S. Murphy, M. McJury, E. J. Adams, A. P. Warrington, M. O. Leach, and S. Webb. The reproducibility of polyacrylamide gel dosimetry applied to stereotactic conformal radiotherapy. *Physics in Medicine and Biology*, 45:1195–1210, 2000.

[100] G. Grebe, M. Pfaender, M. Roll, and L. Luedemann. Dynamic arc radiosurgery and radiotherapy: commissioning and verification of dose distributions. *International Journal of Radiation Oncology, Biology, Physics*, 49(5):1451–1460, 2001.

[101] A. Jirasek and C. Duzenli. Relative effectiveness of polyacrylamide gel dosimeters applied to proton beams: Fourier transform Raman observations and track structure calculations. *Medical Physics*, 29(4):569–577, April 2002.

[102] S. Ceberg, I. Gagne, H. Gustafsson, J. B. Scherman, S. S. Korreman, F. Kjaer-Kristoffersen, M. Hilts, and S Å. J. Bäck. RapidArc treatment verification in 3D using polymer gel dosimetry and Monte Carlo simulation. *Physics in Medicine and Biology*, 55:4885–4898, August 2010.

[103] R. W. M. Underberg, F. J. Lagerwaard, B. J. Slotman, J. P. Cuijpers, and S. Senan. Use of maximum intensity projections (MIP) for target volume generation in 4DCT

scans for lung cancer. *International Journal of Radiation Oncology, Biology, Physics*, 63(1):253–260, 2005.

[104] J. D. Bradley, A. N. Nofal, I. M. El Naqa, W. Lu, J. Liu, J. Hubenschmidt, D. A. Low, R. E. Drzymala, and D. Khullar. Comparison of helical, maximum intensity projection (MIP), and averaged intensity (AI) 4D CT imaging for stereotactic body radiation therapy (SBRT) planning in lung cancer. *Radiotherapy and Oncology*, 81:264–268, 2006.

[105] S. St James, P. Mishra, F. Hacker, R. I. Berbeco, and J. H. Lewis. Quantifying ITV instabilities arising from 4DCT: a simulation study using patient data. *Physics in Medicine and Biology*, 57:L1–L7, February 2012.

[106] S. Ceberg, A. Karlsson, H. Gustavsson, L. Wittgren, and S. Å. J. Bäck. Verification of dynamic radiotherapy: the potential for 3D dosimetry under respiratory-like motion using polymer gel. *Physics in Medicine and Biology*, 53:N387–N396, September 2008.

[107] S. L. Brady, W. E. Brown, C. G. Clift, S. Yoo, and M. Oldham. Investigation into the feasibility of using PRESAGE^{TM}/optical-CT dosimetry for the verification of gating treatments. *Physics in Medicine and Biology*, 55:2187–2201, March 2010.

[108] C. J. Niu, W. D. Foltz, M. Velec, J. L. Moseley, A. Al-Mayah, and K. K. Brock. A novel technique to enable experimental validation of deformable dose accumulation. *Medical Physics*, 39(2):765–776, February 2012.

[109] U. J. Yeo, M. L. Taylor, L. Dunn, T. Kron, R. L. Smith, and R. D. Franich. A novel methodology for 3D deformable dosimetry. *Medical Physics*, 39(4):2203–2213, April 2012.

[110] T. Juang, S. Das, J. Adamovics, R. Benning, and M. Oldham. On the need for

comprehensive validation of deformable image registration, investigated with a novel 3-dimensional deformable dosimeter. *International Journal of Radiation Oncology, Biology, Physics*, 87(2):414–421, 2013.

[111] Y. De Deene, K. Vergote, C. Claeys, and C. De Wagter. Three dimensional radiation dosimetry in lung-equivalent regions by use of a radiation sensitive gel foam: Proof of principle. *Medical Physics*, 33(7):2586–2597, July 2006.

[112] P. Haraldsson, A. Karlsson, E. Wieslander, H. Gustavsson, and S. Å. J. Bäck. Dose response evaluation of a low-density normoxic polymer gel dosimeter using MRI. *Physics in Medicine and Biology*, 51:919–928, February 2006.

[113] L. W. Goldman. Principles of CT and CT technology. *Journal of Nuclear Medicine Technology*, 35(3):115–128, September 2007.

[114] W. J. H. Veldkamp, R. M. S. Joemai, A. J. van der Molen, and J. Geleijns. Development and validation of segmentation and interpolation techniques in sinograms for metal artifact suppression in CT. *Medical Physics*, 37(2):620, February 2010.

[115] W. G. Campbell, D. A. Rudko, N. A. Braam, D. M. Wells, and A. Jirasek. A prototype fan-beam optical CT scanner for 3D dosimetry. *Medical Physics*, 40(6):061712, June 2013.

[116] S. J. Doran and D. N. B. Yatigammana. Eliminating the need for refractive index matching in optical CT scanners for radiotherapy dosimetry: I. Concept and simulations. *Physics in Medicine and Biology*, 57:665–683, January 2012.

[117] D. Ramm, T. P. Rutten, J. Shepherd, and E. Bezak. Optical CT scanner for in-air readout of gels for external radiation beam 3D dosimetry. *Physics in Medicine and Biology*, 57:3853–3868, May 2012.

[118] L. Rankine and M. Oldham. On the feasibility of optical-CT imaging in media of different refractive index. *Medical Physics*, 40(5):051701, May 2013.

[119] S. G. Bosi, S. Brown, S. Sarabipour, Y. De Deene, and C. Baldock. Modelling optical scattering artefacts for varying pathlength in a gel dosimeter phantom. *Physics in Medicine and Biology*, 54:275–283, December 2008.

[120] T. Olding, O. Holmes, and L. J. Schreiner. Cone beam optical computed tomography for gel dosimetry I: scanner characterization. *Physics in Medicine and Biology*, 55:2819–2840, April 2010.

[121] G. N. Hounsfield. Computerized transverse axial scanning (tomography): Part I. Description of system. *The British Journal of Radiology*, 46:1016–1022, 1973.

[122] Y. Xu, C. S. Wuu, and M. J. Maryañski. Performance of a commercial optical CT scanner and polymer gel dosimeters for 3-D dose verification. *Medical Physics*, 31(11):3024–3033, November 2004.

[123] M. Oldham, J. H. Siewerdsen, A. Shetty, and D. A. Jaffray. High resolution gel-dosimetry by optical-CT and MR scanning. *Medical Physics*, 28(7):1436–1445, July 2001.

[124] O. Lopatiuk-Tirpak, K. M. Langen, S. L. Meeks, P. A. Kupelian, O. A. Zeidan, and M. J. Maryañski. Performance evaluation of an improved optical computed tomography polymer gel dosimeter system for 3D dose verification of static and dynamic phantom deliveries. *Medical Physics*, 35(9):3847–3859, September 2008.

[125] H. S. Sakhalkar and M. Oldham. Fast, high-resolution 3D dosimetry utilizing a novel optical-CT scanner incorporating tertiary telecentric collimation. *Medical Physics*, 35(1):101–111, January 2008.

[126] X. Qian, J. Adamovics, and C. Wuu. Performance of an improved first generation optical CT scanner for 3D dosimetry. *Physics in Medicine and Biology*, 58:N321–N331, November 2013.

[127] J. G. Wolodzko, C. Marsden, and A. Appleby. CCD imaging for optical tomography of gel radiation dosimeters. *Medical Physics*, 26(11):2508–2513, November 1999.

[128] S. Bosi, P. Naseri, A. Puran, J. Davies, and C. Baldock. Initial investigation of a novel light-scattering gel phantom for evaluation of optical CT scanners for radiotherapy gel dosimetry. *Physics in Medicine and Biology*, 52:2893–2903, May 2007.

[129] S. Al-Nowais and S. J. Doran. CCD-based optical CT scanning of highly attenuating phantoms. *Journal of Physics: Conference Series*, 164:012023, 2009.

[130] P. DeJean, R. Senden, K. McAuley, M. Rogers, and L. J. Schreiner. Initial experience with a commercial cone beam optical CT unit for polymer gel dosimetry I: Optical dosimetry issues. *Journal of Physics: Conference Series*, 56:179–182, 2006.

[131] S. G. Bosi, S. Brown, S. Sarabipour, Y. De Deene, and C. Baldock. Light scattering artefacts in a funnel phantom using optical CT. *Journal of Physics: Conference Series*, 164:012021, 2009.

[132] N. Krstajić and S. J. Doran. Focusing optics of a parallel beam CCD optical tomography apparatus for 3D radiation gel dosimetry. *Physics in Medicine and Biology*, 51:2055–2075, April 2006.

[133] A. Thomas, J. Newton, and M. Oldham. A method to correct for stray light in telecentric optical-CT imaging of radiochromic dosimeters. *Physics in Medicine and Biology*, 56:4433–4451, June 2011.

[134] N. Krstajić and S. J. Doran. Characterization of a parallel-beam CCD optical-CT apparatus for 3D radiation dosimetry. *Physics in Medicine and Biology*, 52:3693–3713, May 2007.

[135] A. Thomas, J. Newton, J. Adamovics, and M. Oldham. Commissioning and benchmarking a 3D dosimetry system for clinical use. *Medical Physics*, 38(8):4846–4857, August 2011.

[136] M. Oldham, A. Thomas, J. O'Daniel, T. Juang, G. Ibbott, J. Adamovics, and J. Kirkpatrick. A quality assurance method that utilizes 3D dosimetry and facilitates clinical interpretation. *International Journal of Radiation Oncology, Biology, Physics*, 84(2):540–546, 2012.

[137] K. Iqbal, K. A. Gifford, G. Ibbott, R. L. Grant, and S. Buzdar. Comparison of an anthropomorphic PRESAGE® dosimeter and radiochromic film with a commercial radiation treatment planning system for breast IMRT: a feasibility study. *Journal of Applied Clinical Medical Physics*, 15(1):363–374, 2014.

[138] L. J. Rankine, J. Newton, S. T. Bache, S. K. Das, J. Adamovics, D. G. Kirsch, and M. Oldham. Investigating end-to-end accuracy of image guided radiation treatment delivery using a micro-irradiator. *Physics in Medicine and Biology*, 58:7791–7801, October 2013.

[139] T. van Doorn, M. Bhat, T. P. Rutten, T. Tran, and A. Costanzo. A fast, high spatial resolution optical tomographic scanner for measurement of absorption in gel dosimetry. *Australasian Physical & Engineering Sciences in Medicine*, 28(2):76–85, 2005.

[140] J. Conklin, R. Deshpande, J. Battista, and K. Jordan. Fast laser optical CT scanner with rotating mirror and Fresnel lenses. *Journal of Physics: Conference Series*, 56:211–213, 2006.

[141] N. Krstajić and S. J. Doran. Fast laser scanning optical-CT apparatus for 3D radiation dosimetry. *Physics in Medicine and Biology*, 52:N257–N263, May 2007.

[142] J. Vandecasteele and Y. De Deene. Optimization of a fast optical CT scanner for nPAG gel dosimetry. *Journal of Physics: Conference Series*, 164:012024, 2009.

[143] N. Krstajić and S. Doran. Initial characterization of fast laser scanning optical CT apparatus for 3-D dosimetry. *Journal of Physics: Conference Series*, 164:012022, 2009.

[144] A. E. Papadakis, T. G. Maris, G. Zacharakis, V. Papoutsaki, C. Varveris, J. Ripoll, and J. Damilakis. Technical Note: A fast laser-based optical-CT scanner for three-dimensional radiation dosimetry. *Medical Physics*, 38(2):830–835, February 2011.

[145] A. Jirasek, D. Rudko, and D. Wells. A prototype fan-beam optical CT scanner for polymer gel dosimetry. *Journal of Physics: Conference Series*, 164:012025, 2009.

[146] W. G. Campbell, A. Jirasek, and D. Wells. Preliminary investigations with a photodiode-based fan-beam optical CT scanner. *Journal of Physics: Conference Series*, 250:012024, 2010.

[147] A. J. Venning, S. Brindha, B. Hill, and C. Baldock. Preliminary study of a normoxic PAG gel dosimeter with tetrakis (hydroxymethyl) phosphonium chloride as an anti-oxidant. *Journal of Physics: Conference Series*, 3:155–158, 2004.

[148] S. Brindha, A. J. Venning, B. Hill, and C. Baldock. Experimental study of attenuation properties of normoxic polymer gel dosimeters. *Physics in Medicine and Biology*, 49:N353–N361, October 2004.

[149] P. DeJean, R. Senden, K. McAuley, M. Rogers, and L. J. Schreiner. Initial experience with a commercial cone beam optical CT unit for polymer gel dosimetry II: Clinical potential. *Journal of Physics: Conference Series*, 56:183, 2006.

[150] A. Jirasek, M. Hilts, C. Shaw, and P. Baxter. Investigation of tetrakis hydroxymethyl phosphonium chloride as an antioxidant for use in x-ray computed tomography polyacrylamide gel dosimetry. *Physics in Medicine and Biology*, 51:1891–1906, March 2006.

[151] P. Baxter, A. Jirasek, and M. Hilts. X-ray CT dose in normoxic polyacrylamide gel dosimetry. *Medical Physics*, 34(6):1934–1943, 2007.

[152] C. Xu, F. Verhaegen, D. Laurendeau, S. A. Enger, and L. Beaulieu. An algorithm for efficient metal artifact reductions in permanent seed implants. *Medical Physics*, 38(1):47, January 2011.

[153] Y. Chen, Y. Li, H. Guo, Y. Hu, L. Luo, X. Yin, J. Gu, and C. Toumoulin. CT metal artifact reduction method based on improved image segmentation and sinogram in-painting. *Mathematical Problems in Engineering*, 2012(786281):1–18, 2012.

[154] T. Olding and L. J. Schreiner. Cone-beam optical computed tomography for gel dosimetry II: imaging protocols. *Physics in Medicine and Biology*, 56:1259–1279, February 2011.

[155] B. Azadbakht and K. Adinehvand. Comparison of energy dependence of PAGAT polymer gel dosimeter with electron and photon beams using magnetic resonance imaging. *Research Journal of Applied Sciences, Engineering and Technology*, 4(3):236–240, February 2012.

[156] W. G. Campbell, A. Jirasek, and D. Wells. Recent developments with a prototype fan-beam optical CT scanner. *Journal of Physics: Conference Series*, 444:012066, 2013.

[157] D. T. Moore. Gradient-index optics: a review. *Applied Optics*, 19(7):1035–1038, April 1980.

[158] A. Savitzky and M. J. E. Golay. Smoothing and differentiation of data by simplified least squares procedures. *Analytical chemistry*, 36(8):1627–1639, July 1964.

[159] T. Li, X. Li, J. Wang, J. Wen, H. Lu, J. Hsieh, and Z. Liang. Nonlinear sinogram smoothing for low-dose X-ray CT. *IEEE Transactions on Nuclear Science*, 51(5):2505–2513, October 2004.

[160] P. J. La Rivière and D. M. Billmire. Reduction of noise-induced streak artifacts in X-ray computed tomography through spline-based penalized-likelihood sinogram smoothing. *IEEE Transactions on Medical Imaging*, 24(1):105–111, January 2005.

[161] W. G. Campbell, A. Jirasek, and D. Wells. Revealing the impact of radiation-induced refractive index changes in polymer gel dosimeters. *Journal of Physics: Conference Series*, 444:012077, 2013.

[162] W. G. Campbell, D. M. Wells, and A. Jirasek. Radiation-induced refraction artifacts in the optical CT readout of polymer gel dosimeters. *Medical Physics*, 41(11), November 2014.